

Dissertation

submitted to the

Combined Faculties for the Natural Sciences and for Mathematics

of the

Ruperto-Carola University of Heidelberg, Germany

for the degree of

Doctor of Natural Sciences

Put forward by

Dipl.-Phys.: Daniil Nekrassov

born in: Moscow, Russia

Oral examination: 21 May 2010

A detailed study of
The H.E.S.S. data from the
Galactic Center region

Referees: Prof. Dr. Werner Hofmann
Prof. Dr. Heinz Völk

Abstract

The High Energy Stereoscopic System, H.E.S.S., is an array of four imaging atmospheric Cherenkov telescopes, located in the Khomas highlands of Namibia, designed for the exploration of very high-energy ($E > 100$ GeV) γ -ray emission in the universe, arising in non-thermal processes. Its location in the southern hemisphere renders sensitive observations of a large region of the Galactic Plane possible. In particular, a deep exposure of the Galactic Center region allows detailed studies of the observed emission, helping to identify the sources of the radiation and the physics processes at play. In this thesis, new methods are developed to study both the morphological and spectral properties of diffuse very high-energy γ -ray emission from the Galactic Center region. Assuming that the radiation originates from hadronic interactions of diffusing cosmic rays with the ambient matter, this study helps to constrain the parameter space of cosmic-ray diffusion in the Galactic Center region. The second part of this work introduces new methods to search for signals of Dark Matter annihilations, putting upper-limits on the production of spectral line features in the H.E.S.S. Galactic Center data. Finally, an upper-limit on the total annihilation cross-section of Dark Matter particles is derived.

Kurzfassung

H.E.S.S. ist ein System aus vier abbildenden Cherenkov-Teleskopen und untersucht sehr hochenergetische ($E > 100$ GeV) Gammastrahlung aus dem Universum, die bei nicht-thermischen Prozessen entsteht. Aufgrund seiner Lage in der Süd-Hemisphäre kann das H.E.S.S.-Experiment sehr empfindliche Beobachtungen von einem großen Teil der Galaktischen Ebene durchführen. Die große Menge an gesammelten Daten aus der Region des Galaktischen Zentrums erlaubt detaillierte Studien der dort detektierten Emission, die dazu dienen, den Ursprung der Strahlung sowie die dort stattfindenden physikalischen Prozesse zu untersuchen. Neuentwickelte Methoden für die Analyse der diffusen Emission aus dem Galaktischen Zentrum ermöglichen eine weitgehende Einschränkung der Diffusionsparameter für die hadronische kosmische Strahlung, falls diese für die beobachtete Gamma-Emission verantwortlich ist. Der zweite Teil der Arbeit handelt von der Analyse der Daten im Bezug auf mögliche Signale von Paar-Annihilation der Dunklen Materie in der gleichen Region, die zur Bestimmung der oberen Grenzen sowohl für einen möglichen Fluß-Beitrag durch spektrale Signaturen als auch für den gesamten Wechselwirkungsquerschnitt der Paar-Annihilation führt.

Contents

List of Figures	III
List of Tables	VII
Preface	1
1 Non-thermal phenomena in the Galactic Center Region	3
1.1 Morphology and main components of the Galactic Center region	3
1.2 TeV observations of the Sgr A region	6
1.2.1 Detection in TeV γ -rays	6
1.2.2 Related observations at other wavelengths	7
1.2.3 Interpretation of the origin of very high-energy γ -ray emission	12
1.3 Other sources	13
1.4 Diffuse emission	14
1.5 Galactic Center halo	16
1.6 Open questions	16
2 Detection of very high-energy γ-rays with H.E.S.S.	19
2.1 Air showers	19
2.1.1 Electromagnetic air showers	20
2.1.2 Hadronic air showers	20
2.1.3 Cherenkov radiation from air showers	20
2.2 H.E.S.S. experiment and the imaging atmospheric Cherenkov technique . .	22
2.2.1 Imaging atmospheric Cherenkov technique	23
2.2.2 The H.E.S.S. experiment	24
2.3 H.E.S.S. data analysis	26
2.3.1 Data taking	26
2.3.2 Data preparation and calibration	26
2.3.3 Event reconstruction	27
2.3.4 Event selection	28
2.3.5 Background subtraction	30
2.3.6 Spectrum reconstruction	32
3 Analysis of the diffuse emission from the Galactic Center Region	35
3.1 Theoretical background and modelling	35
3.1.1 Short overview of propagation models	35
3.1.2 Cosmic ray diffusion	37
3.1.3 Diffusion model	39
3.2 Analysis of H.E.S.S. data	46
3.2.1 Dataset	47

3.2.2	Study of the diffuse emission	49
3.2.3	Improvement on parameter space restriction using the energy information	58
3.3	Interpretation and conclusions	79
4	Search for γ-rays from Dark Matter annihilations in the Galactic Center halo	83
4.1	Evidences for the existence of Dark Matter	83
4.2	γ -rays from DM interactions in space and their observations	85
4.2.1	DM particle candidates	85
4.2.2	DM density distribution	87
4.2.3	Searches for DM signals performed by IACTs	88
4.2.4	New approach: Search for spectral features	90
4.3	Development of the peak search algorithm and application to the GC halo .	90
4.3.1	Calculation of the spectral distribution	91
4.3.2	Development of the peak search procedure	95
4.3.3	Application to the H.E.S.S. data from the GC halo	97
4.3.4	Background subtraction for the GC halo: The reflected pixel method	100
4.3.5	Combination of results	102
4.4	Determination of upper limits on $\langle\sigma v\rangle$ for a continuum spectrum	103
4.5	Discussion and conclusions	109
5	Summary and outlook	113
A	Supplementary information for the diffuse emission analysis	115
A.1	Supplementary figures and tables	115
A.2	Standard spectral analysis	127
B	Supplementary information for the dark matter analysis	133
B.1	Supplementary figures	133
B.2	Analysis of off-data	139
	Bibliography	147

List of Figures

1.1	Galactic Center region in radio	7
1.2	Galactic Center region in infrared and X-rays	8
1.3	Molecular clouds in the Galactic Center region	9
1.4	Galactic Center region in VHE γ -rays in 2004	10
1.5	Compilation of spectral points for HESS J1745–290	11
1.6	Determination of position of HESS J1745–290	11
1.7	SED of HESS J1745–290	14
2.1	Electromagnetic and hadronic showers	21
2.2	Shower imaging	23
2.3	Cherenkov images in a H.E.S.S. camera	24
2.4	The site of H.E.S.S.	24
2.5	Stereoscopic reconstruction	28
2.6	Distribution of MRSW and MRSL for γ -rays and background	30
2.7	PSF and energy resolution for different cut sets	31
2.8	Background subtraction methods	33
2.9	Example of spectrum reconstruction	34
3.1	γ -ray flux from the energy independent diffusion model	40
3.2	Energy dependent diffusion	41
3.3	Face-on velocity distribution in the Galactic Center region	42
3.4	Face-on distribution of molecular clouds in the Galactic Center region	43
3.5	Mean distances of molecular clouds for 2-D and 3-D diffusion models	44
3.6	Photons from proton-proton collisions	45
3.7	γ -ray flux from 2-D diffusion model	46
3.8	γ -ray flux maps from 2-D and 3-D diffusion models	47
3.9	Current view on Galactic Center region in VHE γ -rays	50
3.10	Longitude profiles of the diffuse emission region	53
3.11	Published longitude profile of the diffuse emission region	54
3.12	Latitude profiles before source subtraction	54
3.13	Latitude profiles after source subtraction	55
3.14	Profiles of the fit region around HESS J1745–290	56
3.15	Profiles of the fit region around G0.9 + 0.1	57
3.16	χ^2 scan using total excess without systematic errors (2-D)	59
3.17	χ^2 scan using total excess with systematic errors (2-D)	60
3.18	χ^2 scan using total excess with systematic errors (3-D)	61
3.19	Longitude profiles of the best fit models	62
3.20	Correlation between predicted and measured γ -ray flux (2-D)	62
3.21	Correlation between predicted and measured γ -ray flux (3-D)	63
3.22	Simulated energy distributions for γ -rays and background	63

3.23	Radial acceptance profiles for the low and high energy band	64
3.24	Galactic Center region in low and high energy bands	65
3.25	Difference between the PSF for the low and high energy bands.	66
3.26	Longitude profiles for low and high energy bands before source subtraction	67
3.27	Longitude profiles for low and high energy bands after source subtraction .	68
3.28	χ^2 scan using excess in energy bands with systematic errors (2-D)	69
3.29	χ^2 scan using excess in energy bands with systematic errors (3-D)	70
3.30	Longitude profiles of the best fit models for low and high energy band . . .	71
3.31	Predicted and measured γ -ray flux (2-D) for low energy band	72
3.32	Predicted and measured γ -ray flux (3-D) for low energy band	72
3.33	Predicted and measured γ -ray flux (2-D) for high energy band	73
3.34	Predicted and measured γ -ray flux (3-D) for high energy band	73
3.35	Example of a bad fit model not excluded by scans	74
3.36	Contrast and index distribution of the diffuse emission region	76
3.37	Contrast latitude profiles	77
3.38	Compilation of scans for the 2-D diffusion model	79
3.39	Compilation of scans for the 3-D diffusion model	80
4.1	Rotational curve of the NGC6503	84
4.2	Spectrum from hard internal bremsstrahlung	86
4.3	Einasto and NFW density profiles	88
4.4	Upper limits for Sgr Dwarf	89
4.5	On and off-regions for the Dark Matter analysis	91
4.6	Energy distribution of on-events	92
4.7	Effective area distribution for on-region	94
4.8	Spectral distribution of on-events	94
4.9	Weighted spectral distribution of on-events	95
4.10	Weighted spectral distribution of on-events and MC protons	95
4.11	Working principle of the peak search algorithm	98
4.12	Various γ -ray peaks used in the analysis	99
4.13	Peak upper limits without background subtraction	100
4.14	Working principle of the reflected pixel method	102
4.15	Acceptance distribution of the reflected pixel method	103
4.16	Spectral distribution from the on and the off-region (all-tel)	104
4.17	Spectral distribution from the on and the off-region (4-tel)	105
4.18	Reconstructed spectrum of HESS J1745–290	106
4.19	Peak upper limits with background subtraction	107
4.20	Compilation of peak upper limits	108
4.21	Final peak upper limits	108
4.22	Parametrization of the γ -ray spectrum from Dark Matter interactions . . .	109
4.23	Upper limits on $\langle\sigma v\rangle$ (Einasto profile)	110
4.24	Upper limits on $\langle\sigma v\rangle$ (NFW profile)	110
4.25	Compilation of H.E.S.S. (galactic halo) and Fermi peak upper limits	111
4.26	Compilation of upper limits on $\langle\sigma v\rangle$	112
A.1	Example for derivation of face-on MC distribution	116
A.2	Off-significance from the Galactic Center region	117
A.3	Off-significance from the Galactic Center region (low energy)	117

A.4	Off-significance from the Galactic Center region (high energy)	118
A.5	Latitude profiles before source subtraction (low energy)	118
A.6	Latitude profiles after source subtraction (low energy)	119
A.7	Latitude profiles before source subtraction (high energy)	119
A.8	Latitude profiles after source subtraction (high energy)	120
A.9	Ratio of longitude profiles between low and total energy bands	120
A.10	Ratio of longitude profiles between high and total energy bands	121
A.11	Ratio of longitude profiles between low and high energy bands	121
A.12	Allowed parameter space for the 2-D diffusion model	122
A.13	Allowed parameter space for the 3-D diffusion model	123
A.14	On-regions for standard spectral analysis	127
A.15	Index distribution of the diffuse emission region	128
A.16	Correlation between flux and index	130
A.17	χ^2 scan using index distribution	131
B.1	Pointing positions	133
B.2	Core distances for on and off-events (all-tel)	134
B.3	Core distances for on and off-events (4-tel)	135
B.4	Offset distributions for on and off-events.	136
B.5	Peak upper limits for 10% energy resolution	137
B.6	Peak upper limits for 20% energy resolution	137
B.7	Peak upper limits for 30% energy resolution	138
B.8	Pointings for the analysis of off-data	140
B.9	Spectral distribution for off-data	141
B.10	Peak upper limits for off-data (all-tel)	142
B.11	Peak upper limits for off-data (4-tel)	143
B.12	Compilation of peak upper limits for off-data	144
B.13	Final peak upper limits for off-data	144
B.14	Compilation of H.E.S.S. (off-data) and Fermi peak upper limits	145

List of Tables

2.1	Hard and standard cut sets	30
3.1	Statistical results for HESS J1745–290 for different analysis configurations	49
3.2	Statistical results for the diffuse emission for different analysis configurations	51
3.3	Statistical results for HESS J1745–290 for low and high energy bands . . .	64
4.1	Statistical results for the Galactic Center halo analysis	92
4.2	Peak upper limits for all configurations	109
A.1	Statistical results for the diffuse emission for the low energy band	115
A.2	Statistical results for the diffuse emission for the high energy band	115
A.3	Allowed parameter space for the 2-D diffusion model	124
A.4	Allowed parameter space for the 3-D diffusion model	125
A.5	Results from the standard spectral analysis of the diffuse emission	132
B.1	Statistical results for the analysis of off-data	139
B.2	Peak upper limits for all configurations for off-data	141

Preface

Since 1989 – the year of the discovery of the first very high-energy ($E > 100$ GeV) γ -ray source, the Crab Nebula (Weekes et al. 1989) – the field of ground-based γ -ray astronomy has rapidly evolved. Nowadays, more than 100 astrophysical sources are known to emit photons in the TeV range, both of galactic and extragalactic origin. The majority of these sources were discovered by H.E.S.S., the currently most successful experiment in the very high-energy γ -ray astronomy. Since its completion in December 2003, H.E.S.S. has been conducting dedicated observations of various objects of interest as well as an extensive scan of Galactic plane (Aharonian et al. 2006c), which revealed a large number of Galactic TeV emitters. Amongst others, remnants of supernova explosions, pulsars and active galactic nuclei are now known to constitute astrophysical laboratories, in which charged particles are accelerated to ultra-relativistic energies. Even though one of the main goals of this field - the determination of the origin of hadronic cosmic rays that bombard the Earth's atmosphere, first detected by Victor Hess in 1912, is still not doubtlessly achieved – there has been a significant scientific progress, in particular the characteristics of sources detected so far contribute a lot to the understanding of particle acceleration processes.

During now more than 6 years of operation, H.E.S.S. has in particular performed deep exposures of some regions of the sky, which raise a special interest for high-energy astrophysics. The collected data allows sophisticated studies of the detected emission, going beyond pure source detection (see e.g. Aharonian et al. (2006e) and Aharonian et al. (2007)), aiming at detailed understanding of the underlying astrophysical processes. Among those regions, the **Galactic Center region** is the most prominent Galactic representative. The presence of the super-massive black hole Sgr A* at the dynamical center of the Galaxy makes it an unique environment, offering the possibility to study the non-thermal processes in vicinities of galactic nuclei in general. Moreover, this area is populated with a high density of objects of various types, also hosting several regions of non-thermal interactions. In particular, several very high-energy sources were discovered in this region, including a point source coincident with Sgr A* and a region of diffuse radiation (**diffuse emission**). The latter is believed to arise from interactions of a local, diffusing hadronic cosmic ray population, accelerated by a central source, with ambient matter (Aharonian et al. 2006d). The current data set allows detailed studies of this emission, leading to a restriction of the parameter space of cosmic-ray diffusion, taking place in the Galactic Center region. Moreover, the gravitational center of the Milky Way presumably hosts the largest density of Galactic **Dark Matter**, which according to common knowledge is the dominant matter component of the universe. Interactions of Dark Matter constituents in the Galactic Center region might be noticeable in very high-energy γ -rays, both as γ -ray line signals and a continuum emission, hence a careful search for its signals in the available H.E.S.S. data is performed.

This work is organized as follows:

- ◇ In Chapter 1 the non-thermal view of the Galactic Center region is introduced and the motivation for the studies performed within the scope of this work is given.
- ◇ In Chapter 2 the working principle of the H.E.S.S. experiment is described, including the data analysis techniques.
- ◇ The analysis of the diffuse emission in the Galactic Center region is described in Chapter 3. It is shown, how studies of its spectral and morphological properties, using new developed analysis methods, help to constrain the parameter space of cosmic-ray propagation in this region.
- ◇ Chapter 4 deals with the analysis of the Galactic Center region data with respect to possible signals from Dark Matter interactions. New methods are developed to search for possible spectral signatures in H.E.S.S. data, also helping to generally restrict the parameter space for annihilations of Dark Matter particles.
- ◇ Finally, the obtained results are summarized and a brief outlook is given.

1 Non-thermal phenomena in the Galactic Center Region

The inner part of the Milky Way belongs to the most complex regions studied in high-energy astrophysics. First of all, it hosts a **super-massive black hole** (SMBH) that was discovered in radio in 1974 (Balick & Brown 1974), which, given its distance of 8.5 kiloparsecs (kpc) (Ferrière et al. 2007), is the closest Galactic Nucleus to Earth and is therefore used to study the physical phenomena in such environments. Various observations in radio, microwave, infrared, X-rays and γ -rays followed that discovery and revealed an enormous density of emitting objects in every waveband, while optical and ultra-violet observations are completely obscured by dust in the line of sight. In this chapter, first the overall morphology and constituents of the **Galactic Center region** (GC region) are presented and then TeV observations, including published results from H.E.S.S. and other Cherenkov telescopes, and observations in other wavebands relevant for non-thermal interactions, are summarized and discussed. Finally, based on the presented observational results, the motivation for the studies developed within the framework of this work is given.

1.1 Morphology and main components of the Galactic Center region

The Milky Way has a density distribution of matter forming essentially five spiral arms. This shape is dominant down to the galactocentric ¹ radius of 3 kpc. For smaller radii, the density strongly decreases, defining the so-called "zone of avoidance", which surrounds the **Central Molecular Zone** (CMZ). The latter extends over about 600 pc in galactic longitude and 200 pc in latitude around the dynamical center of the Milky Way (around $4^\circ \times 1.5^\circ$ in angular coordinates), revealing an ellipsoidal shape (Ferrière et al. 2007), (Goldwurm 2008)). It is a very dense region hosting, among other objects, about 10% of the total molecular mass of the Galaxy that can predominantly be found in **Giant Molecular Clouds** (GMC), a large number of objects producing thermal and non-thermal emission and the SMBH Sgr A*. The shape of the CMZ is believed to be due to a barred gravitational potential acting in the central part of the Galaxy (Ferrière et al. 2007), making the Milky Way belong to the class of **spiral barred galaxies**.

The spatial extension of the CMZ defines the GC Region, as it is used throughout this work. A good impression about its complexity provides the image obtained with the VLA telescope at 90cm wavelength (see Fig. 1.1) (LaRosa et al. 2000). It shows a complex morphology consisting mainly of **molecular clouds** (MCs), **supernova remnant** (SNR)

¹ The galactocentric radius is the distance from the center of our Galaxy. The Sun is located at a galactocentric radius of $R = 8.5$ kpc.

shells and HII regions. A large population of stars is seen in the infra-red waveband (Fig. 1.2), of which some are concentrated in stellar clusters Arches and Quintuplet (X-ray image in Fig. 1.2).

Sgr A region

When the radio counterpart of the SMBH, Sgr A*, was first detected (Balick & Brown 1974), the resolution of the instrument was too low to resolve the overall morphology of the Sgr A region. As observations improved, it was discovered that apart from the non-thermal emission from the SMBH, the region exhibits an expanding non-thermal shell from the SNR called Sgr A East, a thermal, spiral-shaped diffuse HII nebula Sgr A West, the stellar cluster IRS 16 and two GMCs (Goldwurm 2008). Since these objects are located within just a few parsecs, their interactions are especially interesting from the point of view of high energy astrophysics, knowing that SMBHs, SNR shells and objects in stellar clusters² can accelerate particles to relativistic energies, while regions of dense molecular gas provide sites of γ -ray creation both for hadrons and leptons. However, such a density of possible candidates for high energy radiation is a challenge for a proper source identification, as described in Sec. 1.2.

Sgr A*

Since the discovery of the radio source Sgr A*, many observations at different wavelengths have been carried out (see Sec. 1.2). An important confirmation for its existence was provided by infra-red measurements of the orbits of stars within 1" distance from Sgr A* by VLT and Keck (Eisenhauer et al. (2005), Ghez et al. (2008)). The latest results allow the conclusion that a mass of $3 - 4 \times 10^6 M_{\odot}$ is confined within a radius smaller than 100 astronomical units, what in fact can be only fulfilled by the presence of a SMBH (Reid & Brunthaler 2004). The spectrum of Sgr A*, measured from radio to the infrared domain helped to establish the understanding of its quiescent non-thermal low energy radiation as synchrotron emission from relativistic electrons (Duschl & Lesch (1994), Melia et al. (2000)). Additionally, the overall flux level of near-infrared emission from Sgr A* was monitored by VLT (Melia et al. 2000), which measured the flaring activity of Sgr A* in the infrared domain, later confirmed by Keck (Ghez et al. 2004). The spectrum of flaring emission can again be explained by synchrotron emission from a population of electrons, accelerated to relativistic energies or, as an alternative explanation, by expansion of hot plasma, occurring like in extragalactic radio jets (Goldwurm 2008).

Sgr A* was also detected in X-Rays (Muno et al. 2004), however its luminosity, $L = 2 \cdot 10^{33} \text{ erg s}^{-1}$ in the 2-10 keV band, is very low compared to other galactic nuclei (Narayan et al. 1998). This fact is explained by a now widely accepted theory of Radiative Inefficient Accretion Flow, which explains that the inefficiency of the accretion activity of Sgr A*, suggested by the level of X-ray emission, is due to convection effects, leading to outflow or

² It is also assumed that stellar clusters themselves can accelerate particles through collective effects such as colliding winds of massive stars or the interactions of several SNR ejecta (Ohm et al. 2009).

winds of accreting material (Goldwurm 2008). The observational results for X-rays and for other wavelengths must be taken into account by models that describe possible mechanisms for particle acceleration in the vicinity of the SMBH. At the same time, the low luminosity of Sgr A* from IR to optical, which accounts to $10^{-8}L_{\text{edd}}$, with L_{edd} being the Eddington luminosity³, makes the vicinity of the SMBH transparent to γ -rays, otherwise shielded by pair-production of very high-energy γ -rays with ambient radiation (Aharonian & Neronov 2005). Furthermore, X-ray satellites detected bright flares from Sgr A* and also took part in multiwavelength campaigns monitoring its flaring activity (Baganoff 2005), (Goldwurm et al. 2003). Like already discussed above, synchrotron emission from relativistic electrons close to the SMBH is one way to explain the observed spectra. But expanding hot plasma can also account for at least some of the flare emission (Goldwurm 2008).

Molecular clouds

For understanding of the propagation and interaction of accelerated relativistic particles, knowledge about the matter distribution and the magnetic field configuration (and also radiation fields for electrons/positrons) in the region of interest is important. As far as the matter distribution is concerned, as already mentioned, the GC region hosts about 10% of the total molecular material of the galaxy. Usually, its distribution is mapped using CO^{12} and CO^{13} rotational state transition lines, which effectively trace the H_2 density profile (Bania (1977), Dame et al. (2001)). However, this method is inappropriate for the GC region, due to the high foreground and background contamination in the corresponding velocity bands. Instead, the emission line of the CS molecule (J=1-0) is used. Its advantage is a higher critical density $n(H_2) \approx 10^4 \text{ cm}^{-3}$ of molecular material that is essentially only reached in the vicinity of the GC. Additionally, MCs with lower densities would be destroyed due to tidal forces present in this region (Tsuboi et al. 1999), so one can expect the entire molecular content of the GC region to be properly imaged by such observations. The most complete measurement so far was achieved by the NRO telescope (see Fig. 1.3 and Fig. 1.4). The total mass of the molecular clouds in the mapped area was estimated to be $3 - 7 \times 10^7 M_{\odot}$. Most of the molecular material is found at low rotational velocities, organized in GMCs. Such a crowded and dense environment can provide a very efficient interaction region for cosmic rays accelerated GC region.

Magnetic field

For the magnetic field configuration, the situation is much less certain. The radio map in Fig. 1.1 exhibits several thin filaments of non-thermal emission, of which the Radio Arc is the most prominent one, that are believed to harbour a population of relativistic electrons that emit synchrotron photons (LaRosa et al. 2000). Based just on these observations, the magnetic field in the GC region appears to have a poloidal shape, due to the outward curvature of these filaments, and its strength was estimated to be in the order

³ The Eddington luminosity denotes the level of electromagnetic radiation of an object, for which the gravitational and radiative pressures cancel against each other.

of ($B \sim 1$ mG) (see Ferrière (2009) and references therein). However, further radio observations of Faraday rotation and Zeeman splitting effects in the region suggested that the field strength is not uniform, ranging from ~ 10 μ G in the **Interstellar Matter** (ISM) to a few mG in the Sgr A region. Also the shape of the magnetic field appeared to be more complicated than the simple poloidal assumption. Further insights could be gathered by infrared observations of dust grains in the MCs, from which it was concluded that inside the MCs, the magnetic field is parallel to the galactic plane and is less strong than in the radio filaments (Ferrière 2009). A recent measurement puts a lower limit on the magnetic field in the GC region of 50 μ G by analyzing the large-scale non-thermal radio spectrum, given its origin as emission of relativistic electrons (Crocker et al. 2010). However, there exists no general agreement on the field strength between different observational methods and a conclusive picture of the magnetic field properties is missing, particularly affecting the understanding of particle propagation in the GC region (see Sec. 1.6 and 3.1.2).

1.2 TeV observations of the Sgr A region

The unique environment makes the GC region a prime target for very high-energy (100 GeV - 100 TeV) observations. These were extensively performed by Imaging Atmospheric Cherenkov Telescopes (IACTs) of past (Whipple, (Kosack et al. 2004)) and current generation (Cangaroo, (Tsuchiya et al. 2004), MAGIC (Albert et al. 2006), H.E.S.S. (Aharonian et al. 2004a)). Among those, the H.E.S.S. array is the most sensitive instrument, thanks to its location in the southern hemisphere, its wide field of view (5°) and the excellent hardware performance (see also chapter 2). Thus, data collected by the HESS experiment provide the most detailed picture of the GC region to date and is therefore mostly used in the following discussion.

1.2.1 Detection in TeV γ -rays

In 2004, Cangaroo II (Tsuchiya et al. 2004) and Whipple (Kosack et al. 2004) experiments reported the detection of a point source in the very center of our galaxy, positionally coincident with the SMBH Sgr A*. Cangaroo II spent 67 hours on this source, detecting it at $\approx 10\sigma$ significance (Li & Ma 1983), whereas the Whipple telescope needed 26 hours of observations, which were carried out at large zenith angles due to its location in the northern hemisphere, for a 3.7σ signal. The most sensitive measurement was then provided by the HESS experiment, which observed the GCR in 2004 for 49 hours with a complete four-telescope array⁴. The central point source (henceforth called HESS J1745–290) was detected with a significance of 38σ above background (see Fig. 1.4), its spectrum⁵ could be described with a hard power law with the photon index of $\Gamma = 2.25 \pm 0.04_{stat} \pm 0.10_{sys}$ and an integral flux of $\Phi = 1.87 \pm 0.10_{stat} \pm 0.30_{sys} \times 10^{-12}$ cm⁻² s⁻¹ above 1 TeV (see Fig. 1.5). The luminosity of the source accounts to 10^{35} erg/s between 1 TeV and 10 TeV.

⁴ First detection by HESS was based on observations with only two telescopes, the point source was detected with 9.2σ significance (Aharonian et al. 2004b).

⁵ The spectrum, first derived by Cangaroo II, largely deviated from the spectra obtained by other experiments, i.e. the spectral shape was determined as $\propto E^{-4.7 \pm 0.5}$. A new analysis by Cangaroo III yielded results, consistent with other experiments (Mizukami 2008).

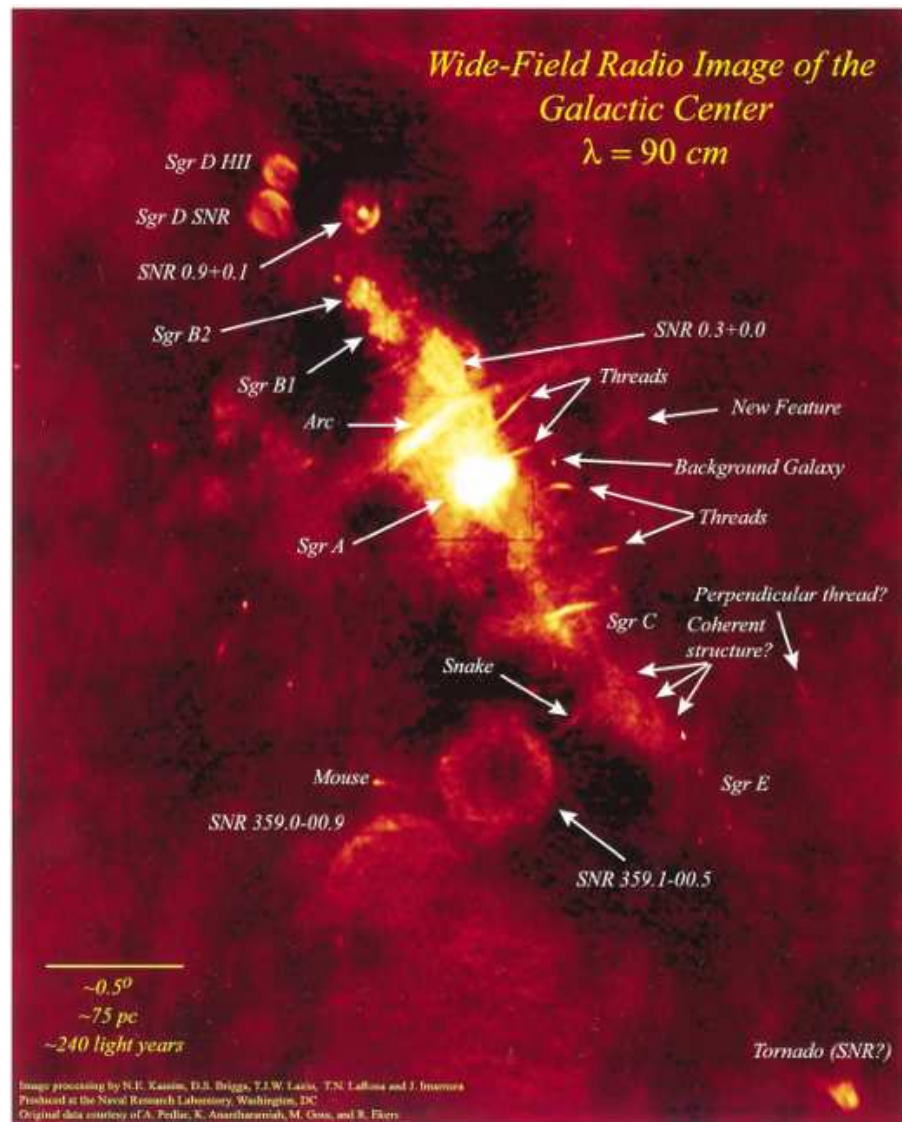
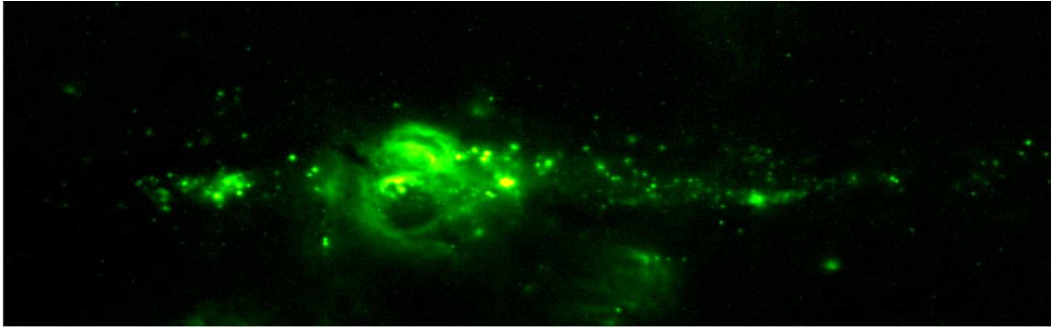


Figure 1.1: The galactic center region as observed by VLA at 90cm (LaRosa et al. 2000). Numerous features like SNR shells, thin non-thermal filaments and HII regions are visible at this wavelength.

With observations by MAGIC (Albert et al. 2006), Cangaroo III (Mizukami 2008) and a reanalysis of Whipple (Kosack 2005) data the spectral properties of HESS J1745–290 derived by H.E.S.S. were confirmed.

1.2.2 Related observations at other wavelengths

Beside emission from Sgr A*, X-ray emission was also detected from Sgr A East (Maeda et al. 2002). However, in this frequency range, the source turns out to be smaller in diameter ($\approx 4 \text{ pc}$ vs $\approx 20 \text{ pc}$ in radio) and reveals a non-thermal shell together with a thermal



(a) Spitzer's (IR) view of the GC region



(b) Chandra's (X-rays) view of the GC region

Figure 1.2: The GC region as observed Spitzer (top) (Ramírez et al. 2008), and Chandra (bottom) (Muno et al. 2009). The scale of both images is matched. A large number of point and extended sources is visible in both wavebands. In the X-ray image, the counterparts to the TeV point sources at the positions of G0.9+0.1 and Sgr A are visible.

core region. The latter is explained by a reverse shock of the expanding shell that heats the matter inside the remnant. With the help of X-ray observations it was possible to estimate that the explosion took place $\approx (10 \pm 2.5) 10^3$ years ago and the mass of the exploding star was $M = 13 - 20 M_{\odot}$, contradicting earlier estimates based on radio observations that stated the emission seen from Sgr A East is a result of up to 40 supernova explosions (Goldwurm 2008). Additionally, Chandra has discovered an energetic pulsar wind nebula G359.95-0.04 (Wang et al. 2006). It is located only $8.7''$ away from the position of Sgr A*, making it a suitable candidate for TeV emission, since despite its low X-ray luminosity $L = 10^{34}$ erg s $^{-1}$, the very dense radiation fields of the GC region provide enough photons for efficient IC interactions (see Sec. 1.2.3).

Although not related to the TeV point source at first glance, analyses of X-ray observations carried out by ASCA and Suzaku of the Sgr B HII area, the non-thermal radio filament Sgr C and the complex with the SNRs 359.0-0.09 and 359.1-0.05, reveal, that they appear to be so-called **X-ray reflection nebulae** (Murakami et al. 2000), (Ryu et al. 2009). This term means that most part of the X-ray emission received from an object is not produced there but is rather due to reflection of and fluorescence caused by X-ray photons coming from a different site, with a strong fluorescent 6.4 keV iron line located on top of a non-

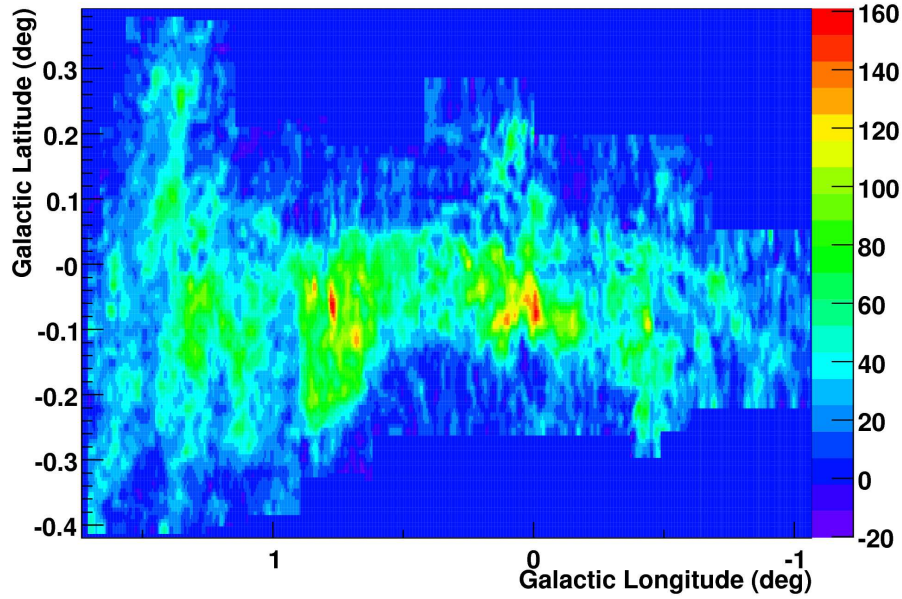


Figure 1.3: A map of molecular clouds in the galactic center region obtained by NRO telescope imaging the CS line (units are arbitrary). The map is essentially free of background, confirming the ability of CS observations to properly map the molecular content in this region (Tsuboi et al. 1999).

thermal continuum as its main characteristic. The connection to HESS J1745–290 is, that in all three cases it is assumed that the source of primary emission is the SMBH Sgr A*. The flux produced by Sgr A* that is required to fit the observations from the reflection nebulae is about 10^6 times higher than the quiescent emission observed during the last years (Goldwurm 2008). From the distance of Sgr B and Sgr C to the GC it was concluded that Sgr A* must have been very bright in X-rays some hundreds of years ago. Due to a possible correlation between X-ray flux and particle acceleration in the GC, this fact is important for studies of TeV emission from this region (see also Sec. 1.4).

Concerning counterparts at higher energies, INTEGRAL performed a deep exposure of the GC region in the energy range between 20 and 400 keV (Bélanger et al. 2006). These observations revealed several point sources, among which a source coincident with the position of Sgr A* was detected, however due to Integral’s angular resolution of $\approx 10'$ it is not yet conclusive, whether the emission has its origin directly at the SMBH or whether it is rather a diffuse radiation. The combined spectrum of soft and hard X-rays from the GC can be fit by a thermal component, produced in hot plasma, in soft and a non-thermal power law component in hard X-ray, which origin is still under exploration. Additionally, some observations were carried out together with XMM-Newton and during that period several soft X-ray flares were detected, while the emission in hard X-rays stayed steady, therefore mostly favouring the diffuse hypothesis and a link to the very high-energy emission. Besides, the detection of hard X-rays from Sgr B2 supports the interpretation that this region is a X-ray reflection nebula and therefore strengthens the indications for a past GC X-ray activity (Goldwurm 2008).

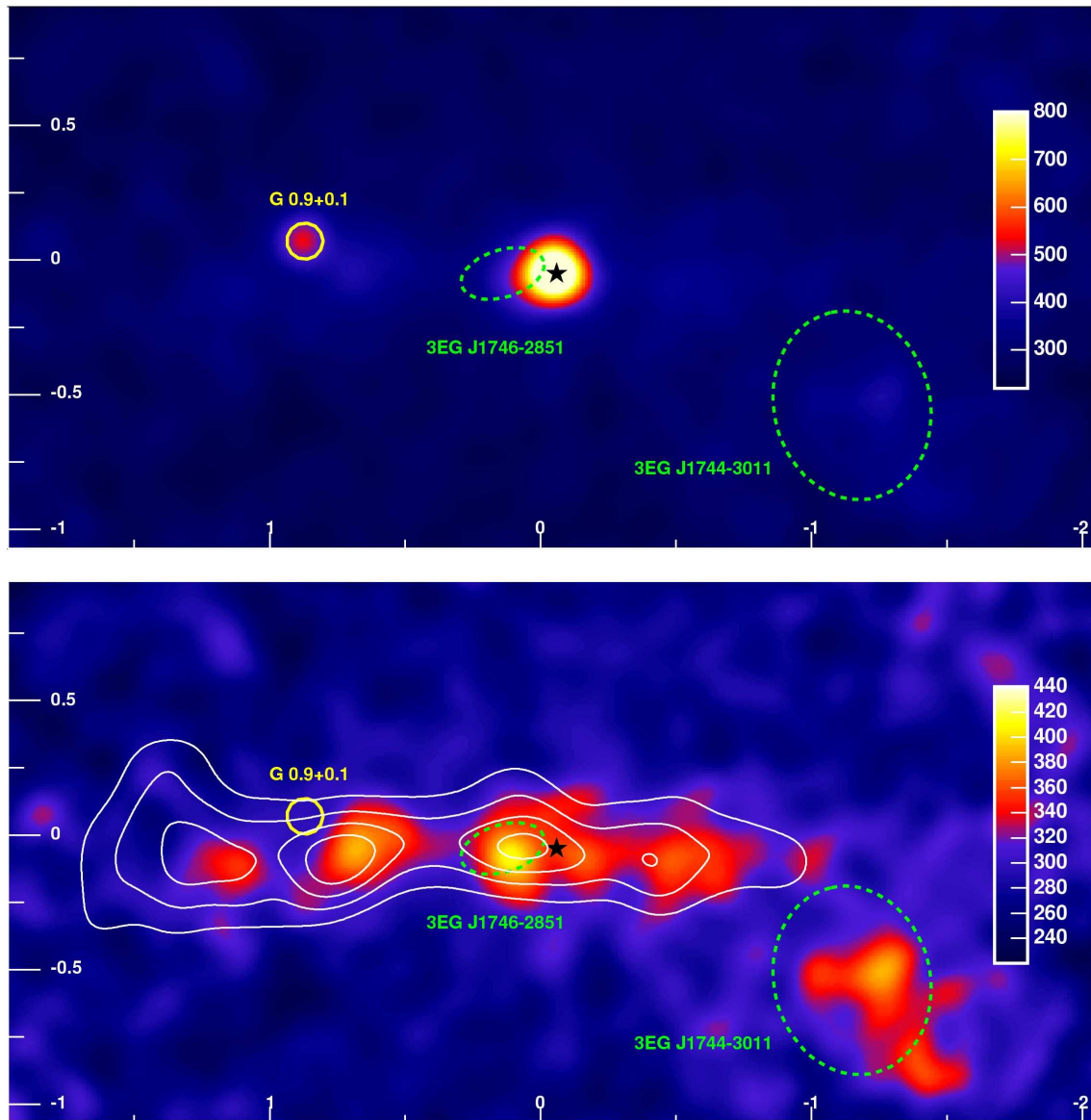


Figure 1.4: Galactic center region as seen by H.E.S.S. in 2004. In the upper image both point sources, HESS J1745–290 and G0.9+0.1 are seen. The green circles correspond to the sources detected by EGRET (Hooper & Dingus 2002). In the lower image, the faint diffuse emission appear after both point sources were subtracted. The white contours represent the density distribution of molecular clouds. Coincident with the EGRET source in the low right corner, the unidentified H.E.S.S. source HESS J1745 – 303 is visible. Image taken from (Aharonian et al. 2006d).

In the γ -ray domain (20 MeV - 100 GeV), a point source close to the position of Sgr A* was seen by EGRET (Hooper & Dingus 2002) and by the FERMI satellite launched last year (Atwood et al. 2009). While a detailed analysis of FERMI data is still under way, the spectrum of this source derived by EGRET suggests a hadronic origin for the high-energy

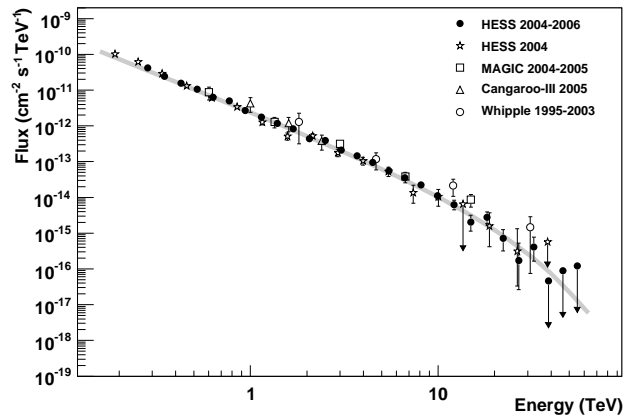


Figure 1.5: Compilation of spectral energy distributions of the GC source HESS J1745–290. Using combined H.E.S.S. data from 2004–2006 allows to extract the spectral cut-off, undetermined by previous analyses (Aharonian et al. 2009b).

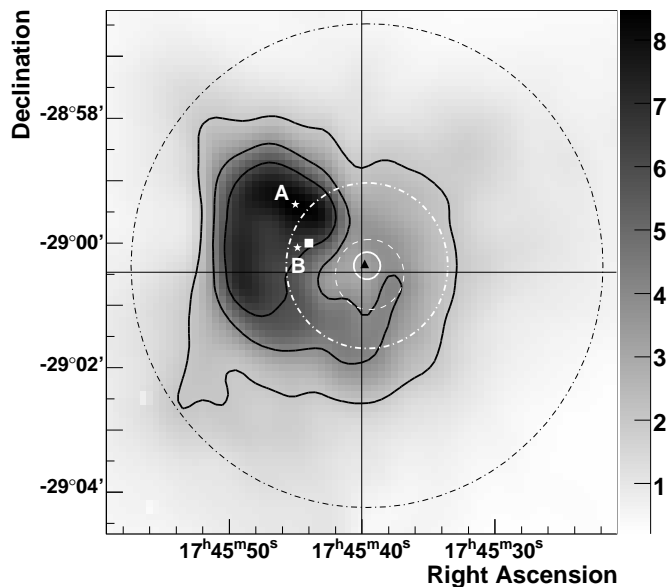


Figure 1.6: Improved position determination of HESS J1745–290 achieved by H.E.S.S. overlaid on a smoothed VLA 90cm image of Sgr A East. The centre of the SNR is denoted by the white square, the positions of Sgr A* and G359.95-0.04 are given by the cross hairs and the black triangle, respectively. The dashed white circle represents the uncertainty on the position of 2004 achieved with the standard pointing procedure, while the white circle indicates the improvement reached with the new method described in (The HESS Collaboration & Acero 2009).

emission (Mayer-Hasselwander et al. 1998). However, due to a large error on position around 0.2° , it was not possible to determine the exact location and extension of detected emission, similar to the case of INTEGRAL. Furthermore, the analysis of data from GCR is very complicated for both γ -ray experiments because of the large diffuse background in this energy range (Strong et al. 2009).

1.2.3 Interpretation of the origin of very high-energy γ -ray emission

As it was already pointed out above, the Sgr A region hosts several objects that can serve as candidates for particle acceleration. In particular, the SNR Sgr A East, the pulsar G359.95-0.04 (see Sec. 1.2.2) and Sgr A* itself were considered as viable counterparts for the central point source. Based only on the data available in 2004, no discrimination could be achieved between these possible counterparts, since the angular extension as well as spectral properties could in principle be reproduced by all these candidates (van Eldik 2008). Besides, also annihilation of Dark Matter particles was proposed as origin of the TeV emission, however the spectral analysis of 2004 data excluded the level of DM contribution higher than 10% (for a further DM discussion, see chapter 4). However, the H.E.S.S. experiment continued to observe the GC region throughout the last years, roughly tripling the total observation time. New analyses of HESS J1745-209 allowed an improved position determination (The HESS Collaboration & Acero 2009), as well as a precised measurement of spectral properties (Aharonian et al. 2009b), see Fig. 1.5.

As far as spectral analysis is concerned, it was shown for the first time that the γ -ray spectrum of HESS J1745-209 is better described with a power law having a harder index than previously published of $\Gamma = 2.10 \pm 0.04_{stat} \pm 0.10_{sys}$ together with an exponential cut-off at $E_{cut-off} = 14.7 \pm 3.4$ TeV, than by a pure power law (see Fig. 1.5). Additionally, some of observations were carried out simultaneously with X-ray telescopes. During this time, several flares occurred in the vicinity of Sgr A* in X-ray waveband, increasing the flux by up to a factor of 9, while no significant flux changes were detected in the very high-energy regime. A contemporaneous detection of flares in X-rays and very high-energy γ -rays would immediately pinpoint at least a part of the detected emission to originate from the SMBH. On the other hand, the absence of such correlation does not exclude Sgr A* as a source candidate, since some models predict absence of correlation between X-ray and γ -ray flares. The presence of a cut-off in the spectrum indicates either escape of highest energetic particles or that the energetic limit of the accelerator is reached. Still, the spectral properties can be reproduced by all source candidates, thus based just on that, no discrimination is possible (see also Fig. 1.7 for the full spectral energy distribution).

The optimization of the pointing accuracy of the H.E.S.S. telescopes results in a reduction of the systematic error on the position determination from $28''$ down to $9''$, thus making the systematic error comparable with the statistical error (see Fig. 1.6) on the position determination, if the full collected dataset is used (The HESS Collaboration & Acero 2009). The new position determination method allows to exclude the SNR Sgr A East as the source of the very high-energy emission at high significance. Both Sgr A* and

G359.95-0.04 are still compatible with the source position within errors, thus making a definite statement about the origin of the radiation impossible by means of source position determination for the current IACT generation.

Hence, with currently only Sgr A* and G359.95-0.04 as possible astrophysical counterparts for the central source HESS J1745–290, a question about the emission mechanism should be addressed. While PWNe belong to a rather standard class of very high-energy accelerators, serving as counterparts for a number of H.E.S.S. sources discovered in the galactic plane survey (Aharonian et al. 2006c), for Sgr A* specific acceleration mechanisms are required, which are valid for its extreme environment. Here, on the one hand, the unusually low luminosity of the SMBH in other wavelengths must be satisfied by models trying to explain the TeV emission, but at the same time it allows the very high-energy γ -ray photons to escape the proximity of the SMBH without significant absorption and therefore renders the study of relativistic phenomena in its direct neighbourhood possible. There are several models that were proposed to explain the TeV emission of Sgr A*, including its broad-band spectrum (see Fig. 1.7). Some use interactions of highly relativistic protons with either ambient radiation fields, followed by production of π -mesons and subsequent decays into γ -rays (for neutral pions), or interactions with other protons/nuclei from matter either in direct vicinity of the SMBH or in the local environment, where the protons diffuse, also resulting in meson production. As acceleration processes, strong electric and magnetic fields or shocks in the ambient matter are proposed (Aharonian & Neronov 2005). Also electrons are suggested as producers of the very high-energy radiation, being accelerated by well-ordered electric and magnetic fields and creating γ -rays by IC upscattering of surrounding radioation photons (van Eldik 2008). It is worthwhile mentioning, that for some acceleration mechanisms correlations with other wavelengths are implied, of which the most convincing proof would be detection of simultaneous flares e.g. of X-rays and γ -rays, that has not occurred to date, whereas for protons diffusing out from SMBH interaction zone no flaring activity is predicted (see Sec. 1.2.2).

On the other hand, the PWN G359.95-0.04 can account for the TeV emission despite its low luminosity in the X-ray band, because the radiation fields in the GC region have a sufficient density to allow electrons, accelerated by the PWN to relativistic energies, to produce the right level of very high-energy flux (Hinton & Aharonian 2007). A hint for the presence of relativistic electrons is the fact, that the non-thermal spectrum of the PWN in X-ray steepens with increasing distance to the pulsar. This effect can be caused by synchrotron cooling of the electron population in a strong magnetic field, estimated by Hinton & Aharonian (2007) as $B > 100 \mu\text{G}$.

1.3 Other sources

The thus far unprecedented sensitivity achieved in the H.E.S.S. data collected in 2004 allowed the detection of additional sources in the GC region, beside HESS J1745-209. A point source coincident with the SNR (see Fig. 1.1) G0.9+0.1 and the extended source HESS J1745-303 are visible in Fig. 1.4, which were detected by H.E.S.S.. While the origin for the emission from latter is still unclear due to a lack of adequate counterparts in other

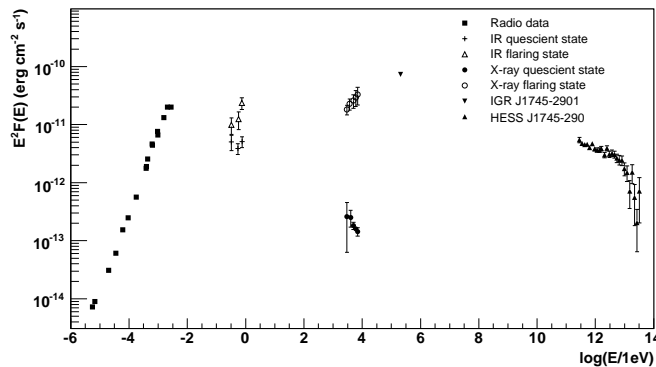


Figure 1.7: Broad-band spectrum of the GC source. Figure is taken from (Aharonian et al. 2009b).

wavebands (see Aharonian et al. (2008a) and Bamba et al. (2009) for possible interpretations), the situation for G0.9+0.1 appears to be much simpler. In fact, the TeV-emission detected from this object is most likely due to IC interactions of electrons, accelerated by a PWN inside the SNR shell, which was discovered by Chandra (Gaensler et al. 2001), see Fig. 1.2. The shell of the SNR as a source of the main part of the very high-energy emission is unlikely, given the fact that the extension of the object is compatible with a point source assumption and its position corresponds to the location of the Chandra PWN within errors.

1.4 Diffuse emission

Apart from the very high-energy sources already discussed above, H.E.S.S. has also discovered an extended emission component in the GC region (Aharonian et al. 2006d), using 55 hours of observational time, collected in 2004. This emission was revealed after subtraction of the point sources HESS J1745-209 and G0.9+0.1, see Fig 1.4. Its main morphological property is a correlation between the intensity of γ -ray emission and the density distribution of molecular clouds. Since no population of sources is present at other wavelengths, which could account for the detected emission, it seems likely that the origin of the emission is hadronic, arising through interactions of relativistic hadrons with the gas in the MCs. If this holds, it was the first time that emission in the very high-energy domain was detected that is apparently not associated with an active source, i.e. with an object, which accelerates particles. Thus, this emission can be defined as **diffuse emission**.

For γ -ray satellite experiments like EGRET or FERMI, diffuse emission from the Galactic plane is a large background for active sources, originating from interactions of the Galactic cosmic ray population with the environment⁶. For the energy range of H.E.S.S. however,

⁶ The galactic cosmic ray population is assumed to have, on average, the same spectral properties as measured on Earth. Local fluctuations are accounted for by propagation models like GalPROP (Strong et al. 2009).

this background is negligible. In fact, even in the GC region, the flux caused by the ‘sea’ of cosmic rays, would be much lower than the flux of the diffuse emission observed (Aharonian et al. 2006d), being $\Phi = 1.9 \pm 0.10_{stat} \pm 0.30_{sys} \times 10^{-11} \text{ cm}^{-2} \text{ s}^{-1}$ above 1 TeV. So either the density of the cosmic ray ‘sea’ in the GC region is higher, or the cosmic rays come from a local source. The clear lack of correlation between γ -rays and MC density for $|l| > 1 \text{ deg}$ (see Fig. 3.11) can be explained by diffusion of protons from a central source but not by a constant CR density and is thus a strong argument for the presence of a local source. Besides, the spectral shape of diffuse emission is very similar to the spectrum of HESS J1745–290, based on 2004 observations. More precisely, the spectral index of diffuse emission was measured as $\Gamma = 2.29 \pm 0.07_{stat} \pm 0.10_{sys}$ compared to $\Gamma = 2.25 \pm 0.04_{stat} \pm 0.10_{sys}$ estimated for HESS J1745–290. This fact suggests a connection between central point source HESS J1745–290 and the diffuse emission.

Using the diffusion assumption, it is possible to search for an optimal value for the diffusion coefficient of protons in the GC region that describes the morphology of diffuse emission. In (Aharonian et al. 2006d), it was stated that the data puts an upper limit on the diffusion coefficient of $D \leq 3.5 \frac{\text{kpc}^2}{\text{Myr}} (10^{30} \frac{\text{cm}^2}{\text{s}})$, if Sgr A East is taken as the source of protons, assuming that the progenitor star exploded 10^4 years ago. Besides, also Sgr A* can be the source of diffusing protons, since it might have had an explosive event, e.g. merging with a star at some time in the past. As hints for its stronger activity in the past the presence of the X-ray reflection nebula can be considered (see 1.2.2). Thus, for the SMBH as the source of protons and an active time being 10^5 years ago as assumed in (Aharonian et al. 2006d), a good description of data is achieved with $D = 0.3 \frac{\text{kpc}^2}{\text{Myr}}$.

There are several papers that followed on this topic, adopting different methods for determination of the diffusion coefficient. In Büsching et al. (2007), an analytical approach was applied by solving the transport equation for protons in the GC region using simple parametrisations for the MC density distribution. The diffusion coefficient was found to be $D = 1.6 \frac{\text{kpc}^2}{\text{Myr}}$, close to the value determined by the simple estimation in (Aharonian et al. 2006d). However, due to various uncertainties, amongst others in the actual distribution of the MCs along the line-of-sight, a systematic error of 50% was quoted. These authors later extended their study to include different “on”-times of the proton source, i.e. the time during which the source was accelerating particles (Büsching & de Jager 2008). A different approach, tracking the paths of simulated protons in a grid of molecular material, representing the density distribution in the GC region, was implemented in (Dimitrakoudis et al. 2009) for various diffusion coefficients. Taking into account the energy losses of protons through strong interactions with surrounding gas, the optimal diffusion coefficient was found to be $D = 3.0 \pm 0.2 \frac{\text{kpc}^2}{\text{Myr}}$, again consistent with the H.E.S.S. result⁷. However, a yet another method was used in (Wommer et al. 2008), which included tracking of particles exposed to the Lorentz force in a turbulent magnetic field, assumed to be present close to the GC (for observational results on magnetic field configuration, see Sec. 1.1). The outcome of this analysis was that the diffusion of particles from a central source appears to be too slow to be able to account for the morphology of the emission seen by H.E.S.S.. Instead, acceleration of particles inside the molecular clouds by e.g. Fermi-II process was

⁷ This result is also in agreement with buesching, despite the higher value for D , since the deviation is due to the inclusion of energy losses of protons, that was not taken into account in (Büsching et al. 2007).

proposed, as a natural way to achieve a correlation between γ -rays and MCs. See Sec. 3.1 for more details on CR diffusion.

1.5 Galactic Center halo

The GC halo in general is a very interesting region from the point of view of very high-energy observations not only because of acceleration processes of charged particles, but also because of more exotic sources of γ -rays like annihilation or decay of **Dark Matter** (DM) particles, since the density distribution of the galactic DM profile peaks in the GC (see Sec. 4.2.2). As far as the observations of the point source, HESS J1745–290, are concerned, it was already discussed that its origin is astrophysical, so that just an upper limit on the DM flux contribution was obtained. However, beside the stripe of the diffuse emission, containing also G0.9 + 0.1, the inner degree of the halo is free from further astrophysical sources (see Sec. 3.2) in the TeV domain. This is supported by current X-ray observations, revealing a large point source population, which show similar spectral properties and thus are believed to be of the same class of objects. Most of the “standard” X-ray sources like normal stars or X-ray binaries were essentially ruled out and currently the widely accepted interpretation of these sources are **magnetic cataclysmic variables**. This source class never appeared as site of very high-energy processes, supporting the idea that the GC region is undisturbed by astrophysical very high-energy γ -ray sources and hence a good target for DM search.

Recent results, connecting the GC halo with the DM topic, come from WMAP and FERMI observations. In the microwave frequency range, dedicated observations of the GC region are pointless because of the foreground thermal emission outshining the galactic disk. However, an interesting feature related to the GC region was found in the three-year WMAP dataset (Finkbeiner 2004), which is supposedly an excess of synchrotron emission from relativistic electrons. This so-called WMAP Haze exhibits a spherical morphology being centered in or close to the GC with a radius of 20 – 40° and is also found by an analysis of now public FERMI data, where a diffuse feature with a morphology matching the WMAP Haze was discovered (Dobler et al. 2009), which is, however, disputed in Linden & Profumo (2010). The derived spectrum can be described by IC interactions of a population of relativistic electrons, confirming the assumption that the emission seen by WMAP is synchrotron radiation of presumably the same population, which can originate from DM interactions (Finkbeiner & Weiner 2007). However, also astrophysical explanations, like massive star explosions, were proposed (Biermann et al. 2010). See Sec. 4.1 for further DM discussion.

1.6 Open questions

As it was shown in previous sections, the GC region is a very complex environment and observations are often difficult to interpret, especially in view of non-thermal processes, despite of the intensity of observations already carried out. There are a number of open questions, like the origin of the high-energy emission at the GC and the physics responsible

for the flares of Sgr A*. Additionally, the nature of diffuse emission in very high-energy γ -rays remains uncertain. Currently, there are still multiwavelength campaigns planned for monitoring the Sgr A* flaring activity and results from FERMI observations of the GC region might be promising for understanding of the γ -ray emission. For the future, experiments like Planck (microwaves), Simbol-X (hard X-rays) and CTA (next generation IACT array) will shed more light on the high-energy phenomena in this area.

However, it is worthwhile to summarize the current status of available very high-energy data to see whether there is still room for improving the understanding of the TeV view on the GC region:

- ◇ For HESS J1745–290, it appears that H.E.S.S. observations collected to date already exhaust the capabilities of the current IACT generation, allowing to reject of Sgr A East as a possible counterpart, but yet not being able to distinguish between Sgr A* and PWN G359.95-0.04 both in terms of position in spectral characteristics, due to a limited energy coverage especially for lower energies and comparably poor angular resolution. As long as no γ -ray flares will be detected, a definite statement about the nature of this source will be very difficult with the next generation of Cherenkov instruments like CTA (Wagner et al. 2009) as well. However, some insights may already be gathered from results of the FERMI experiment, if the spectrum would allow a discrimination between leptonic and hadronic origin. In latter case, the PWN interpretation might become more unlikely.
- ◇ The PWN G0.9+0.1 has an established counterpart and the emission processes seem to be understood and, while for HESS J1745–303 more multiwavelength data, especially in radio and X-ray domain, would possibly help understanding its nature, e.g. strengthen the interpretation of MCs being illuminated by SNRs (Gabici et al. 2009).
- ◇ The physical processes responsible for the diffuse emission are still unclear (see Sec. 1.4), since neither particle propagation nor the magnetic field configuration, which influences the diffusion, are fully understood (see Sec. 3.1.1). In this case, a new analysis of the diffuse emission using the now available dataset has not yet been done and might be able to determine its morphological and spectral properties more precisely. In particular, it is important to find out whether the diffusion hypothesis is still in agreement with new data, e.g. whether there is still a correlation between MCs and γ -ray that vanishes for large distances from the GC.
- ◇ Additionally, the collected dataset allows to perform searches for Dark Matter signals from the GC halo. Since for the point source DM annihilations are excluded as the main contribution (see 1.2.1), areas with less astrophysical background in the GC region can be studied.

The last two aspects are treated in the current thesis. A new analysis of the diffuse emission is developed with the aim of revising the diffusion hypothesis and constraining its parameter space, if applicable (chapter 3). Moreover, a search for DM signals from the GC halo is performed (chapter 4).

2 Detection of very high-energy γ -rays with H.E.S.S.

Energetic γ -rays from space can not be directly detected on the ground because they get absorbed in the Earth's atmosphere. Thus for a direct detection, the detector must be placed on board of a satellite orbiting the Earth, with EGRET (Hartman et al. 1999), INTEGRAL (Winkler et al. 2003) and FERMI (Atwood et al. 2009) as well-known representatives of this detector type. Such detectors can observe γ -rays up to energies of several hundreds of GeV, but due to a strongly decreasing flux of CRs with energy, their detection area, typically of the order of 1 m^2 , is not sufficient for detection of particles with even higher energies. However, particle cascades in the atmosphere, induced by very high-energy γ -rays and other CRs, can be detected on the ground due to the Cherenkov radiation, emitted by charged particles in such cascades. Thus in the energy range between $\sim 100 \text{ GeV}$ and $\sim 100 \text{ TeV}$, indirect detection is carried out by ground based **Imaging Atmospheric Cherenkov Telescopes** (IACTs). The detection area of such instruments exceeds the detection area of satellite experiments by up to six orders of magnitude, thus accounting for the decreasing flux of very high-energy particles.

The section is organized as follows: In section 2.1, the characteristics of air showers produced by γ -rays and hadronic CRs and the implications on the resulting Cherenkov light emission are discussed. In section 2.2, the H.E.S.S. instrument and the detection technique are introduced. The data analysis procedure, including methods for the rejection and subtraction of hadronic background and the reconstruction of energy spectra, is described in section 2.3.

2.1 Air showers

A particle cascade (or shower) is produced in the atmosphere, when a high-energetic particle from space hits molecules and ions in its outer layers. The type of the impinging particle influences the characteristics of such a shower. In case the particle undergoes only electromagnetic (and weak) interactions, like a photon or electron, a purely electromagnetic shower develops, containing only electromagnetically interacting particles as well. If the shower is produced by a proton or nucleus, which also interact via strong force, the created shower is partly hadronic. In the following the different characteristics of electromagnetic and hadronic showers are introduced and the implications on the profile of the subsequently emitted Cherenkov light are discussed.

2.1.1 Electromagnetic air showers

An electromagnetic air shower develops, if a high-energetic electron¹ or photon interacts with the atmosphere. In case of a photon, the first interaction with the electromagnetic field of an air nuclei leads to an electron-positron (e^\pm) pair creation, occurring after the traversed mean free path of $7/9X_0$, with $X_0 = 37.2 \text{ g cm}^{-2}$ being the radiation length for electrons², whereas the interaction of an incoming electron with an air nuclei leads to irradiation of an energetic photon due to bremsstrahlung. These two processes are responsible for a subsequent exponential rise of the particle number, until the mean energy of particles drops below 80 MeV and energy losses due to ionization start to become dominant. From this point on, the number of particles decreases and the shower starts to die out.

The number of particles in the shower is proportional to the energy of the primary particle. This fact is exploited by IACTs for the energy reconstruction of the latter (see Sec. 2.3). The trajectories of created particles remain close to the direction of the incident one, however due to multiple Coulomb-scattering of created e^\pm -pairs electromagnetic showers get a certain lateral extent, which is, however, small compared to its longitudinal extent, which accounts to several kilometers, as it can be seen in Fig. 2.1.

2.1.2 Hadronic air showers

Like electrons and photons, CR nuclei initiate a particle cascade in the atmosphere as well. However, since its constituent quarks also undergo strong interactions, a hadronic shower deviates from the electromagnetic one. For a hadronic shower, the dominant process for creation of secondary particles is hadronization, in which further hadronic particles like mesons and baryons are produced. Due to meson decays into leptons and photons, each hadronic shower also comprises an electromagnetic component (see Sec. 2.1.3). The mass of particles, created in strong interactions, is much higher than the mass of electrons, thus their transverse momentum is larger and the shower has a greater lateral extent, compared to the electromagnetic one (see Fig. 2.1). Besides, the complex multiplicity of strong interactions results in a much more irregular shape of the shower, whereas for electromagnetic showers mainly three-particle processes play a role, as explained above. Moreover, a part of the energy of a hadronic shower is carried away by muons and neutrinos, created in charged mesons' decay, whereas the energy of electromagnetic showers mostly remains in its constituent particles. These different characteristics affect the properties of the subsequently produced Cherenkov radiation, which is discussed in the following.

2.1.3 Cherenkov radiation from air showers

Particles, which move faster than the speed of light in a medium with the refraction index n , emit the so-called Cherenkov light. Many particles in an electromagnetic or hadronic

¹ The term electron stands here for both electrons and positrons.

² Since the atmosphere has a thickness of $\sim 1000 \text{ g cm}^{-2} \approx 27X_0$, no initial photons or electrons can reach the ground.

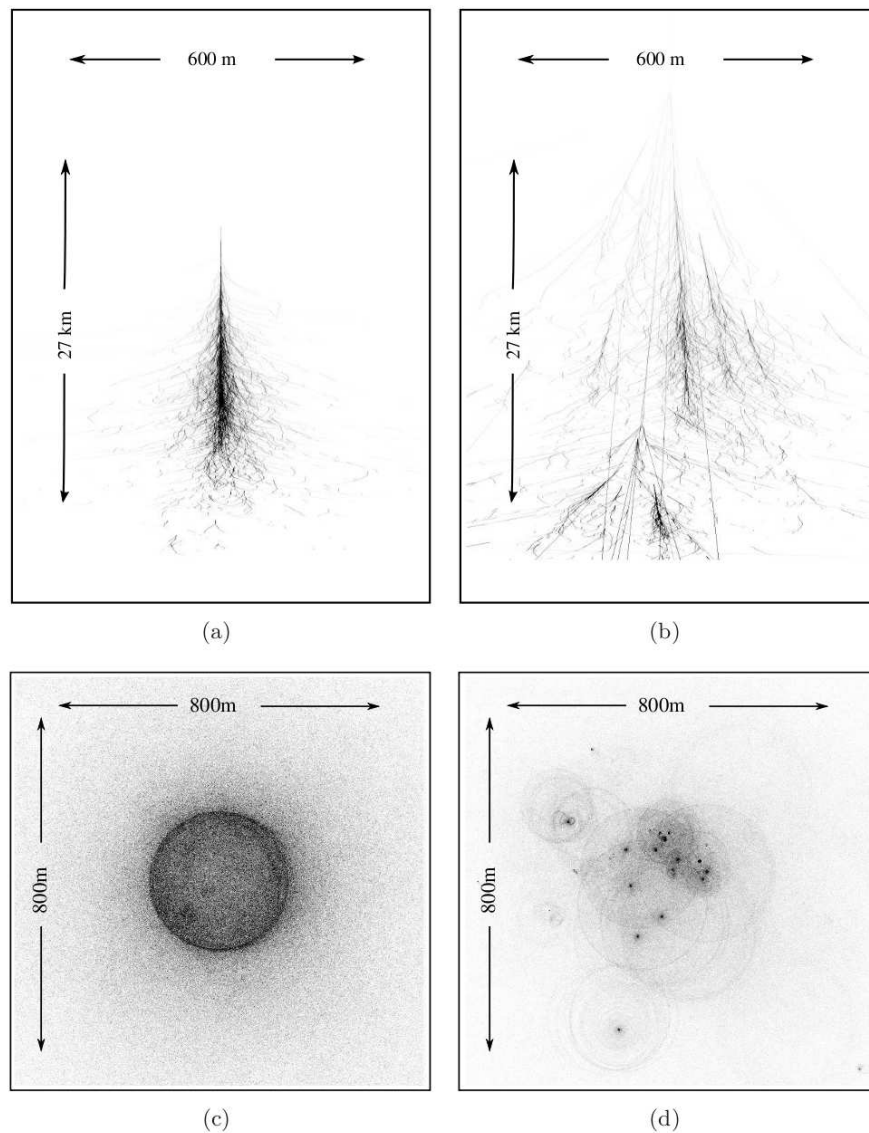


Figure 2.1: Comparison between shower shapes induced by a γ -ray (a) and by a proton (b). The distribution of Cherenkov light on the ground, emitted by relativistic shower constituents, images the shape of the shower, yielding a regular circular shape for γ -rays (c), while Cherenkov light from a proton shower has a rather disperse distribution (d). The image is kindly provided by Konrad Bernlöhner.

shower have sufficient energy to emit this radiation, if the impinging particle is energetic enough. The opening angle Θ_c of the radiation cone can be calculated as:

$$\Theta_c = \frac{1}{\beta n},$$

where β is the particle velocity, expressed in units of the speed of light. For showers in air, $\Theta_c \approx 1 - 2^\circ$, assuming $n = 1.0003$, the refraction index at sea level. Most of the

Cherenkov emission is located in the UV regime, however, due to absorption in air, the peak of the emission on the ground is shifted towards optical blue component (see Sec. 2.2).

The distribution of the Cherenkov light on the ground, emitted by particles in a shower, resembles the structure of the shower with high precision, due to the small opening angle of the Cherenkov cone. In Fig. 2.1 the distribution of light on the ground is shown for a simulated electromagnetic (c) and hadronic shower (d). For the electromagnetic shower, the light pool on the ground exhibits a homogeneous and circular shape. Given that the shower maximum, from which most of the Cherenkov light originates, occurs at ~ 10 km height, the radius of the light pool on the ground is ~ 120 m. The ring structure, that surrounds the main part of the emission, arises due to the increasing refraction index with decreasing height, resulting in such "focusing" of the Cherenkov light. Outside the ring, the light intensity on the ground rapidly decreases. The total duration of a Cherenkov light "flash" from an electromagnetic shower is of the order of 10 ns, since the shower develops along the Cherenkov light path with approximately the same velocity. As far as the hadronic case is concerned, due to an irregular and scattered shape of the hadronic shower, the light yield on the ground is irregular as well. Since the energy of a particle, needed for the production of Cherenkov photons, is proportional to its mass, electrons and muons contribute most to the Cherenkov light in a hadronic shower, making its pool on the ground even more dispersed.

The total number of Cherenkov photons reaching the ground amounts to 100 photons per m^2 for a 1 TeV γ -ray. Such a low number of photons makes a large collecting area and sensitive electronics necessary for the detection of Cherenkov light from particle cascades in the atmosphere.

2.2 H.E.S.S. experiment and the imaging atmospheric Cherenkov technique

In the energy range between ~ 50 GeV and ~ 100 TeV, the atmospheric imaging technique has proven to be the most successful and efficient one. This technique was first invented by the Whipple collaboration, which discovered the Crab nebula, the first very high-energy γ -ray source (Weekes et al. 1989), operating a single IACT with the focal length of 10 m and the energy threshold of ~ 350 GeV. The operation of multiple telescopes, enabling the stereoscopic mode, was first used by e.g. HEGRA (Daum et al. 1997) and is implemented in all detectors of the current generation: H.E.S.S. (Hinton 2004), Cangaroo III (Kubo et al. 2004), Veritas (Weekes et al. 2002) and Magic (Lorenz 2004). The stereoscopic approach, together with larger mirror areas and improved sensitivity of the optical and electronic components, rendered it possible to lower the energy threshold to 100 GeV (50 GeV for Magic) and improve the overall performance of IACTs.

2.2.1 Imaging atmospheric Cherenkov technique

Cherenkov light, emitted by constituents of a particle cascade, carries information about properties of the primary particle, i.e. its type, energy and incident direction. In order to determine these characteristics with sufficient precision, telescopes with mirror areas of the order of $\sim 100 \text{ m}^2$ are placed on the ground to collect the Cherenkov photons. These are subsequently reflected onto a camera, that is sensitive and fast enough to be able to detect such weak Cherenkov flashes of 10 ns duration. Such cameras are comprised of highly sensitive **photo-multiplier tubes** (PMTs), which are capable to provide the needed sensitivity and time resolution.

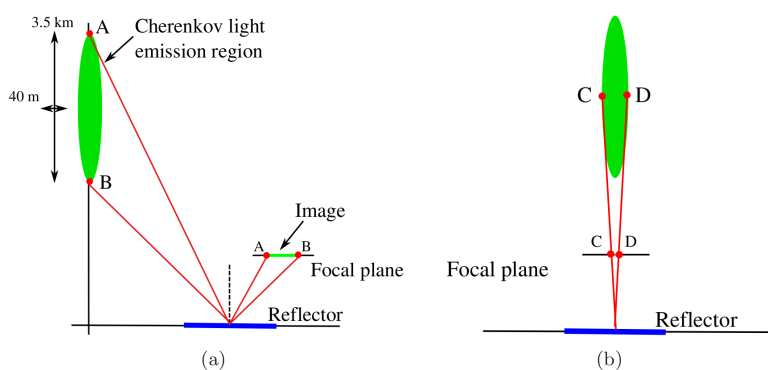


Figure 2.2: Illustration of the imaging principle, used in IACTs: The longitudinal extension of the shower defined the length of the image in a Cherenkov camera, while its latitude extent defines its width. The angle between the shower and the axis defined the position of the shower image in the camera plane. Image taken from (Hoppe 2008).

In Fig. 2.2, an image of such a Cherenkov light pulse is sketched. It is evident, that the resulting image on the camera is a two-dimensional projection of the corresponding particle shower. Its shape is ellipsoidal and thus characterized by the long (major) and short (minor) axes. The size of the major axis, also called the length of the image, is determined by the angle between the observation position and the shower direction, while the size of the minor axis (width of the shower) is determined by the lateral extension of the particle cascade. As described above, electromagnetic showers have a smaller lateral extent, compared with hadronic ones, hence usually images from hadronic showers have a larger width, in this way offering a selection criterium for the rejection of the hadronic background (see Sec. 2.3).

The major axis of a shower image in the camera points towards the incident direction of the primary particle, which can in principle be reconstructed by a single telescope. However, operating multiple telescopes proved to improve the performance concerning the direction reconstruction. Moreover, the irregular shape of hadronic showers leads to deviating images between individual telescopes, yielding an improved background rejection potential for a multiple telescope array.

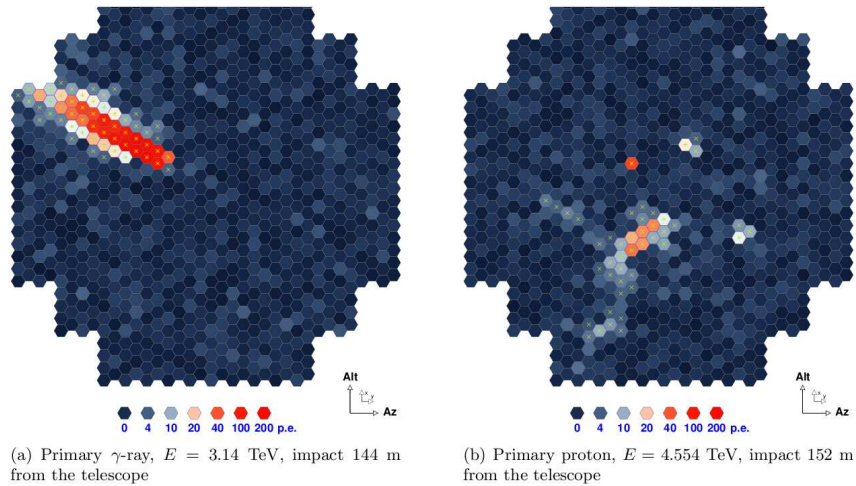


Figure 2.3: Cherenkov light distribution from a simulated γ -ray shower, caused by a 3.14 TeV photon (a), and from a proton shower, with the energy of 4.554 TeV. Pixels, which are kept for the subsequent Hillas parametrization, are marked with crosses. The regular shape of a γ -ray shower and the irregular distribution of Cherenkov photons from a proton shower are clearly visible.

2.2.2 The H.E.S.S. experiment

The **High Energy Stereoscopic System** (H.E.S.S.) is an array of four IACTs, designed for observations of very high-energy γ -ray radiation in the energy range between ~ 100 GeV and ~ 100 TeV. The first observations were conducted in summer 2002, when the construction of the first telescope was completed. From december 2003 on, observations have been carried out with the completed 4-telescope array (see Fig. 2.4).



Figure 2.4: The site of the H.E.S.S. experiment.

The site

The H.E.S.S. array is located in the Khomas Highlands Of Namibia ($23^{\circ}16'17''\text{S}$, $16^{\circ}29'58''\text{E}$) at 1800 m above sea level. The site was chosen due to its excellent astronomic conditions, in particular a cloudless sky is present for $\sim 54\%$ of all moonless nights and the humidity hardly reaches 90% for almost all nights, thus enabling safe operation of electronic equipment. Beside, the location in the southern hemisphere allows for observations of the most part of the Milky Way, including the GC region (see chapter 1).

The telescopes

The four identically designed IACTs of the H.E.S.S. array are placed on a square of 120m side length. For the choice of an appropriate distance between telescopes, two basic principles needed to be taken into account: On the one hand, it is desirable to have a large distance between telescopes in order to have an optimal stereoscopic reconstruction. On the other hand, the size of the Cherenkov light pool on the ground limits the distance between telescopes, since for the stereoscopic approach at least two telescopes need to see the same shower. Each of the telescopes consists of a mirror dish of 13 m in diameter, its support structure and a camera. On each dish, 382 spherical mirrors are arranged in a Davies-Cotton design (Davies & Cotton 1957) with a total mirror area of $\sim 107\text{ m}^2$ and a focal length of 15.28 m. At the peak of the Cherenkov light on the ground at $\sim 330\text{ nm}$, the reflectivity of the mirrors accounts to 80%. The optical point spread function after alignment of individual mirror segments lies between 0.25 mrad on-axis and 2.8 mrad at the edge of the field of view (for comparison with the γ -ray point spread function of H.E.S.S., see Sec. 2.3). The rotation of the telescopes in azimuth direction is performed on a circular steel rail of 13.6 m in diameter, while rotation in altitude is done by friction drive systems acting on altitude rails at $\approx 7\text{ m}$ radius from the axes, with a maximum rotation velocity of $100^{\circ}/\text{min}$ in both directions. The total weight of the dish and its support structure is $\sim 60\text{ t}$, ensuring a sufficient rigidity of the telescope. The pointing of each telescope is monitored by two optical CCD cameras, and with all systems in use, the pointing accuracy of the H.E.S.S. array can be reduced from $28''$, being the standard pointing accuracy, to $9''$ for selected sources (The HESS Collaboration & Acero 2009).

The camera

As discussed above, the short and weak Cherenkov light flashes render the use of fast and sensitive PMTs necessary. Each of H.E.S.S.' cameras comprises 960 of such PMTs (see Fig. 2.3), which are integrated in 60 individual moduls (drawers), containing also trigger and readout electronics and the high voltage supply (Aharonian et al. 2004c). The readout time is adjusted to 16 ns, thus taking into account the short duration of a Cherenkov pulse and reducing background photons from the night sky. In order to reduce light losses, Winston cones are installed in front of each PMT, focusing the incident light into the active volume of PMTs. The angular size of each PMT is 0.16° , thus the total field of view of a H.E.S.S. camera accounts to 5° , adapted for observations of extended γ -ray sources.

The trigger

The trigger of the H.E.S.S. experiment consists of two levels, a telescope trigger and a central trigger system (Funk et al. 2004). As far as the telescope trigger is concerned, it is implemented by dividing the camera into 64 overlapping trigger sectors. A telescope trigger signal is generated, if more than 3 pixels within such a sector receive a signal of more than 4 **photo-electrons** (p.e.) within a time window of 1.5 ns. The frequency of telescope triggers depends, beside atmospheric conditions, on the zenith angle of observations and has a rate between 300 Hz and 500 Hz. The telescope trigger signal is subsequently sent to the hardware central trigger, located in the control building on the site. The central trigger checks, whether at least two telescope trigger signals arrive within a time window of 80 ns. If this is the case, the central trigger sends a readout signal to the telescopes, and the information of the individual telescopes is subsequently read out and stored on the data acquisition system on the H.E.S.S. site. The requirement of at least two triggered telescopes reduces the system trigger rate to ~ 150 to ~ 200 Hz and effectively discriminates against Cherenkov light from myons, mostly seen only by single telescopes.

2.3 H.E.S.S. data analysis

In this section the analysis chain of the H.E.S.S. experiment is described. The different steps are described in the order of their usage during H.E.S.S. analysis, consisting of data taking (Sec. 2.3.1), data calibration (Sec. 2.3.2), image processing (Sec. 2.3.3), signal selection (Sec. 2.3.4) and calculation of statistical (Sec. 2.3.5) and physical source parameters (Sec. 2.3.6).

2.3.1 Data taking

H.E.S.S. carries out observations of γ -ray sources during moonless nights with good weather conditions, which amount to maximum ~ 1700 hrs per year, while the mean total data taking time is ~ 1000 hrs per year. The light from the Moon would severely influence the sensitivity of the telescopes, making the detection of the Cherenkov light from very high-energy photons at energies close to the energy threshold of 100 GeV impossible, thus only some data taking for calibration purposes is possible. The observations are split in 28 min runs, during which a potential target is tracked on the sky. The observational program of H.E.S.S. consists of the scan of the accessible part of the Galactic plane, dedicated observations of galactic and extragalactic targets and observations of the so-called targets of opportunity, which show flaring activity in relevant wavebands (X-rays to very high-energy γ -rays), detected by other instruments.

2.3.2 Data preparation and calibration

The data, recorded during γ -ray observations, need to be prepared for its analysis. Therefore, corresponding observation runs are first checked for the stability of the system performance. This means, that beside the hardware performance, also the stability of the

weather conditions is checked, since the atmosphere is used as a calorimeter and is thus an integral part of the detection system. This is checked by requiring a certain absolute value and maximal spread of the system trigger rate, to reject runs with clouds in the field of view or a dusty atmosphere. As far as the hardware performance is concerned, it is required that the number of disabled PMTs due to hardware failures or bright stars in the field of view does not exceed 10%. The decreasing optical efficiency of the system due to aging of the mirrors and the PMTs, is accounted for by analyzing muon rings, occurring within images of hadronic showers. From the geometrical parameters of such a ring image in the camera, conclusions can be drawn about the energy of the muon. By comparing the expected³ and the detected intensity in the ring, the change of optical efficiency, compared to the initial state of the particular telescope, can be accurately measured. A full description of calibration steps can be found in (Bolz 2004).

2.3.3 Event reconstruction

Calibrated camera images undergo dedicated processing steps in order to extract information about the properties of detected particle showers. First, recorded images are cleaned in order to remove pixels containing only random background photons and/or electronic noise. For further processing, only those pixels are kept, which contain at least 5(10) p.e. and have a direct neighbouring pixel, containing at least 10(5) p.e. The result of such image cleaning are spatially connected pixels, which resembles a two-dimensional projection of the detected shower (see Fig. 2.3). These pixel regions are subsequently used for the parametrization of shower images according to (Hillas 1985). This parametrization yields a set of five **Hillas parameters**, comprising the **center of gravity** (CoG) of the shower image, the length and width of the shower, defined as the length of the major and minor axes, respectively, the orientation of the shower with respect to the particular camera coordinate system and the overall image intensity. These parameters are illustrated in Fig. 2.5. Other parametrizations of showers exist as well (Naumann-Godó et al. (2009), de Naurois & Rolland (2009)).

Hillas parameters, extracted from a shower image in the camera, contain the necessary information to reconstruct the incident direction and the energy of the primary particle. Since for all events at least two telescopes exist, which have observed the same particle shower, the determination of particle's incoming direction is possible by intersecting the major axes of the reconstructed ellipses. If N_{tel} telescopes have triggered for the same shower, the number of intersection points is $N_{\text{tel}}(N_{\text{tel}} - 1)/2$, i.e. one intersection point for a two-telescope event and six intersection points for a four-telescope event. In case $N_{\text{tel}} > 2$, the direction is reconstructed by calculating a weighted mean (Aharonian et al. 2006a). It is obvious, that the more telescopes have seen the shower, the more accurate is the direction reconstruction. The precision of the direction reconstruction depends on the applied event selection and is discussed later.

In order to estimate the energy of the primary particle⁴, beside the intensity of the pixels

³ The expected light yield from a single muon is determined by Monte-Carlo simulations, assuming a certain optical efficiency of the array, e.g. 100%.

⁴ In the standard analysis chain it is always assumed, that the detected event is a γ -ray, thus the recon-

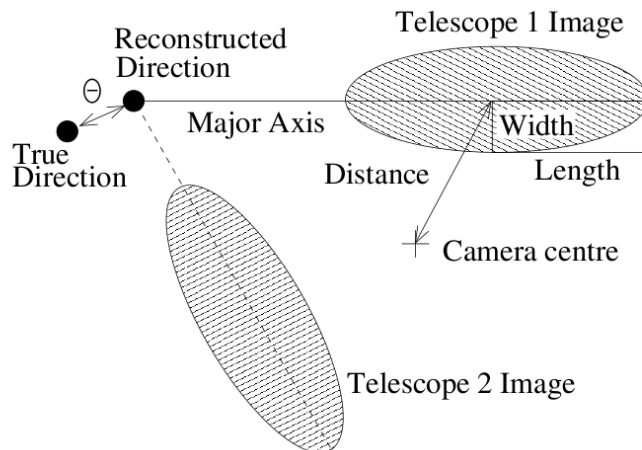


Figure 2.5: Illustration of Hillas parameters and of the stereoscopic direction reconstruction. The intersection of the major axes of shower ellipses provides the direction of the incident particle. The accuracy of such reconstruction depends on the set of selection criteria and the number of telescopes, having recorded the particular shower. The parameters width and length are used for background rejection. See text for further details. Image taken from (Aharonian et al. 2006a).

within a shower image, knowledge is needed about the distance between the incident direction of the particle and the observation position, called the **offset** angle Ψ , the position of the shower **impact point** and the zenith angle of the observation. The impact point of a shower depicts the hypothetical position, where the shower axis would hit the ground. This position is determined, as well as the offset angle Ψ , by the reconstructed direction of the shower. It is obvious, that for the same energy of a shower inducing particle, the light yield in a telescope would decrease with increasing distance between the impact point and the telescope position. The expected light yield for a given γ -ray energy, impact point, offset angle and zenith angle must be determined by Monte-Carlo simulations. These are used to reconstruct the particle's energy in data, taking into account the current optical efficiency of the telescope, determined with the muon method, described above. The performance of the energy reconstruction also depends on the applied event selection and is discussed later.

The fitted shower parameters length and width carry information about the shape of the shower, thus these parameters are used to determine the type of the incident particle, described in the following. Other parametrizations use different methods for the rejection of hadronic background (Naumann-Godó et al. (2009), de Naurois & Rolland (2009)).

2.3.4 Event selection

For the analysis of recorded data, several selection criteria are applied in order to improve the precision of the reconstruction of shower parameters and discriminate against

structed energy for hadronic particles is always a factor of ~ 3 too low.

the numerous hadronic background. As far as the **image quality** criteria are concerned, it is required that a certain minimum intensity, also called **size**, is reached by a shower image in a camera (see Tab. 2.1). Besides, to avoid edge effects, the reconstructed CoG of the shower image must be located within 2° with respect to the camera center. Since H.E.S.S. applies the stereoscopic mode for further parameter reconstruction, at least 2 telescopes have to fulfill these requirements.

As described in Sec. 2.1, electromagnetic and hadronic air showers exhibit a quite different shape, therefore parameters like length and width of the corresponding Hillas ellipse can be used for discriminating between air showers induced by γ -rays (and electrons) and hadronic CRs. The reconstructed parameters of individual shower images are used for determination of the system-wide shape parameters **mean reduced scaled width** (MRSW) and **mean reduced scaled length** (MRSL). These parameters are calculated by using, beside the measured width for a telescope i , the simulated quantities $\langle \text{width} \rangle_i$ and $\sigma_{w, i}$, with $\langle \text{width} \rangle_i$ being the mean reconstructed width and $\sigma_{w, i}$ its spread for simulated γ -ray showers, observed by the telescope i under the same zenith angle and utilizing the same offset angle of the shower Ψ :

$$\text{MRSW} = \frac{1}{\sum_{i=1}^{N_{\text{tel}}} \omega_i} \sum_{i=1}^{N_{\text{tel}}} \left(\frac{\text{width}_i - \langle \text{width} \rangle_i}{\sigma_{w, i}} \right) \omega_i, \text{ where } \omega_i = \frac{\langle \text{width} \rangle_i^2}{\sigma_i^2}$$

The parameter MRSL is calculated accordingly. The distribution of these parameters for simulated γ -rays, protons and data from empty regions in the sky (off-data) is shown in Fig. 2.6. It can be seen that the distributions for simulated γ -ray events are highly concentrated around 0, whereas the distributions for simulated protons exhibit a much more extended shape, being in good agreement with off-data, which almost entirely consists of hadronic CRs. In the same figure, cut values, introduced to reject the most part of the hadronic background, both for MRSW and MRSL distributions, are depicted by vertical lines.

A set of selection criteria is chosen upon the expected or known properties of the γ -ray source under study. For sources with a flux of the order of 10% of the flux from the Crab nebula, or simply Crab flux, and a spectral index of $\Gamma = -2.6$, the **standard** cut set is used. If weak sources with a flux of $\sim 1\%$ Crab flux are analyzed, having at the same time a harder spectrum of $\Gamma = -2.0$, then **hard** cuts are used. Corresponding cut values are summarized in Tab. 2.1. It should be noted here, that the additional cut on θ , being the distance between the reconstructed direction of a shower and the presumed position of the source, is optimized for analyses of point sources. This cut can be adapted to the actual size of the source, in order not to reject events because of a larger source extension.

The performance of the instrument concerning the energy and direction reconstruction is shown in Fig. 2.7 for both cut configurations. Due to the tighter event selection for hard cuts, both the energy and direction reconstruction performance is superior compared with the standard event selection.

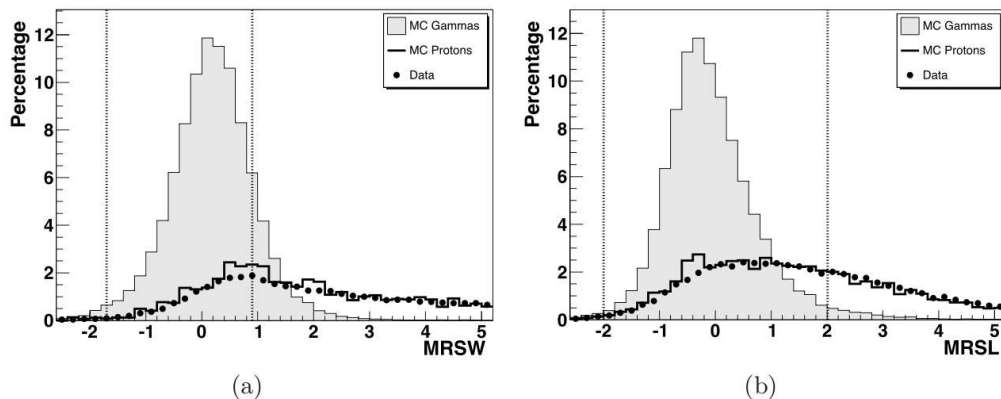


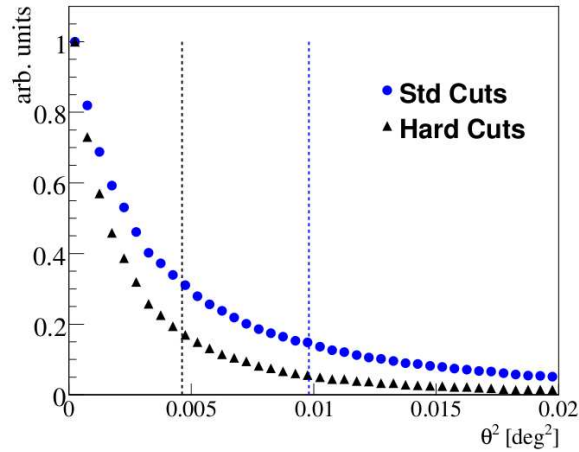
Figure 2.6: Distribution of mean (a) reduced scaled width (MRSW) and (b) mean reduced scale length parameters (MRSL) for simulated γ -rays and protons, and data taken from empty regions in the sky (off-data). The simulations were performed at a zenith angle of 20° . Proton and off-data distribution show a nice agreement, leading to the conclusion that the distribution are understood and can be used as selection variables. The standard cut values are indicated by vertical lines. Image taken from (Hoppe 2008).

Cut set	MRSW		MRSL		θ^2 [deg ²]	Size [p.e.]
	min	max	min	max	max	min
Standard	-2.0	0.9	-2.0	2.0	0.0125	80
Hard	-2.0	0.7	-2.0	2.0	0.01	200

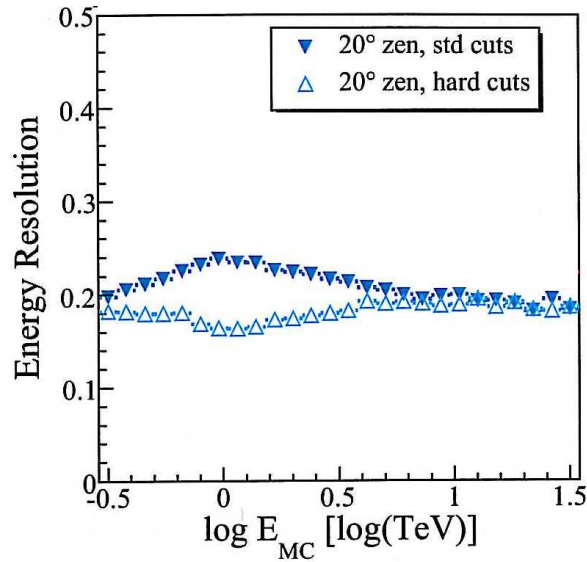
Table 2.1: Two sets of cut values, optimized for different source types. The standard cut set is optimized for a luminous source, having a flux of 10% Crab and a spectral index of $\Gamma = -2.6$. Hard cuts were optimized for weak ($\sim 1\%$ Crab) and hard ($\Gamma = -2.0$) sources. At least two telescopes must have properly reconstructed the shower (see text for further details).

2.3.5 Background subtraction

After the application of selection criteria, a considerable number of hadronic events still remains in the dataset, for which the shower parameters happen to be reconstructed in the γ -ray phase space, thus they are undistinguishable from true photons. In order to calculate the number of γ -ray events, located within a source region, and to reconstruct the spectrum of the potential source (see Sec. 2.3.6), the number of background events, located within the source region, needs to be estimated. The number of γ -ray events can be calculated as: $N_\gamma = N_{\text{on}} - \alpha N_{\text{off}}$, with N_{on} being the number of events within the source region, called **on-region**, N_{off} the number of events within dedicated background regions, called **off-regions**, and α being a method-dependent weighting factor. Off-regions can be defined from the same field of view (geometrical subtraction), making use of the fact, that the hadronic background is isotropic, or a certain off-range for a cut parameter is taken



(a) PSF of H.E.S.S. for standard and hard cut sets



(b) Energy resolution for standard and hard cut sets

Figure 2.7: Performance of direction and energy reconstruction for the standard and hard cut sets. Image (a) shows the PSF of H.E.S.S. for both cut sets. Image (b) shows the energy resolution as function of energy for both cut sets. Hard cuts show to be superior in both cases, thus being the preferable selection set, if a precise morphological and spectral analysis is desirable. Image a) is taken from (Hoppe 2008). Image b) is taken from (Gast 2009).

(phase space subtraction)⁵:

- ◇ **Reflected (background) method:** This algorithm utilizes a geometrical background subtraction. Therefore, first the offset between a potential source and the observation position for a given run is determined. $N_{\text{off-reg}}$ non-overlapping off-

⁵ The methods for background subtraction, described here, are the ones also used for this work. There are additional methods, not mentioned here (Hoppe 2008).

regions are then placed around the observation position at the same offset. Their size (and shape) is identical with the size (and shape) of the on-region, which is, for point source analyses, usually a circle with a radius corresponding to the used θ^2 -cut, centered at the source positions (see Fig. 2.8). Assuming that the acceptance of the detector is radially symmetric around the observation position, this means that α is simply $\alpha = \frac{1}{N_{\text{off-reg}}}$. Besides, due to the same detector acceptance for on and off-events, this method is used for the spectrum reconstruction (see Sec. 2.3.6).

- ◇ **Ring (background) method:** This algorithm defines a ring around the potential source as off-region, hence also using geometrical background subtraction, with the inner ring radius and the ring width adopted to the expected source extension. Contrary to the reflected method, this off-region is selected only once for the total data analysis of a particular source and is valid of all runs, independent of the actual observation position. Since background events are extracted from a region with deviating detector acceptance, compared with the on-region, the latter has to be modelled for each run individually. Thus α is here not simply the relation between the source and the background region areas, but rather a relation of detector acceptance, integrated over the on and off-regions, respectively. Due to the difference in detector acceptance, this method is not used for spectrum reconstruction but for maps production and morphological studies.
- ◇ **Template (background) method:** This algorithm uses a certain phase space region for background estimation. As described above, discrimination against hadronic background is mainly done by cuts on the MRSW and MRSL distributions, i.e. these distributions show explicit regions, either dominated by γ -rays or by hadronic background. Hence a parameter range, fully dominated by the background, can be used to estimate the number of background events in the γ -like phase space. For the template method, the following off-range is defined: $3 \leq \text{MRSW} \leq 9$. The geometrical off-region is the same as the on-region, thus α is completely determined by the relation of the detector acceptance for off-events between the γ -like and hadron-like phase space. This method is currently used only for morphological studies, like the ring-method (Rowell 2003).

Both methods of geometrical background subtraction use only empty regions of the sky for background estimation. Sources of γ -ray emission are masked with so-called exclusion regions, which can not be used as off-regions.

The statistical significance of a source candidate is determined using the number of on- and off-events as well as the acceptance factor α (Li & Ma 1983):

$$S = \sqrt{2} \left(N_{\text{on}} \ln \left[\frac{(1 + \alpha)N_{\text{on}}}{\alpha(N_{\text{on}} + N_{\text{off}})} \right] + N_{\text{off}} \ln \left[\frac{(1 + \alpha)N_{\text{off}}}{N_{\text{on}} + N_{\text{off}}} \right] \right)$$

2.3.6 Spectrum reconstruction

For the reconstruction of the spectral distribution of a γ -ray source, based on a particular dataset, knowledge is needed about the energy distributions of on- and off-events, as well as of the detector acceptance of the source region. As it is implemented in the reflected method, reconstructed energy values of events within the on and off-regions are stored, see

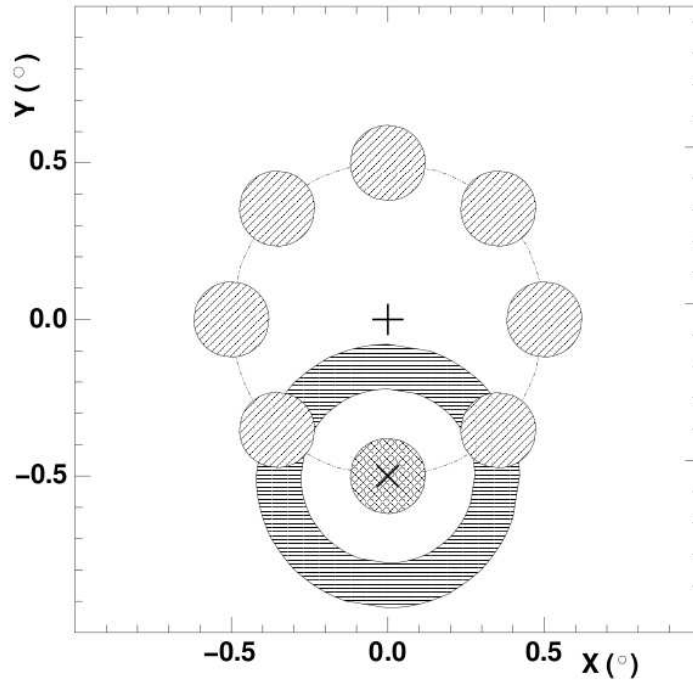


Figure 2.8: Illustration of both geometrical methods for background subtraction. The on-region is cross hatched. The off-regions for the reflected-method are distributed around the observation position, marked with a “+”, and are filled with diagonal lines. The off-region for the ring-method is filled with horizontal lines. See text for further details. Image is taken from (Aharonian et al. 2006a).

Fig. 2.9 (a). The distribution of off-events is weighted with α_i for each run i . Beside, the detector acceptance of the on-region, also called **effective areas**⁶ (EAs), is determined as a function of energy for each run, weighted with its livetime⁷ and integrated for the total dataset, see Fig. 2.9 (b). EAs are determined from a large set of Monte-Carlo γ -ray events, simulated to originate from point sources at various zenith and offset angles, and stored as lookup tables for usage during data analysis. Spectral points for an energy E_i for the on- and off-events are thus determined as⁸:

$$\frac{d\Phi_{\text{on},i}}{dE dt} = \frac{1}{\delta E_i} \left(\frac{N_{\text{on}}}{A_{\text{eff},i}} \right), \quad \frac{d\Phi_{\text{off},i}}{dE dt} = \frac{1}{\delta E_i} \left(\frac{\alpha N_{\text{off}}}{A_{\text{eff},i}} \right)$$

with δE_i being the width of the bin i and $A_{\text{eff},i}$ being the dataset integrated, time-weighted effective area value for the energy E_i , see Fig. 2.9 (c). The residual spectral distribution, see Fig. 2.9 (d), can be used for a fit with a dedicated function, chosen upon the assumed physical process at work producing the observed γ -ray emission, e.g. a power law: $\frac{d\Phi_i}{dE dt} = f(E) = \Phi_0 \times E^\Gamma$. The fitted function can be used to calculate the integral flux:

⁶ Effective areas are nothing else but cut efficiencies for γ -like events, multiplied with the total detection area of the H.E.S.S. array, which is of the order of $\sim 10^6 \text{ m}^2$

⁷ Livetime of an observation run is the for the dead-time of the system corrected run duration.

⁸ It is hereby assumed, that the bin-weighted method for the integration of EAs is used (Aharonian et al. 2006a).

$\frac{d\Phi}{dt} = \int_{E_{\text{thr}}}^{\infty} f(E) dE$. As determined in (Aharonian et al. 2006a), the systematic error on the reconstructed integral flux is 20%.

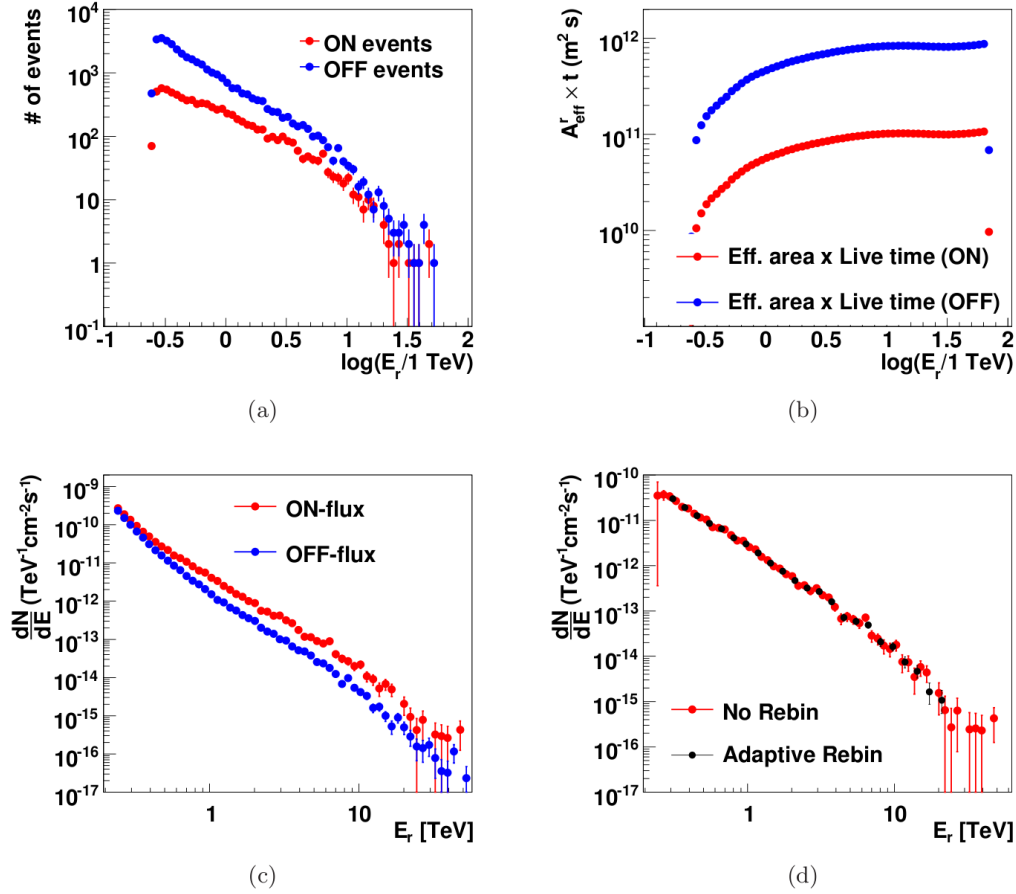


Figure 2.9: The reconstruction of the spectrum of a γ -ray source. a) Energy distribution of events in the on and off-regions. b) Integrated effective area distribution for the particular dataset. c) Spectral distributions for the on and off-regions. d) Residual distribution, being the spectrum of γ -ray emission. As a source, the GC point source HESS J1745–290 is used. See text for further details. Image taken from (Hoppe 2008).

3 Analysis of the diffuse emission from the Galactic Center Region

In this chapter the new analysis of the diffuse emission from the Galactic Center is described. First, in Sec. 3.1 the diffusion process in the context of cosmic ray propagation is introduced, followed by the description of the method to simulate gamma-ray maps for the GC region. In Sec. 3.2 the analysis of H.E.S.S. data is presented, including the comparison to the simulations introduced before. Finally, in Sec. 3.3 the results of the analysis are summarized and discussed.

3.1 Theoretical background and modelling

As described in Sec. 1.4, the detected extended emission from the GC region is believed to be due to the interaction of hadronic CRs accelerated at the center, which then diffuse to the ambient space. This hypothesis is strongly supported by the observed correlation between the flux of the gamma-ray emission and the density of GMCs, that decreases for $|l| > 1^\circ$. If this assumption holds, it is not only the first time that very high-energy gamma-ray emission is detected having a (confirmed) hadronic origin, but is also a unique possibility to directly observe the diffusion of CRs. This is especially important because, as discussed in the following, the knowledge about the propagation of CRs in the galaxy is still very limited and on the observational side mostly relying on the measurements of the abundance of different elements in the total cosmic ray flux.

3.1.1 Short overview of propagation models

Since the discovery of the cosmic ray radiation in 1912 by Victor Hess a fully conclusive proof for its origin is still missing. It is however common to assume that the CRs below the so-called “knee-energy” of several PeV stem from galactic sources like SNRs. Under this assumption one can try to explain the observational data of this cosmic ray population using models describing their propagation. These have a large spread of complexity and are mainly based upon two different concepts:

- ◇ **Box concept:** The galaxy is considered as a disk of 15 kpc radius and several hundreds pc height, framed by reflecting boundaries and having an uniform distribution of matter and CRs that can propagate freely inside the disk. The most prominent representative of this concept is the “Leaky Box Model” (Cesarsky 1980), in which the CRs have a finite probability to escape the galaxy each time they interact with the boundaries. Additionally, a (spherical) halo with a smaller density of matter can also be included in this concept to match the data (Kachelriess 2008).

- ◇ **Diffusion concept:** After leaving the acceleration region, CRs perform a diffusive “random walk” in the galaxy due to irregularities in the galactic magnetic field structure. In contrary to the box concept, there are no boundaries that prevent the CRs from leaving the galaxy. This concept should be closer to reality than the box concept, however it contains a number of additional parameters like diffusion coefficients, e.g. along and across the disk, distribution of sources and matter and other (Le Guet (1977), Skilling & Strong (1976)).

These propagation models are meant to explain the following main experimental results (Cesarsky 1980):

- ◇ CRs are almost completely isotropic¹.
- ◇ The pure power law shape of the cosmic ray spectrum. Since also acceleration processes like the diffusive shock acceleration produce power-law spectra $\Phi \propto E^{-\alpha}$ ($\alpha > 0$), the propagation is not supposed to change the overall shape, however a change of α is possible.
- ◇ The abundance of secondary particles as measured in the energy range $1 \text{ GeV}/n < E < 100 \text{ GeV}/n$, with n being the number of nucleons, and its energy dependence. Elements like Li, Be, B outnumber the solar abundance by orders of magnitude. They are believed to be almost entirely created from primary elements like O or Fe by nuclear spallation. Since these cross sections are reasonably well known, it is possible to calculate the amount of matter the CRs have traversed. The result is $\lambda_{CR} \sim 5 - 10 \frac{\text{g}}{\text{cm}^2}$, which compared to the line of sight integrated density through the whole galactic disc of $\lambda_0 \sim 10^{-3} \frac{\text{g}}{\text{cm}^2}$ immediately yields that CRs propagate distances orders of magnitude larger than the size of the Milky Way before they reach the Earth.
- ◇ The abundance of unstable isotopes can be used to measure the age of the cosmic ray population that turns out to be $t_{esc} \approx 1 - 2 \times 10^7$ years. This yields that the mean density CRs encounter is $\sim 0.3 \text{ cm}^{-3}$, which, taking into account the measured local ISM density of $\sim 1 \text{ cm}^{-3}$, leads to the conclusion that CRs spend most of their time not in the galactic disc but rather in regions of low density, e.g. in a spherical halo.

For calculations of space-averaged mean values like mean traversed distance λ_{CR} or the mean escape time t_{esc} both concepts lead to basically equal results, justifying the fact why the so dramatically simplified box concept is still in use. However, for more sophisticated applications like the GalPROP model (Strong et al. 2009), where spatial (and temporal) inhomogeneities are important, box models are not usable and diffusion models are used. For this reason, the basic aspects of diffusion are summarized in the following together with the question, which contribution the current analysis of very high-energy γ -ray data from the CG region may have on this topic.

¹ The anisotropy for low energies $E \approx 1 \text{ GeV}/N$ is mostly due to solar wind modulation. The anisotropy for higher energies of the order of $\approx 0.1\%$ can be understood as moving of the solar system with respect to the Galactic Center (Kachelriess 2008).

3.1.2 Cosmic ray diffusion

The basic concept of diffusion of CRs is understood as a result of interactions between the CR particles and the magnetic field in the Galaxy. Given the strength of the magnetic field in the solar neighbourhood of $\sim 3 \mu\text{G}$ that is assumed to be a typical order of magnitude at least for the interstellar and intercloud medium, the following expression for the gyroradius of protons can be obtained: $r_g \approx 3 \times 10^{-7} (\frac{E}{1 \text{ GeV}})$ pc. When comparing this value with the height of the galactic disk of ~ 300 pc it becomes evident that CRs move closely attached to the magnetic field lines (Cesarsky 1980). Here, both small and large-scale characteristics of the magnetic field play an important role. But until now, the knowledge about its configuration on various scales is still insufficient. While the situation seems to be clear for the solar neighbourhood, where the magnetic field is parallel to the galactic plane and has a strength of $\sim 3 \mu\text{G}$, its characteristics e.g. in the GC region is still disputable, as was shown in Sec. 1.1. Moreover, there is no conclusive view on its large-scale fluctuations (~ 100 pc) and on magnetic field configuration inside molecular clouds (Cesarsky 1980).

For the discussion of theoretical aspects of diffusion, it is worthwhile to introduce first the diffusion equation, since its solution is also required for the description of simulation models in Sec. 3.1.3. The diffusion equation connects the net flow of particles $\vec{J}(\vec{r}, E, t)$ with the spatial gradient of particle density $\vec{\nabla}n(\vec{r}, E, t)$:

$$\vec{J}(\vec{r}, E, t) = -D(\vec{r}, E, t)\vec{\nabla}n(\vec{r}, E, t) \quad (3.1)$$

Since $\vec{\nabla}\vec{J}(\vec{r}, E, t) = \frac{\partial n(\vec{r}, E, t)}{\partial t}$ one obtains following differential equation:

$$\frac{\partial n(\vec{r}, E, t)}{\partial t} = -\vec{\nabla}D(\vec{r}, E, t)\vec{\nabla}n(\vec{r}, E, t) \quad (3.2)$$

For scalar, constant diffusion $D(\vec{r}, E, t) = D(E)$, and assuming spherical symmetry $n(\vec{r}, E, t) = n(r, E, t)$ the solution is:

$$n(r, E, t) = \frac{n(0, E, t)}{[4\pi D(E)t]^{\frac{1}{2}}} \exp\left[\frac{-r^2}{4D(E)t}\right] \quad (3.3)$$

The relation $n(t)/n(0)$ simply gives the probability of finding a particle at a distance r for a given time t . It is obviously a Gaussian function with a width of $\sigma = \sqrt{2Dt}$. From this relation it follows that the mean distance a particle travels away from its source is proportional to the square-root of time: $\langle r(t) \rangle = \sigma \propto \sqrt{Dt}$.

Insights about the nature of diffusion of CRs in magnetized environment come from **magnetohydrodynamics** (MHD). It is assumed that particles are scattered by perturbations in a MHD fluid, consisting of the magnetic field, ions and electrons, that are treated with

² Box models provide the possibility to calculate a diffusion coefficient across the disk, by using the box height h as σ and the mean age of CRs as t .

a wave approach. These waves are called ‘‘Alfven waves’’³ and extensive studies were performed to determine their energy density and power spectrum in the galaxy (Cesarsky 1980). It turns out that the major part of the power spectrum is described by a power law $\omega(k) \propto k^{-2+a}$, with $a = 1/3$ as a typical value for Kolmogorov-like turbulences (see Strong et al. (2007) and references therein). Given this power spectrum it is in principle possible to calculate the diffusion coefficient D (for diffusion along field lines) and its energy dependence:

$$D = \left[\frac{B}{\delta B(k)} \right]^2 \frac{\beta c r_g}{3}, \quad (3.4)$$

where B is the overall strength of the magnetic field, $\delta B(k)$ the amplitude of Alfven waves at wavenumber k and r_g the particle’s gyroradius. The diffusion coefficient has a lower limit, the so-called Bohm limit, given by $D = cr_g/3$, for which the mean free path l , defined as $l = 3D/c$, equals to the gyroradius r_g of the particle (Aharonian 2004). Assuming $\delta B(k) = 5 \mu\text{G}$ one obtains a theoretical value for the diffusion coefficient $D_{th} \approx 10^{27} \beta R^{1/3} \text{ cm}^2 \text{ s}^{-1}$, with magnetic rigidity $R = \frac{E(\text{GeV})}{Z}$, that is close to the value obtained from the secondaries data for GeV particles: $D_{exp} \approx 10^{28} \text{ cm}^2 \text{ s}^{-1}$ (Kachelriess 2008). However, despite this rather good agreement between theory and experiment, a detailed treatment of diffusion along and across field lines for a wide energy range is very complicated, in particular concerning the role of the diffusion across magnetic field lines (see Casse et al. (2002)), so that the determination of diffusion coefficients still has to be done empirically (Strong et al. (2007), Strong et al. (2009)). But still, two main outcomes should be emphasized here: The diffusion concept can provide the diffusion coefficient in the right range at least for GeV particles and its energy dependence is a power law, as required in Sec. 3.1.1.

For completeness it should be noted that empirical models like GalPROP also include a distribution of sources of CRs (1st term), convection (3rd term), energy losses (and gains) (4th - 6th term) as well as fragmentation from heavier nuclei are taken into account (last term). Thus the **transport equation** for CRs of species i :

$$\begin{aligned} \frac{\partial n_i(\vec{r}, E, t)}{\partial t} &= Q(\vec{r}, E, t) + \vec{\nabla} \cdot (D \vec{\nabla} n_i - \vec{v} n_i) - \\ &- \frac{\partial}{\partial E} (b(E) n_i) - \left[\frac{c\rho}{\lambda(E)} + \frac{1}{\gamma\tau_d} \right] n_i + \\ &+ \frac{c\rho}{m} \sum_k \int_E^{\text{inf}} \frac{d\sigma_{ki}(E', E)}{dE} n_k(E') dE' \end{aligned} \quad (3.5)$$

is solved numerically.

It is clear that for empirical models that make predictions on scales much smaller than the size of the Galaxy the simplification of a scalar diffusion with a space-independent diffusion

³ Galactic Alfven waves can be generated by astrophysical sources such as pulsars or be excited by CRs themselves. The latter is also plausible because the energy densities of CRs and the galactic magnetic field are similar and both fields are coupled to each other (Gaisser 1991).

coefficient does not hold and several parameters have to be varied, including the diffusion coefficient and the source distribution (see Sec. 3.1.1), in order to fit the already existing observations, which in their turn have an impact only on CRs up to energies of a few TeV (Atwood et al. 2009). And here a connection to the analysis of the TeV diffuse emission from the GC region can be established: It is for the first time possible to directly measure the properties of diffusion of multi-TeV CRs released by a single source with presumably established position (Aharonian et al. 2006d). Moreover, it is possible to get an impression of deviations of the diffusion speed in different regions of the Galaxy. Given corresponding future advances in theoretical understanding of interactions in turbulent magnetic fields and a precise measurement of the magnetic field configuration in the GC region, it could also be possible to compare this measurement with predictions from a theoretical model (see also Sec. 3.1.3). So the current analysis may help to improve the understanding of diffusion properties of highly relativistic particles and therefore contribute to the total picture of propagation of galactic CRs.

3.1.3 Diffusion model

In the last section it was emphasized how important the understanding of diffusion is for the propagation of (Galactic) CRs. The measurement presented in this thesis aims at better knowledge of diffusion parameters at least for the GC region. In order to interpret the H.E.S.S. data with regard to the diffusion hypothesis, it is desirable to be able to compare the data that was collected during observations with theoretical expectations. In (Aharonian et al. 2006d), this comparison was done using a simple model, in which the expected emission from diffusing hadrons was estimated in the following way: Since it is assumed, that the γ -ray flux coming from hadronic interactions between CRs and ambient matter is proportional to the matter density, the two-dimensional map of molecular material, obtained by means of CS observations (Fig. 1.3), is folded with the solution of the diffusion equation (Eq. 3.3), assuming a burst-like injection of the primary hadrons. For each bin of this map, the hadron density $n(r)$ is obtained by calculating the distance r between the bin center and the center of the map, while assuming a certain diffusion coefficient D and diffusion time t (see also Sec. 1.4). The normalisation is arbitrary and is later matched to the data. The distance r is calculated in degrees, since the CS map and all H.E.S.S. maps are shown in angular coordinate systems. The conversion between distance in pc and degrees is done using the relation $1^\circ \equiv 140$ pc for the distance of 8.5 kpc between Sun and the GC. In order to match the angular resolution of H.E.S.S., the map is smoothed with the PSF corresponding to the cuts used in the analysis (see Sec. 2.3). The result can be seen in Fig. 3.1. The underlying simplifications are that CRs diffuse isotropically from the GC and the interaction probability is linearly proportional to the density of ambient matter and is independent of energy, time and space. Besides, the GMCs are all assumed to have the same line of sight coordinate as the GC. It should be pointed out that $n(r)$ does not depend on the diffusion coefficient or time individually, but on their product: $n(r, D, t) = n(r, Dt)$. This means that as long as the exact diffusion time is unknown, only the product Dt can be measured, allowing to obtain the diffusion coefficient D only by **assuming** a diffusion time t .

The approach used by Aharonian et al. (2006d) was sufficient to roughly estimate the diffusion coefficient of CRs and the result was in a fair agreement with more sophisticated

methods (see Sec. 1.4). However, studies described in this thesis not only aim at the determination of the diffusion coefficient, but also, for the first time, probe its energy dependence, while the simple method described above only yields an energy-averaged diffusion coefficient $D = \langle D(E) \rangle$. Clearly, there is a need for a more elaborate model that allows for the search for the energy dependence. This is described in the following.

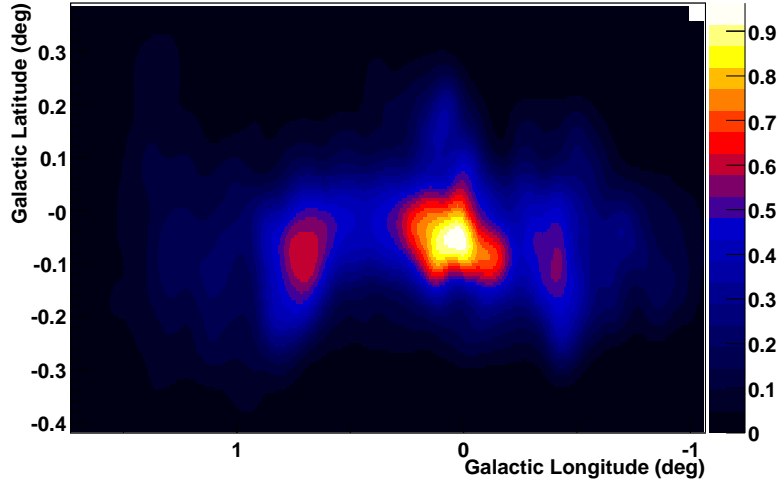


Figure 3.1: The resulting γ -ray count map for the diffusion model from (Aharonian et al. 2006d). The underlying CS-map was folded with a Gaussian, of which the width σ corresponds to the diffusion coefficient of $3 \frac{\text{kpc}^2}{\text{Myr}}$ (see Eq. 3.3), smoothed to match the angular resolution of H.E.S.S..

Development of the 2-D diffusion model

The starting point for the new diffusion model remains the same: It is assumed that the GMCs mapped in CS-observations provide the target material for hadronic interactions of diffusing CRs. So once again the CS map (Fig. 1.3) is used. It is again supposed that the GMCs are aligned along the same coordinate with respect to the line of sight, i.e. assuming the same line of sight density distribution for all MCs: $\rho(l, b, z) = \rho(l, b) \rho(z)$, with (l, b) denoting the longitude and latitude positions, while z denotes the line of sight position. However, an upgrade to a three-dimensional model was also done within the scope of this work and is described at the end of this section.

A possible energy dependence of the diffusion coefficient now needs to be taken into account. Its effect implies different diffusion speeds for different energies because of $\langle r(t) \rangle \propto \sqrt{D(E)t}$. If $D(E) \sim E^\delta$ with $\delta > 0$, then particles with higher energy diffuse faster than those with lower energy. This effect is visualized in Fig. 3.2, where the particle density $n(r, E)$ as a function of distance r and energy E is shown (see Eq. 3.3). The energy dependence of the diffusion coefficient is set to $\delta = 0.6$. It can be seen that while the density for particles with $E < 1$ TeV drops rapidly for $r > 1^\circ$, an almost homo-

geneous density distribution is reached for particles with $E > 100$ TeV. Thus a certain spectral hardening of γ -ray emission with increasing distance from the center could be expected in this case.

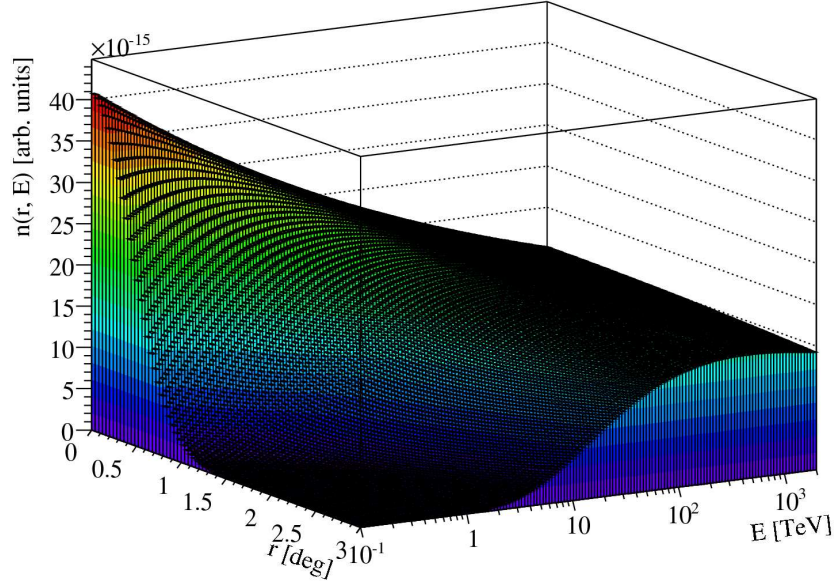


Figure 3.2: Density distribution $n(r, E)$ of diffusing particles for $D_{E=3.2 \text{ TeV}} = 1.5 \text{ kpc}^2/\text{Myr}$ and $\delta = 0.6$. One observes a rapid drop of density of low-energetic particles with increasing distance, while the density of high-energetic ($E > 100$ TeV) particles is almost constant within the considered distance range.

To include the energy dependence the corresponding energy range of primary hadrons (100 GeV – 2 PeV) is divided into steps much smaller than the energy resolution (15% - 20%) of the H.E.S.S. experiment, like it is shown in Fig. 3.2, and the particle density $n(r, E)$ is calculated for every applicable pair of r and E . The relative normalisation $n(0, E)/n(0, E_0)$ with respect to a certain energy E_0 , e.g. $E_0 = 1$ TeV, is given by the initial spectral index Γ_p of the accelerated CR populatio. The absolute normalisation is done later by fits to the data.

Expansion to a 3-D diffusion model

As mentioned above, the 2-D diffusion model does not take into account the density distribution of GMCs along the line of sight, thus assuming the same $\rho(z)$ for all GMCs. Distances between two points are calculated by means of their angular coordinates l and b , using the relation $1^\circ \equiv 140 \text{ pc}$ (see 3.1.3). Of course, the assumption that the GMCs all have the same line of sight density distribution is not very realistic. Thus it is desirable to find a model that is able to adequately distribute the molecular material along the line

of sight. Such a model was developed in (Sawada et al. 2004). In this paper, the authors used observations of CO emission from MCs in the GC region and compared it with the magnitude of OH absorption lines to estimate their z -coordinates with respect to the GC. This method was used, among others, to obtain a face-on velocity distribution map (see Fig. 3.3) of the GC region. It assigns a velocity value to the corresponding position in the x - y plane, where the x -axis coincides with the galactic longitude and the y -axis denotes the line of sight coordinates relative to the GC.

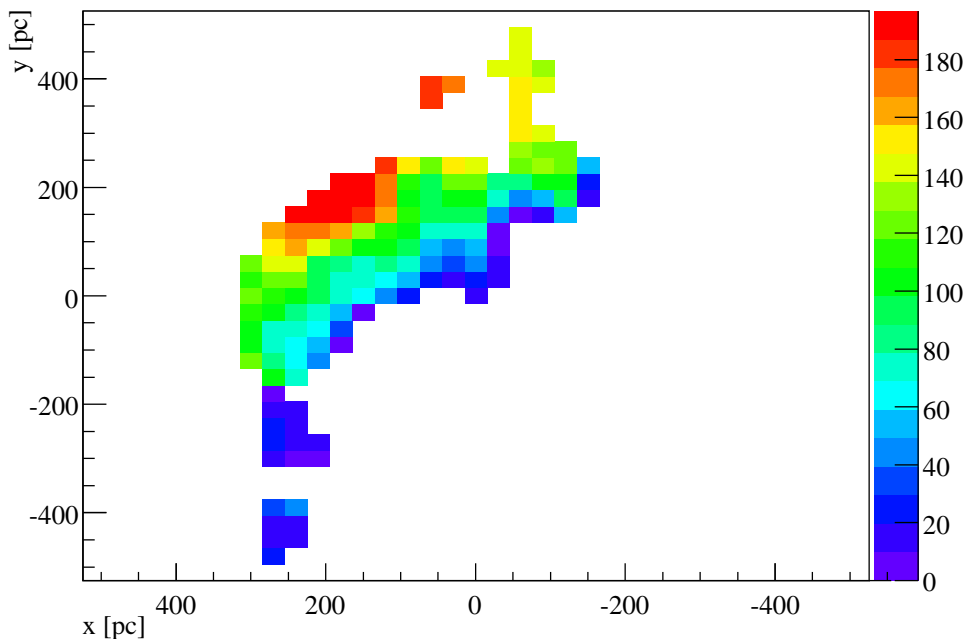


Figure 3.3: Distribution of velocities of MCs in the GCR in a face-on representation. The x -axis coincides with the galactic longitude, whereas the y -axis denotes the line of sight coordinate with the origin at the GC (Sawada et al. 2004).

The CS map that is used for the diffusion model is obtained by integrating CS maps in velocity bands $\sum_i f(l, b, v_i)$, where $f(l, b, v_i)$ is the distribution of the molecular material as a function of l , b and the velocity $v_i \in [-200 \frac{\text{km}}{\text{s}}, -190 \frac{\text{km}}{\text{s}}, \dots, 190 \frac{\text{km}}{\text{s}}, 200 \frac{\text{km}}{\text{s}}]$ (Tsuboi et al. 1999). The face-on map, derived in (Sawada et al. 2004), can thus be used as a look-up table, allowing the conversion $f(l, b, v_i) \rightarrow f(l, b, z)$ for the position of GMCs in the GC region. This can be done as follows (see Fig. A.1 for an example):

- ◊ For a CS map in a given velocity range $[v_1..v_2]$, for each longitude position l it is checked, whether there is a bin $B(l, z)$ at the same longitude position in the face-on velocity map, containing a velocity value $v(l, z)$ within the current range, i.e. $v_1 \leq v(l, z) \leq v_2$. If this is the case, all bins in the CS map, which have the same longitude value, are moved to the corresponding line of sight position z of bin B , assuming that the face-on map is valid throughout the latitude range under

consideration. If no matched bin B could be found, then all bins in the CS map at longitude l are assigned the z -value 0.

- ◇ All maps in velocity bands are added up to obtain the total 3-D map of MCs (see fig. 3.4). At the end it is tested, whether the sum over all bin entries is the same for both 2-D and 3-D maps, to check errors in the algorithm.

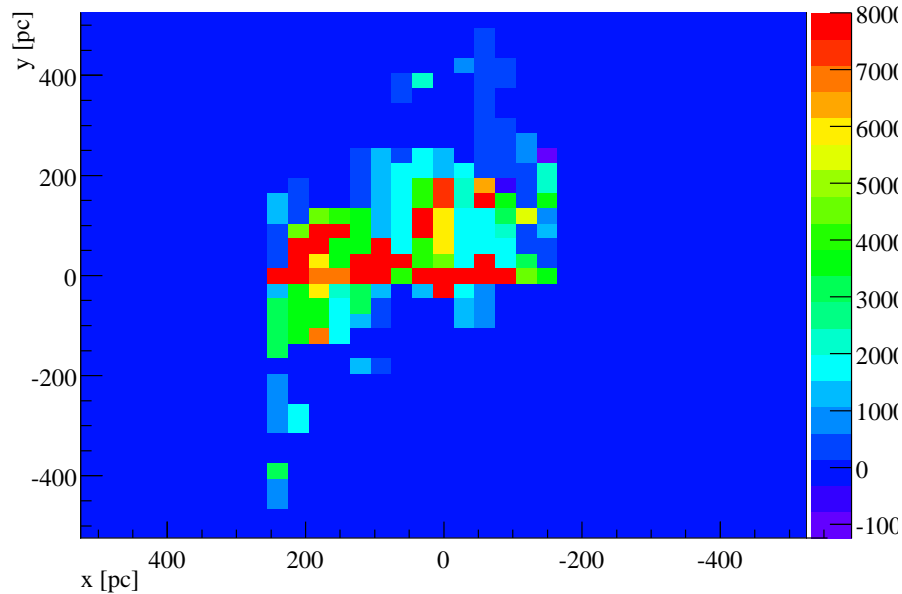


Figure 3.4: Derived face-on distribution of molecular material as seen by CS observations using the face-on velocity map from (Sawada et al. 2004). The MCs are mostly moved towards positive z -values and the distribution appears to be elongated and far from exhibiting a circular or ellipsoidal shape. The density stripe at $z = 0$ is partly due to MCs for which no adequate z -position could be determined.

With this method it was possible to find a line of sight coordinate according to the model by Sawada et al. (2004) for more than 75% of the total mass of MCs. It should be noted, however, that due to high foreground contamination in the velocity range $[-60 \frac{\text{km}}{\text{s}} .. 10 \frac{\text{km}}{\text{s}}]$ the model provides no information for the MCs in that range. Nevertheless, the 3-D map is expected to reproduce the actual three dimensional distribution of molecular material and thus the regions of interactions for CRs more accurate than the 2-D map. The corresponding difference in the longitude profiles of the mean distance between MCs and the GC is shown in Fig. 3.5. As expected, the mean distance is always larger for the 3-D realisation, and the differences between the 2-D and 3-D cases are most pronounced at the GC.

Calculation of the γ -ray maps

In order to achieve an additional improvement on the precision of the measurement, no simplification is applied concerning the conversion of the primary proton spectrum into

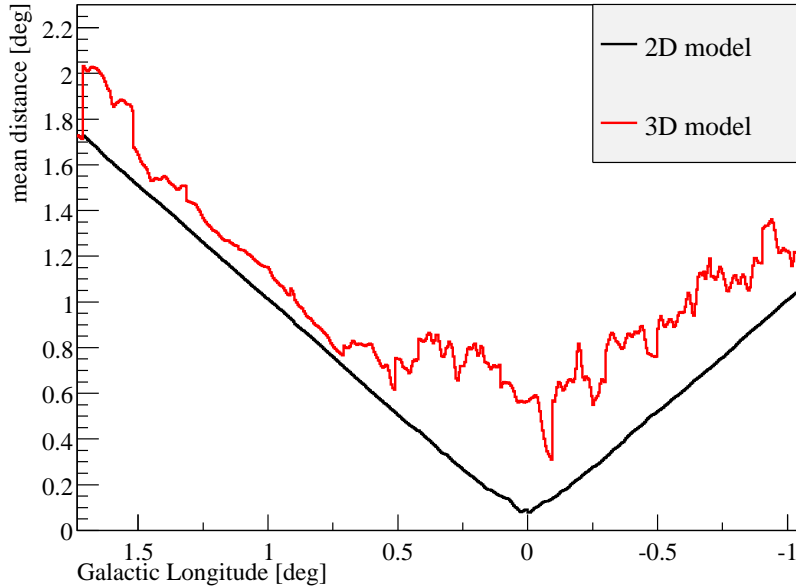


Figure 3.5: Comparison of profiles of distances from MCs to the GC for the 2-D and 3-D gas distributions. While the distance distribution for the 2-D case is basically linear, the distance profile for the 3-D realisation is more complex and shows deviations especially in the central region.

a corresponding γ -spectrum. Instead, the results described in (Kelner et al. 2006) are used. In this paper, the authors applied Monte-Carlo simulations of inelastic, fixed target proton-proton interactions, for incident protons having energies above $E_p > 100$ GeV and found analytical expressions describing the arising spectra $\Phi = \Phi(E_i, E_p)$ of stable secondary particles i like γ -rays or neutrinos.

Thus, to calculate the γ -ray emission for an energy E_γ at a certain position $P(l, b)$ in the map, the contribution from protons having energies $E_p \geq E_\gamma$ needs to be integrated. In reality, this was done using a two-dimensional look-up table (see Fig. 3.6), that was built upon the formula for the γ -ray spectrum provided in (Kelner et al. 2006), fine-binned both in E_γ and E_p , to speed up the calculations. Thus one obtains γ -ray emission (flux) maps for $E_{\gamma,i}$, with $E_{\gamma,i}$ being corresponding γ -energies for each bin i from the look-up table (see Fig. 3.2), having correct relative normalisations. To transform the flux maps into count (event) maps, they have to be folded with the detector acceptance for the corresponding energy, obtained from the observational dataset (see Sec. 2.3.6). Two example maps are shown in Fig. 3.7.

In this way it is possible to easily access simulated flux or count maps for every possible set of diffusion parameters (D, δ, Γ) and in any chosen energy bands, later necessary for the analysis (see Sec. 3.2).

As far as the differences between the 2-D and 3-D realisations are concerned, they are

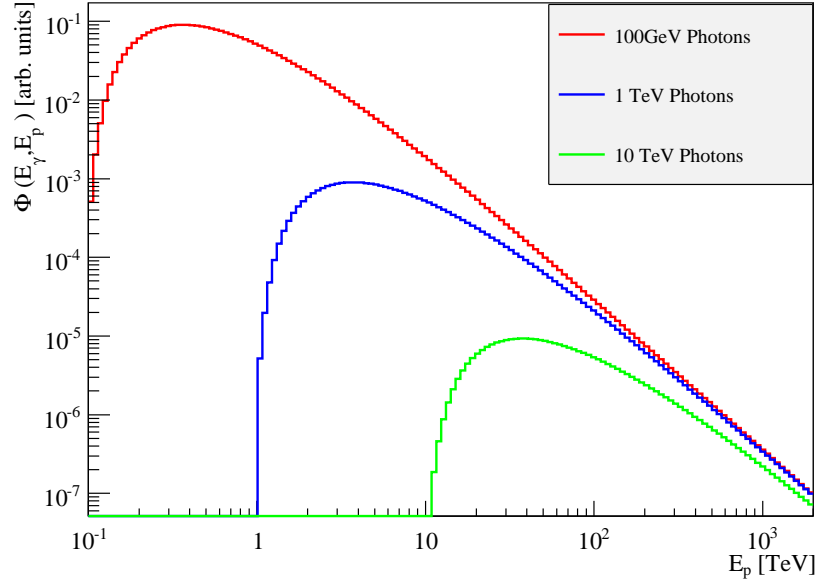


Figure 3.6: Spectrum $\Phi(E_\gamma, E_p)$ of secondary photons from fixed target proton-proton collisions, as a function of the incident proton energy E_p for three photon energies $E_\gamma = 0.1, 1,$ and 10 TeV. The spectrum is weighted with E_p^{-2} . For this weighting, the spectra reach their maximum at $E_p \approx 4 E_\gamma$, e.g. 100 GeV photons are mainly created in interactions of 400 GeV protons. The relation is taken from (Kelner et al. 2006).

demonstrated by showing their longitude profiles for an example set of diffusion parameters, see Fig. 3.8. The differences originate from deviations in the mean distance profiles of the GMCs, especially pronounced in the central region (see Fig. 3.5). It is visible that for 3-D diffusion the predicted γ -ray distribution appears wider, meaning that restricting the analysis to the use of the 2-D model tends to overestimate the diffusion coefficient.

As aforementioned, the purpose of the diffusion models is to provide a possibility to compare the theoretical predictions for CR diffusion with observational results. The models introduced in this section should be better suited with regard to the determination of diffusion parameters than the one used in (Aharonian et al. 2006d), especially concerning parameters influencing the spectrum of the detected very high-energy emission δ and Γ . However, there are still important simplifications involved, that are worth emphasizing:

- ◇ The acceleration of CRs happens instantly, i.e. the acceleration time is a delta function.
- ◇ The diffusion occurs completely isotropically. In reality, the diffusion coefficient is rather a 3×3 tensor, which depends on the actual location. This means that the diffusion coefficient determined later within the scope of this work is a space-averaged value.
- ◇ The cross-section of interactions between CRs and MCs is assumed to be energy-

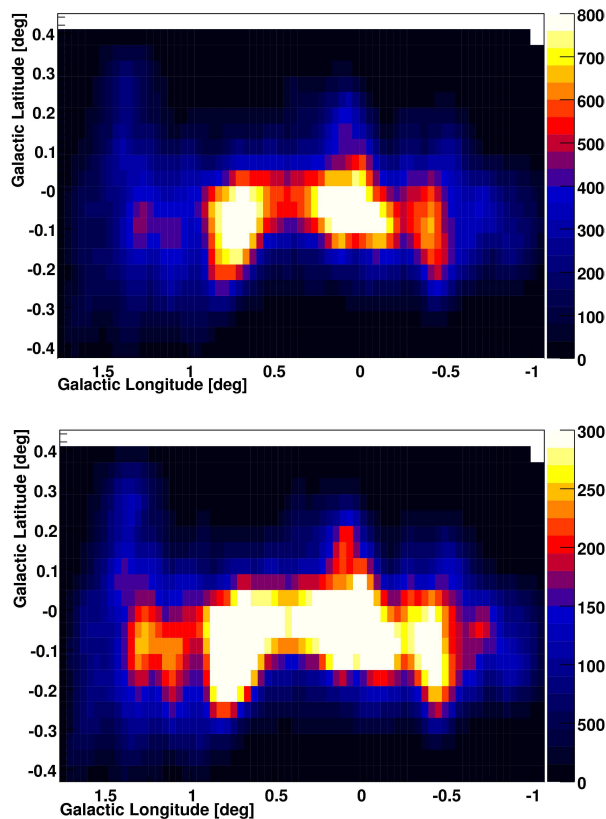


Figure 3.7: Excess maps obtained with the 2D diffusion model for the GC region. The diffusion parameters are $D_{E=3.2 \text{ TeV}} = 3 \text{ kpc}^2/\text{Myr}$, $\Gamma = -2.1$ and $\delta = 0, 1$ for the top and bottom plot, respectively. One can see that taking into account the energy-dependence of the diffusion coefficient leads to different predictions for different δ -values.

independent and the γ -ray flux scales linearly with the density of MCs, i.e. CRs can freely penetrate into all clouds.

It is sensible to make these simplifications because there is an insufficient knowledge concerning these points and studies on these subjects would go beyond the scope of this work. Despite this, it can be expected that the diffusion models, presented in this section, offer enough power for interpreting the H.E.S.S. data, for which the analysis is described in the following section.

3.2 Analysis of H.E.S.S. data

In this section the analysis of H.E.S.S. data and its interpretation using the diffusion model introduced in the last section is described. The purpose of this study is to use the full dataset collected throughout the years 2004-2008, which is roughly a factor of three larger than the subset used for the discovery of the diffuse emission (Aharonian et al. 2006d). It

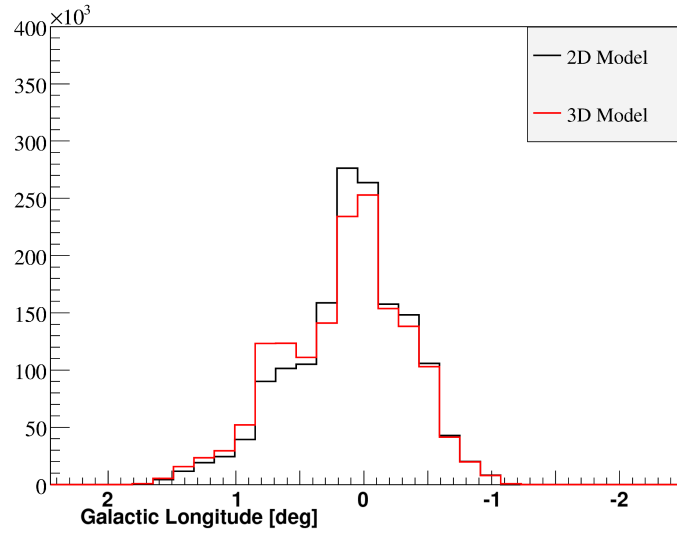


Figure 3.8: Comparison of longitude profiles for predicted γ -ray emission for 2-D and 3-D diffusion models for an example set of diffusion parameters: $D_{E=3.2 \text{ TeV}} = 0.2 \text{ kpc}^2/\text{Myr}$, $\Gamma = -2$ and $\delta = 0.5$ ($t = 10^4 \text{ yrs}$). The incorporation of the third dimension in the diffusion model leads to a broader distribution, thus the 2-D model would overestimate the diffusion coefficient.

offers the ability to test the proposed diffusion hypothesis and may restrict the parameter space of diffusion, in particular with regard to a possible spectral hardening of the emission towards its outer regions due to energy-dependence of the diffusion speed. There is as well a chance to recognize individual sources in case they amount a larger part to the extended emission in the GC region.

3.2.1 Dataset

Since morphological and spectral characteristics of the diffuse emission are especially important, it is desirable to have a dataset that has a superior quality in terms of energy and direction reconstruction. For that purpose, the dataset used for this analysis is chosen to consist only of runs, for which the data of all 4 telescopes satisfy the quality criteria described in Sec. 2.3. Besides, the maximum angular distance between observation position and the GC point source HESS J1745–290 is set to 1.5° to avoid systematic effects due to low detector acceptance at the edge of the field of view. The resulting dataset consists of 329 runs taken from March 2004 until July 2008. These dataset partly comprises pointed observations on HESS J1745–290 (288 runs), mostly taken with an offset of 0.7° , dedicated observations of G0.9+0.1 (19 runs), dedicated observations of the unidentified source HESS J1745-303 (10 runs), 11 runs belonging to the Galactic scan program and 1 run targeting at the GRB 060603A. The zenith angles range from 5° to 61° , while the mean zenith angle is 21° . 194 runs were taken at a zenith angle of less than 20° , thus the lowest ener-

gies are accessible for a large number of runs, what will become important in the following.

For optimal angular and energy resolution, and for superior background rejection, hard cuts as described in Sec. 2.3 are used. As far as background subtraction is concerned, the ring-method is used (see Sec. 2.3.4), with a ring radius of 1.2° . The significance map, obtained with the described analysis configuration, is shown in Fig. 3.9. With regard to the number of sources and extension of the diffuse emission in the field of view, the exclusion region (see Sec. 2.3.5), selected for this analysis, is very large and consists of a rectangle centered on $l = 0^\circ$ and $b = -0.1^\circ$, having an extension of 6° in longitude and 1.4° in latitude, and circular regions covering contamination from the unidentified source HESS J1745-303, the newly discovered unidentified source HESS J1741-302 (Tibolla et al. 2009), and possible emission from the Sgr D region. Because of such unusually large exclusion regions, the acceptance in the field of view is determined from lookup-tables and the systematic of geometrical background subtraction must be cross-checked. For that purpose, two other ring radii were used, 1.0° and 1.4° , as well as the template-method. As described in Sec. 2.3.4, the template method uses a certain region of the shower parameters space, MSCW between 3 and 9, to estimate the γ -like hadronic background, thus is less affected by the size of the exclusion regions. On the other hand, this method does not correct for gradients in the field of view like the ring-method, hence the ring-method is taken as the default background subtraction algorithm.

Additionally, to reduce possible systematic effects due to differences between the assumed and real energy thresholds during performed observations, which might influence on the comparison between data and the diffusion models, a cut at $E_\gamma \geq 350$ GeV on the event energy is applied (see also Sec. 3.2.3).

Statistical results are summarized in table 3.1. They refer to the on-region of 0.1° radius around the central source HESS J1745–290, and serve as a first consistency check between the background methods. As one can conclude from the results, there is a good agreement between different analysis configurations. A comparison of resulting distributions is shown in Fig. 3.10.

The following analysis methods will be explained by means of results from the analysis using the ring-method with a ring radius of 1.2° , whereas results from other ring and template configurations will serve as systematic crosschecks.

γ -ray emission in the field of view

It is now worthwhile to take a closer look at different emission regions, seen in Fig. 3.9. As far as individual sources are concerned, one recognizes the point sources HESS J1745–290 and G0.9+0.1, the unidentified source HESS J1745-303 and the recently discovered unidentified source HESS J1741-302 (Tibolla et al. 2009). Possible counterparts for HESS J1745–290 were already extensively discussed in chapter 1, the only recent development concerning the map shown in (Aharonian et al. 2006d) is that now also Fermi sees a positionally coinciding source (Abdo et al. 2009). There is an emission region showing

	Ring 1.0°	Ring 1.2°	Ring 1.4°	Template
Number of processed runs	329			
Livetime [h]	139.89			
Mean zenith of on-region [°]	21.27			
Mean offset of on-region [°]	0.74			
Number of on-events N_{on}	8393			
Number of off-events N_{off}	10769	10967	7797	49393
α	0.3449	0.3291	0.4687	0.0752
Number of excess events N_{γ}	4676.4 ± 98.1	4783.9 ± 97.9	4736.5 ± 100.5	4676.9 ± 93.1
Significance [σ]	54.4	56.4	52.4	62.6
Significance per $\sqrt{\text{hour}}$ [$\sigma/\sqrt{\text{h}}$]	4.6	4.8	4.4	5.3

Table 3.1: Summarized statistics referring to an 0.1° radius region around the central point source HESS J1745–290 from the analysis of the GC region using different configurations of background subtraction. While the number of excess events agrees within errors between different configurations, the template analysis, according to these results, is the most sensitive one due to the intrinsically low α -value.

up at the position of the Sgr D complex, that was not seen before. For that, an obvious counterpart is missing and it is located well outside the area covered by CS observations, so it can not be included in the studies involving the diffusion model, because predictions of γ -ray emission are only possible for the regions containing GMCs. Therefore, a close examination of this source would go beyond the scope of this work.

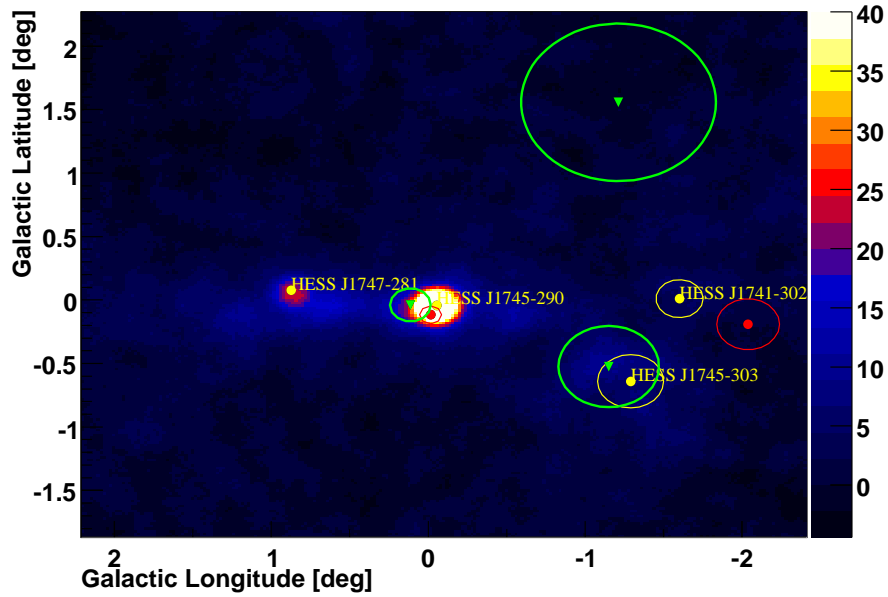
The diffuse emission still appears to be elongated along the Galactic plane and a visual correlation with GMCs remains. From the map alone, there is no obvious hint for existence of further sources that would be located within the diffuse emission region (see also Fig. 3.10 and 3.12 for a plot of longitude and latitude profiles, respectively). To probe the new data more quantitatively, a detailed study of the excess distribution with regard to the diffusion model is needed, for which first both point sources have to be subtracted from the map. For that, the methodology is described in the following.

3.2.2 Study of the diffuse emission

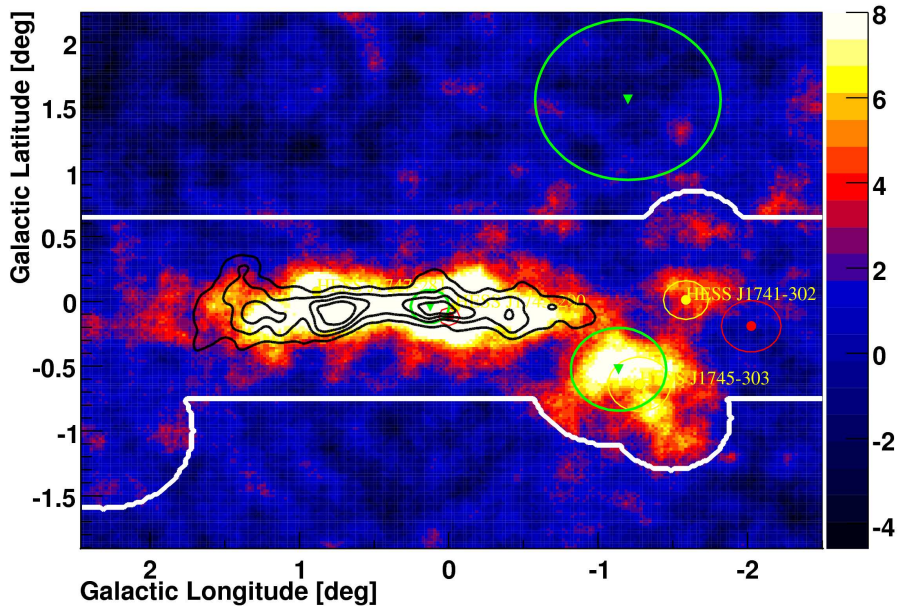
After having defined the dataset and the basic analysis configuration, the further discussion deals with the analysis methods used to extract and to study the extended diffuse emission in the GC region. In this section the basic procedures for point source subtraction and scan of the parameter space of diffusion is described, while the following section treats modifications of the analysis, which make use of the event energy information.

Point source subtraction

In Sec. 2.3 it was explained, that morphological characteristics of a H.E.S.S. point source are described by the PSF. The PSF is modelled by two radial-symmetric Gaussian functions with different normalisations and widths and a common center (Berge 2006). So if



(a) Significance map of the GC region saturated at 40σ



(b) Significance map of the GC region saturated at 8σ

Figure 3.9: Significance maps of the GC region obtained from the full dataset using hard cuts and the ring background method. The distribution is saturated at 40σ and 8σ to simultaneously display both point sources HESS J1745–290 and G0.9 + 0.1 (labeled in the map as HESS J1747 – 281), and the regions of extended emission, respectively. Positions of H.E.S.S. sources are indicated with yellow markers. Positions of EGRET and FERMI sources are shown in green and red, respectively. Unidentified sources HESS J1745 – 303 and HESS J1741 – 302 are extended and weak, hence only visible in bottom map. Beside, the contours of the CS map are overlaid (black lines), as well as regions excluded from background estimation (white lines).

the position of a point source needs to be determined, usually the excess distribution is fitted with the PSF, including another Gaussian function for extended sources, and thus its center is taken as the position of the particular source. If the fit is reasonably good, then a subtraction of the fit function from the map should yield residuals that are compatible with zero.

However, for this analysis the situation is more complicated. Before HESS J1745–290 and G0.9+0.1 can be modelled with the corresponding PSF and subtracted from the excess map, the diffuse emission needs to be taken into account. This can happen in two ways:

- ◇ A map describing the diffuse emission is subtracted from the excess map, before the point source fits are performed. Subsequently, the point sources are fitted and subtracted and the diffusion model is added back to the map.
- ◇ A second possibility is to include the normalisation of the model map as an additional parameter in the fit, thus fitting the diffuse emission and the point sources simultaneously. This method should be able to describe the diffuse emission in the vicinity of point sources more accurately than the first one, but it must be controlled that the normalisation factor converges in a physically sensible range.

For this analysis the second approach is chosen. The diffuse emission is here modelled by simple energy-independent diffusion. This choice is justified, because even though the influence of a choice of a certain model map on source fits was not studied, the effect is not expected to be large (The HESS Collaboration & Acero 2009). Applying the method described above one obtains a point source subtracted excess map which longitude profile is shown in Fig. 3.10 for all configurations of background subtraction (see Fig. 3.13 for point source subtracted latitude profiles.). The binwidth of the longitude profile is chosen as 0.16° , so given the fact that the area of such a bin corresponds to $\sim 92\%$ PSF containment radius (see Sec. 2.3), bins are considered to be approximately uncorrelated. The quantitative agreement is verified in Tab. 3.2, where the number of γ -rays before and after point source subtractions are summarized. As a check, in Fig. 3.14 and 3.15 one-dimensional profiles are made for the point source regions before and after the point source subtraction, and additionally after the subtraction of the diffuse component. They show that the final residua agree quite well with zero within errors, meaning that both the point sources and the diffuse emission are reasonably well described.

	Ring 1.0°	Ring 1.2°	Ring 1.4°	Template
Number of excess events before point subtraction	13038.2	13133.5	13159.5	13216.5
Number of excess events after point subtraction	9237.2	9502.6	9355.27	9686.7

Table 3.2: Summarized statistics referring to the region of the diffuse emission, before and after point source subtraction, using different configurations of background methods. The number of excess events of the diffuse emission region was calculated for $-1.07 < l < 1.65$ and $-0.31 < b < 0.33$.

Comparing the longitude profiles obtained with current dataset (Fig. 3.10)⁴ and published in (Aharonian et al. 2006d) (Fig. 3.11), there is a qualitative agreement between the published and the new results. For both datasets, there are three pronounced peaks in the distribution ($l \approx 0^\circ$, $l \approx 0.6^\circ$, $l \approx -0.5^\circ$) and an overall decreasing flux for larger longitudes. However, still non-zero emission can be observed for $l > 1.7^\circ$ and $l < -1^\circ$, that is due to the emission from the Sgr D and HESS J1745 – 303 regions, respectively. Moreover, still no discrete sources are observable in the new distributions.

First comparison with diffusion models

The point source subtracted excess map of the diffuse emission region can now be used to get a first impression of how well the diffusion hypothesis is compatible with the newest data and for testing the performance of the diffusion model, not making use of any spectral information. For that purpose, event maps obtained by means of the 2-D diffusion model, which is taken for this first assessment, are compared with the excess map (more precisely: profile) from the data. The approach is the following: The parameter space of diffusion is divided into small steps and for each set of parameters (D_0 , Γ_p , δ) an event map is produced, using the acceptance of the studied dataset, and its normalisation is fitted to the data, within the range $-1^\circ \leq l \leq 1.7^\circ$. The diffusion parameters are selected as follows in order to cover the whole region of interest, as will be shown in the course of the analysis:

- ◇ Diffusion coefficient: $0.03 \frac{\text{kpc}^2}{\text{Myr}} \leq D_0 = D_{E=3.2 \text{ TeV}} \leq 3 \frac{\text{kpc}^2}{\text{Myr}}$ ⁵ divided into logarithmic steps $\log_{10}(\Delta D_{E=3.2 \text{ TeV}}) = 0.2$. The age is set to 10^4 years.
- ◇ Spectral index of primary particles: $-2.2 \leq \Gamma \leq -1.65$ in linear steps of $\Delta\Gamma = 0.05$.
- ◇ Energy dependence of diffusion: $0 \leq \delta \leq 1$ in linear steps of $\Delta\Gamma = 0.1$.

The resulting χ^2 of the fit is stored, so at the end a (reduced) χ^2 -distribution over the total parameter space under study is obtained, see Fig. 3.16. One observes that the best χ^2/NDF -values, lying within the 95% confidence level, calculated as $\chi_{95\%}^2 = \chi_{min}^2 + 9.49$,⁶ are obtained within a stripe-like region extending over a large range of spectral indices. Besides, the absolute value of the reduced χ^2 is quite large $\chi_{min}^2 = 6.33$, indicating that the fit does not perform well.

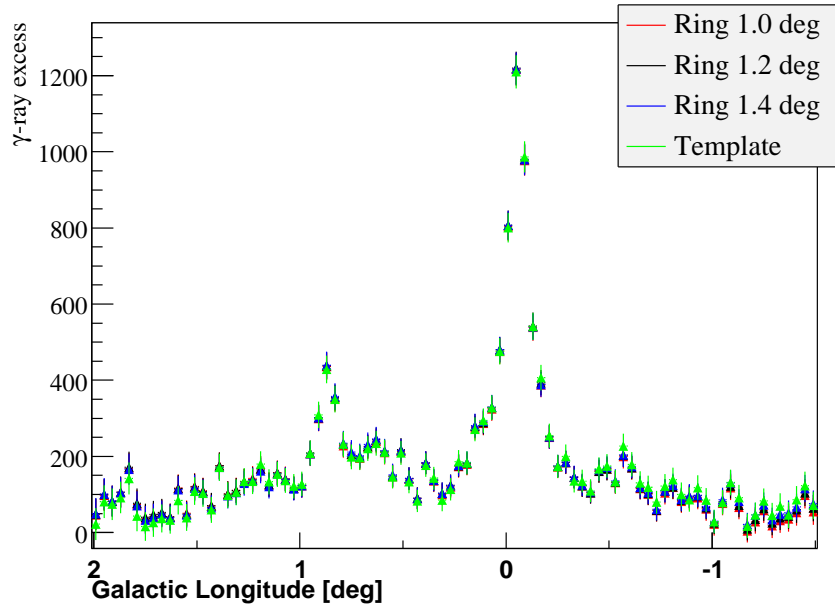
Systematics

As discussed in Sec. 3.1.3, the diffusion model used in this analysis is not expected to reproduce the observations exactly for small scales, given all the simplifications that were

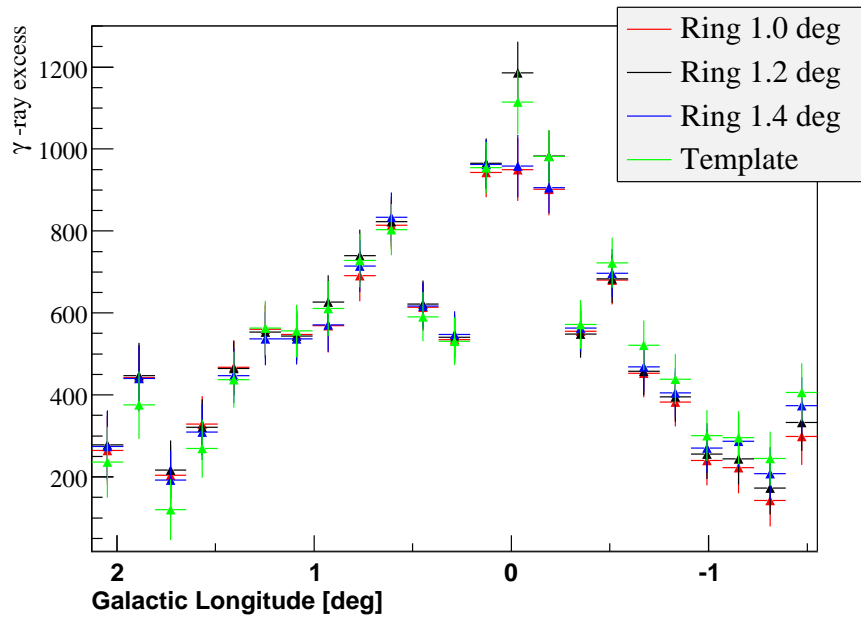
⁴ The slight gradient along the field of view that is visible for the template method is due to the zenith dependence of the detector acceptance within the same field of view, which cannot be corrected for in the current dataset due to the large size of exclusion regions.

⁵ The value $E = 3.2 \text{ TeV}$ is chosen for easier comparisons with results from (Dimitrakoudis et al. (2009), citetBuesching1), since these papers publish diffusion coefficients relating to particle energies of 3 TeV and 3.2 TeV, respectively.

⁶ The definition of the 95% confidence region implies, that the total number of fit parameters is 4, being the 3 parameters of diffusion and the normalisation of the simulated γ -ray maps.



(a) Longitude profile before point source subtraction.



(b) Longitude profile after point source subtraction.

Figure 3.10: Longitude profiles of the exposure-corrected excess distribution between $-0.31^\circ < b < 0.33 \text{ grad}$ (a) before and (b) after subtraction of both point sources HESS J1745–290 and G0.9+0.1. Note the finer binning used for the profile in (a). All four analyses agree within errors. The observed excess for $l > 1.7^\circ$ and $l < -1^\circ$ is due to emission from SgrD and HESS J1745 – 303 regions, respectively.

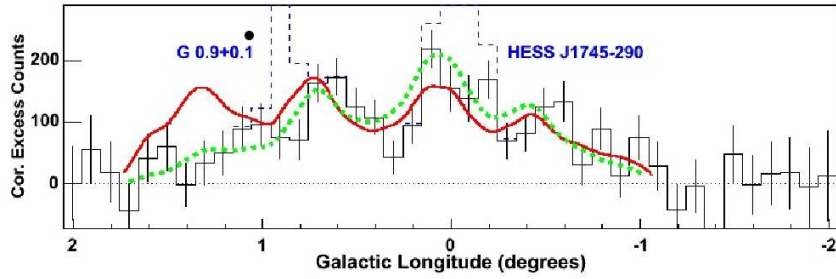


Figure 3.11: The longitude profile of the γ -ray exposure-corrected excess, shown together with the profile of MC density (red curve) and the prediction for the diffusion model. Image is taken from (Aharonian et al. 2006d). The diffusion model well reproduces the observed excess distribution.

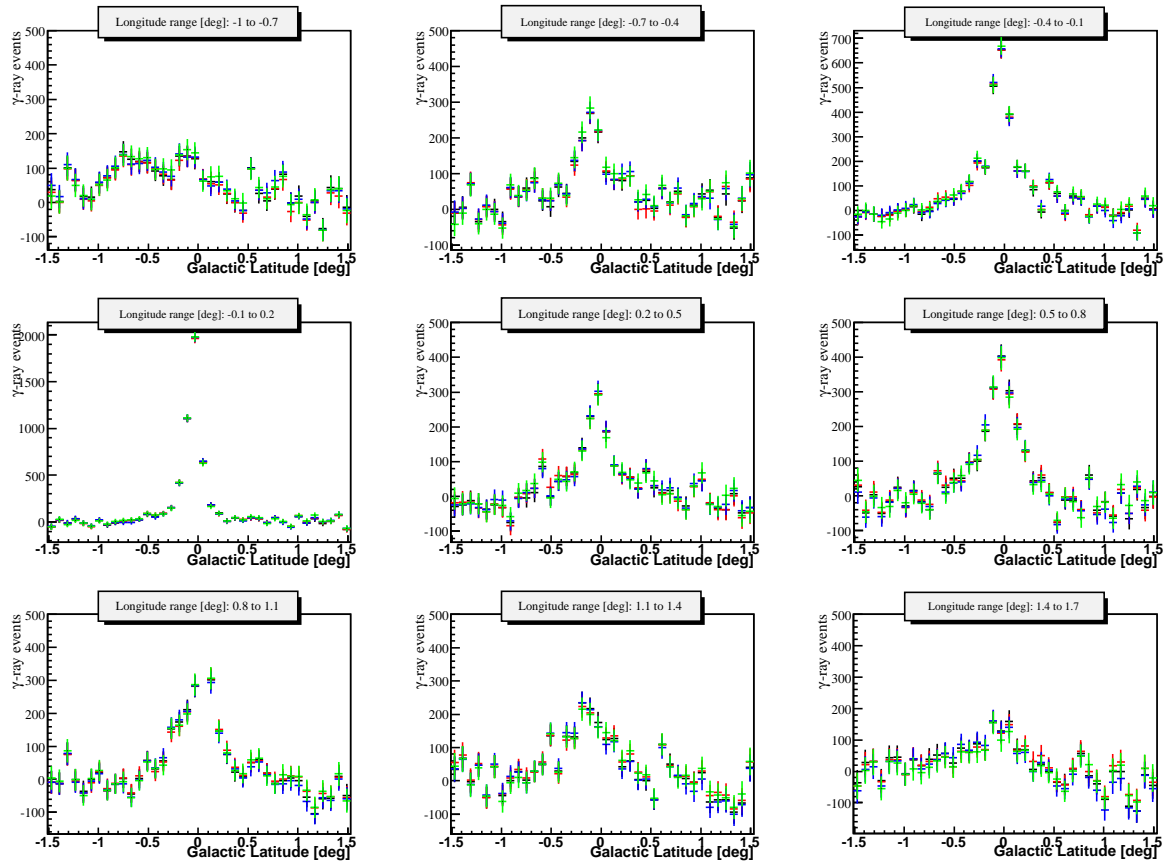


Figure 3.12: Latitude profiles of the exposure-corrected excess distribution, obtained for the indicated longitude ranges. Colour code: Ring 1.0° : red, Ring 1.2° : black, Ring 1.4° : blue, Template: green. Both point sources, HESS J1745–290 and $G0.9 + 0.1$, are clearly visible.

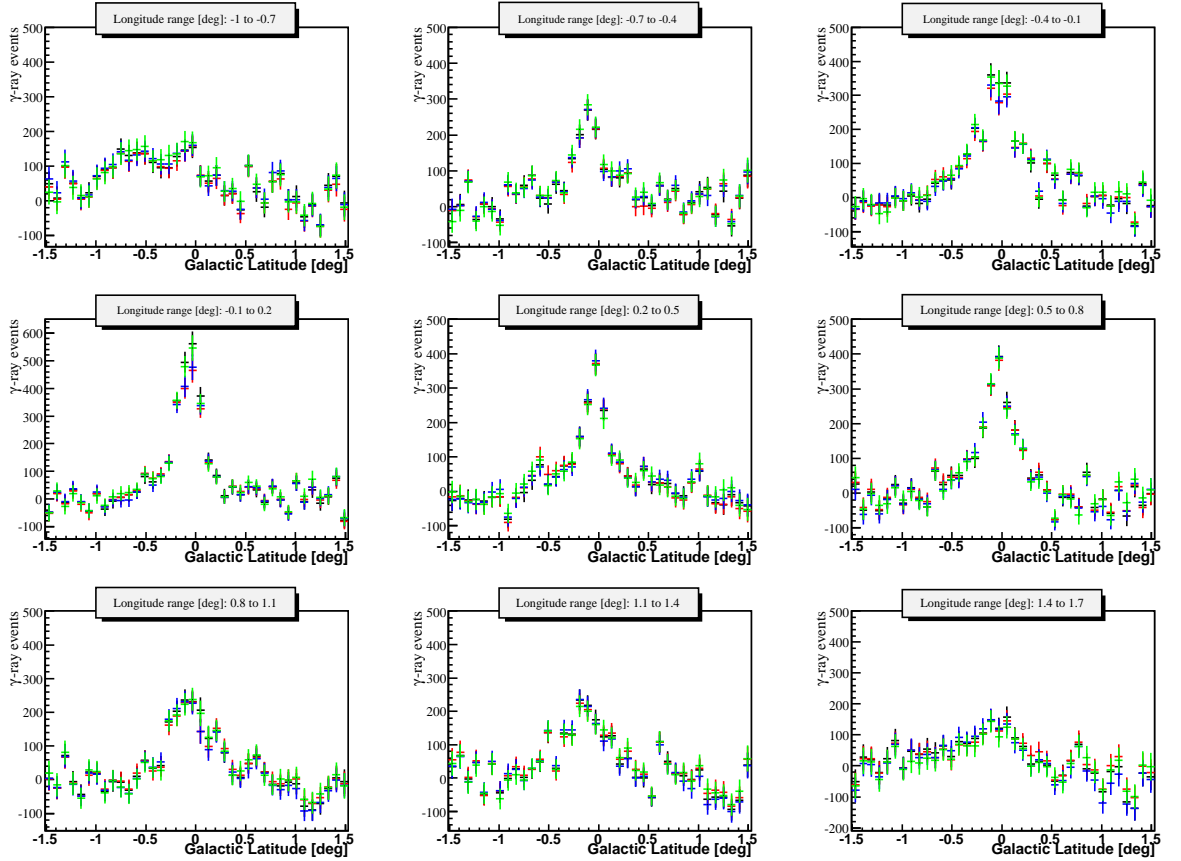


Figure 3.13: Latitude profiles of the exposure-corrected excess distribution after subtraction of point sources, obtained for the indicated longitude ranges. Colour code: Ring 1.0°: red, Ring 1.2°: black, Ring 1.4°: blue, Template: green.

applied. Thus taking into account only statistical uncertainties for the scans of the parameter space underestimates possible systematic effects. An additional systematic error can be included that takes into account experimental and model-related uncertainties. This is chosen to be calculated from the number of excess events as $0.2 * N_\gamma$, i.e. a systematic error of 20% is assumed. This uncertainty comprises the experimental part, given that for source spectra obtained by the H.E.S.S. experiment a systematic error on the total flux of 20% is quoted (see Sec. 2.3.6), as well as theoretical uncertainties leading to possible bin-to-bin variations. Taking such a systematic error into account, now for 2-D (Fig. 3.17) and also the 3-D diffusion model (Fig. 3.18), makes the area of low χ^2 -values more extended, as expected. Besides, the now lowest achieved reduced χ^2 -values are $\chi^2_{min} = 1.14$ for 2-D and $\chi^2_{min} = 0.98$ for the 3-D model, suggesting a good agreement between the data and the model, if systematic uncertainties are included. In Fig. 3.20 and 3.20 the correlations between the measured and simulated excess are plotted for both the 2-D and 3-D diffusion models. As it can be expected from the comparison of excess profiles, a linear correlation is obtained. However, since non-zero fluxes are measured for regions where the simulated emission vanishes, the correlations exhibit small offsets.

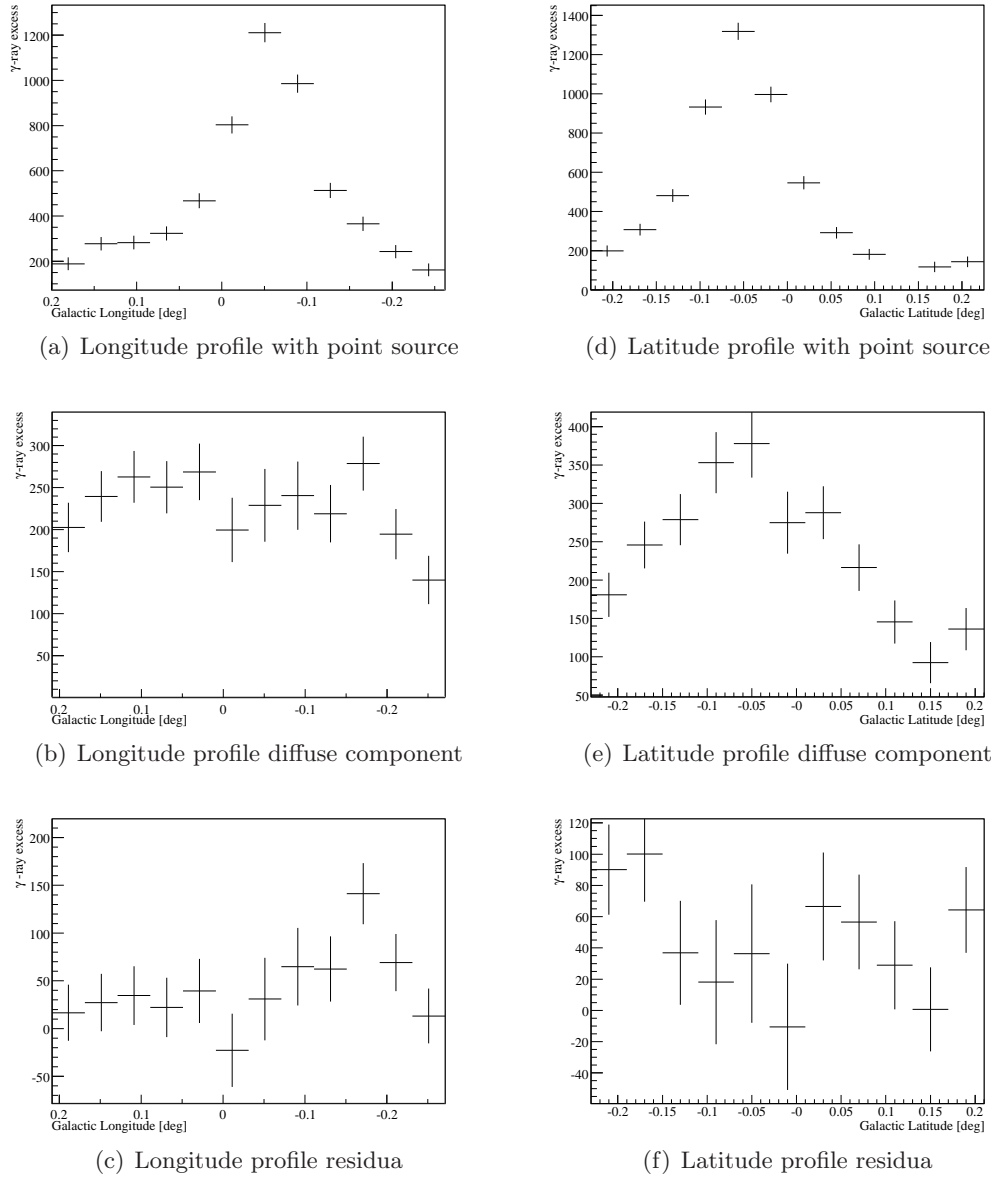


Figure 3.14: Profiles of the HESS J1745–290 region after fitting and subtraction of the point source. The normalisation of the diffuse component was included as a parameter in the fit. a) Longitude profile of emission before subtraction of the point source. b) Longitude profile of emission after subtraction of the point source. c) Longitude profile of emission after subtraction of both the point source and diffuse component. d) Latitude profile of emission before subtraction the point source. e) Latitude profile of emission after subtraction of the point source. f) Longitude profile of emission after subtraction of both the point source and diffuse component. The profiles were produced within $\pm 0.25^\circ$ around the position of HESS J1745–290. In comparison it becomes visible that most of the diffuse emission was properly modelled and only a small fraction still remains in the residua. (see also Fig. 3.15).

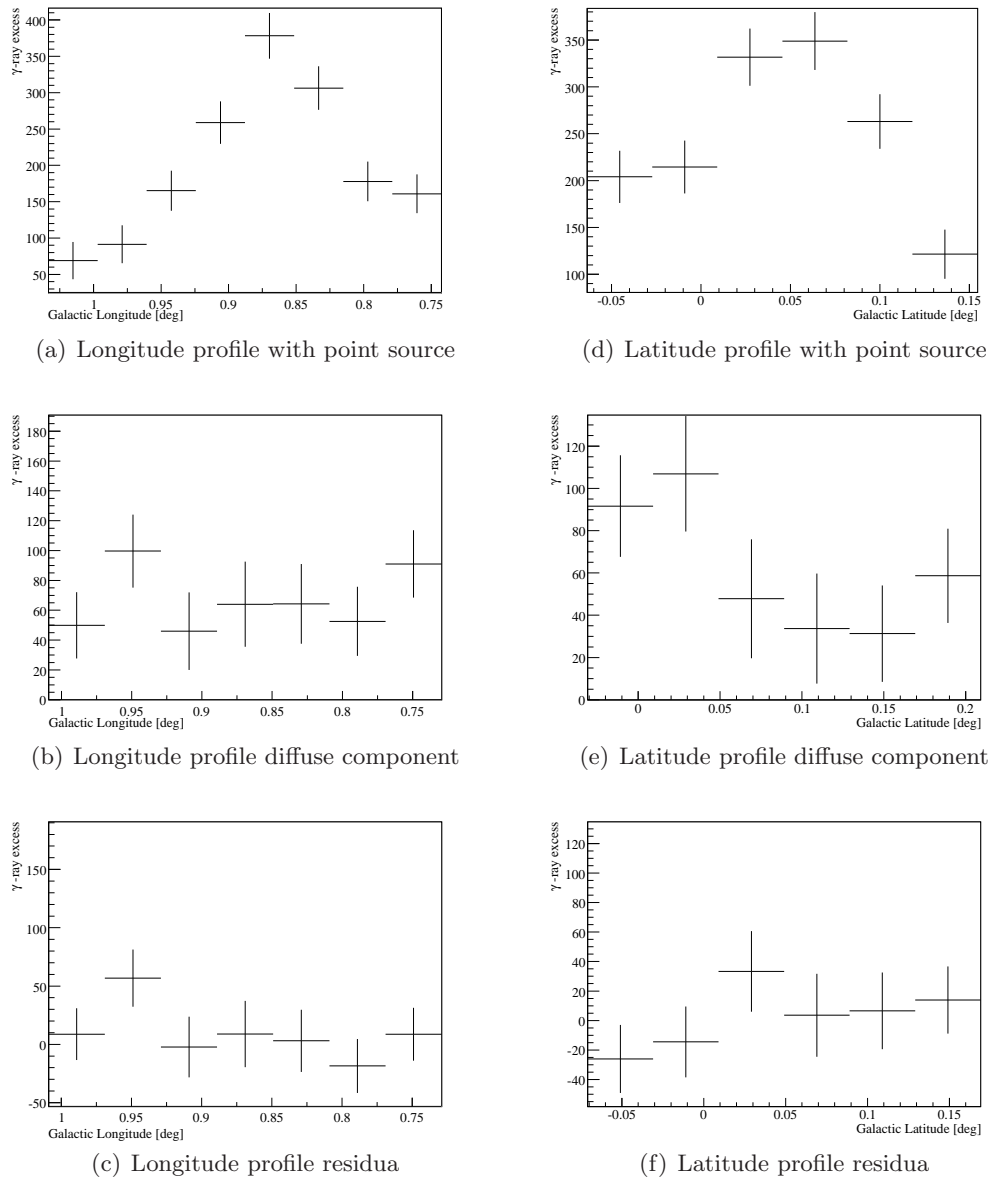


Figure 3.15: Profiles of the G0.9+0.1 region after fitting and subtraction of the point source. The normalisation of the diffuse component was included as a parameter in the fit. a) Longitude profile of emission before subtraction of the point source. b) Longitude profile of emission after subtraction of the point source. c) Longitude profile of emission after subtraction of both the point source and diffuse component. d) Latitude profile of emission before subtraction the point source. e) Latitude profile of emission after subtraction of the point source. f) Longitude profile of emission after subtraction of both the point source and diffuse component. The profiles were produced within $\pm 0.15^\circ$ around the position of G0.9 + 0.1. As in Fig. 3.14, also for G0.9 + 0.1 one can see that the diffuse component was modelled properly and the residua in c) and f) are compatible with zero within errors.

In Fig. 3.19 the excess longitude profile together with the best-fit diffusion models (2-D and 3-D) is shown, determined in the scans which included systematic uncertainties (Fig. 3.17 and Fig. 3.18). The data is well described by both models, however for negative (positive) longitudes towards the outer regions of the emission the emission is over(under)estimated by the model predictions. Besides, as already shown in Fig. 3.11, the peaks in the data distribution at $l = 0.6^\circ$ and $l = -0.5^\circ$ are shifted relative to the peaks in MC.

As aforementioned, this scan of the parameter space is not meant to be the final result, but rather to serve as a test of the diffusion model and to determine what restrictions on the parameter space can be achieved if the spectral information is not used, like it was done in publications before. As one can see, only having the total number of γ -ray events at hand, it is not possible to draw a more precise conclusion about the parameters Γ and δ . Moreover, no significant differences are seen between the use of the 2-D and the 3-D diffusion model. Both should be achieved by taking into account the spectral properties of the emission.

3.2.3 Improvement on parameter space restriction using the energy information

In the last section it was shown that the morphology of the extended emission from the GC region derived with the new dataset is still compatible with the diffusion hypothesis and can be used for a restriction of the diffusion parameter space. However, this restriction is not very tight, since from the morphological properties alone it is difficult to learn more about the spectral parameters Γ and δ . In this section, the spectral analysis of the diffuse emission is described and its implications on the diffusion parameters are demonstrated. An analysis in energy bands is motivated and discussed, followed by the description of the developed and applied statistical analysis using contrast values. The discussion about the application of the standard spectral analysis technique can be found in A.2.

Analysis in energy bands

In Sec. 3.1 it was shown, that the energy dependence of the diffusion coefficient $D(E) = D_0 E^\delta$ has the effect that particles with higher energies propagate faster than those with lower energies (see also Fig. 3.2). Thus in this case, the difference of diffusion speeds should become most apparent if the lowest and highest energies of the accessible range are considered.

The way to address this issue is to perform an analysis in two energy bands, a low and high energy band, and study the resulting γ -ray maps. Therefore, first suitable energy bands must be selected. These have to fulfill the compromise of being an optimal choice for the study of the expected physical effect on the one hand while still having enough statistical sensitivity on the other. The latter point implies that both bands should have approximately the same expected signal-to-signal and square-root of background-background ratio ($S_{\text{low}}/S_{\text{high}} \approx \sqrt{B_{\text{low}}/B_{\text{high}}}$). In order to determine such energy bands, one can consider

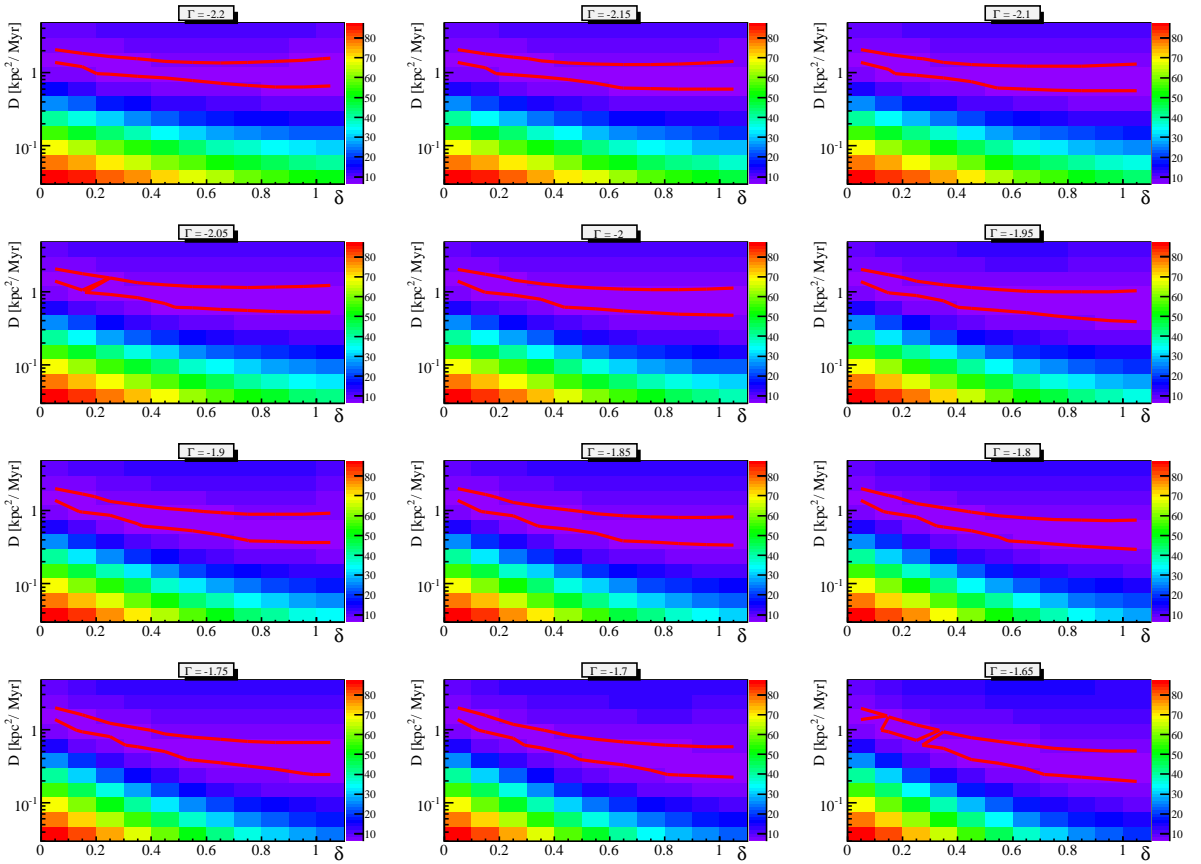


Figure 3.16: Results of the scan of the parameter space of diffusion using the point source subtracted excess profile distribution from Fig. 3.10 by fitting the normalisation factor of the maps from the diffusion model. Only statistical errors of the number of excess events are taken into account. The reduced χ^2 (z-axis) of the fits is plotted as a function of (D_0, δ, Γ_p) . The red line denotes the 95% confidence regions (see text). The minimum reduced χ^2 -value $\chi^2_{min} = 6.33$ is obtained for $D_0 = 0.3 \frac{\text{kpc}^2}{\text{Myr}}$ (for $t = 10^4$ yr), $\Gamma_p = -1.65$ and $\delta = 0.6$.

distributions of excess events at the position of HESS J1745–290 for a power law spectrum with $\Gamma = -2.29$ and $\Gamma = -2.43$.⁷ These distributions are obtained by folding the power-law spectrum with the acceptance from the data (see Sec. 3.1.3), and reach their maximum at $E \approx 0.45$ TeV, thanks to the large number of runs at low zenith angles (see Sec. 3.2.1). Demanding $S_{low}/S_{high} \approx \sqrt{B_{low}/B_{high}}$ for the selected bands, which at the same time should be separated from each other as far as possible in order to emphasize the difference of diffusion effects, then based on the present distributions following energy bands are suggested: $0.35 \text{ TeV} \leq E_{low} \leq 0.6 \text{ TeV}$ and $2.55 \text{ TeV} \leq E_{high} \leq 100 \text{ TeV}$. The ratios are $\sqrt{B_{low}/B_{high}} = 2.1$, $S_{low}/S_{high} \approx 1.7$ for $\Gamma = -2.29$ and $S_{low}/S_{high} \approx 2.3$ for $\Gamma = -2.43$, respectively. These energy bands are used for the rest of the analysis.

⁷ The indices used here were determined in (Aharonian et al. 2006d) (Fig. 3.22) and using the standard spectral analysis of the GC region (see Sec. A.2 and Fig. A.15)

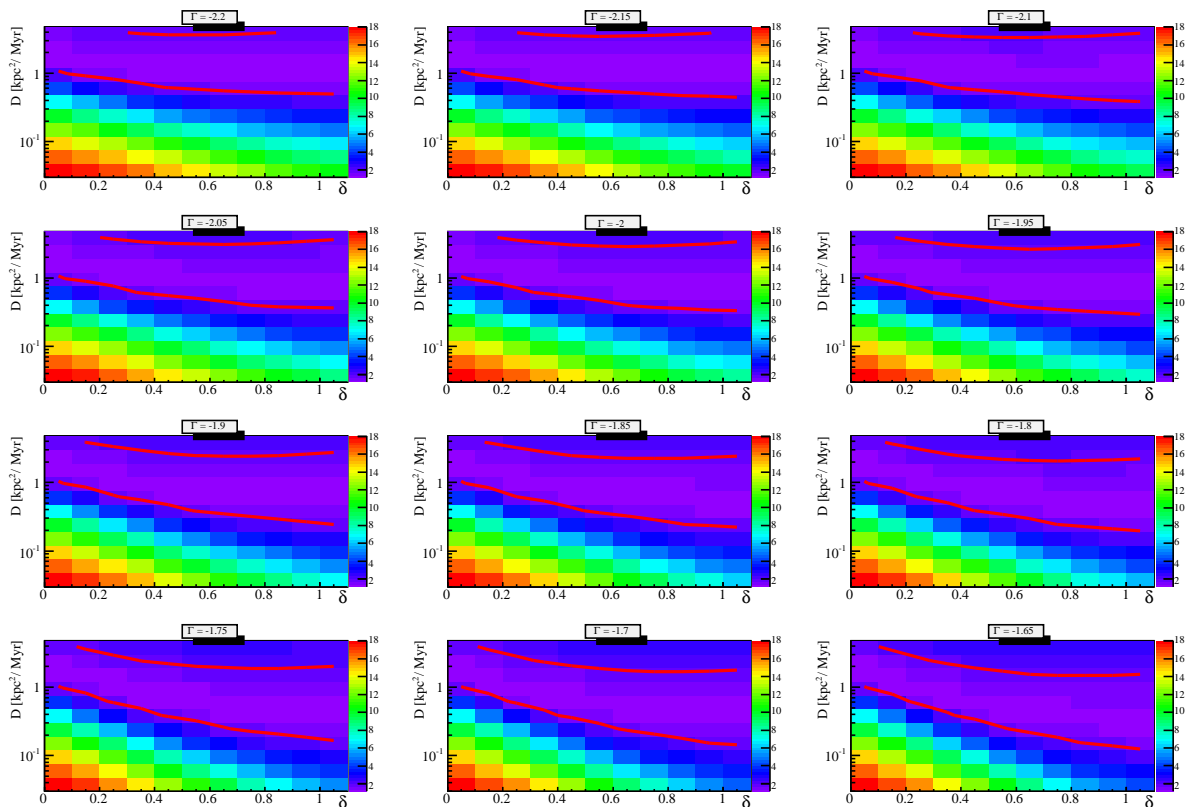


Figure 3.17: Results of the scan of the parameter space of diffusion using the point source subtracted excess profile distribution from Fig. 3.10 by fitting the normalisation factor of the maps from the 2-D diffusion model. Statistical and systematic errors (20%) of the number of excess events are taken into account. The reduced χ^2 (z-axis) of the fits is plotted as a function of (D_0, δ, Γ_p) . The red line denotes the 95% confidence regions (see text). The minimum reduced χ^2 -value $\chi^2_{min} = 1.14$ is obtained for $D_0 = 0.75 \frac{\text{kpc}^2}{\text{Myr}}$ (for $t = 10^4 \text{ yr}$), $\Gamma_p = -1.65$ and $\delta = 0.2$.

In Sec. 3.2.1 it was explained that due to the large size of the exclusion regions in the field of view, the acceptance of the detector cannot be determined from the data but is read from dedicated look-up tables. However, these acceptance distributions are created for the whole energy range, and since it is known that the acceptance has a non-negligible energy dependence, these look-up tables should not be used for analyses incorporating cuts on the event energy. Thus new look-up tables were created from off-data (see Sec. 2.3.5), for which only events of the corresponding energy range were used. In Fig. 3.23, two acceptance distributions for the low and high energy bands as a function of the offset angle (for 20° zenith angle) are shown, which are meant to reveal the different behaviours of the detector acceptance for lowest and highest energies. One observes that while for the low energy range the acceptance rapidly drops, the distribution for the high energy range is much smoother and has a non-zero acceptance even for very large offset angles ($\Psi \gtrsim 2^\circ$).

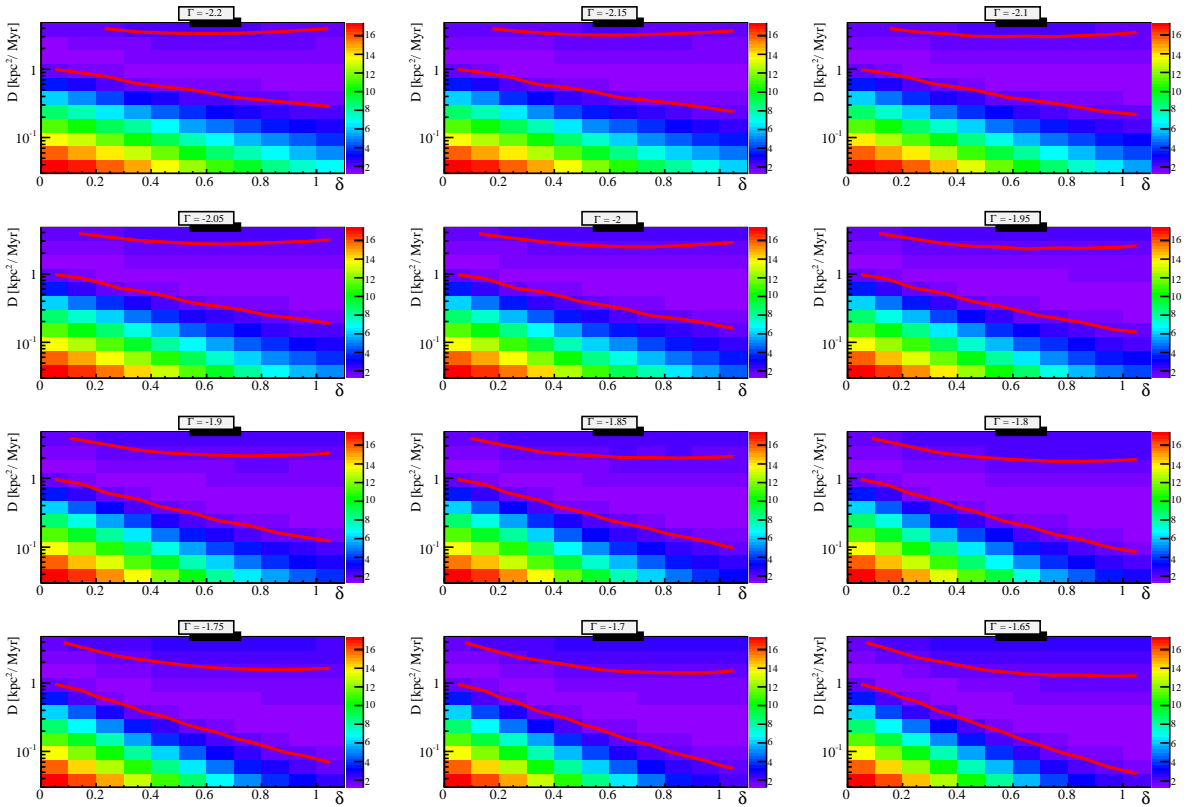


Figure 3.18: Results of the scan of the parameter space of diffusion using the point source subtracted excess profile distribution from Fig. 3.10 by fitting the normalisation factor of the maps from the 3-D diffusion model. Statistical and systematic errors (20%) of the number of excess events are taken into account. The reduced χ^2 (z-axis) of the fits is plotted as a function of (D_0, δ, Γ_p) . The red line denotes the 95% confidence regions (see text). The minimum reduced χ^2 -value $\chi^2_{min} = 0.93$ is obtained for $D_0 = 1.89 \frac{\text{kpc}^2}{\text{Myr}}$ (for $t = 10^4$ yr), $\Gamma_p = -2.2$ and $\delta = 0$.

The analysis of the GC region in both energy bands is then performed using the same background subtraction methods as described in 3.2.1. Statistical results are summarized in Tab. 3.3. They show that the emission from the HESS J1745–290 region is more significant in the high-energy band, as expected, since the spectrum of HESS J1745–290 is harder than determined for the diffuse emission: $\Gamma = -2.1$, according to new measurements. The statistical results concerning the diffuse emission (see Tab. A.1 and Tab. A.2) show that the number of low energy events, $N_{\gamma, \text{low}} = 2053$ exceeds, as expected, the number of high energy events, $N_{\gamma, \text{high}} = 1767$, although their ratio is different from the predicted, suggesting an overall harder spectrum than assumed: $\Gamma > -2.29$. Significance maps obtained for the ring method (1.2° ring radius) are shown in Fig. 3.24. The fact that aside the exclusion regions the map only shows usual background fluctuations confirms the validity of the used acceptance curves for the corresponding energy bands (see also Fig. A.3 and A.4). The emission in the high-energy range appears to be more smooth, while the low energy band shows rather clumpy structure.

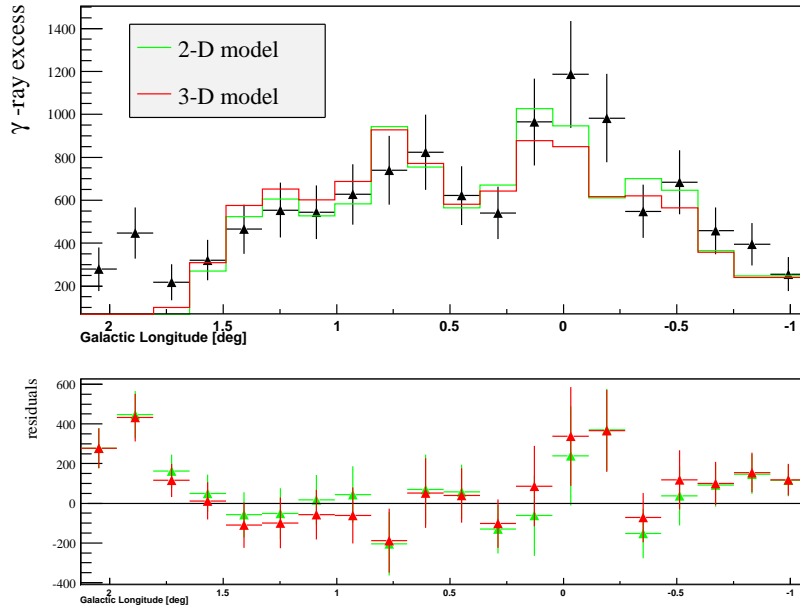
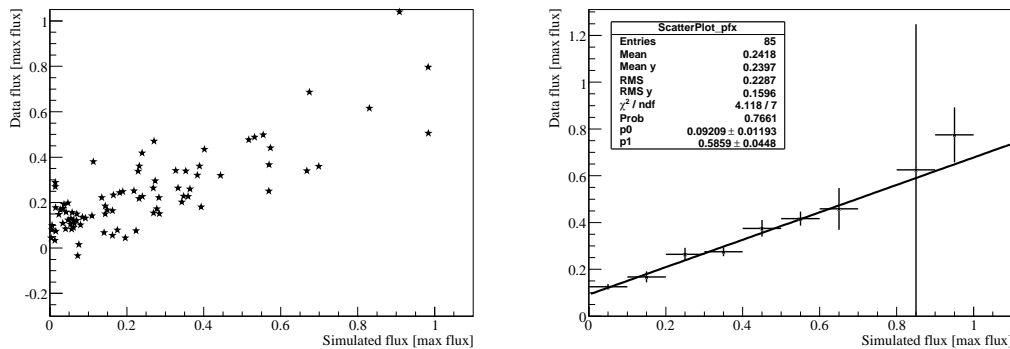


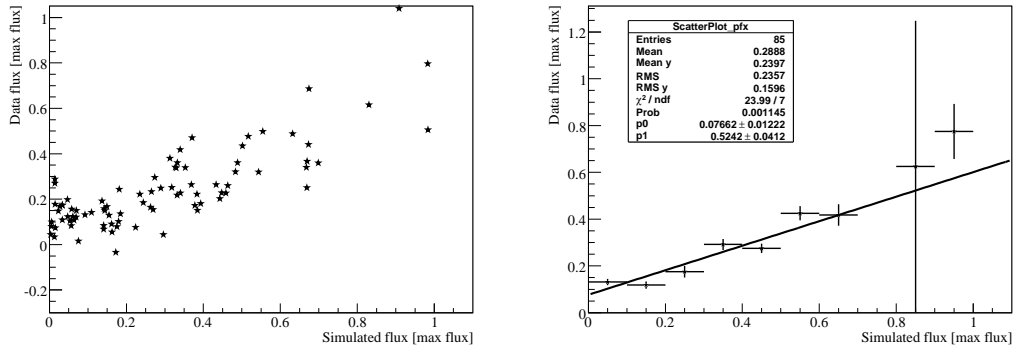
Figure 3.19: Longitude profile of the exposure-corrected γ -ray excess map from data and from the best-fit diffusion model and their residua integrated between $b = -0.31$ and $b = 0.33$. Systematic uncertainties of 20% on the number of excess events are included. Despite deviations on small scales, the overall description of the emission by the diffusion model looks solid.



(a) Correlation between predicted and measured γ -ray flux. (b) Profile of the correlation between predicted and measured γ -ray flux.

Figure 3.20: Correlation of measured flux vs. predicted flux from the 2-D diffusion model, normalized to their maximum values. The values are obtained from excess maps, binned in $0.16^\circ \times 0.16^\circ$ squares. The correlation is well described by a linear fit. See text for further details.

As for the analysis of the total energy range, point sources need to be removed from maps in energy bands as well. For the point source subtraction the same method as above was used. For the fits, the PSF was matched to the particular energy ranges (see Fig.



(a) Correlation between predicted and measured (b) Profile of the correlation between predicted and measured γ -ray flux in a 2D representation.

Figure 3.21: Correlation of measured flux vs. predicted flux from the 2-D diffusion model, normalized to their maximum values. The values are obtained from excess maps, binned in $0.16^\circ \times 0.16^\circ$ squares. The correlation is well described by a linear fit. See text for further details.

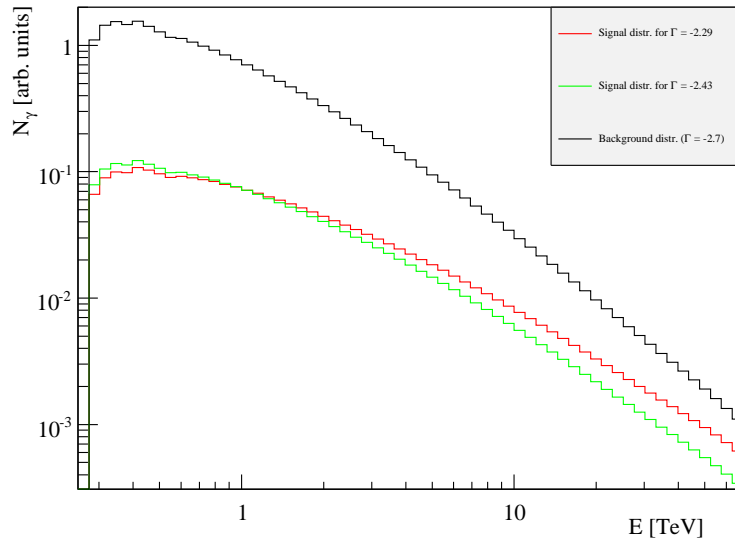


Figure 3.22: Calculated distribution of γ -ray events using the effective areas at the position of HESS J1745–290 for $\Gamma = -2.29$ (red line) and $\Gamma = -2.43$ (blue line). For the distribution of γ -like hadron events, $\Gamma_{CR} = -2.7$ was assumed. The signal and background distribution were used to determine optimal energy bands for the diffuse emission analysis (see also text).

3.25). Longitude profiles from the the resulting excess distributions are shown in Fig. 3.27 for all configurations involved (see Fig. A.5 and A.7 for latitude profiles). One can see that the distributions obtained with different background subtraction configurations agree within statistical uncertainties. The low energy profiles exhibit several peaks of emission,

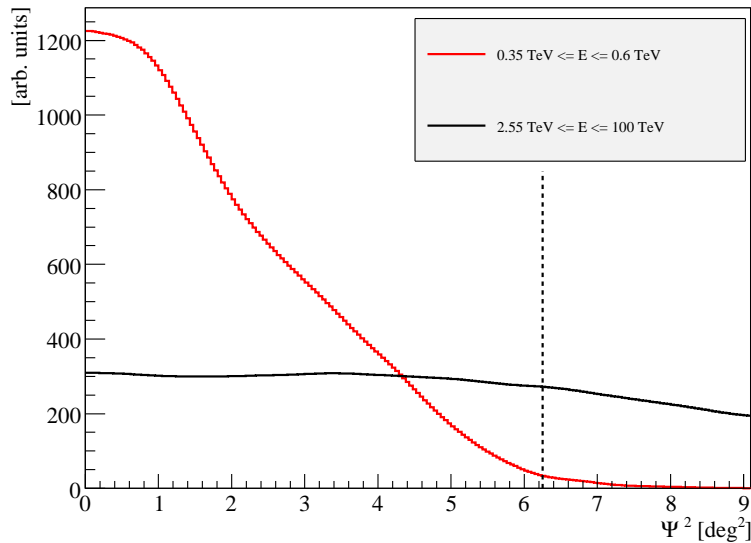


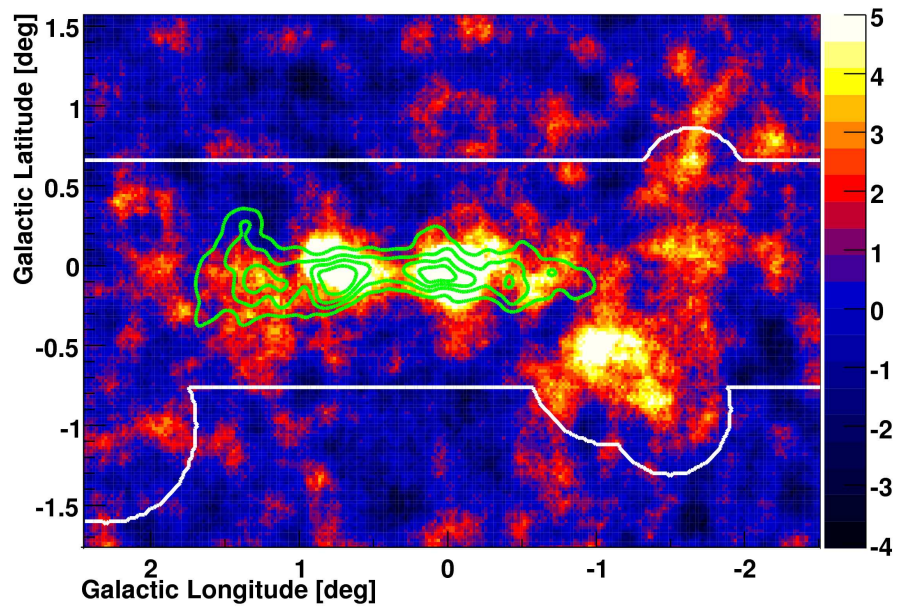
Figure 3.23: Comparison of radial profiles of detector acceptance for the low and high energy bands for 20° zenith angle. One notices that the acceptance for low energies is decreasing rapidly with increasing angular distance Ψ from the observation position, while the acceptance for the high energies does not show a significant decrease. The energy dependence of acceptance renders the use of lookup-tables necessary, that are dedicated to the particular energy bands used in the analysis.

	$0.35 \text{ TeV} \leq E_\gamma \leq 0.6 \text{ TeV}$	$2.55 \text{ TeV} \leq E_\gamma \leq 100 \text{ TeV}$
Number of processed runs	329	
Livetime [h]	139.89	
Mean zenith of on-region [$^\circ$]	21.27	
Mean offset of on-region [$^\circ$]	0.74	
Number of on-events	2655	1331
Number of off-events	3266	1341
α	0.50	0.26
Number of excess events	1011.3 ± 58.9	979.9 ± 37.7
Significance [σ]	18.1	33.2
Significance per $\sqrt{\text{hour}}$ [$\sigma/\sqrt{\text{h}}$]	1.68	2.81

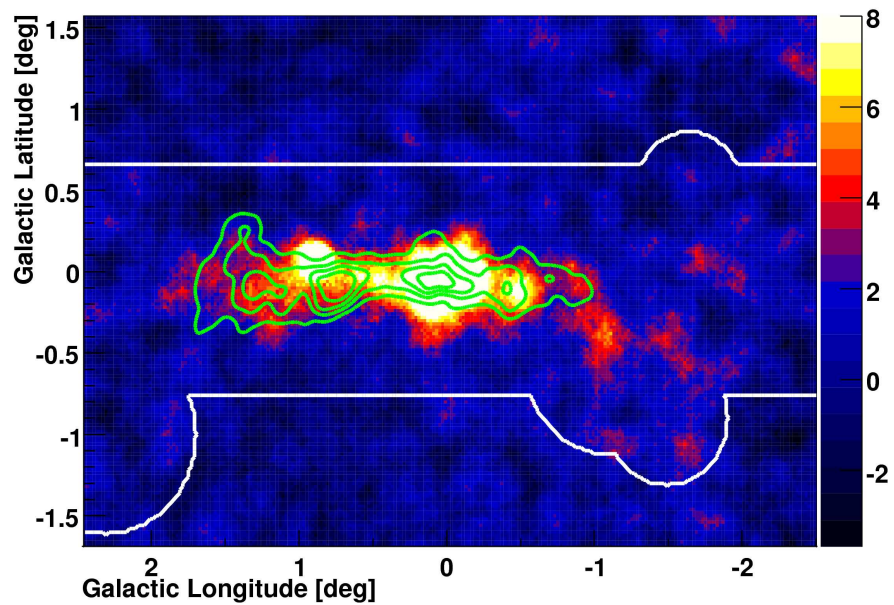
Table 3.3: Summarized statistics referring to an 0.1° radius region around the central point source HESS J1745–290 from the analysis of the GC region using different configurations of background subtraction for the analyses of low and high energy bands.

explaining the clumpiness observed in the significance map, while the high energy profile is much more smooth. Another interesting point is that the emission in the GC is clearly the one with the highest flux for the high energy band, while it is not standing out for the low energy range (see also Sec. 3.3).

After the subtraction of point sources the excess distributions in both bands can be used



(a) Significance map for low energy band



(b) Significance map for high energy band

Figure 3.24: Significance maps, overlaid with CS contours, obtained from analyses of low and high-energy bands. Each map is saturated at $\sim 20\%$ of maximal significance at the position of HESS J1745–290. The diffuse emission appears to be more clumpy in the low-energy map, whereas it looks much more smooth for the high-energy band.

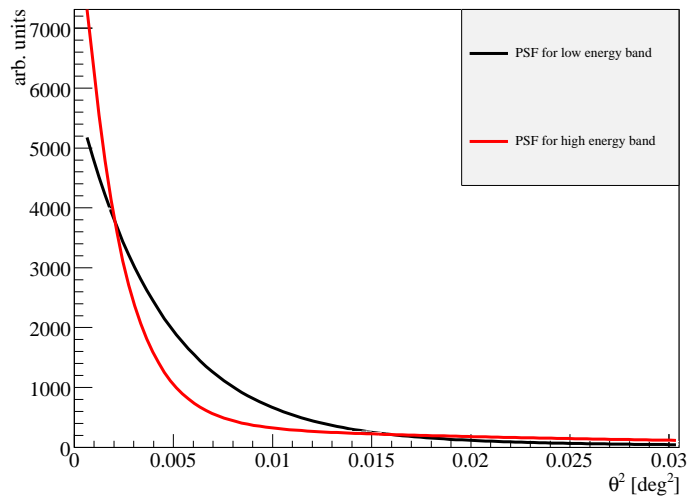
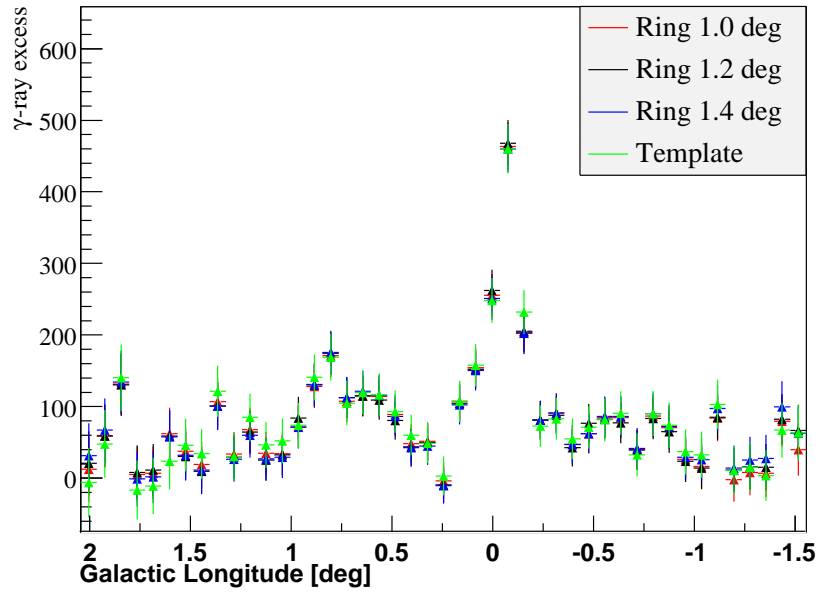


Figure 3.25: Difference between the PSF for the low and high energy bands.

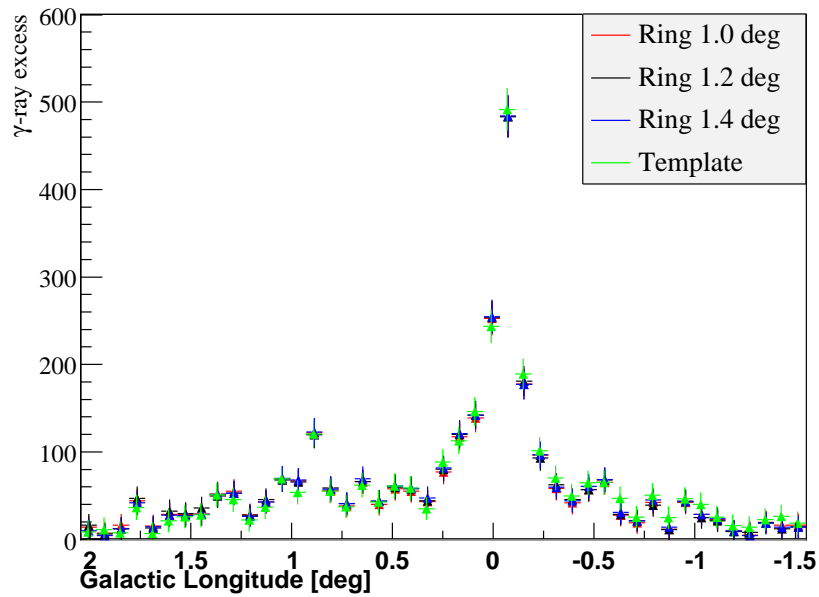
for another scan of the parameter space. Therefore, simulated excess maps for both energy bands are created by means of the diffusion model (see Sec. 3.1.3). These maps are properly normalized relative to each other, solely their absolute normalisation is arbitrary. The idea of the following scan is that simulated excess maps in both bands are now fitted simultaneously to the data, i.e. a simulated low-energy (high energy) excess map is fitted to the low-energy (high-energy) excess map from data and a common normalisation for both bands is obtained from the fit. This means that now, unlike the scan performed in Sec. 3.2.1, a particular diffusion model is required to properly describe emission profiles for different energies, what should be more sensitive to Γ and δ . For this scan, a 20% systematic error was applied to the excess in both bands. The resulting χ^2_{tot} is a sum of χ^2 -values for both energy bands. Its distribution as a function of diffusion parameters can be studied in Fig. 3.28, from which one can justify the choice of parameter space described in Sec. 3.2.1, since it fully contains the allowed region in the physically meaningful range.

In this plot one can observe that the shape of the parameter space, restricted at 95% confidence level ($\chi^2_{\text{tot}} \leq \chi^2_{\text{tot, min}} + 9.49$), deviates from the one obtained in the scan of the total excess profile. While the latter revealed a stripe-like shape in the D_0 - δ plane extending in all spectral indices under study, the former exhibits an ellipsoidal shape, restricting the allowed δ -values, depending on the assumed spectral index Γ . This fact once again confirms the presumption expressed in Sec. 3.2.1, that the use of spectral data should allow to improve the constrains on Γ and δ . However, one should stress here, that there are still allowed parameter ranges with $\delta = 0$, i.e. an energy-independent diffusion is not excluded based on this scan.

The same scan is performed using the 3-D diffusion model (see Fig. 3.29). In comparison of both scans differences in position and shape of allowed regions can be assessed. While for the 2-D model there is an allowed region for every spectral index within the selected

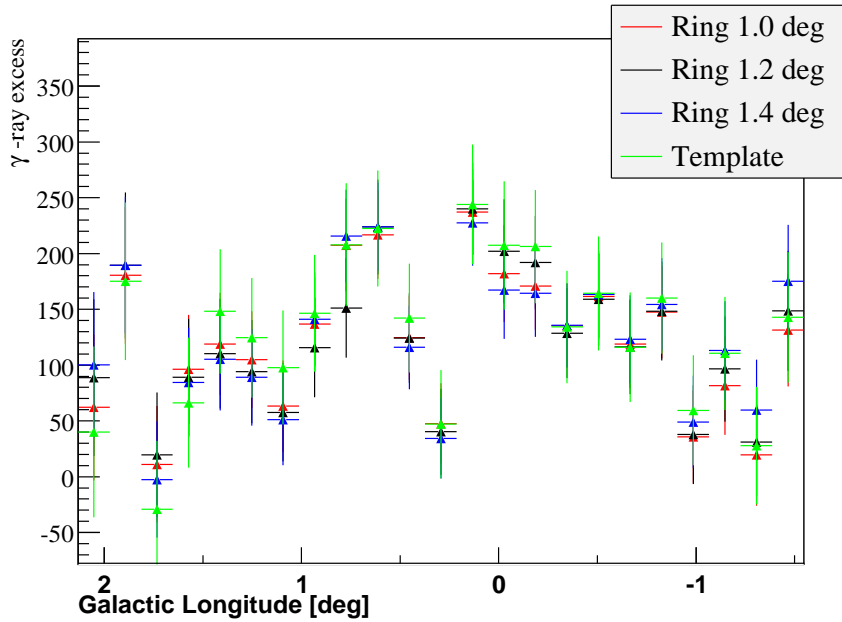


(a) Longitude profiles for low-energy maps after subtraction of point sources.

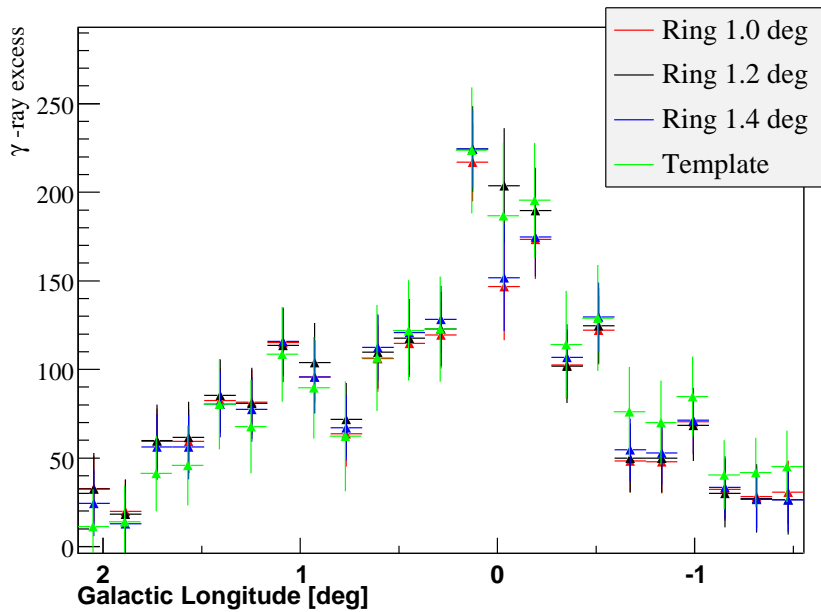


(b) Longitude profiles for high-energy maps after subtraction of point sources

Figure 3.26: Longitude profiles for exposure-corrected excess maps for both energy bands before subtraction of point sources for all configurations of background subtraction. The emission was integrated between $b = -0.31^\circ$ and $b = 0.33^\circ$ galactic latitude. Results from all configurations agree within errors.



(a) Longitude profiles for low-energy maps after subtraction of point sources.



(b) Longitude profiles for high-energy maps after subtraction of point sources

Figure 3.27: Longitude profiles for exposure-corrected excess maps for both energy bands after subtraction of point sources for all configurations of background subtraction. The emission was integrated between $b = -0.31^\circ$ and $b = 0.33^\circ$ galactic latitude. Results from all configurations agree within errors.

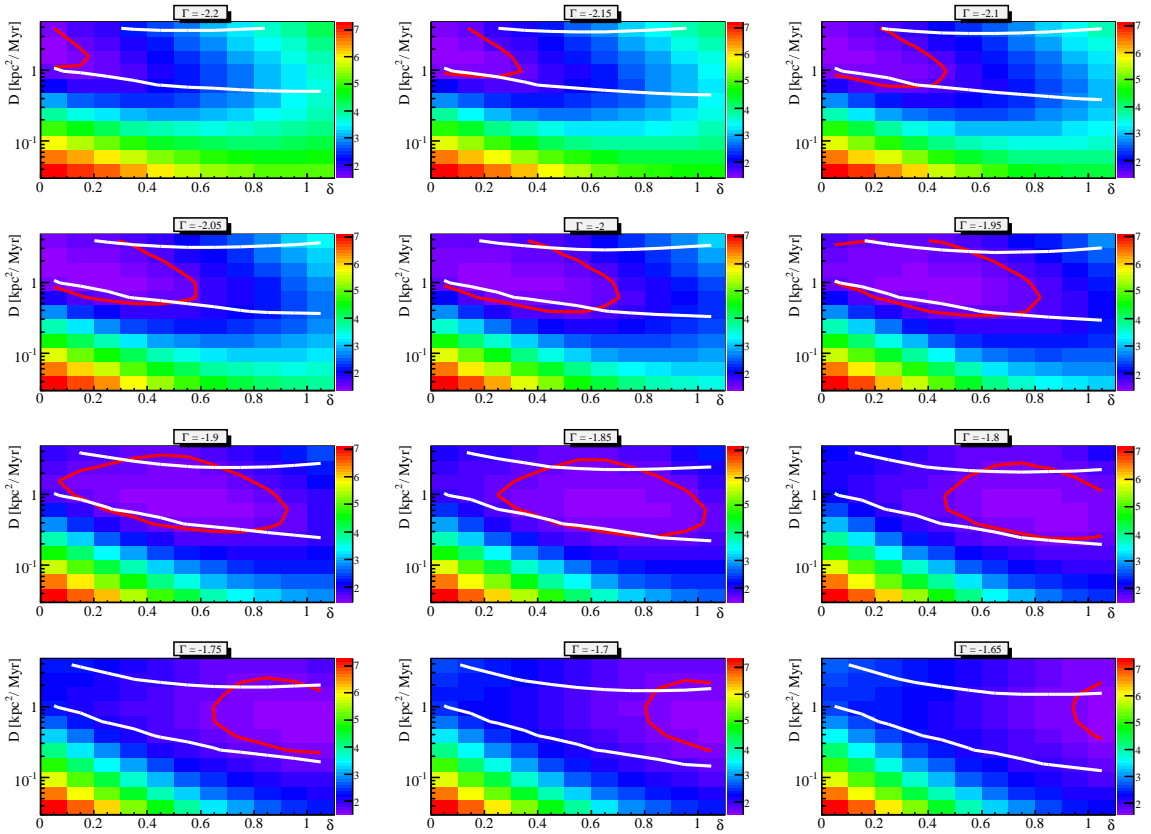


Figure 3.28: Results of the scan of the parameter space of diffusion using the excess profile distributions from Fig. 3.27 by fitting the normalisation factor of the maps from the 2-D diffusion model. Statistical and systematic errors are taken into account. The reduced χ^2 (z-axis) of the fits is plotted as a function of (D_0, δ, Γ_p) . The red line denotes the 95% confidence regions (see text). The white contours represent the allowed region according to the scan of the total excess distribution. The minimum reduced χ^2 -value $\chi^2_{min} = 1.34$ is obtained for $D = 1.19 \frac{\text{kpc}^2}{\text{Myr}}$ (for $t = 10^4 \text{ yr}$), $\Gamma = -2.05$ and $\delta = 0.1$.

range, the 3-D model excludes (at 95% conf. level) indices smaller than -2, i.e. the allowed regions are shifted towards harder spectra. Besides, for the 3-D model there is a tighter correlation between the diffusion coefficient and its energy dependence, which is observable as a more stretched and inclined shape of the allowed regions.

A comparison between the best-fit diffusion models and the data for the scan in energy bands is shown in Fig. 3.30. One observes that despite small scale deviations, which are also different between the energy bands, the data is reasonably well described, which is especially due to large statistical errors for the low energy band. In Fig. 3.31 to 3.34 the correlations between the measured and simulated excess are plotted for both energy bands and both the 2-D and 3-D diffusion models. As for the total excess distributions, the correlations are reasonably well described by linear fits.

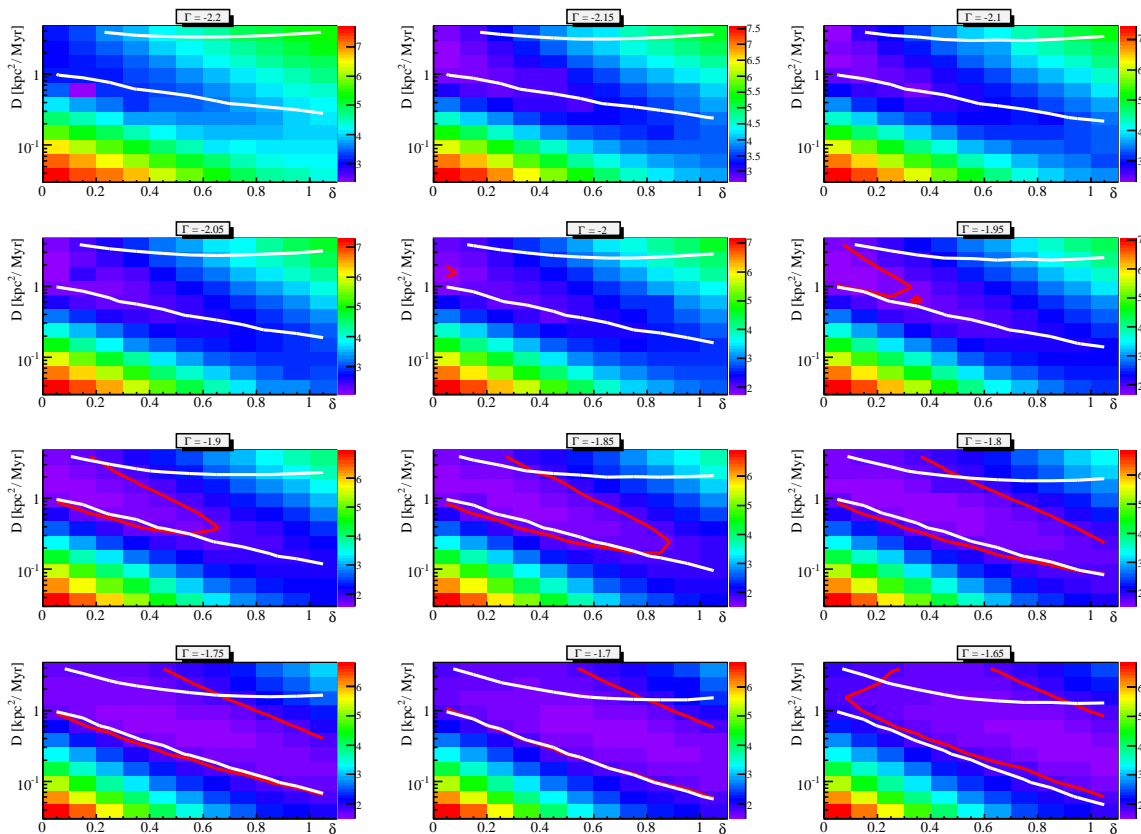
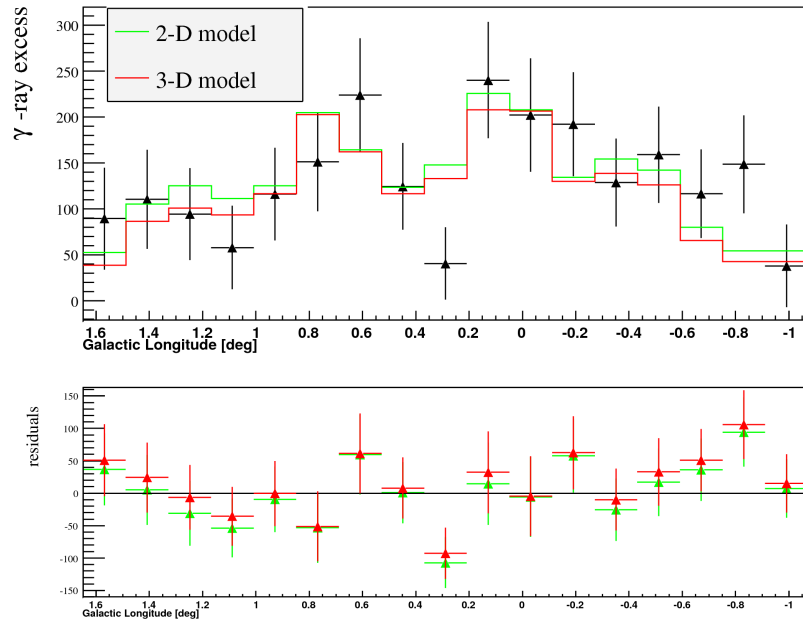
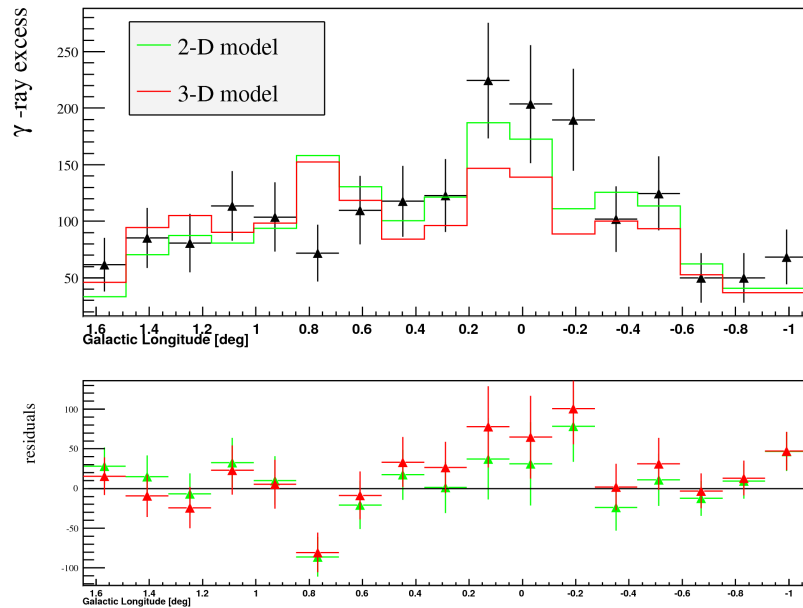


Figure 3.29: Results of the scan of the parameter space of diffusion using the excess profile distribution from Fig. 3.27 by fitting the normalisation factor of the maps from the 3-D diffusion model. Statistical and systematic errors are taken into account. The reduced χ^2 (z-axis) of the fits is plotted as a function of (D, δ, Γ) . The red line denotes the 95% confidence regions (see text). The white contours represent the allowed region according to the scan of the total excess distribution. The minimum reduced χ^2 -value $\chi^2_{min} = 1.48$ is obtained for $D = 0.48 \frac{\text{kpc}^2}{\text{Myr}}$ (for $t = 10^4 \text{ yr}$), $\Gamma = -1.75$ and $\delta = 0.5$.

Despite the already achieved improvement on the restriction of the parameter space of diffusion, compared to the results shown in Sec. 3.2.2, it is worthwhile to discuss whether there might be an additional method capable of further constraining the parameter space. Indeed, the scans introduced above only use the fit of the overall normalisation as a method to determine the validity of a particular set of diffusion parameters. With a view to the fits in energy bands, this means that even though a proper common normalisation for both bands is found in the fit procedure, this normalisation might systematically under(over)-estimate the number of excess events in the low(high)-energy band and vice versa. In Fig. 3.35 such an example is shown for following values lying within the allowed region: $D = 1.19 \frac{\text{kpc}^2}{\text{Myr}}$, $\Gamma = -1.95$ and $\delta = 0.2$ (2-D model). From the residua one clearly recognizes that while the high-energy band is sufficiently well described by the model, i.e. the



(a) Longitude profiles for low energy maps after subtraction of point sources.



(b) Longitude profiles for high energy maps after subtraction of point sources.

Figure 3.30: Longitude profile of the exposure-corrected γ -ray low energy (top) and high energy (bottom) excess maps from data and from the best-fit (see text) 2-D (green lines and points) and 3-D (red line and points) diffusion models and their residua, integrated between $b = -0.31$ and $b = 0.33$. Systematic uncertainties of 20% on the number of excess events are included. Deviations between the data and the models are observable on small scales, but still the overall description of the emission by the diffusion model looks quite solid.

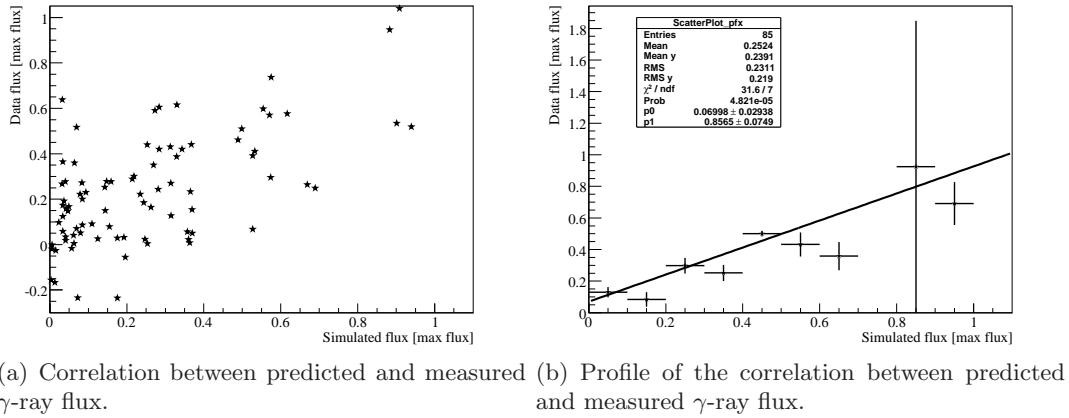


Figure 3.31: Correlation of measured flux vs. predicted flux for the low energy band from the 2-D diffusion model, normalized to their maximum values. The values are obtained from excess maps, binned in $0.16^\circ \times 0.16^\circ$ squares. The correlation is well described by a linear fit. See text for further details.

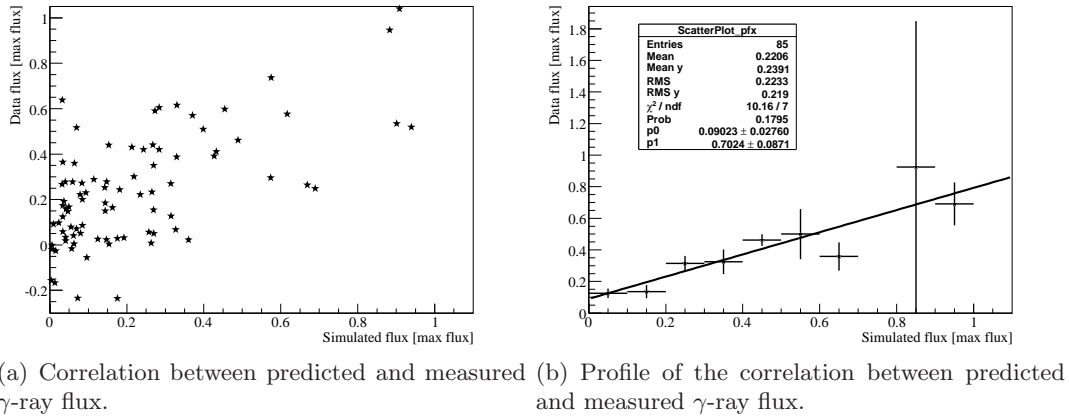
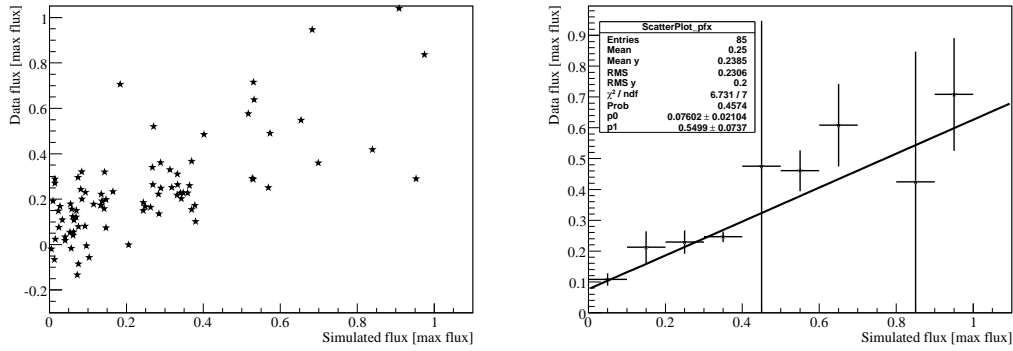


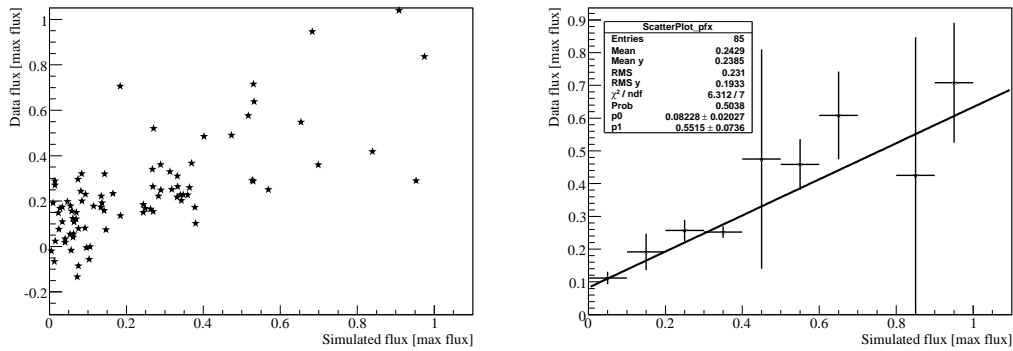
Figure 3.32: Correlation of measured flux vs. predicted flux for the low energy band from the 2-D diffusion model, normalized to their maximum values. The values are obtained from excess maps, binned in $0.16^\circ \times 0.16^\circ$ squares. The correlation is well described by a linear fit. See text for further details.

sum of data events and simulated events agrees within 3% within the fit range, for the low-energy band the normalisation is underestimated, resulting in a difference of 23% related to the total number of data events. And despite such a strong evidence for a systematic effect, the total χ^2 is still located within the 95% confidence region and a further method is needed to discriminate against these cases.



(a) Correlation between predicted and measured γ -ray flux. (b) Profile of the correlation between predicted and measured γ -ray flux.

Figure 3.33: Correlation of measured flux vs. predicted flux for the high energy band from the 2-D diffusion model, normalized to their maximum values. The values are obtained from excess maps, binned in $0.16^\circ \times 0.16^\circ$ squares. The correlation is well described by a linear fit. See text for further details.

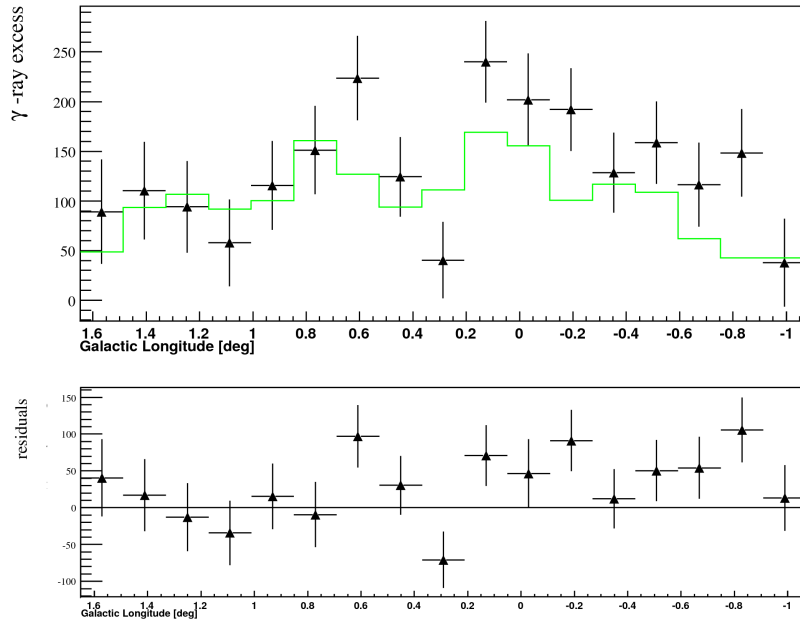


(a) Correlation between predicted and measured γ -ray flux in a 2D representation. (b) Profile of the correlation between predicted and measured γ -ray flux.

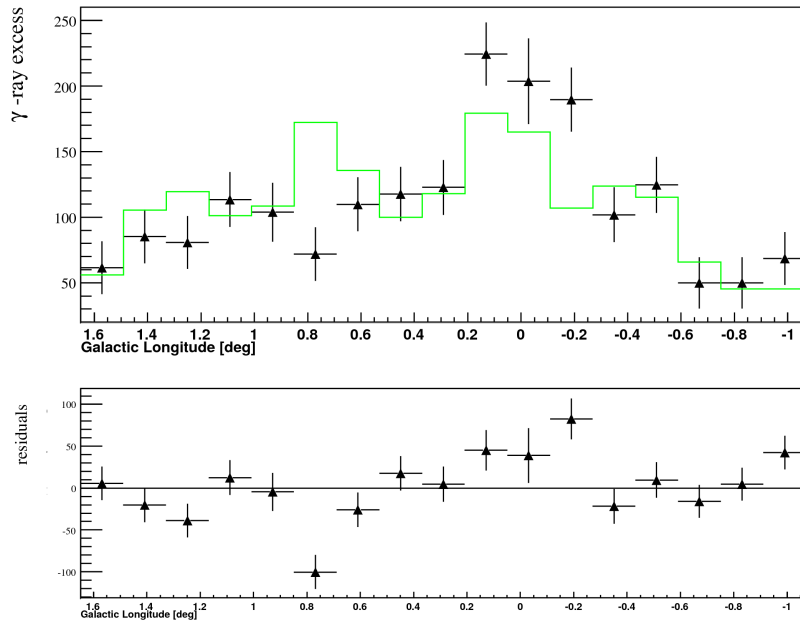
Figure 3.34: Correlation of measured flux vs. predicted flux for the high energy band from the 2-D diffusion model, normalized to their maximum values. The values are obtained from excess maps, binned in $0.16^\circ \times 0.16^\circ$ squares. The correlation is well described by a linear fit. See text for further details.

Contrast analysis

In order to get a handle on the regions of the parameter space showing the systematic problems described in the last paragraph, the number of coincident low and high energy events must be related. Therefore, commonly applied parameters like hardness ratios (HR), defined as $HR = N_{\text{high}}/N_{\text{low}}$, with N_{low} and N_{high} being the number of low and high energy excess events, respectively, or contrast values, defined as $C = \frac{N_{\text{high}} - N_{\text{low}}}{N_{\text{high}} + N_{\text{low}}}$ can be used. The latter has the advantage of not only having a defined range of values between -1 and 1, but



(a) Longitude profile for low-energy map after subtraction of point sources.



(b) Longitude profile for high-energy map after subtraction of point sources.

Figure 3.35: Longitude profiles for exposure-corrected excess maps for both energy bands after subtraction of point sources together with the distributions obtained from the 2-D diffusion models using $D = 1.19 \frac{\text{kpc}^2}{\text{Myr}}$ (for $t = 10^4 \text{ yr}$), $\Gamma = -1.95$ and $\delta = 0.2$. The emission was integrated between $b = -0.31^\circ$ and $b = 0.33^\circ$. These values were selected as an example for those parts of the parameter space, which can not be rejected by the fits of excess profiles in energy bands, while having obvious systematic problems: The norm of the model distributions matches well the high-energy data within 3%, while the norm of the low-energy band is underpredicted by 23%, clearly visible for positive longitudes.

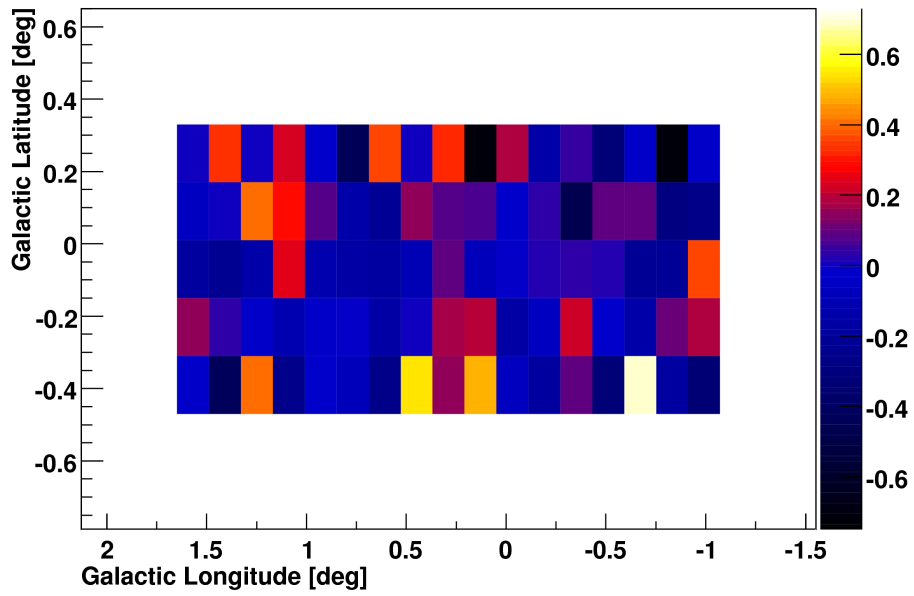
also rendering it possible to extract corresponding index and flux values, if a power-law spectrum is assumed (Clapson et al. 2008).⁸ Thus, the usage of the contrast parameter is adopted for the further analysis. However, since the presented contrast definition is only valid for $N_{\text{high}}, N_{\text{low}} > 0$ and the case of $N_{\text{high}} < 0$ or $N_{\text{low}} < 0$ can in principle occur (see below), the contrast parameter used for this analysis has a slightly different definition: $C = \frac{N_{\text{high}} - N_{\text{low}}}{N_{\text{total}}}$, where N_{total} is the total number of events obtained in the data analysis for the particular bin. This definition still implies $C = -1$ and $C = 1$ as extreme cases, where the number of events in one energy band equals the total number of events, but in addition also works for the case $N_{\text{low}} = -N_{\text{high}}$, for which the former contrast formula has a gap in definition.

Applying this contrast definition a contrast map is obtained for the GC region, see Fig. 3.36. The map gives a qualitative impression about the differences in excess distributions of both energy bands. One observes that the region is mostly dominated by regions of different shapes and sizes, in which the bins show similar contrast values, but there are also single bins that have contrast values clearly deviating from their close environment, e.g. at position $l = 1.25^\circ$, $b = -0.4^\circ$ or at $l = -0.3^\circ$, $b = 0.1^\circ$. The differences seen in comparison of longitude profiles for both bands, already discussed above, emerge as latitude bands of contrast values largely deviating (within the considered range) from the predicted value, e.g. for $l = 0.3^\circ$. Beside, based on the contrast distribution, spectral indices were calculated for the GC region⁹. The index map is also shown in Fig. 3.36. To get a more quantitative picture contrast values and their statistical uncertainties are plotted in latitude slices in Fig. 3.37. In the same plot, also predicted contrast distributions corresponding to the best-fit 2-D and 3-D diffusion models from the previous scans using energy bands are shown. Most data points seem to be randomly distributed around predictions from diffusion models. Single bins or clusters of bins with striking contrast values in the data, partly mentioned before as examples, exhibit comparatively large statistical uncertainties, so that judging on their significance is impossible without a dedicated statistical analysis. Such an analysis is also needed to validate whether the overall data contrast distribution is compatible with variation of simulated values within the statistical and systematic uncertainties.

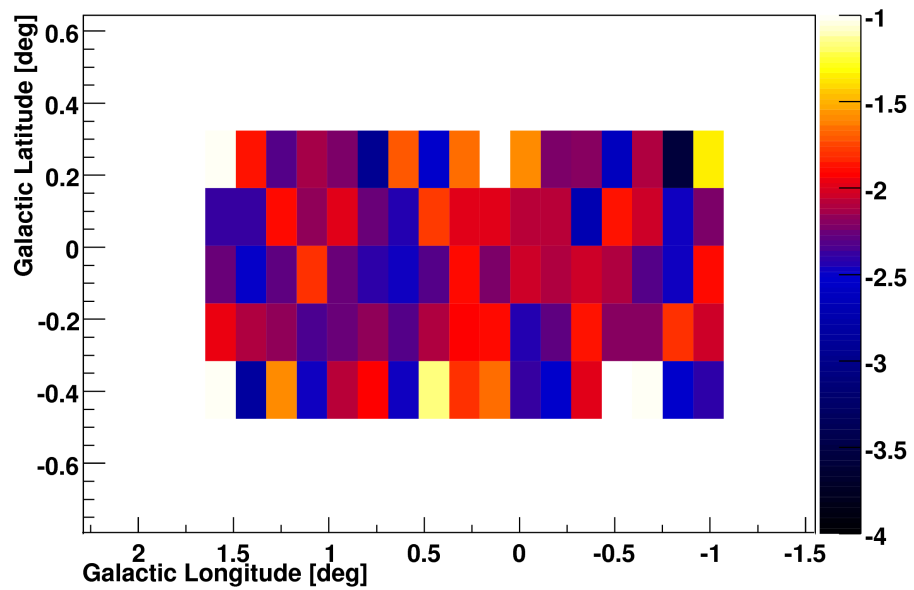
The concept of the method introduced in the following is based on the so-called Kolmogorov-Smirnov test (Bohm & Zech 2004). This procedure tests whether a measured distribution of a variable is compatible with a certain theoretical expectation for this particular variable (or whether two distributions stem from the same parent distribution) by means of the maximum distance between their cumulative probability functions. It is sensitive to systematic trends (or clustering) in the data and is therefore superior to the χ^2 -method for cases like in Fig. 3.35, for which not only the absolute value of deviation between measurement and theory is important, but also its sign. To be able to quantify trends or clustering in the data is the idea of the method, developed within the framework of this thesis for the contrast analysis. It works as follows:

⁸ The extraction of spectral parameters like index Γ and flux normalisation Φ_0 based on contrast values is nothing else but fitting a power law spectrum to solely two spectral points, which correspond to the energy bands in use.

⁹ This is done by determination of the particular index value, using the detector acceptance, which yields the same contrast value as measured in data.



(a) Contrast map for the GC region



(b) Index map for the GC region

Figure 3.36: Top: Distribution of contrast values, as defined in the text, for the GC region. Most bins are concentrated in larger groups of similar contrast values, but there are also single bins deviating from their environment. No clear hint of spectral hardening for outer regions can be observed. See Fig. 3.37 for a more quantitative picture. Bottom: Distribution of index values, calculated from the contrast distribution. See text for details.

◇ For a given bin i in the map, a set of simulated contrast values needs to be created.

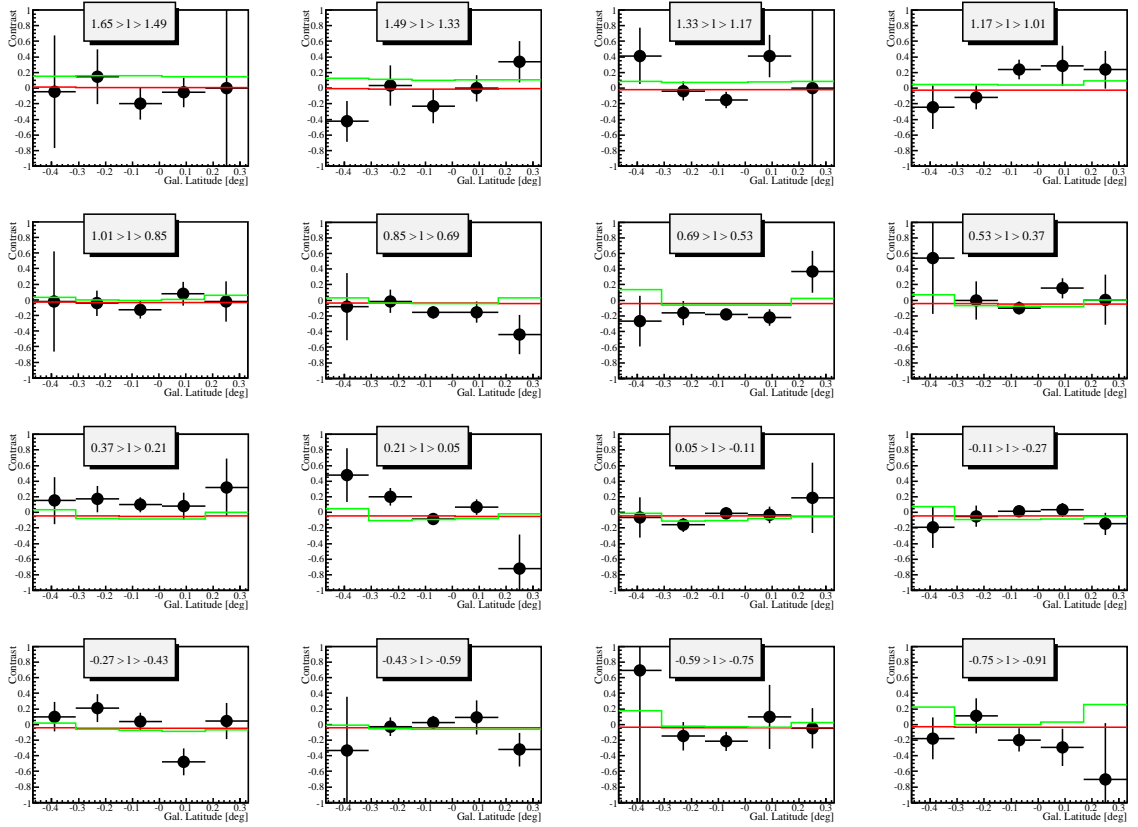


Figure 3.37: Latitude profiles of the distribution of contrast values, as defined in the text, data (points), best-fit 2-D model (red line) and the best-fit 3-D model (green line). Although some clustering of data contrast values occur, like for $l = 0.3^\circ$ or $l = 0.6^\circ$, deviating from model predictions, any quantification of their significance is at least not possible by eye and requires a dedicated statistical test.

For that, first the number of background events from data is calculated: $N_{\text{bkg},i} = N_{\text{on},i} - N_{\gamma,i}$, where $N_{\text{on},i}$ is the number of counts in the bin and $N_{\gamma,i}$ is the number of excess events after subtraction of point sources. This means that γ -rays due to point sources are included in $N_{\text{bkg},i}$. Next the expected number of counts is calculated: $\langle N_i \rangle = N_{\text{on},i}^{mc} = N_{\text{bkg},i} + N_{\gamma,i}^{mc}$, where $N_{\gamma,i}^{mc}$ is the number of predicted γ -rays, which is obtained by using normalisation factors that were fitted in the previous scan of parameter space. Here, $\langle N_i \rangle$ is the mean number of predicted count events, hence it is used to generate a sample of random numbers of count events following the Poisson probability distribution:

$$P(X) = \frac{\langle N_i \rangle^X}{X!} \exp(-\langle N_i \rangle), X \in \mathbb{N}$$

where $P(X)$ is the probability of occurrence of X in the randomized sample. The size of such samples was selected to contain 10^4 entries. For every random number $N_{\text{on},i}^j$ the corresponding number of excess events is calculated: $N_{\gamma,i}^j = N_{\text{on},i}^j - N_{\text{bkg},i}$ (here it can occur that $N_{\text{low-}\gamma,i}^j = -N_{\text{high-}\gamma,i}^j$). The systematic uncertainty of 20%

is included by an additional Gaussian randomization. The calculations have to be carried out for both energy bands.

- ◇ For every randomization step the corresponding contrast value C_i^j in every bin i is calculated and stored. Finally, the mean contrast value and its error is calculated for each bin:

$$\langle C_i^j \rangle = \frac{1}{10^4} \sum_{j=1}^{10^4} C_i^j \text{ and } \Delta \langle C_i^j \rangle = \sqrt{\sum_{j=1}^{10^4} \frac{1}{10^4 - 1} (C_i^j - \langle C_i^j \rangle)^2}.$$

- ◇ For the particular diffusion model, deviations between data and model are calculated for each bin as $\sigma_i = \frac{C_i^D - \langle C_i^j \rangle}{\Delta \langle C_i^j \rangle}$, with C_i^D as the contrast value for the data. Afterwards, the maximum absolute sum of σ_i , integrated over the whole region of diffuse emission, is calculated as:

$$S_{\max}^D = \text{Max}(| \sum_{i=1}^{N_B} \sigma_i |), \text{ with } 1 \leq N_B \leq N_B^{\text{tot}},$$

where N_B^{tot} is the total number of bins. The loop over bins in the map is done in both directions with respect to the galactic longitude, to avoid a bias, and the larger number is kept. Here, S_{\max} is the analogy of the maximum Kolmogorov-Distance applied in Kolmogorov-Smirnov tests.

- ◇ The same procedure as for the data is done with the total set of simulated contrast maps. The only substitution is $C_i^D \Leftrightarrow C_i^j$ for a map j from the simulated set. The resulting maximum sums S_{\max}^j are stored. Finally, they are used to calculate the chance probability of having $S_{\max}^j \geq S_{\max}^D$:

$$P_C = P(S_{\max}^j \geq S_{\max}^D) = \frac{1}{10^4} \sum_{i=1}^{10^4} \Theta(S_{\max}^j, S_{\max}^D),$$

where $\Theta(S_{\max}^j, S_{\max}^D) = 1$ for $S_{\max}^j \geq S_{\max}^D$ and 0 otherwise.

The 95% confidence level obtained with this method contains diffusion models for which $P_C \geq 0.05$.

Using the method described above additional scans of parameter space were performed for the 2-D and 3-D diffusion models. Their results are shown in Fig. 3.38 and Fig. 3.39 together with the results obtained from previous scans. One can see that compared to the scan using excess maps in energy bands, the regions allowed with the contrast method are larger, i.e. the contrast method is overall less sensitive for the available dataset, but in some cases they exclude parts of allowed regions derived from scans of excess maps in energy bands, amongst others the parameter set taken above as an example and motivation for the development of the contrast method (Fig. 3.35). Besides, they show the similar correlations with the diffusion parameters, from which one can conclude that the data do not show significant clusterings of data points or systematic trends for most models that lie in the regions allowed by the previous scan. Nevertheless, this method puts a more constraining lower limit on the energy dependence of the diffusion coefficient for harder proton spectra ($\Gamma \geq -2$ and $\Gamma \geq -1.75$ for the 2-D and 3-D models, respectively) for both 2-D and 3-D diffusion models.

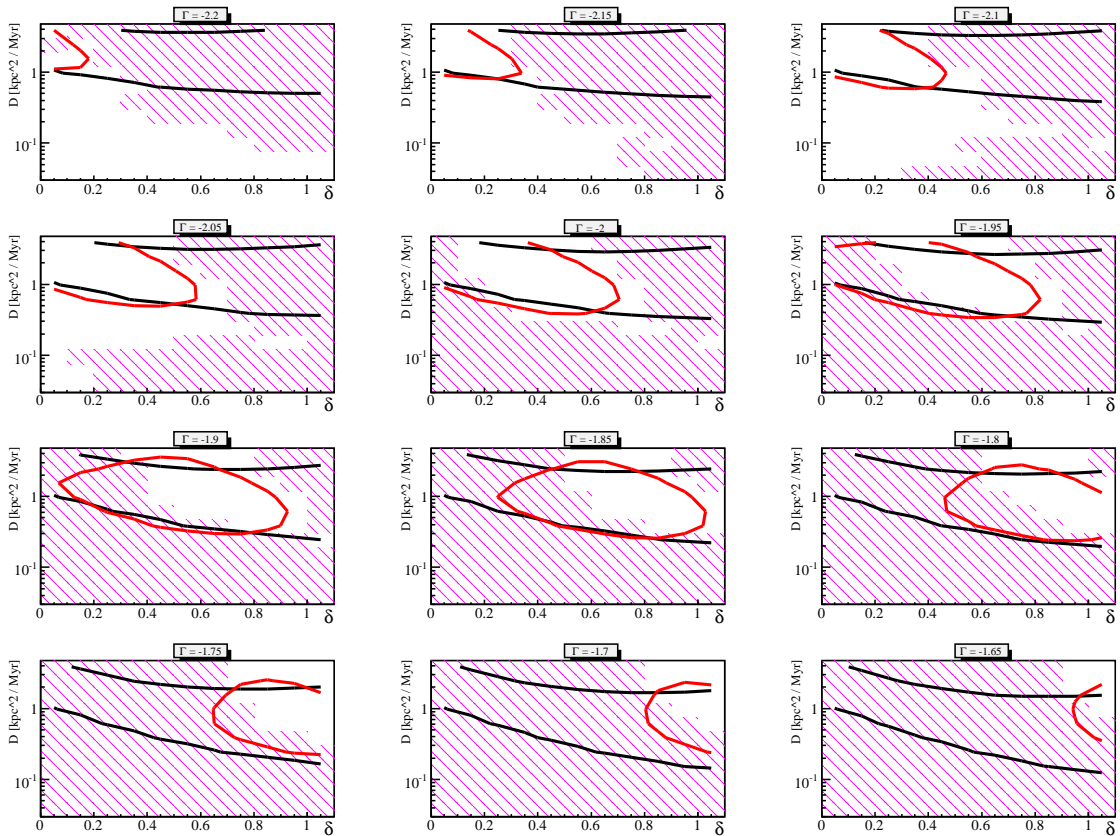


Figure 3.38: Results of the scan of the parameter space of diffusion for the 2-D model using the contrast distribution from Fig. 3.36 for the method described in the text. Systematic uncertainties are taken into account. Besides, also results from the previous scans are shown, where black and red lines denote the region allowed by fits of total excess profile and profiles in energy bands, respectively. With the help of contrast method it is possible in some cases to further constrain the allowed parameter space, in particular put a lower limit on δ .

3.3 Interpretation and conclusions

In the previous section it was described how the full H.E.S.S. dataset of the GC region is analyzed with regard to the diffusion hypothesis and the methods used to constrain the parameter space of diffusion were introduced. The results of the analysis, illustrated as regions of the parameter space, allowed at 95% confidence level, are shown in Fig. 3.38 and 3.39. These plots show, that if the information about the energy of events is not used, the parameter space can only be constrained concerning the diffusion coefficient D_0 , whereas no meaningful constraints can be obtained for the parameters Γ_p and δ that influence the spectral properties of the detected γ -ray emission. Besides, no substantial differences between the 2-D and 3-D diffusion model can be observed. On the contrary, if spectral information is used, e.g. by performing analysis in energy bands, then the constraints get tighter, especially regarding Γ_p and δ . Moreover, differences between 2-D and 3-D model start to emerge that manifest as a shift of allowed regions towards harder spectra for the

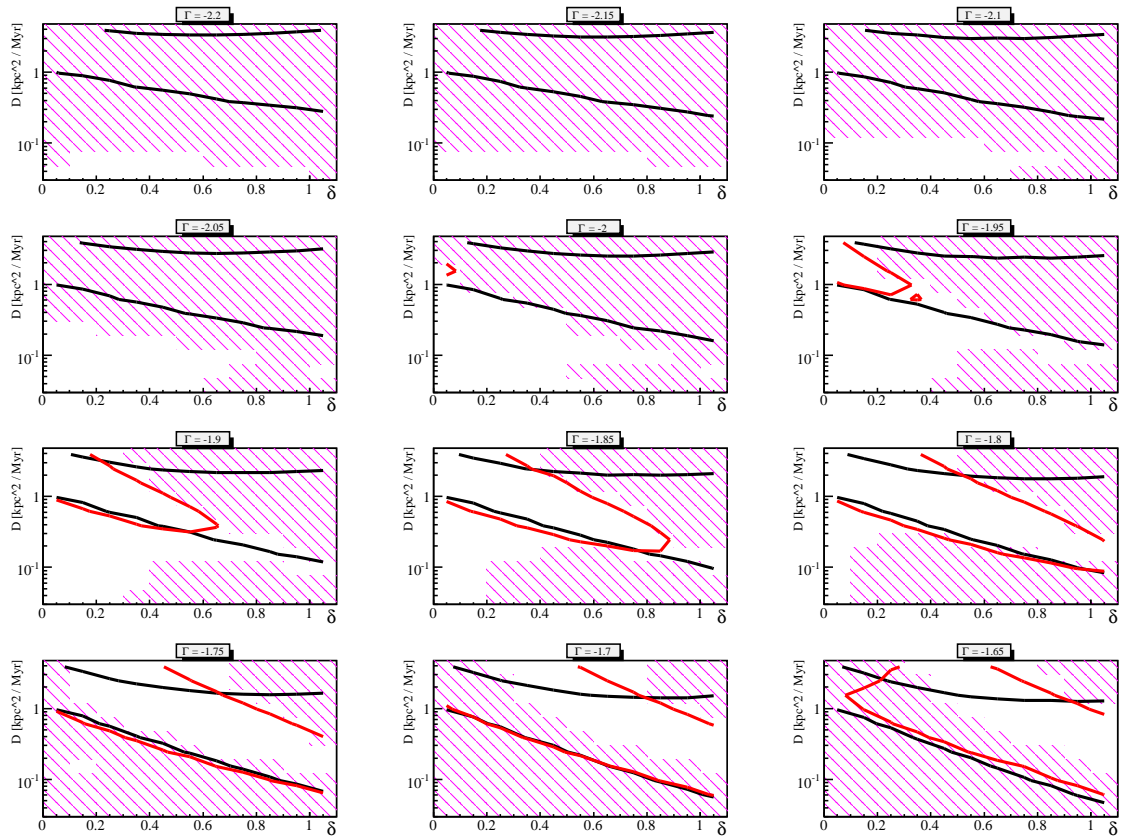


Figure 3.39: Results of the scan of the parameter space of diffusion for the 3-D model using the contrast distribution from Fig. 3.36 for the method described in the text. Systematic uncertainties are taken into account. Besides, also results from the previous scans are shown, where black and red lines denote the region allowed by fits of total excess profile and profiles in energy bands, respectively. With the help of contrast method it is possible in some cases to further constrain the allowed parameter space, in particular put a lower limit on δ . The parameter space for $\Gamma < -2$ is excluded by the contrast scan as well, confirming the results obtained by the fits of excess profiles in energy bands.

3-D realisation.

All the results obtained with different methods can now be combined in the most natural way by requesting that a set of diffusion parameters is considered to be in an allowed region if it satisfies the 95% confidence level criteria of every scan method.¹⁰ The allowed parameter space defined in such a way is plotted in Fig. A.12 and Fig. A.13, showing also results from other configurations of background subtraction, which agree very well

¹⁰ It is hereby assumed that all three methods have the same a-priori weight. This is not necessarily the case, but it is not straightforward to quantify the importance of each single method, given the fact that these are sensitive to different characteristics of the diffuse emission and use different statistics. Hence it is waived to determine such in this work.

with each other. Main facts relating to the shape of parameter space constrained in this analysis are summarized in the following:

- ◇ 2-D model: The allowed parameter space is mostly constrained by the fits of low and high-energy excess distributions. For softer spectra $\Gamma_p \leq -2$, the preferred range for δ is $\delta < 0.6$, in particular including $\delta = 0$, i.e. an energy-independent diffusion can not be discarded for commonly assumed values of Γ_p (e.g. $\Gamma_p = -2.1$, see Sec. 1.4). In general the allowed region moves with increasing spectral index towards larger δ , excluding $\delta = 0$ for $\Gamma_p \geq -2$ and $\delta < 0.6$ for $\Gamma_p \geq -1.8$. The diffusion coefficient D_0 reveals an anti-correlation with δ , i.e. smaller diffusion coefficients are preferred if δ increases. These correlations can be understood as an effect of the basic methodology of the measurement: It is sensitive to the absolute values and the relation of spectrum-averaged diffusion coefficients of the primary particles contributing most to the γ -ray flux in the particular energy band, i.e. if the norm of the diffusion coefficient decreases, its higher energy-dependence compensates for this and the mean diffusion coefficient roughly remains the same.
- ◇ 3-D model: The most striking outcome of the 3-D model scans is that very hard initial spectra are preferred: $\Gamma_p > -2$, by both fits of excess profiles in energy bands and the contrast analysis. The allowed regions exhibit an even more pronounced correlation between diffusion coefficient and its energy dependence compared to the 2-D models. The allowed regions shift as for the 2-D case towards larger δ for increasing Γ_p , however an energy-independent diffusion can only be rejected for $\Gamma_p \geq 1.75$. In contrast to the 2-D models, it seems that the allowed parameter space extends towards even harder initial spectra $\Gamma_p > -1.65$, but those are considered to be rather unlikely and are not treated here.

It is now necessary to discuss the physical implications of the results of this analysis. Obviously, the most important one is that the new dataset can still be described by the diffusion hypothesis. Taking into account the systematic error yields χ^2 -values of the fits that suggest a good agreement between models and the data. The diffusion models, both 2-D and 3-D versions, can provide a meaningful scan of the parameter space. The values of diffusion parameters found in other publications $D_0 = 1.3 \frac{\text{kpc}^2}{\text{Myr}}$, $\Gamma_p = 2.29$, $\delta = 0.6$ (Büsching et al. 2007), not using a 3-D model of the GMCs, and $D_0 = 3.2 \frac{\text{kpc}^2}{\text{Myr}}$ ($D_0 \approx 1.7 \frac{\text{kpc}^2}{\text{Myr}}$ if taking into account energy losses), $-2.3 \geq \Gamma_p \geq -2.1$, $\delta = 0.3..0.6$ (Dimitrakoudis et al. 2009), are in agreement with the allowed regions of the 2-D scan (see Tab. A.3). However, due to the very hard spectral indices preferred by the 3-D model, there is a disagreement with the result in (Dimitrakoudis et al. (2009), see Tab. A.4), although the authors used a three-dimensional model of the ambient gas as well. But it should be emphasized that all previous results are based on the longitude profile of the total emission, published in (Aharonian et al. 2006d).

The results obtained by the 3-D model are especially interesting concerning a possible origin of the primary protons. If one assumes the same energy-dependence for the hadrons in the GC region as was measured for the CR spectrum on Earth and puts $\delta = 0.6$, then the 3-D model defines a lower limit on the spectral index: $\Gamma \geq -1.85$. For CRs accelerated in SNRs this is a very hard spectrum and would imply that the hadrons might not undergo just a pure Fermi-I acceleration in the expanding shell, which naturally gives an index of $\Gamma \leq -2$, but a more complicated acceleration process, providing harder spectra

(Berezhko & Völk 1997). On the other hand, the lower limits on the index may be used as an argument for a different source of hadrons like Sgr A*. Indeed, one of the reasons that the diffuse emission was connected with the central source was the spectral similarity, and since Sgr A East seems to be ruled out as the counterpart of the point source, it may also mean that it is ruled out as the source of diffusing hadrons as well. Then the assumed time $t = 10^4$ yrs becomes arbitrary and the absolute value of the diffusion coefficient can differ from the one obtained by at least an order of magnitude (Aharonian et al. (2006d), Dimitrakoudis et al. (2009)). Besides, if the SMBH is considered as the potential source, then it is more natural to find a corresponding acceleration mechanism providing such hard spectra (Aharonian & Neronov 2005).

Even though the diffusion picture still seems to be valid, it is necessary to ask whether there are indications that also other processes can be responsible for the diffuse emission as seen by H.E.S.S.. Looking again at the excess profiles in Fig. 3.10, 3.27 and the contrast distribution in Fig. 3.37, small scale deviations from the predictions of the diffusion models are visible. Such are of course expected, since, as it was already mentioned in 2.1, the diffusion model that is used in this thesis is meant to represent the space-averaged diffusion process, because the diffusion coefficient is in reality certainly space-dependent. Besides, it is unclear how deep CRs of different energies can penetrate dense molecular clouds (Gabici et al. 2009), i.e. if the diffusion can take place everywhere in the GC region. But if the small-scale deviations are considered as indications of the invalidness of the diffusion hypothesis, then especially the non-smooth shape of the excess profile in the low energy band, including the low level of the emission in the central region (see Fig. 3.30), can be a hint for the presence of further source(s) with a softer spectrum than the surrounding emission. And if in the region of the diffuse emission additional sources are located (besides the known ones), then the observed emission could be due to a population of extended sources having the same longitude and latitude distribution as the GMCs. But as long as the diffusion hypothesis is not rejected, the latter assumption remains speculative.

Further insights about the origin of the diffuse emission may be achieved by an analysis of FERMI data from the GC region (Abdo et al. 2009), and the future array of Cherenkov telescopes CTA (Wagner et al. 2009). However, in the energy range of Fermi, from 30 MeV to 300 GeV, the contamination from foreground and background galactic diffuse γ -ray emission is much more important and its proper modelling is essential for localising the emission from the GC region. This might lead to further systematic effects. The target sensitivity of the CTA array, which is assumed to be ~ 10 times better than the one of H.E.S.S., and a better angular resolution of a factor ~ 3 to ~ 5 should render it possible to map the GC region with a high precision, both in terms of morphological and spectral properties. Thus if systematic uncertainties, both on experimental and theoretical sides, can also be reduced, then the origin of the diffuse emission will presumably be established without ambiguity.

4 Search for γ -rays from Dark Matter annihilations in the Galactic Center halo

In this chapter the search for Dark Matter signals from the GC halo in very high-energy γ -rays is described. First the theoretical properties of Dark Matter, both on the particle physics and the cosmology side, are briefly introduced (Sec. 4.1), followed by a discussion of the related observations conducted by IACTs so far (Sec. 4.2). Then the analysis of H.E.S.S. data, developed within the scope of this work, is introduced and described (Sec. 4.3 and 4.4). Finally, the results of this analysis are discussed.

4.1 Evidences for the existence of Dark Matter

Nowadays it is considered as a confirmed fact, that the matter density of the universe mainly consists of an unknown component, the **Dark Matter** (DM). This component is called dark, because it appears not to undergo electromagnetic interactions and therefore cannot be detected by usual direct observations of electromagnetic radiation. However, a large variety of indirect observations exists, which all require the existence of DM in order to explain the data (see Bergström (2000), Bergström (2009) for current reviews and references therein), of which the most important are summarized in the following:

- ◇ The first observations suggesting the existence of DM were measurements of the velocity distributions of stars and gas in galaxies (Zwicky 1933). While acting on the assumption that the total mass of a galaxy can be estimated relying on its luminous area, the expectation is that for larger radial distances the rotation velocities decrease (see Fig. 4.1). However, it has been observed, that the velocity stays nearly constant up to very large radii. This fact can be explained by a large abundance of a dark mass, of which the density profile reaches much further out than the density profile of the luminous material.
- ◇ Observations of gravitational lensing caused by galaxy clusters revealed that the mass enclosed in such clusters is clearly dominated by a dark component (Tyson et al. 1998).
- ◇ Observations of hot gas in galaxy clusters like the Coma cluster show that in order to keep the gas with the measured temperature inside the cluster, the gravitational potential should be much larger than the one provided by visible matter, once again requiring a dominant dark component that interacts gravitationally (Briel et al. 1992).
- ◇ Observations of the **Cosmic Microwave Background** (CMB), a radiation component stemming from the time of recombination of ions and electrons ~ 300.000 years after the big bang, contributed a lot to the understanding of the modern cosmology.

These observations require a large DM component as well, in order to explain the density fluctuations, detected in the CMB (Hinshaw et al. 2009), and to establish a connection between these fluctuations and the structures in the present universe (Bergström 2000).

To complete the picture, it must be noted that modern cosmology describes the universe based on Einstein's theory of general relativity, from which one obtains the relation between different energy densities in the universe:

$$\Omega_0 = \Omega_M + \Omega_\Lambda, \text{ with } \Omega_0 = 1,$$

where Ω_M is the matter density and Ω_Λ the density of the vacuum energy, which is responsible for the currently observed accelerated expansion of the universe (Bergström 2000). By putting $\Omega_0 = 1$ it is assumed that the metric of the universe is flat. Recent measurements of SNe of type 1A favour $\Omega_\Lambda > 0$ and combined with the measurements mentioned above, the best-fit values for the vacuum energy and matter density are currently $\Omega_\Lambda \sim 0.7 \pm 0.2$ and $\Omega_M \sim 0.3 \mp 0.2$. The obtained limit on the contribution of baryonic matter is $\Omega_B \leq 0.05$ (Bergström 2009), reflecting the fact that the DM is the dominant matter component in the universe.

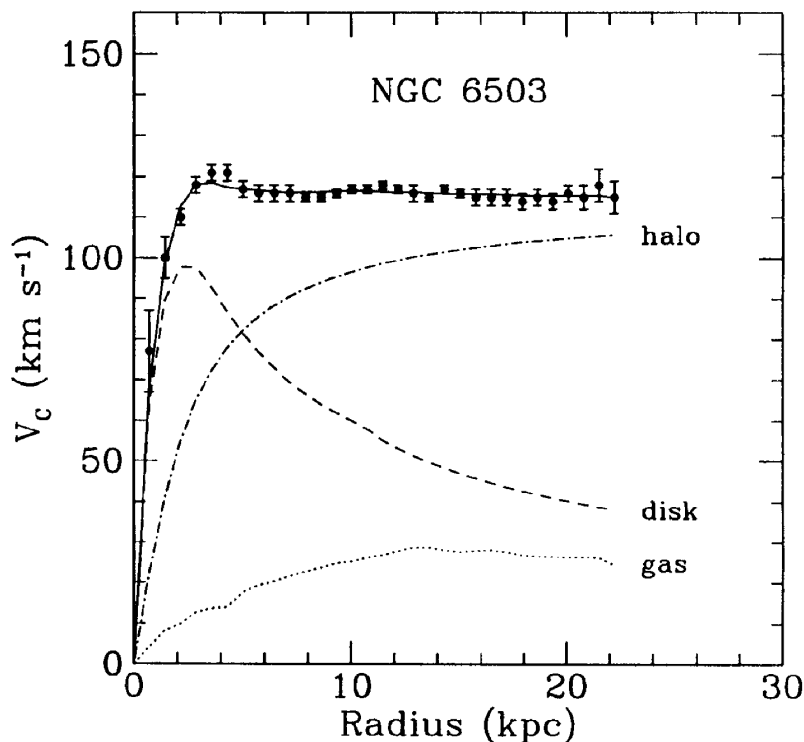


Figure 4.1: Rotational curve of the NGC6503 galaxy, broken down to its individual components. For small radii, gravitational potential stems from the matter in the galactic disk, whereas for larger radii the influence of the DM halo is clearly dominant. Figure is taken from (Freese 2009).

4.2 γ -rays from DM interactions in space and their observations

Although the presence of DM until now is only suggested by its gravitational interaction, it might nevertheless be possible to observe e.g. γ -ray photons from the annihilation (or decay, not treated here) of its constituent particles. In fact, the **standard model of particle physics** (SM) does not provide the right particle candidate as a DM building block, since this particle needs to be stable and electromagnetically non-interacting. The only suitable particle within the scope of SM, the neutrino, is not considered as a viable DM candidate, due to its light mass (Bergström 2000). However, expansions of the SM like the theory of **Supersymmetry** (SUSY) or the model of **universal extra dimensions** (UED) introduce additional set of particles, of which the lightest one must be stable due to quantum number conservation (see (Haber & Kane 1985) for an extensive SUSY review and (Servant & Tait 2003) for review on UED in the context of DM detection). If this particle is also electrically neutral, then it can be considered as a candidate for DM. If such a particle is additionally a Majorana-particle, i.e. it is at the same time its own anti-particle, then it can, despite its stability, annihilate with another particle of the same kind and produce SM particles, like γ -rays, which then can be observed on Earth (see Feng et al. (2001), Hooper (2001) for reviews on indirect detection of particle DM). The probability of such an interaction depends on the local density of DM, influencing observational strategies. Hence in the following, first the interactions of DM particles producing γ -rays are briefly discussed followed by a short summary of the present knowledge about its density distribution. Then observations performed by IACTs are discussed and the method used in this paper is put in their context.

4.2.1 DM particle candidates

As it was mentioned above, promising candidates for particle DM can be found in the expansions of the SM. Most interesting candidates from the point of view of γ -ray observations are **Weakly Interacting Massive Particles** (WIMPs), which have a mass in the range of the electroweak breaking scale (several hundreds of GeV). The cross-section of weak interactions matches quite well the requirements for the proper development of DM abundance throughout the history of the universe (Bergström 2000). In the SUSY model, the lightest neutralino χ constitutes the most interesting WIMP candidate, having its mass in the range $10 \text{ GeV} \leq M_\chi \leq 10 \text{ TeV}$, thus partly in the energy range of H.E.S.S.. It is a Majorana particle, i.e. it can annihilate in the interaction with another χ , producing SM particles (Bergström 2009). The most probable annihilation channels are $\chi\chi \rightarrow ff$, preferring heavy quarks like b or t -quarks, $\chi\chi \rightarrow W^+W^-$ and $\chi\chi \rightarrow ZZ$ (Feng et al. 2001). These processes are followed by the subsequent hadronisation and creation of, amongst others, neutral mesons like π^0 , which then decay into γ -rays. The resulting photon spectrum is soft and featureless and several parameterizations exist for its description (see e.g. Bergström et al. (1998), Tasitsiomi & Olinto (2002)). In particular, the spectrum later used in this work is taken from (Tasitsiomi & Olinto 2002) and has the form:

$$\frac{dN}{dE_\gamma} = 5 * \left(\frac{1}{12} x^{-1.5} - 0.5 \frac{1}{\sqrt{x}} - 0.25 \sqrt{x} + \frac{2}{3} \right), \text{ with } x = E_\gamma/M_\chi \quad (4.1)$$

However, recent theoretical developments show that there might exist a possibility of non-

negligible spectral features, coming e.g. from a boosted annihilation cross-section for $\chi\chi \rightarrow \gamma\gamma/\gamma Z$ (Hisano et al. 2004), which is usually suppressed by several orders of magnitude for helicity reasons, creating a line on top of the continuum spectrum for $E_\gamma = M_\chi$. Another discovery was a possible large contribution from internal bremsstrahlung, peaking as well at $E_\gamma \approx M_\chi$ (Fig. 4.2) (Bringmann et al. 2008). A detection of such a feature in the γ -ray spectrum would be a much stronger proof for DM as its origin than the continuum spectrum, that is difficult to discriminate against astrophysical sources.

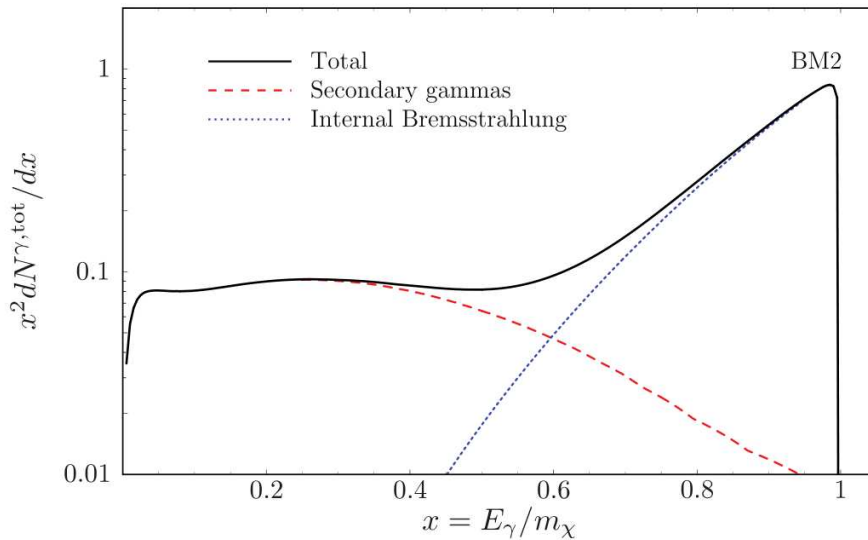


Figure 4.2: γ -ray spectrum from neutralino pair-annihilations, including the component arising due to hard internal bremsstrahlung, that causes a distinct feature at $E_\gamma \approx M_\chi$. The figure refers to the model BM2 from (Bringmann et al. 2008).

Another viable WIMP candidate for DM is given by the theory of UED and is the lightest **Kaluza-Klein** (KK) particle $B^{(1)}$ (Bergström (2009), Bergström et al. (2006)), having its mass in the TeV-range, again coinciding with the energy range of H.E.S.S.. Contrary to the neutralino, the pair-annihilation of KK particles into pairs of light leptons in the final state is not suppressed (Bergström 2009), which can give rise to spectral features in the resulting e^\pm spectrum (and subsequently in the γ -ray spectrum). This is the reason that KK particles were considered as the origin of the infamous ATIC peak (Chang et al. 2008), which is however disputed by other experiments (Latronico & for the Fermi LAT Collaboration (2009), Aharonian et al. (2009a)). Concerning spectral features in the γ -ray spectrum, sharp cut-offs at $E_\gamma = M_{B^{(1)}}$ can be expected due to internal bremsstrahlung off light final state fermions. Also, the annihilation process $B^{(1)}B^{(1)} \rightarrow \gamma\gamma/\gamma Z$ is possible, however suppressed (Bertone et al. 2005).

Thus, to summarize, annihilation of both SUSY and KK particles can produce a spectrum of γ -rays, that can in principle be seen by H.E.S.S., if the mass is in the accessible range. However, a spectrum of secondary photons is difficult to discriminate against a possible astrophysical background, while spectral features, that would provide a clear signal for DM, mostly suffer from low reaction probability, with some exceptions described above.

4.2.2 DM density distribution

The rate of DM particle annihilations, e.g. in the Milky Way, is proportional to the squared density of DM in a given region: $\frac{dN_{\chi\chi}}{dt} \propto \rho^2(r)$, where $\rho(r)$ is the DM density as a function of the distance to the GC, and of the (velocity-averaged) annihilation cross-section $\langle\sigma v\rangle$. Consequently, the total flux of γ -rays from DM annihilations, observed on Earth within a certain field of view $\Delta\Omega$ can be calculated as:

$$\frac{d\Phi(\Delta\Omega, E_\gamma)}{dE_\gamma} = \frac{1}{4\pi} \frac{\langle\sigma v\rangle}{M_\chi^2} \frac{dN}{dE_\gamma} \times J\Delta\Omega, \text{ where } J = \frac{1}{\Delta\Omega} \int_{\Delta\Omega} \int_{\text{line-of-sight}} \rho^2(r) ds \quad (4.2)$$

where $\frac{dN}{dE_\gamma}$ is the spectrum of γ -rays produced in DM annihilations (see Sec. 4.2.1 and Fig. 4.22).

Thus in order to perform promising γ -ray observations of DM signals, regions with high density along the line of sight should be preferred. A first estimate of the density distribution of DM can be obtained by studying the rotational curves of galaxies (including the Milky Way), yielding the following phenomenological relation:

$$\rho(r) \propto \frac{\rho_c}{(r/a)^\gamma [1 + (r/a)^\alpha]^{(\beta-\gamma)/\alpha}} \quad (4.3)$$

with e.g. $(\alpha, \beta, \gamma) = (1, 3, 1)$ for the famous Navarro-Frenk-White (NFW) profile (Navarro et al. 1996), and with the scale length $a = 20 - 30$ kpc for a Milky Way sized galaxy. From this relation it is obvious, that the highest density is expected in the very centers of galaxies, whereas it vanishes for large radii (see also Fig. 4.3). To increase the precision of the density profile parameterizations especially for the central region of the Galaxy and also to study the role of local overdensities of DM, the so-called subhalos (see e.g. Berezhinsky et al. (2003)), one needs to apply N-body simulations (being based on the current knowledge of cosmology), which track the evolution of the universe and its structure formation from an early stage until the present time (see Bertschinger (1998) for an extensive review of N-body simulations). Since the contribution of DM is essential for structure formation, the evolution of DM distribution is precisely pursued. Most recent N-body simulations were performed by the Aquarius (Springel et al. 2008) and Via Lactea II groups (Diemand et al. 2008). Both the smooth and subhalo components of a Milky-way sized DM halo were studied. The smooth density profile obtained by Via Lactea II is in agreement with a NFW profile, while Aquarius results are better described by the Einasto profile, that predicts a less dense central region (see Fig. 4.3):

$$\rho^{Aq}(r) = \rho_s \exp \left[-\frac{2}{\alpha} \left(\left(\frac{r}{r_s} \right)^\alpha - 1 \right) \right], \text{ with } \alpha = 0.17 \quad (4.4)$$

Subhalos could be resolved down to a mass of $10^{4.5}M_\odot$ and 10^5M_\odot for Aquarius and Via Lactea II, respectively. However, according to Pieri et al. (2009) their contribution to the total γ -ray flux from DM interactions is negligible, and for Aquarius results even

dominated by the extragalactic component¹. The main contribution remains the flux from the center of the galaxy, unless a subhalo is located very close to the observer.

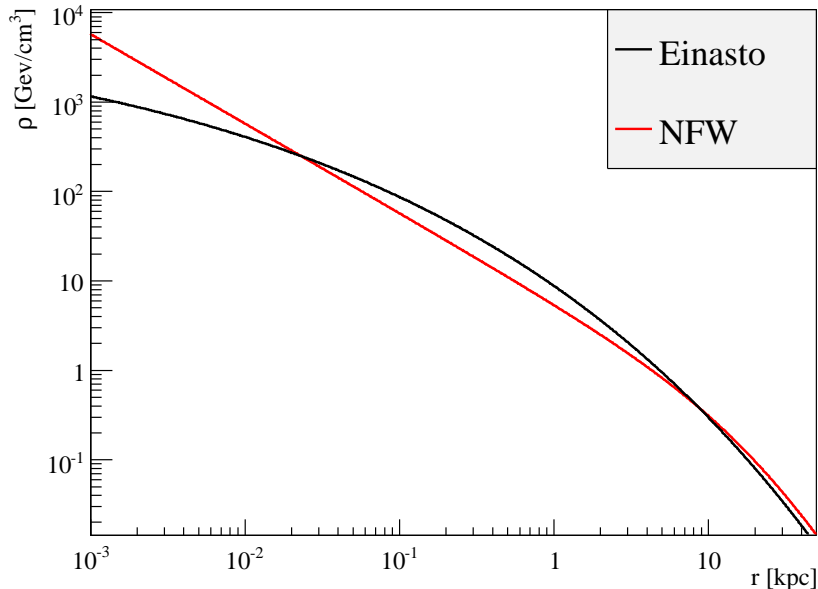


Figure 4.3: Einasto and NFW density profiles in comparison. The parameters are set as follows: $\alpha = 0.17$ and $r_s = 20$ kpc for Einasto profile and $a = 27.6$ kpc for NFW, respectively. Both profiles are normalized to $\rho = 0.39$ GeV/cm³ at the $r = 8.5$ kpc distance to the GC, according to (Catena & Ullio 2009).

4.2.3 Searches for DM signals performed by IACTs

Based on the insights discussed above it is clear that the best targets for the search for DM signals in γ -rays are centers of galaxies, first and foremost the Milky Way. In Sec. 1.2 it was already described, that based on the spectrum obtained by H.E.S.S. from the point source in the GC, HESS J1745–290, a possible contribution of DM induced γ -rays to the total flux was strongly limited (Aharonian et al. 2006b). Besides, it would be difficult to prove that DM and not an astrophysical process causes the observed emission, if just a smooth spectrum is obtained from this source, lacking any spectral features, due to the presence of various particle accelerating objects. Thus it is desirable to observe regions with less or without any astrophysical background. Therefore, IACT experiments carried out observations of local dwarf galaxies, which on the one hand must be strongly DM dominated due to their high mass-to-light ratio and on the other hand do not possess SMBHs, that would serve as an astrophysical background, in their centers (Ibata et al. 1995). In particular, H.E.S.S. has observed Sgr Dwarf (Aharonian et al. 2008b) and Canis Major

¹ The extragalactic distribution mainly consists of DM concentrated in other galaxies and galaxy clusters. The resulting γ -ray flux from extragalactic DM is isotropic and negligible compared with the contribution from central regions of the Milky Way, but depends less on the assumed profile shape (Pieri et al. 2009). See off-analysis for further details.

(Aharonian et al. 2009c). No significant excess was detected and hence upper limits on the velocity-averaged annihilation cross-section $\langle\sigma v\rangle$ (see Fig. 4.4) were obtained for some of the particle candidates. Other experiments observed dwarf galaxies as well, in particular MAGIC (Lombardi et al. 2009) and VERITAS (Wagner & for the VERITAS Collaboration 2009) conducted observations on dSph Draco and dSph Willman 1, also resulting in determinations of upper limits. In turn, observations of local group galaxies again suffer from possible astrophysical backgrounds. The detection of M87 in very high-energy γ -rays (Beilicke et al. 2005), led to another upper-limit estimation on $\langle\sigma v\rangle$, since the detected emission showed variability, disproving a DM dominated origin of the radiation.

A further ansatz explored by the H.E.S.S. experiment was the search for γ -rays from **intermediate mass black holes** (IMBH) (Aharonian et al. 2008c). These are believed to be left over from the time of galaxy formation and have masses between $10^2 M_\odot$ and $10^5 M_\odot$, as suggested by N-body simulations. Such objects would serve as gravitational potentials for DM, forming a subhalo in their vicinity. They are expected to appear in γ -rays as point sources with identical spectra and no counterparts in other wavelengths. However, no suitable objects were found in the H.E.S.S. map of the Milky Way, thus upper limits on the number of IMBH were derived (Aharonian et al. 2008c).

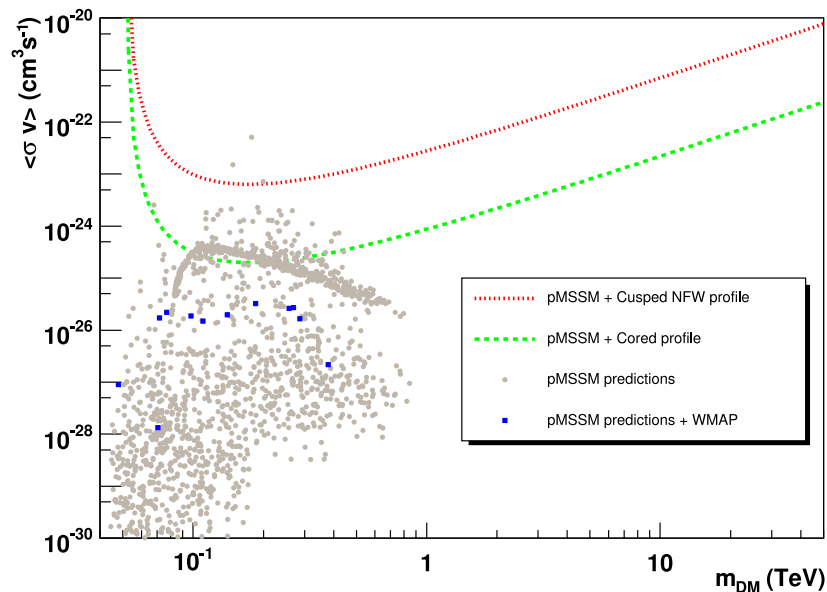


Figure 4.4: Upper limits obtained for the velocity averaged annihilation cross-section $\langle\sigma v\rangle$ from H.E.S.S. observations of the Sgr Dwarf galaxy. For the case of an isothermal cored profile some relevant parameter space for SUSY models can be excluded. Figure taken from (Aharonian et al. 2008b).

4.2.4 New approach: Search for spectral features

All previously conducted searches for DM signals have one important aspect in common: They require that γ -rays from DM annihilations are numerous enough to make them statistically significant compared to the background of mis-identified hadrons throughout the **whole** covered energy range, i.e. $100 \text{ GeV} < E < 100 \text{ TeV}$, in order to have a positive detection as a γ -ray source. Thus the performed observations looked for the smooth continuum spectrum from secondary particles, created in DM pair-annihilations, which spans over a large energy range.

However, in Sec. 4.2.1 it was shown that in some cases the possibility exists that a spectral feature like a γ -ray line from the $\chi\chi \rightarrow \gamma\gamma/Z\gamma$ reaction has a non-negligible cross-section compared to the smooth component. In that case it can happen that even if such a feature would be significant compared to the background within its (comparably limited) energy range, the significance of the overall emission from the particular object/region would be too low to be detected as a source.

Thus in this thesis a method of searching for features in a given spectral distribution is developed, that does not require source detections or background subtraction in general. As spectral signature to look for, a Gaussian function is chosen. This method is then applied to data from the GC halo, where the region of the diffuse emission, including both point sources, is excluded, in order to have an environment free of astrophysical background (see also Sec. 1.5) on the one hand, but still a comparably high density of DM particles on the other hand. The application of this analysis to the off-data, i.e. observations of extragalactic regions without γ -ray sources, can be found in Sec. B.2. Moreover, this method can also be applied to search for spectral features due to any other processes, beside DM annihilations, like the monoenergetic particle wind caused by pulsars (Rees & Gunn (1974), Kennel & Coroniti (1984)). Additionally, the determination of upper-limits for a continuum spectrum, enabled by the developed background subtraction method (see Sec. 4.3.4), is described in Sec. 4.4.

4.3 Development of the peak search algorithm and application to the GC halo

In this section the analysis of H.E.S.S. data from the GC halo with regard to spectral features caused by DM annihilations is described. For this analysis, the same run sample is selected as for the analysis of the diffuse emission (see Sec. 3.2). However, now standard cuts are applied to discriminate against hadronic background, due to their lower energy threshold (see Sec. 2.3.4). Additionally, to keep the energy threshold low, observations performed at zenith angles higher than 30° are rejected from the sample. Events passing the shape cuts (see Sec. 2.3.4) were selected for the further analysis, without performing any geometrical background subtraction. Besides, an additional dataset was created, for which a cut on the event multiplicity was applied, requiring $N_{\text{tel}} = 4$. While this cut slightly increases the energy threshold and rejects a major part of the events (see Tab. 4.1), it

improves the energy resolution of the H.E.S.S. array (see Fig. 4.12). The sensitivity of the analysis with (4-tel configuration) and without (all-tel configuration) the multiplicity cut can thus be compared.

4.3.1 Calculation of the spectral distribution

The γ -ray events collected in the new data samples are not yet selected by their arrival direction. In order to be restricted to the halo close to the GC and to reduce systematics, the following further cuts are applied:

- ◇ $r_\gamma \leq 1^\circ$, where $r_\gamma = \sqrt{l^2 + b^2}$ is the angular distance of the event direction to the origin of the galactic coordinate system, with (l, b) being the event direction in galactic coordinates. In order to exclude astrophysical background, additionally $|b| > 0.3^\circ$ is required. The resulting on-region is shown in Fig. 4.5. Its angular area equals to $5.9 * 10^{-4}$ sr (1.94 [deg]²).
- ◇ $\Psi < 2^\circ$, where Ψ is the angular distance between the shower direction and the direction of observation. This cut reduces systematic effects occurring at the edge of the field of view.

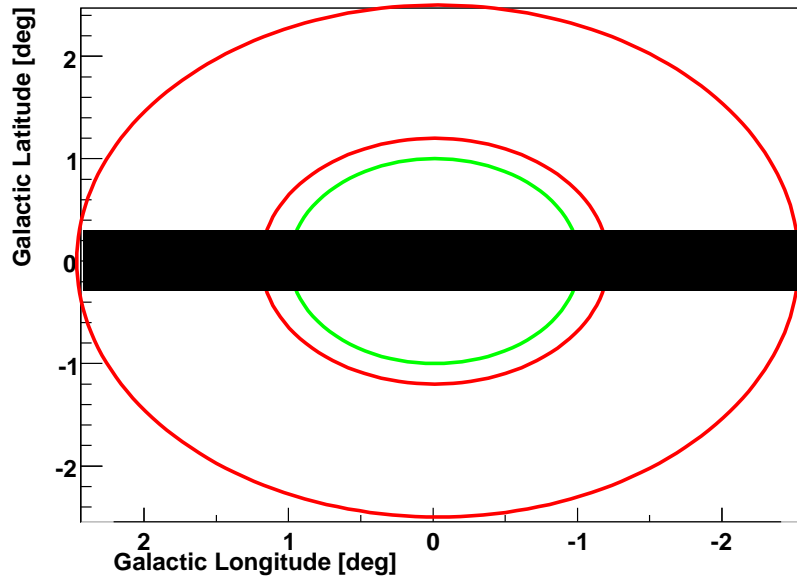


Figure 4.5: Visualisation of the on-region (green circle) and off-region (in between red circles), used for the DM analysis. The purpose and motivation for off-regions can be found in Sec. 4.3.4. The galactic plane within the range $-0.3^\circ < b < 0.3^\circ$ is excluded.

The energy distribution of events remaining after the above selection is shown in Fig 4.6 for both configurations. One observes that most events are located in the low-energy range, e.g. 92% are below $E_\gamma < 1$ TeV for the all-tel configuration, with a threshold at $E_\gamma \approx 250$ GeV, defined as the maximum of the energy distribution (see also Tab. 4.1). However,

	$N_{\text{tel}} \geq 2$	$N_{\text{tel}} = 4$
Number of runs	255	
Livetime [hr]	111.53	
Number of events after shape cuts	2866477	252287
Number of selected events within the on-region	137135	14672
Number of selected events within the off-region	255537	25864
Energy threshold [GeV]	235	310
Number of events with $E < 1$ TeV	118641	12441

Table 4.1: Summarized statistics concerning the analysis of the GC halo. The much lower number of events with $N_{\text{tel}} = 4$ is due to a low size cut (60 p.e.) for the standard cut configuration, for which many events with lower multiplicity pass the cuts. The number of events in the off-region relates to the background subtraction technique, explained in section 4.3.4.

the collected statistics up to several TeV should allow a sensitive measurement.

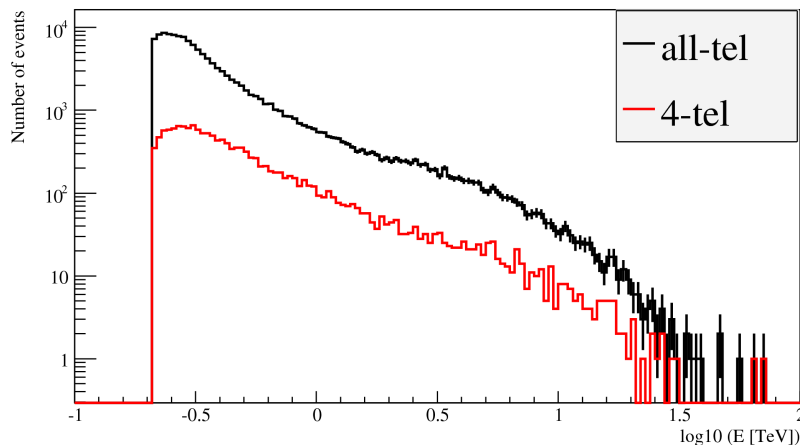


Figure 4.6: Energy distribution of γ -like events from the GC halo region for the all-tel configuration. The energy threshold of the dataset, defined as the maximum of the energy distribution, is found at $E_{thr} \approx 250$ GeV. 92% of events are located at energies below 1 TeV.

To obtain a spectrum from the energy distribution, it is folded with the detector acceptance determined for the given dataset. For the 4-tel configuration, new effective area lookup tables were produced. The total detector acceptance² is calculated as follows:

² The effective area lookup tables are taken for the standard point source cut configuration, assuming a cut on $\theta < 0.6^\circ$. The usage of point source lookup tables, while dealing with extended regions like the GC halo, can be justified in the following way: The applied cut on θ is very loose compared to the typical PSF extension ($\sim 0.1^\circ$) and means that for a data analysis of a point source, no events are rejected due to their reconstructed direction, i.e. due to the non-zero extension of the PSF, if their true arrival direction is located at the point source position. Correspondingly applied to the case of an extended source, this means that as long as for a certain (small) area within the source the same number of γ -rays

- ◇ For each run, the field of view is divided into small bins ($0.02^\circ \times 0.02^\circ$). Bins outside the defined on-region are not used for the acceptance calculation.
- ◇ For the calculation of the effective areas, corresponding offset and zenith angles have to be used. While for the zenith angle the observation position of the particular run is taken, the angular distance to the observation position is calculated for each bin individually.
- ◇ A loop over bins within the on-region is performed, and for each bin the corresponding effective area distribution as a function of energy is obtained and added to the effective areas obtained from other bins. The sum is weighted with the total livetime of the run.

Thus in the end the total effective area as a function of energy for the defined on-region is obtained (see Fig. 4.7). The energy distribution (see Fig. 4.6) is divided by the effective area distribution to obtain the spectral distribution of the region, shown in Fig. 4.8. Here it should be emphasized, that the obtained distribution mainly consists of γ -like hadrons events, as well as a small electron fraction. The potential number of true γ -rays is negligible compared to the hadronic background. Hence it is sensible to weigh the spectral points with $E^{2.7}$, the (inverse) spectral shape of CRs, to study the shape of the distribution more accurately (Fig. 4.9). It is visible that the resulting spectrum is not flat, but decreases for $E < 1$ TeV, rises again for $E > 3$ TeV and decreases for $E > 10$ TeV. This is an effect of the hadronic background efficiency of the applied cut selection, which is obviously energy-dependent. A comparison of the distribution for the all-tel configuration with the 4-tel configuration shows, that the rise of the spectrum for $E > 3$ TeV is mainly due to 2-tel and 3-tel events.

Despite the overall curved shape, the spectral distribution is smooth and can be parametrized by e.g. a curved power-law:

$$\frac{d\Phi_i}{dE dt} = \Phi_0 E^{\Gamma_1 + \log(E) \Gamma_2}$$

within a certain range (see Sec. 4.3.2). Hence the distribution fulfills the only requirement for a meaningful peak search: It should be possible to describe the spectrum with a smooth function (within a certain energy range) and no intrinsic spectral features, e.g. due to systematic effects of the background rejection, are allowed. To verify that the present spectral shape is indeed due to the hadronic background and that it does not introduce systematic effects, a spectral distribution of protons, simulated at 20° zenith angle and reconstructed with the same γ -selection as used for this analysis, is shown in Fig. 4.10. From this, it can be concluded, that the curvature of the data spectrum is indeed due to the hadronic background. Beside, no apparent systematic problems like intrinsic spectral features are visible in the proton distribution. The observed deviations in shape between the data and simulated distribution are not unexpected, given the fact that $\sim 10\%$ of CRs consist of heavier elements, beside protons, which induce showers in the atmosphere with different characteristics (Egberts 2009).

are falsely reconstructed to originate from this area, as are lost due to the extension of the PSF, point source lookup tables can be used as well, since also in this case, in total no events are rejected because of their reconstructed direction.

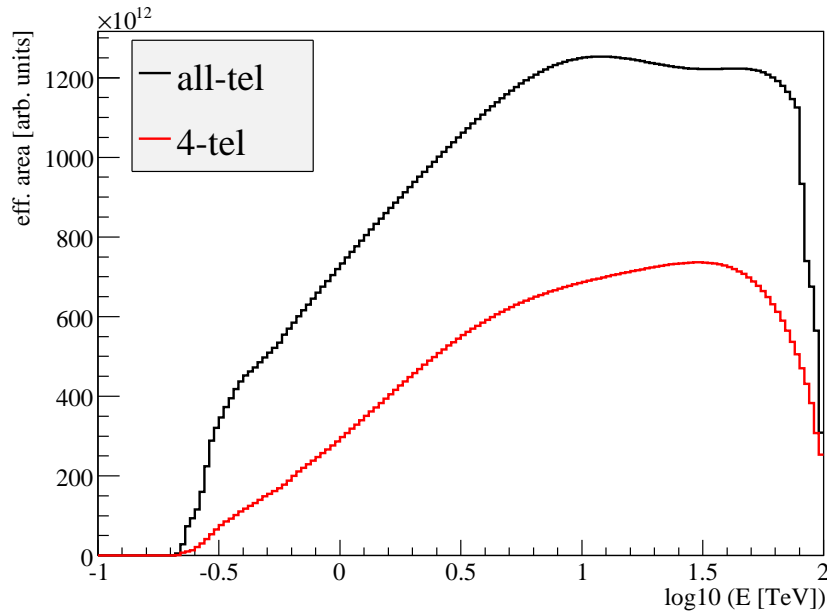


Figure 4.7: Effective area distribution as a function of energy found for the GC halo region for all telescope multiplicities. This distribution is obtained by summing up the contributions from all bins within the on-region for each run of the dataset (see text for further details).

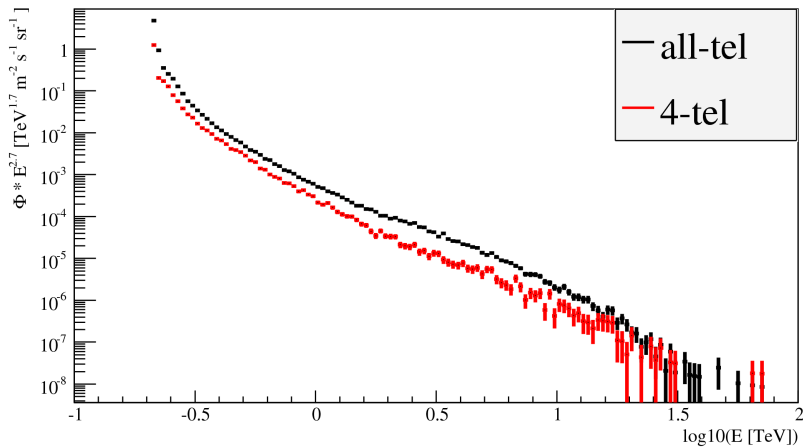


Figure 4.8: Spectral distribution of γ -like events from the GC halo region for the all-tel configuration. Beside the peak due to systematic effects at the low energy threshold, which are excluded from the analysis, the distribution exhibits a smooth, power-law-like shape.

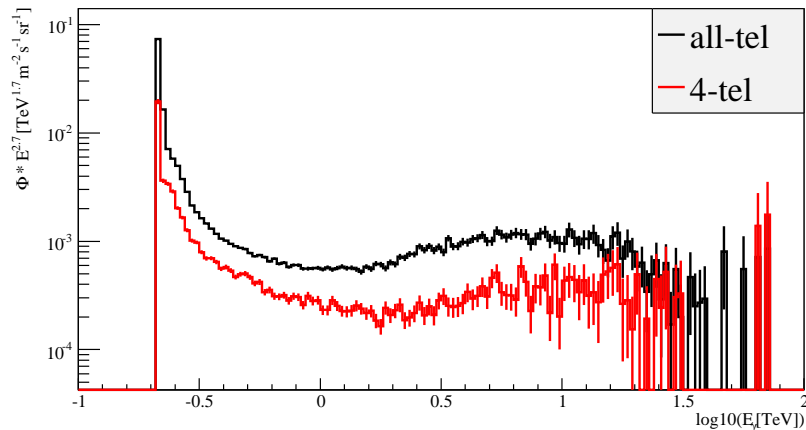


Figure 4.9: Spectral distribution of γ -like events from the GC halo region for both all-tel and 4-tel configurations, weighted with $E_\gamma^{2.7}$. Beside systematic threshold effects, visible as strong peaks for lowest energies, the deviation of the spectra from a constant distribution come from the energy dependence of the background efficiency of the standard cut set.

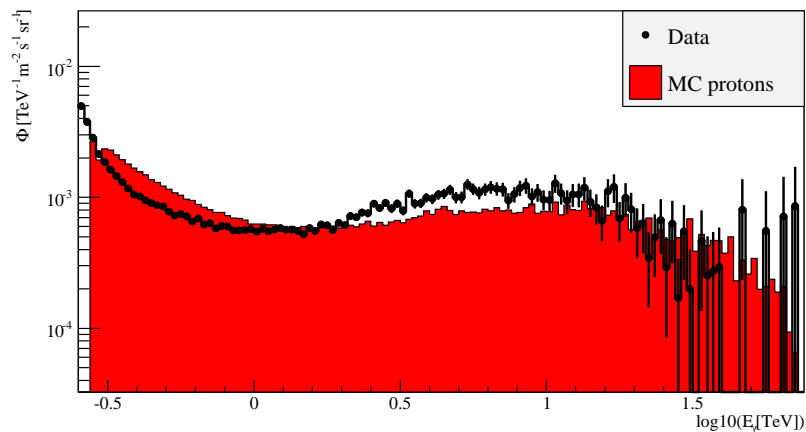


Figure 4.10: Spectral distribution of γ -like events from the GC halo region for the all-tel configuration, weighted with $E_\gamma^{2.7}$, together with the distribution of simulated isotropic protons, obtained with the same analysis. Both distributions have a common overall shape. Deviations in slope may come from systematic effects of the proton shower simulation as well as from the fraction of heavier nuclei in the CR spectrum. Besides, the zenith angles in the data range from 5° up to 30° , while the simulations were performed for a zenith angle of 20° .

4.3.2 Development of the peak search procedure

In the last section it was shown, that the spectrum of γ -like events from the GC halo is smooth and featureless, as expected from simulations of the hadronic background. Thus, if

a spectral feature is introduced by real γ -rays, it should be possible to detect it, if its flux is statistically significant compared to the background flux. The energy range, in which the search for signatures is performed, is restricted to $0.5 \text{ TeV} \leq E_\gamma \leq 5 \text{ TeV}$, with the lower bound being defined by the proximity of the energy threshold, at which systematic effects dominate³.

In order to be able to properly identify Gaussian peaks in the spectrum, there exist essentially two approaches: One is based on the so-called “sliding window” method, for which the background and a potential peak are fitted within overlapping energy ranges, which are determined by the energy resolution of the instrument (for details see e.g. (The Fermi LAT Collaboration et al. 2010)). For the other approach, first peak candidates, i.e. deviations from the smooth shape of the spectrum, are determined by means of a peak search algorithm, like the one implemented in the `TSpectrum`-class (Mariscotti 1966) of the `ROOT`-software (Brun et al. 2006). Once the peak position has been determined, the background level together with the peak contribution around this position can be determined by a fitting procedure. For this work, the latter variant was chosen.

The `TSpectrum`-algorithm searches for peak candidates by using the distribution of the second differences, defined as:

$$S_i = N_{i+1} - 2N_i + N_{i-1},$$

where N_i is the value in the corresponding bin i . The distribution of second differences approximates the second derivative of the studied distribution, which is constant (or zero), if the studied distribution can be approximated by a two-dimensional (one-dimensional) polynomial within a short range around the bin i . Any significant deviations from a constant shape are hints for the presence of features in the studied spectrum.

Having a suitable method for searching for peak candidates at hand, the individual steps of the peak search procedure can be defined (an example is shown in Fig. 4.11):

- ◇ Step 1: The `TSpectrum`-algorithm is applied to the spectral distribution of selected γ -ray like events from data⁴, as described in Sec. 4.3.1, which is weighted with the function $E^{2.7}$ (see Fig. 4.9), using loose search criteria to enable the algorithm to find as many candidates as possible. A selection of potential candidates for a γ -ray induced signature is done in the following.
- ◇ Step 2: For each peak candidate at an energy E_i in the allowed energy range, first the underlying background is modelled. This is done by fitting a curved power-law function⁵ to the spectrum around the peak within a certain range⁶:

$$(E_i - 4.5\sigma_0) \leq E \leq (E_i - 1.5\sigma_0) \text{ and } (E_i + 1.5\sigma_0) \leq E \leq (E_i + 4.5\sigma_0),$$

with σ_0 corresponding to the assumed energy resolution. The fitted function is then subtracted from the spectrum, thus yielding a residual distribution.

³ An extension of the energy range towards higher energies is planned for the future.

⁴ The binwidth of the distribution is selected small compared to the expected width of possible signatures.

⁵ In the logarithmic representation, a curved power-law function is equivalent to a two-dimensional polynomial.

⁶ Variations of this range were allowed to achieve a better fit of the background.

- ◇ Step 3: The residual distribution is fitted by a Gaussian function:

$$f(E) = A \times \exp\left[-\frac{(E - E_0)^2}{2\sigma^2}\right]$$

If the fit does not converge in a meaningful range, e.g. $A < 0$ or $\sigma \ll \sigma_0$, the peak is rejected as a candidate for a spectral signature.

- ◇ Step 4: Now a simultaneous fit of the peak and the background is performed. If the fit again converges within a meaningful range (see above), the peak is kept for a test, determine its statistical significance.
- ◇ Step 5: The determination of the statistical significance of a peak candidate is done by creating a set of statistically randomized background spectra, within the range specified in step 2, using the parameterization of the background spectrum determined in step 2 and taking into account statistical uncertainties of every bin. For each spectral distribution j from the generated set the analysis steps 1-4 are performed and the number of cases is determined⁷, for which a peak is reconstructed, that has, within errors, an equal or larger flux than the peak candidate under study, i.e. norm $A_j \geq A$, having at the same time an equal or larger width $\sigma_j \geq \sigma$.

The statistical significance of a peak candidate is determined by the fraction of randomized spectra, which create an equivalent peak signature by background fluctuations. Thus the confidence level P_i of a peak candidate i is defined as: $P_i = 1 - N_{\text{sim},i}^+ / N_{\text{sim},i}^{\text{tot}}$, where $N_{\text{sim},i}^{\text{tot}} = 500$ is the total number of simulated background spectra, and $N_{\text{sim},i}^+$ is the number of peaks, created by background fluctuations in the simulated sample, that yield the same or larger flux as the peak candidate under study.

4.3.3 Application to the H.E.S.S. data from the GC halo

The algorithm, described in the last section, was applied to the spectral distribution from the GC halo. For both configurations, all-tel and 4-tel, no significant peaks⁸ were found in the studied energy range between $0.5 \text{ TeV} \leq E \leq 5 \text{ TeV}$. Thus upper limits on the integral flux from a Gaussian signature were derived. This was achieved by taking, on the one hand, simulated diffuse γ -ray events at fixed true energies within the considered range: $E [\text{TeV}] \in \{0.5, 0.75, 1, 1.25, 1.5, 2, 2.5, 3, 3.5, 4, 4.5, 5\}$. Their reconstruction in the framework of the H.E.S.S. analysis yields Gaussian peaks, which have widths corresponding to the H.E.S.S. energy resolution of diffuse γ -radiation (see Fig. 4.12), henceforth called MC peaks. On the other hand, generic Gaussian peaks were used, which correspond to the assumed energy resolutions of 10%, 20% and 30% (see Fig. 4.12).

The integral flux from a Gaussian feature is simply calculated as:

$$\Phi(E_0) = \int \Phi(E) dE, \text{ with } \Phi(E) = A \times \exp\left[-\frac{(E - E_0)^2}{2\sigma^2}\right]$$

⁷ If more than one peak is found in a statistically randomized spectrum, than the peak is taken, that is located closest to the position of the peak candidate under study, determined in step 4.

⁸ No peak candidate reached a significance of 2σ .

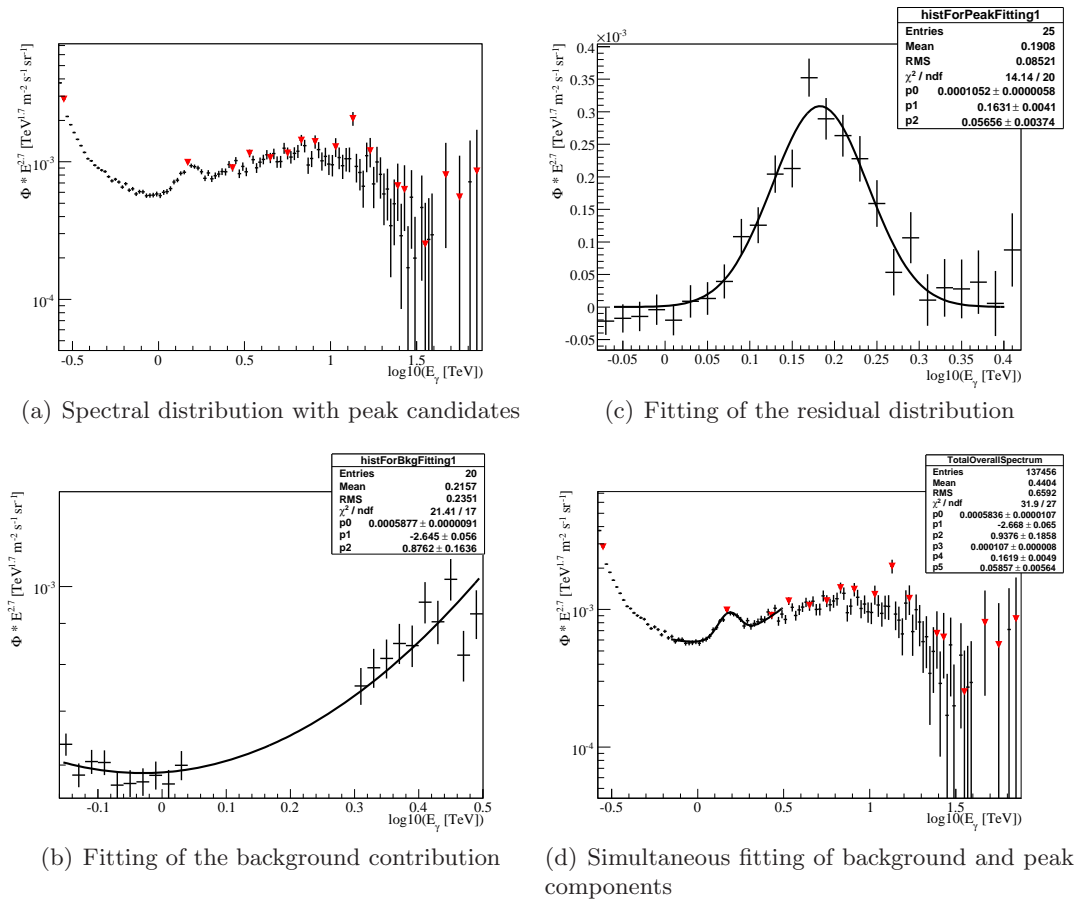


Figure 4.11: Illustration of the working principle of the peak search algorithm for the spectral distribution from the GC Halo (all-tel configuration). Image (a) shows all peak candidates, found by the TSpectrum-class. Among them, the artificial, very pronounced peak at 2 TeV is detected, that was added to the distribution for demonstration purposes. The background around this peak is fitted with a curved power-law in image (b) and then subtracted from the spectral distribution, thus yielding the residua in image (c), which are fitted with a Gaussian function. In the last image (d), the common fit of background and peak contribution is shown. See text for further details.

For the calculation of flux upper limits it is necessary to determine the flux level, i.e. the normalisation of a given Gaussian signature, for which the peak is identified by the peak search algorithm with a certain statistical significance. In this work, all upper limits are given at 95% confidence level. This was done by adding a Gaussian peak to the data spectrum and by increasing its norm until the algorithm successfully identifies and fits the peak with the needed significance. The upper limits, obtained with the method described above, are shown in Fig. 4.13 for both multiplicity configurations (see also Tab. 4.2). The sensitivity of the method for a certain peak energy is determined by the local shape of the background and statistical fluctuations of the underlying background distribution. The effect of the background shape is especially noticeable for $E < 1$ TeV, where the sensitivity of the method is worse, despite the better event statistics, because of the steepness of the

distribution.

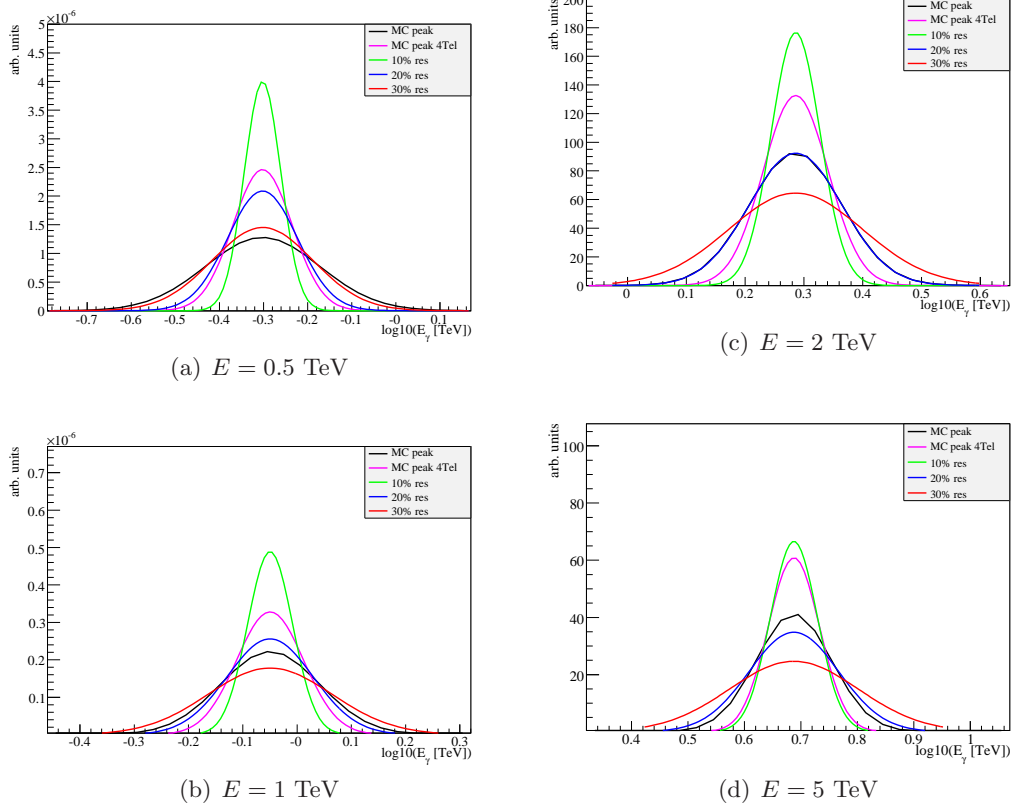
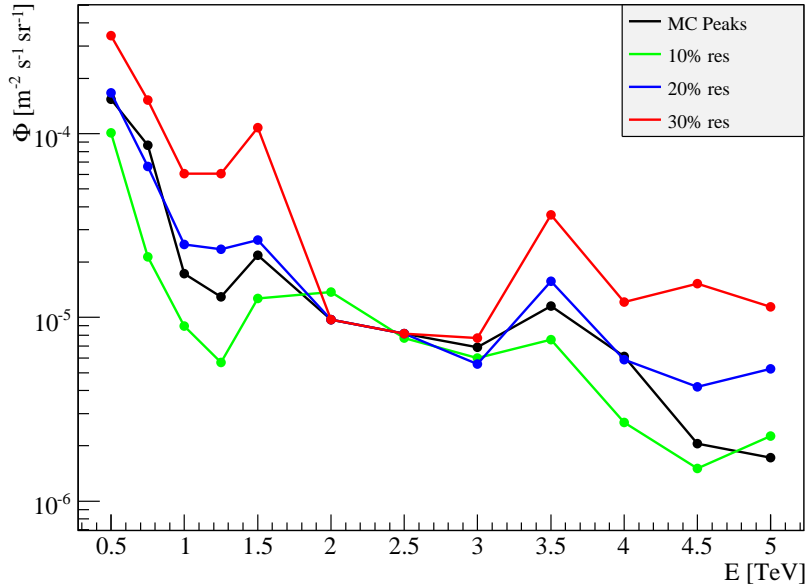
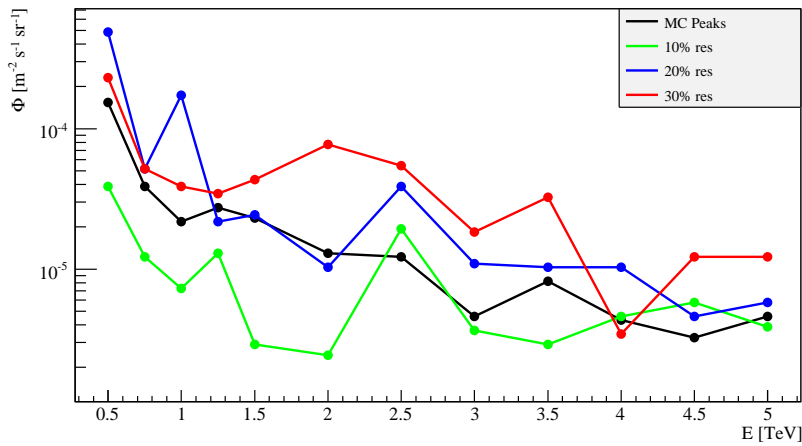


Figure 4.12: Gaussian peaks used for the determination of flux upper limits. Beside peaks corresponding to the energy resolution of H.E.S.S. for diffuse γ -rays, both for all-tel and 4-tel configurations (see text), generic peaks of different widths were used. As it can be seen in the images, the energy resolution ΔE improves throughout the energy range under consideration from $\Delta E > 30\%$ for $E = 0.5$ TeV to $\Delta E < 20\%$ for $E = 5$ TeV.

While it is clear that statistical fluctuations of the measured spectral distributions, influencing the upper limit determination, can not be removed, it is desirable to find a way to better describe the background. In the ideal case, the background would be flat and only one free parameter would be necessary for its parameterization. So for that purpose, background subtraction would be useful, if it would yield a flat residual distribution. A method for background subtraction for the GC halo is thus described in the following section. It should once again be emphasized, that the developed algorithm for the peak search does not require any background subtraction for its general functionality (see Sec. B.1 for off-analysis). Any additional improvements, like background subtraction, are not mandatory and must be checked for systematic effects they might introduce.



(a) Flux upper limits for Gaussian peaks for the all-tel configuration



(b) Flux upper limits for Gaussian peaks for the 4-tel configuration

Figure 4.13: Upper limits on the flux from a Gaussian signature obtained for the all-tel (top image) and 4-tel (bottom image) configurations for MC peaks and different assumed energy resolutions. It is obvious that the sensitivity of the method improves with energy resolution for the most peaks under study.

4.3.4 Background subtraction for the GC halo: The reflected pixel method

The on-region in the GC halo, as it is defined for this analysis, has an angular extension of $r = 1^\circ$ and therefore does not cover the whole Cherenkov camera during observations (see Sec. 2.2). Thus it might be possible to find appropriate off-regions, from which the background can be estimated. However, since the peak search algorithm is sensitive to

systematic effects, the background regions must fulfill stringent requirements, i.e. not introduce additional systematic effects in the spectral distribution throughout the whole accessible energy range. This can be ensured by taking those regions for the background estimation, that have the same detector acceptance for the particular run as the on-region, like it is done in the reflected-method (see Sec. 2.3.4). However, the standard reflected method is inappropriate for this analysis due to the size of the on-region⁹. Hence the reflected-method is modified in order to use it for this analysis. The main idea is not to treat the on-region as a whole, but divide it into small pixels and find corresponding off-pixels for each of them, if possible. The method works as follows:

- ◊ As off-region, a ring around the GC is used, with the inner radius $R_1 = 1.2^\circ$ and the outer radius of $R_2 = 2.5^\circ$ (see Fig. 4.5). Since the DM density profile falls off with increasing distance from the GC, the off-region contains less of the potential DM signal (see Sec. 4.4 for details).
- ◊ For each run, a loop over all pixels $P_{\text{on}}(l_i, b_i)$ in the on-region is performed, with (l_i, b_i) being the angular coordinates of the pixel i . For each pixel, corresponding off-pixels are determined, if possible. This is done by subsequent rotations of the position of the on-pixel by 90° with respect to the observation position, thus at most 3 off-pixels are found¹⁰. A candidate j for an off-pixel $P_{\text{off}}(l_{i,j}, b_{i,j})$ must fulfill the requirements, that it is located in the defined off-region and is not already in use by another on-pixel, except i . If such a candidate pixel is found, it is flagged as ‘used’. Pixels in the on-region, for which no off-pixels were found, are not used.
- ◊ Depending on the number of off-pixels N_i^{off} , found for a particular on-pixel i , the weight α_i is determined for these off-pixels. Since on and off-pixels have the same detector acceptance by construction, α_i simply depends on N_i^{off} , i.e. $\alpha_i = 1, \frac{1}{2}, \frac{1}{3}$ for $N_i^{\text{off}} = 1, 2, 3$ off-pixels, respectively.

An illustration of this algorithm can be found in Fig. 4.14. It is obvious, that if the observation position is located within the on-region, then it is difficult to find off-pixels in the neighbourhood of the observation position. The resulting acceptance distribution of this method is shown in Fig. 4.15.

Using the described method, spectral distributions are obtained for the off-region, using the same effective areas as for the on-region for both analysis configurations, see Fig. 4.16 and 4.17. Based on a qualitative comparison with the corresponding on-distributions, it appears that the spectra agree very well with each other (see also Fig. B.2 - B.4 for comparison of core distances and offset angles, being input parameters for energy reconstruction, between on- and off-regions). A more quantitative statement can be achieved by calculating the residual distribution and fitting the residua with a constant function. For both analysis configurations, the fit results are comparable with zero. A further crosscheck was performed by reconstructing the spectrum of HESS J1745–290, which agree well with

⁹ Since many observations lie within the on-region, these runs would have to be discarded, because it would not be possible to find appropriate off-regions (see Sec. 2.3.5). Thus the sensitivity of the analysis would significantly decrease.

¹⁰ The restriction of the maximum number of off-pixels to 3 is a compromise between finding enough off-pixels for a given on-pixel on the one hand, while not using too much of the off-area, so that this is still usable for other on-pixels on the other hand (see also Fig. 4.14).

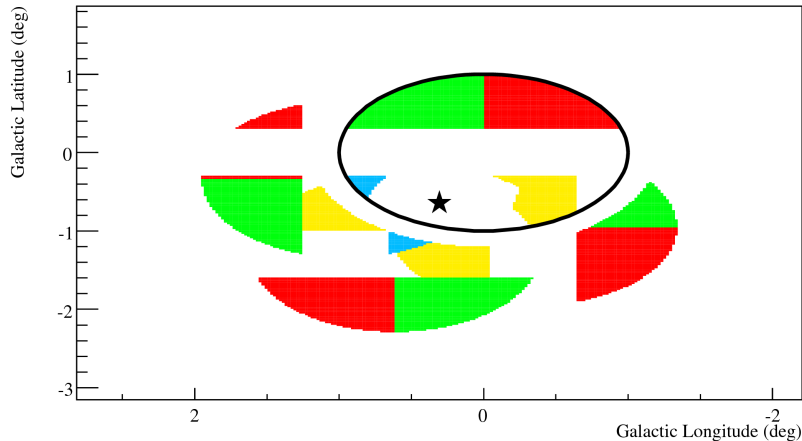


Figure 4.14: Illustration of the working principle of the reflected pixel algorithm. The observation position is marked with a black star. The on-region is located within the black circle and is divided into four differently coloured zones, in order to show where the corresponding off-pixels are located, which have the same color. On-pixels, for which no off-pixels could be found, are not shown. It can be seen, that since the observation position is located inside the lower hemisphere of the on-region, it is difficult to find corresponding off-pixel for the same hemisphere.

the results derived in (Aharonian et al. 2009b), see Fig. 4.18.

The residual spectra can now be used for the peak search algorithm, as described above. Since the distributions are compatible with 0, the background does not need to be fitted, thus steps 2 and 4 of the peak search procedure are omitted in this case. Once again, no significant peaks are found in the data and upper limits on the peak flux are therefore determined. The results are shown in Fig. 4.19.

4.3.5 Combination of results

From the results for MC peaks obtained for different configurations (see Fig. 4.20), the sensitivity of the analysis for the used configurations can be compared. From this figure it is clear, that the sensitivity of a particular configuration depends on the energy. Additionally, in general it appears that subtracting the background yields a better sensitivity for most energies, as expected. Moreover, the 4-tel configuration improves the sensitivity especially for lower energies.

Given that in total four different upper limits for the Gaussian peaks were obtained, it is necessary to provide final values, that take into account the systematic uncertainties. Therefore, the mean value $\langle \Phi_i \rangle$ and the spread $\Delta \Phi_i$ are calculated for each energy i from all four measurements, with $\Delta \Phi_i$ being defined as the systematic uncertainty. The final upper

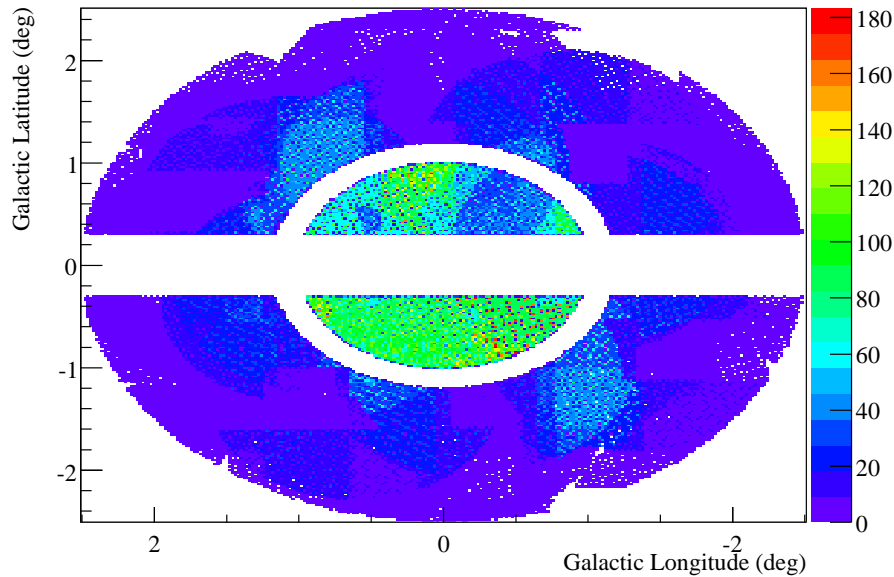
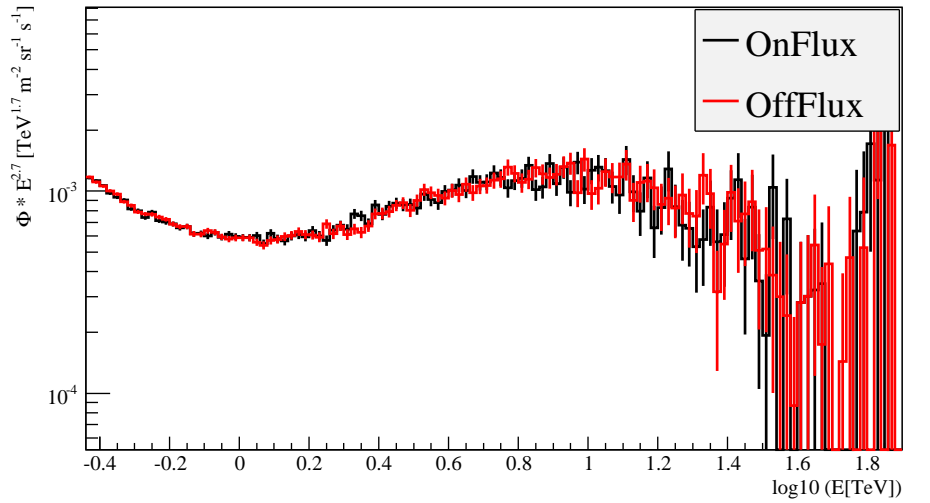


Figure 4.15: Acceptance distribution of the reflected pixel algorithm for the on- ($r < 1^\circ$) and off-regions ($1.2^\circ < r < 2.5^\circ$). For each run, the acceptance value of each pixel in the on-region is defined as 1, if for this pixel suitable off-pixels could be found, and 0 otherwise. If a pixel in the off-region is used as off-pixel in this run, its acceptance is set to $\alpha = 0, 1, 1/2, 1/3$, depending on the total number of off-pixels for the corresponding on-pixel, going from 0 to 3, respectively. See text for further details.

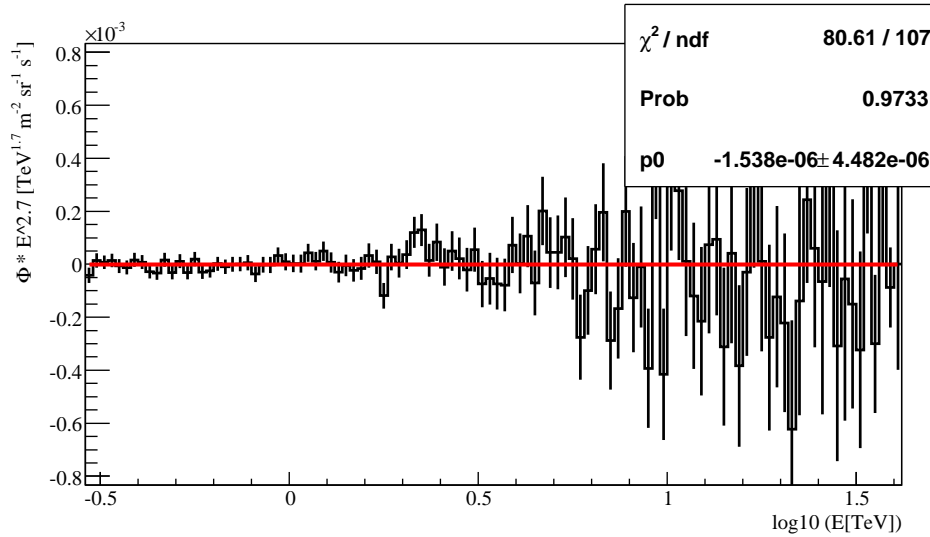
limits are then determined as $\Phi_{\text{final},i} = \langle\Phi_i\rangle + \Delta\Phi_i$, thus taking into account systematic uncertainties in a conservative way (see Tab. 4.2). The final distribution is shown in Fig. 4.21 (see Fig. B.5 - B.7 for generic peaks). Besides, an additional overall systematic error of 20% on the reconstructed flux must be taken into account for all values (Aharonian et al. 2006a).

4.4 Determination of upper limits on $\langle\sigma v\rangle$ for a continuum spectrum

The successful background subtraction, developed for the peak search algorithm, allows to have a background-subtracted spectral distribution. This can not only be used for the peak search, but for determination of flux upper limits, coming from any possible γ -ray spectrum from DM pair-annihilations, as well. Such a measurement can be used for determination of upper limits on the velocity-averaged annihilation cross-section $\langle\sigma v\rangle$, as described in Sec. 4.2.3. In order to obtain a conservative estimate, a smooth parameterization of the γ -ray spectrum from secondary particles, created in DM annihilations, derived in (Tasitsiomi & Olinto 2002), that lacks any distinct features, was used (see Fig. 4.22).



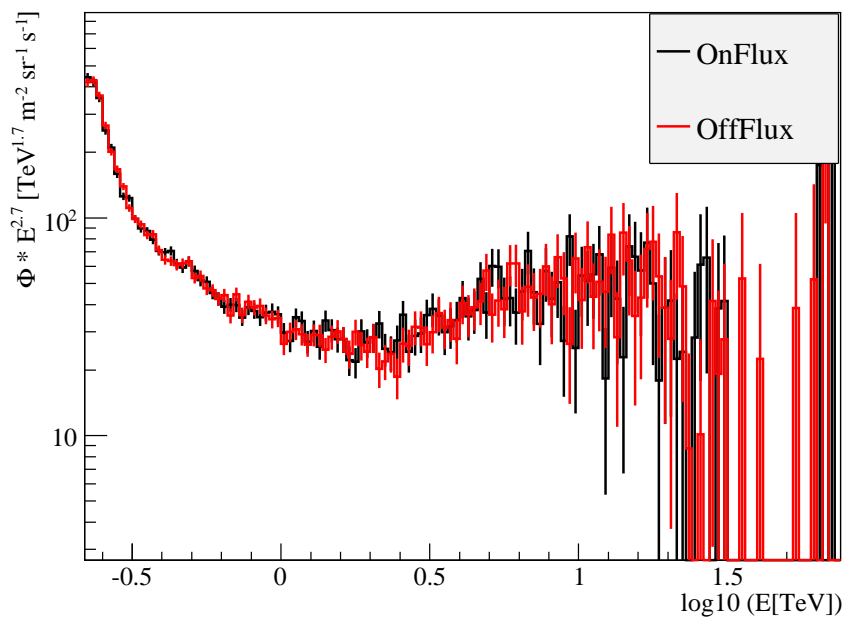
(a) Spectral distribution from the on and the off-region



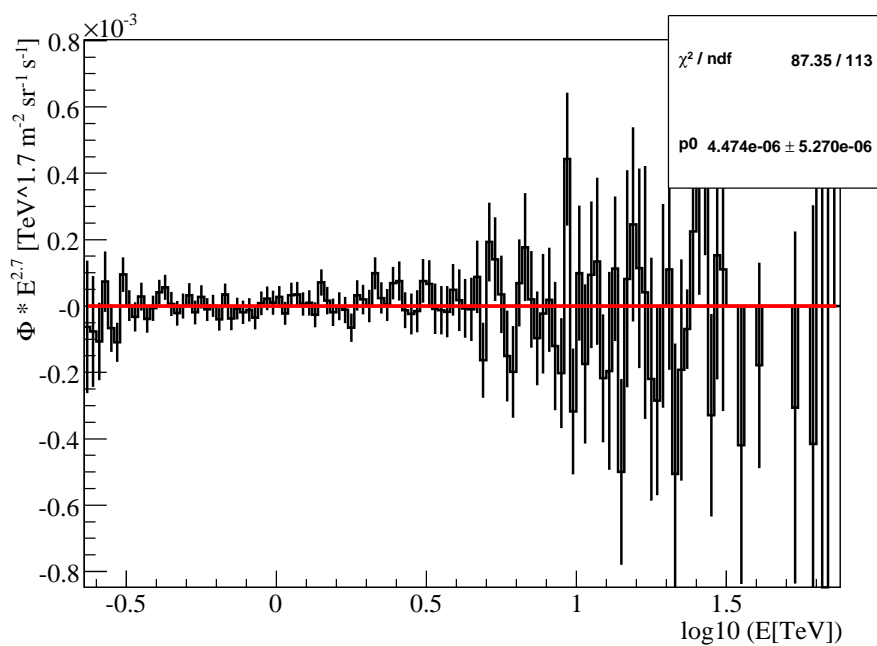
(b) Residual distribution

Figure 4.16: Top: comparison of spectral distributions from the on and the off-regions for the all-tel configuration. Bottom: Residual distribution, fitted with a constant function. Since the result is, as expected, compatible with 0, the reflected pixel method proves to properly subtract the background.

To be able to obtain upper limits on $\langle\sigma v\rangle$, the astrophysical factor $J\Delta\Omega$ must be known (see Eq. 4.2). For that, one needs to assume a DM density profile for the Milky Way. In this work the Einasto profile with $r_s = 20$ kpc and $\rho_c = 7.9 * 10^{-2}$ GeV/cm³ and the NFW profile with $a = 27.6$ were used (see Eq. 4.3 and 4.4). The normalisations of the profiles were selected such that they match the local DM density $\rho_{\text{sun}} = 0.39$ GeV/cm³, estimated in (Catena & Ullio 2009). The astrophysical factor was calculated for the on



(a) Spectral distribution from the on and the off-region



(b) Residual distribution

Figure 4.17: Top: comparison of spectral distributions from the on and the off-regions for the 4-tel configuration. Bottom: Residual distribution, fitted with a constant function. Since the result is, as expected, compatible with 0, the reflected pixel method proves to properly subtract the background.

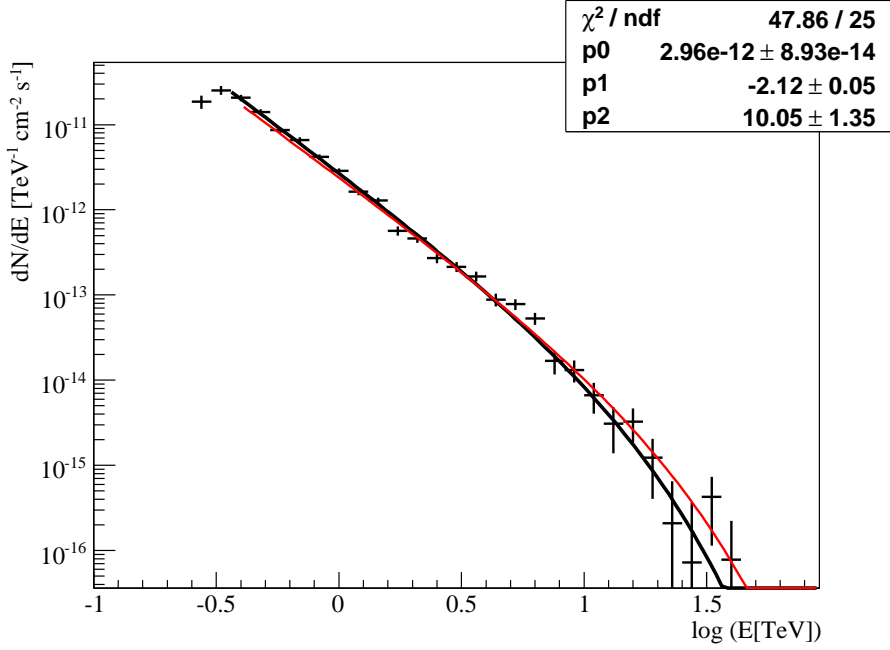


Figure 4.18: The spectrum of a circular on-region with 0.2° radius around the GC, reconstructed with the same analysis technique as described in Sec. 4.3, including the background subtraction method, described in Sec. 4.3.4. As off-region, a circle, centered at the GC with 0.3° inner radius and 1° outer radius, was used. The fit of the spectral distribution was done using a power-law function with an exponential cut-off: $\frac{d\Phi_i}{dE dt} = \Phi_0 \times E^\Gamma \times \exp\left[-\frac{E}{E_0}\right]$, yielding $\Phi_0 = 2.96 \pm 0.09 \times 10^{-12} [\text{TeV}^{-1} \text{cm}^{-2} \text{s}^{-1}]$, $\Gamma = -2.12 \pm 0.05$, $E_0 = 10.1 \pm 1.4 \text{ TeV}$. The fitted parameters agree very well with the spectrum reconstructed in (Aharonian et al. (2009b), red curve): $\Phi_0 = 2.55 \pm 0.06 \times 10^{-12} [\text{TeV}^{-1} \text{cm}^{-2} \text{s}^{-1}]$, $\Gamma = -2.10 \pm 0.04$, $E_0 = 14.7 \pm 3.7 \text{ TeV}$. The higher normalisation is due to the underlying GC diffuse emission (see Sec. 3.2).

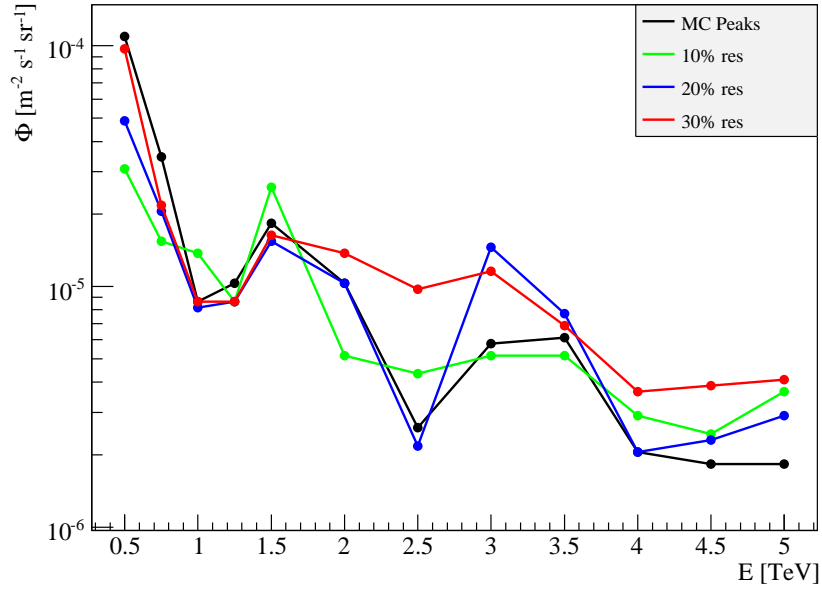
and the off-region and accounts to:

$$J_{on}\Delta\Omega = 3141, J_{off}\Delta\Omega = 1445 \text{ in units of } \frac{1}{8.5 \text{ kpc} * (0.3 \text{ GeV/cm}^3)^2}.$$

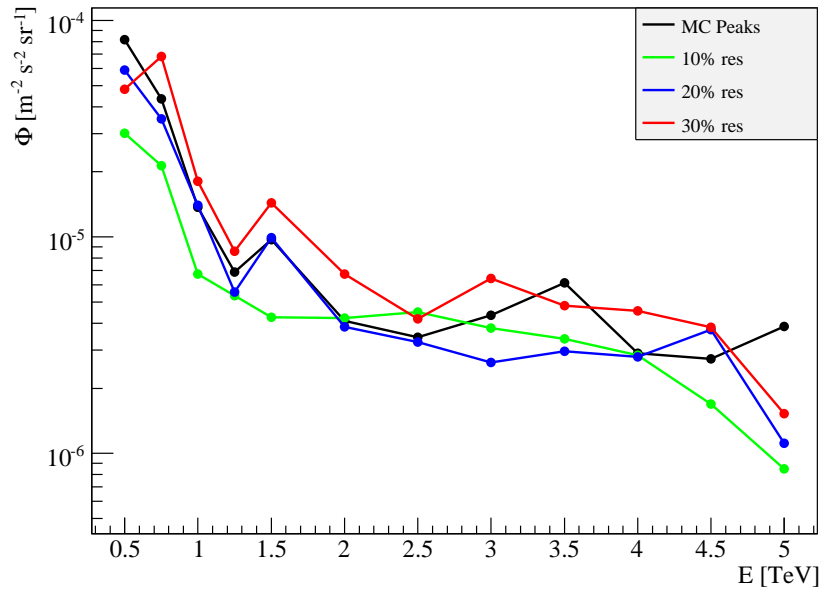
for the Einasto profile and:

$$J_{on}\Delta\Omega = 1217, J_{off}\Delta\Omega = 502 \text{ in units of } \frac{1}{8.5 \text{ kpc} * (0.3 \text{ GeV/cm}^3)^2}.$$

for the NFW profile. The residual astrophysical factor, using the same units, is $J_{res}\Delta\Omega = 1696$ and $J_{res}\Delta\Omega = 715$ for Einasto and NFW, respectively. Thus by background subtraction from the off-region, as defined in this work, 46% for Einasto profile and 40% for NFW profile of the signal is subtracted as well.



(a) Flux upper limits for Gaussian peaks for the all-tel configuration



(b) Flux upper limits for Gaussian peaks for the 4-tel configuration

Figure 4.19: Upper limits on the flux from a Gaussian signature obtained for the all-tel (top image) and 4-tel (bottom image) configurations for MC peaks and different assumed energy resolutions, obtained from background subtracted spectral distributions. It is obvious that the sensitivity of the method improves with energy resolution for the most peaks under study.

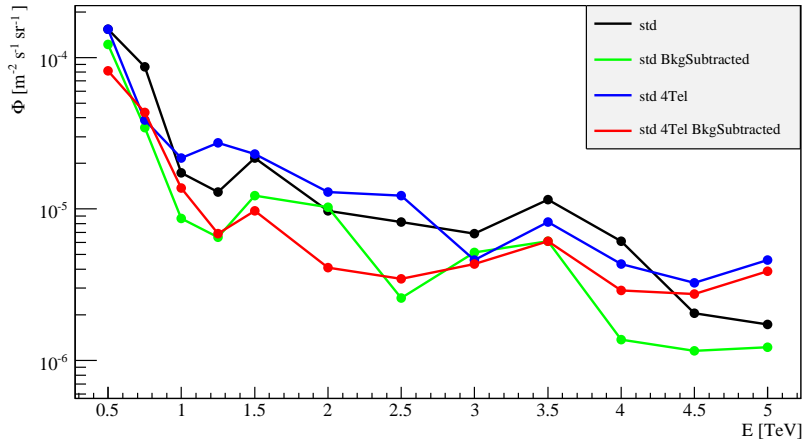


Figure 4.20: Upper limits on the flux from a Gaussian signature for MC peaks for all configurations at 95% conf. level. See text for further details.

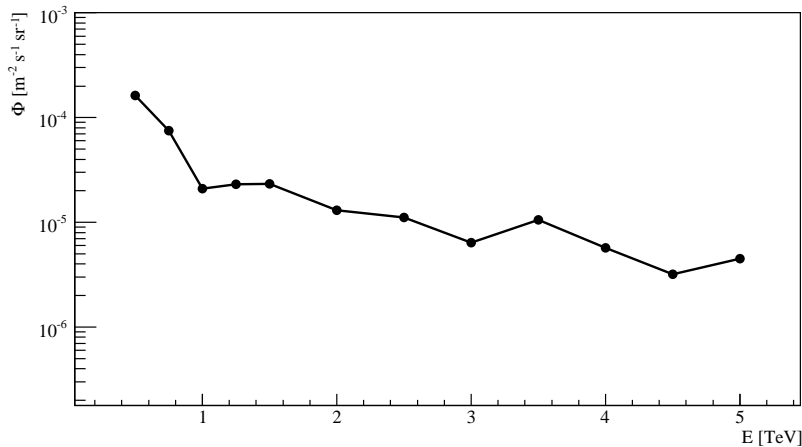


Figure 4.21: Upper limits on the flux from a Gaussian signature for MC peaks at 95% conf. level, obtained by combining all measurements. See text for further details.

The upper limits on $\langle\sigma v\rangle$ were determined by calculating the norm of the γ -ray spectrum for each DM particle mass M_χ , that corresponds to an upper limit at 95% confidence level, taking into account the number of bins involved and their statistical uncertainties. The results are shown in Fig. 4.23 for the Einasto profile and in Fig. 4.24 for the NFW profile, for both analysis configurations. The upper limits, obtained for the all-tel configuration, are slightly more constraining, since the energy resolution does not play a major role for the reconstruction of a smooth spectrum.

Energy [TeV]	$\Phi * 10^5 [\text{m}^{-2} \text{s}^{-1} \text{sr}^{-1}]$						
	std all-tel	std all-tel no bkg	std 4-tel	std 4-tel no bkg	$\langle \Phi \rangle$	$\Delta \Phi$	Final: $\langle \Phi \rangle + \Delta \Phi$
0.5	15.4	10.9	15.4	8.18	12.5	3.56	16
0.75	8.66	3.45	3.87	4.34	5.08	2.41	7.49
1	1.73	0.866	2.18	1.37	1.54	0.554	2.09
1.25	1.3	1.03	2.74	0.688	1.44	0.902	2.34
1.5	2.18	1.83	2.3	0.972	1.82	0.6	2.42
2	0.972	1.03	1.3	0.41	0.927	0.372	1.3
2.5	0.818	0.259	1.22	0.345	0.661	0.448	1.11
3	0.688	0.579	0.46	0.434	0.54	0.117	0.657
3.5	1.15	0.613	0.818	0.613	0.8	0.256	1.06
4	0.613	0.205	0.434	0.29	0.386	0.179	0.564
4.5	0.205	0.183	0.325	0.274	0.247	0.0651	0.312
5	0.173	0.183	0.46	0.387	0.301	0.145	0.445

Table 4.2: Upper limits on the flux from Gaussian peaks for all used analysis configurations. The final upper limits are calculated from the mean values and the spreads of the individual measured limits as $\langle \Phi \rangle + \Delta \Phi$.

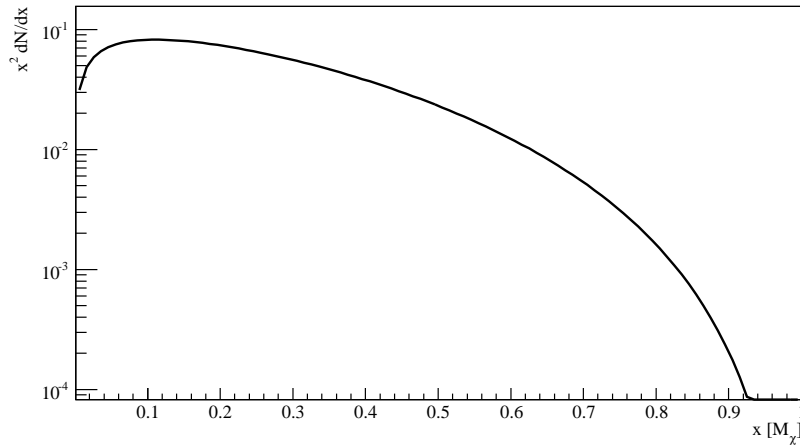


Figure 4.22: Spectrum of γ -ray photons from secondary particles, created in DM annihilations, as a function of $x = E_\gamma/M_\chi$, with E_γ being the photon energy and M_χ the mass of the DM particle. The parameterization was estimated by (Tasitsiomi & Olinto 2002).

4.5 Discussion and conclusions

In this chapter the analysis of the H.E.S.S. data from the GC halo in the context of the search for signals from DM annihilations was presented. First, a method of searching for spectral signatures was described. This method can be applied to search for spectral signatures coming from any possible physical process. In this work, it was used to obtain upper limits on the flux from a Gaussian feature, produced in DM annihilations, in the data from the GC halo (see Fig. 4.21). Non-negligible fluxes from such features are predicted by some theoretical models (Bringmann et al. (2008), Hisano et al. (2004)). Two different

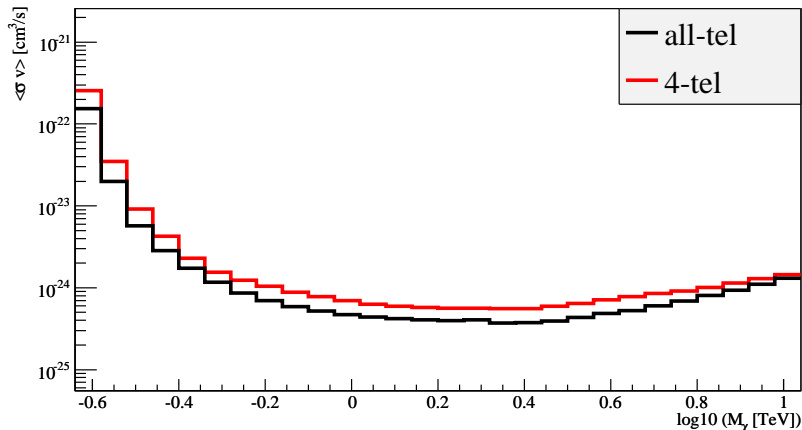


Figure 4.23: Upper limits on the velocity-averaged annihilation cross-section $\langle\sigma v\rangle$ of DM particles at 95% conf. level, obtained for the data from the GC halo for both multiplicity configurations, all-tel and 4-tel. As a γ -ray spectrum, the parameterization derived in (Tasitsiomi & Olinto 2002) was used. The Einasto profile was used for the DM density distribution. The all-tel configuration provides more sensitive results due to better statistics. See text for further discussion.

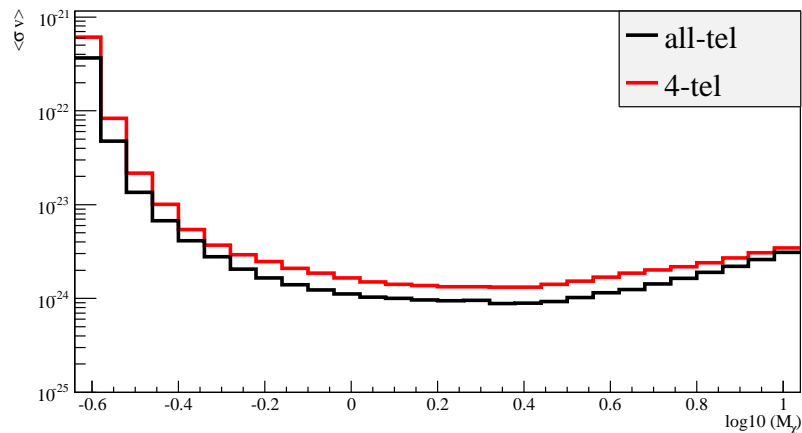


Figure 4.24: Upper limits on the velocity-averaged annihilation cross-section $\langle\sigma v\rangle$ of DM particles at 95% conf. level, obtained for the data from the GC halo for both multiplicity configurations, all-tel and 4-tel. As a γ -ray spectrum, the parameterization derived in (Tasitsiomi & Olinto 2002) was used. The NFW profile was used for the DM density distribution. The all-tel configuration provides more sensitive results due to better statistics. See text for further discussion.

multiplicity configurations were used, $N_{\text{tel}} \geq 2$ and $N_{\text{tel}} = 4$, to study the sensitivity of the method for different quality requirements for the energy reconstruction. Besides, an algorithm for background subtraction for the GC region was developed, allowing to obtain background-subtracted spectra. As already discussed in Sec. 4.2.3, this is the first

time that such upper limits are obtained with a Cherenkov instrument. As far as other instruments are concerned, a similar method was applied to the data from the FERMI telescope in the energy range between 30 GeV and 200 GeV (The Fermi LAT Collaboration et al. 2010). A combination of the results obtained by FERMI and in presented analysis, presented here, of the GC halo data are shown in Fig. 4.25. (see Sec. B.2 for off-data comparison). It has to be taken into account that events used in the FERMI analysis, originate from a much larger area: $|b| > 10^\circ$ and a $20^\circ \times 20^\circ$ square around the GC. Hence overall, FERMI and HESS results (both on GC halo and off-data) provide to date the most sensitive upper limits on spectral signatures in the energy range $20 \text{ GeV} \leq E \leq 5 \text{ TeV}$.

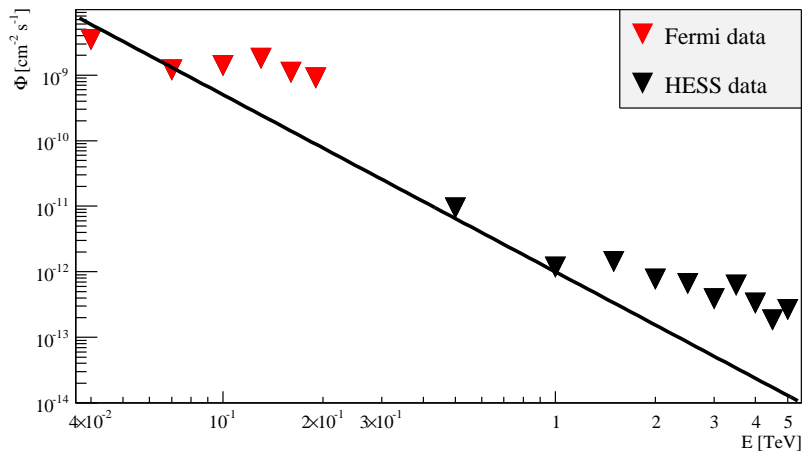


Figure 4.25: Combined upper limits from the measurement presented in this work and from FERMI experiment (The Fermi LAT Collaboration et al. 2010). For the FERMI analysis, extragalactic regions ($b > 10^\circ$) and a $20^\circ \times 20^\circ$ square around the GC were used. A power-law function with an index of -2.7 (spectral shape of galactic CRs) is plotted to guide the eye.

Moreover, the possibility to obtain a background-subtracted spectrum allows one to put upper limits on the velocity-averaged annihilation cross-section $\langle\sigma v\rangle$, using a generic parameterization of the γ -ray spectrum (Tasitsiomi & Olinto 2002), created by secondary particles (neutral mesons) in DM annihilations. For the DM density distribution the Einasto and the NFW profiles were used, which describe best the smooth DM component obtained in recent N-body simulations by Springel et al. (2008) and Diemand et al. (2008), respectively, normalized to the local density of $0.39 \text{ GeV}/\text{cm}^3$. A comparison of the sensitivity of the measurement, presented here, with most sensitive measurements published to date by H.E.S.S. shows, that only the results from the Sgr Dwarf Galaxy have a comparable sensitivity, if a cored profile, providing higher densities at the center, is assumed for the DM distribution in Sgr Dwarf (see Fig. 4.26). Thus the current measurement is the most sensitive upper limit on $\langle\sigma v\rangle$ obtained by a IACT experiment to date, especially concerning the usage of the shallower and more realistic Einasto-profile as the DM density distribution.

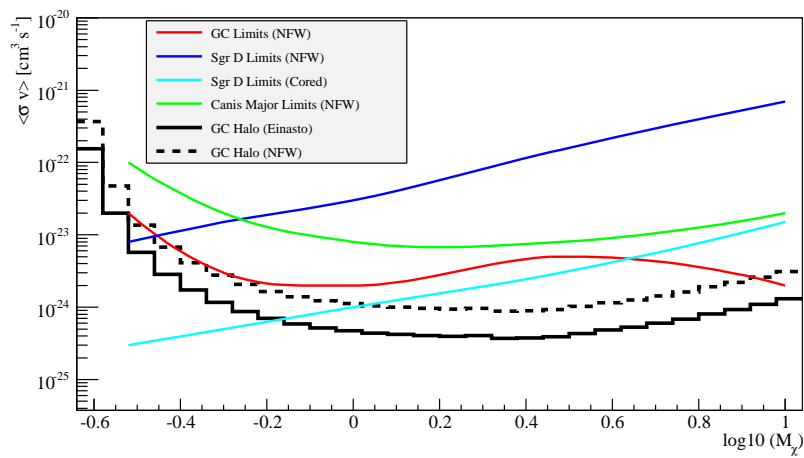


Figure 4.26: Upper limits on the velocity-averaged annihilation cross-section $\langle\sigma v\rangle$ of DM particles at 95% conf. level, obtained for the data from the GC halo with the current analysis (black line), in comparison with other upper limits obtained by with H.E.S.S.. While for this work both the Einasto and the NFW density profiles were assumed, other upper limits were obtained using either the NFW profile or an isothermal cored profile (for Sgr Dwarf), which provide a higher density for the very central region of a galaxy. Thus the measurement described in this work is the most sensitive measurement conducted by an IACT instrument to date, in particular using the Einasto profile. See text for further discussion.

5 Summary and outlook

In this work detailed studies of the very high-energy γ -ray data from the GC region were performed. These were possible thanks to the deep exposure of this region, achieved by the H.E.S.S. experiment throughout the last years. In the first part of this thesis, new analysis methods were developed and applied in order to study the morphological and spectral properties of the diffuse emission in the GC region. The diffuse emission is assumed to originate from interactions of highly energetic hadrons, which were accelerated at a central source and subsequently diffused to the ambient space, with the matter bound in local GMCs. The H.E.S.S. observations allow the first measurement where the propagation of hadronic CRs can be directly observed, and the study of the emerging radiation allows to directly measure the diffusion parameters. The result of the diffuse emission analysis, described in chapter 3, is the so far most limiting restriction of the parameter space of diffusion for multi-TeV hadronic CRs in the GC region. Further improvement on the understanding of CR diffusion in this region can be expected from observations of the CTA experiment, a currently planned large array of Cherenkov telescopes (Wagner et al. 2009), due to its superior angular resolution, energy coverage and sensitivity.

In the second part of this work a search for signals of DM annihilations in the data from the GC region was performed, where the largest density of Galactic DM is presumed. DM annihilations can manifest themselves both in a featureless, continuum spectrum of γ -rays as well as in γ -ray line signals, suggested by several theoretical models. New analysis methods were developed in order to search for spectral signatures in H.E.S.S. data, including a procedure to subtract background originating from γ -ray-like hadrons. The application of these methods to the H.E.S.S. data, described in chapter 4, result in so far best upper limits on the flux from spectral line features in the TeV range. Moreover, assuming a continuum γ -ray spectrum from DM annihilations, upper-limits on the total DM annihilation cross-section were derived. These upper-limits are the best so far derived from very high-energy γ -ray data, for the Einasto profile used to describe the DM density distribution. For the future, more sensitive DM measurements in the TeV range can again be expected from observations of the CTA experiment. For the mass of DM particle below 100 GeV, the data of the currently operating FERMI observatory (Atwood et al. 2009) will improve the existing limits for this particular energy range.

A Supplementary information for the diffuse emission analysis

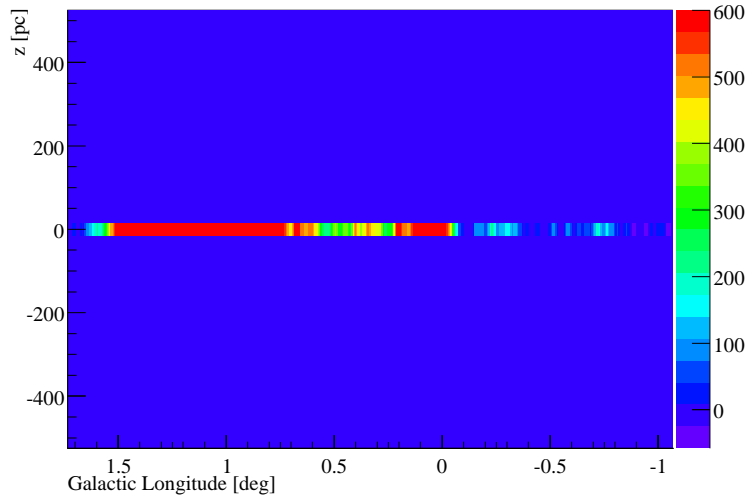
A.1 Supplementary figures and tables

	Ring 1.0°	Ring 1.2°	Ring 1.4°	Template
Number of excess events before point subtraction	2826.1	2797.9	2789.1	2938.09
Number of excess events after point subtraction	2014.7	2052.9	1966.77	2195.8

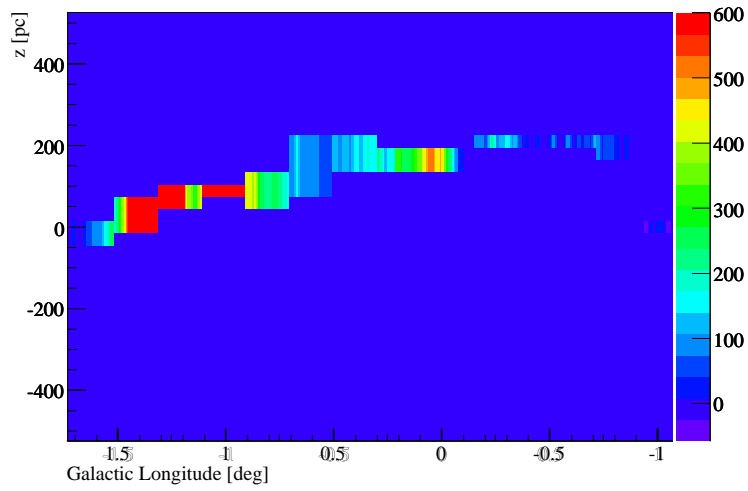
Table A.1: Summarized statistics referring to the region of the diffuse emission for the analysis of the low energy band $0.35 \text{ TeV} < E < 0.6 \text{ TeV}$, before and after point source subtraction, using different configurations of background methods. The number of excess events of the diffuse emission region was calculated for $-1.07 < l < 1.65$ and $-0.31 < b < 0.33$.

	Ring 1.0°	Ring 1.2°	Ring 1.4°	Template
Number of excess events before point subtraction	2553.5	2586.0	2605.75	2620.35
Number of excess events after point subtraction	1706.97	1769.9	1820.44	1829.39

Table A.2: Summarized statistics referring to the region of the diffuse emission for the analysis of the low energy band $2.55 \text{ TeV} < E < 100 \text{ TeV}$, before and after point source subtraction, using different configurations of background methods. The number of excess events of the diffuse emission region was calculated for $-1.07 < l < 1.65$ and $-0.31 < b < 0.33$.



(a) Face-on distribution of MCs in the velocity band between 80 km/s and 120 km/s before expansion to 3-D.



(b) Face-on distribution of MCs in the velocity band between 80 km/s and 120 km/s after expansion to 3-D.

Figure A.1: Example for moving the MCs in the GC region according to the face-on velocity map obtained in (Sawada et al. 2004).

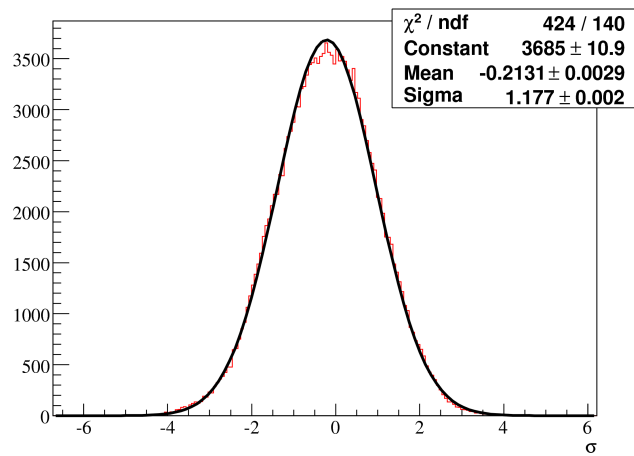


Figure A.2: Distribution of significance taken from bins outside the exclusion regions for the ring-method, using a ring radius of 1.2° . The Gaussian fit yields a slight shift towards negative values $\mu = -0.23 \pm 0.01$ and a larger width $\sigma = 1.17$, than expected from a normal distribution. These effects can be explained due to the size and the shape of the exclusion regions.

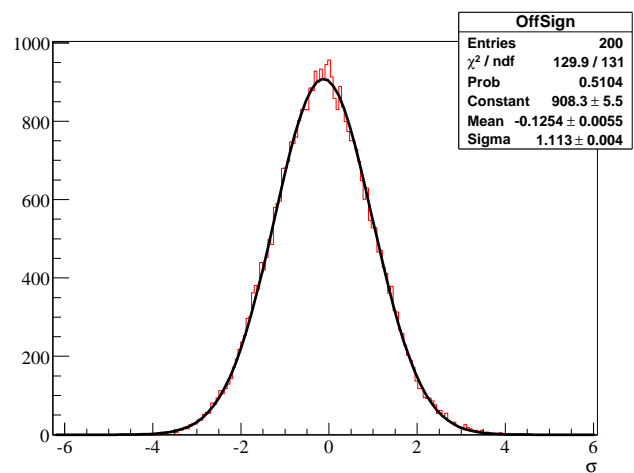


Figure A.3: Distribution of significance taken from bins outside the exclusion regions for the analysis of the low energy band. The Gaussian fit yields a slight shift towards negative values $\mu = -0.23 \pm 0.01$ and larger width than expected $\sigma = 1.11$. However, these values are even better than for the total energy range (see Fig. A.2), thus showing that the acceptance lookup tables, created for this energy band, do not introduce additional systematic effects.

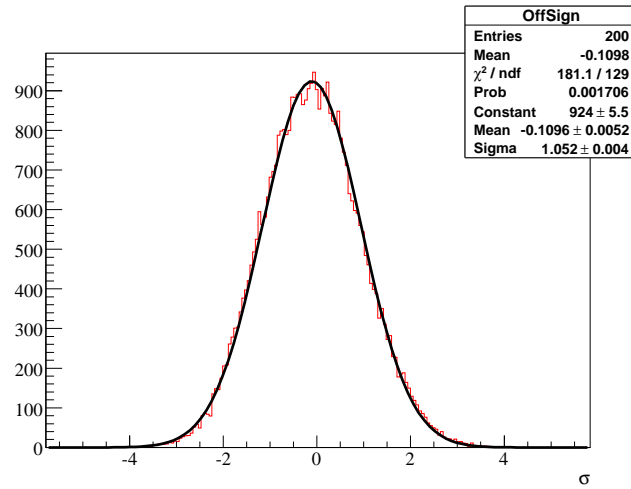


Figure A.4: Distribution of significance taken from bins outside the exclusion regions. The Gaussian fit yields a slight shift towards negative values $\mu = -0.11 \pm 0.01$ and larger width than expected $\sigma = 1.05$. However, these values are even better than for the total energy range (see Fig. A.2), thus showing that the acceptance lookup tables, created for this energy band, do not introduce additional systematic effects

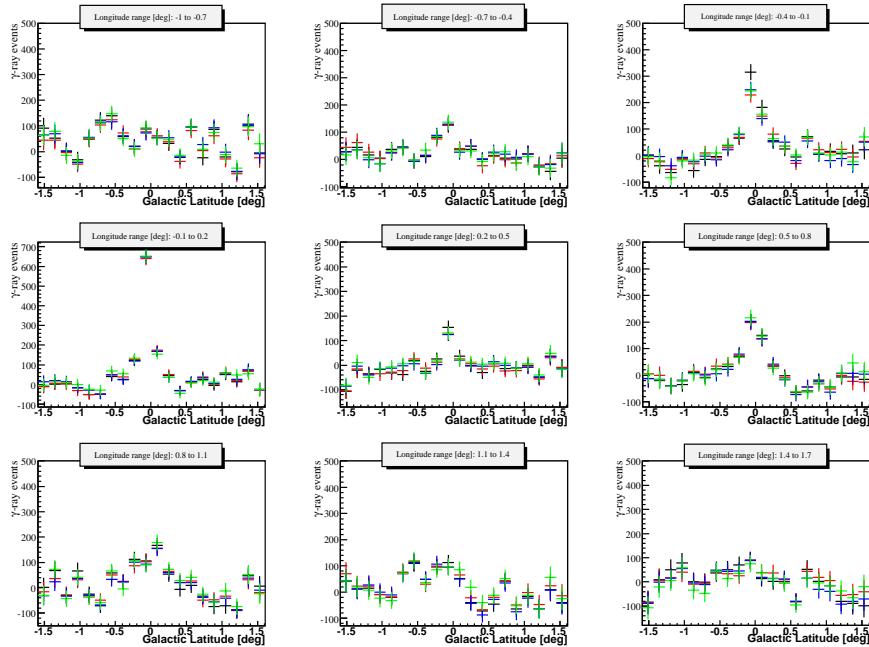


Figure A.5: Latitude profiles of the exposure corrected excess events for the low energy band before source subtraction, obtained for the indicated longitude ranges.

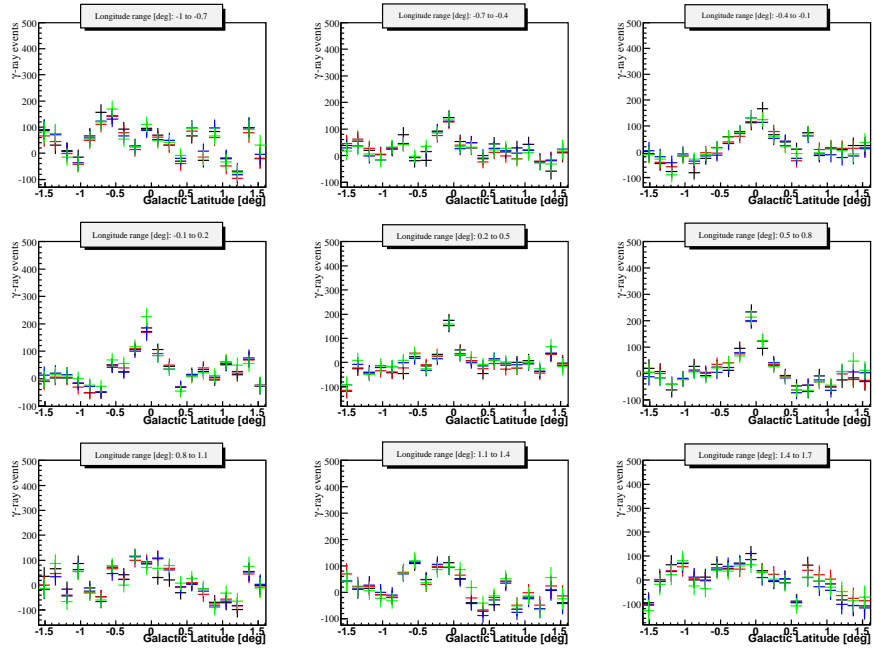


Figure A.6: Latitude profiles of the exposure corrected excess events for the low energy band after source subtraction, obtained for the indicated longitude ranges.

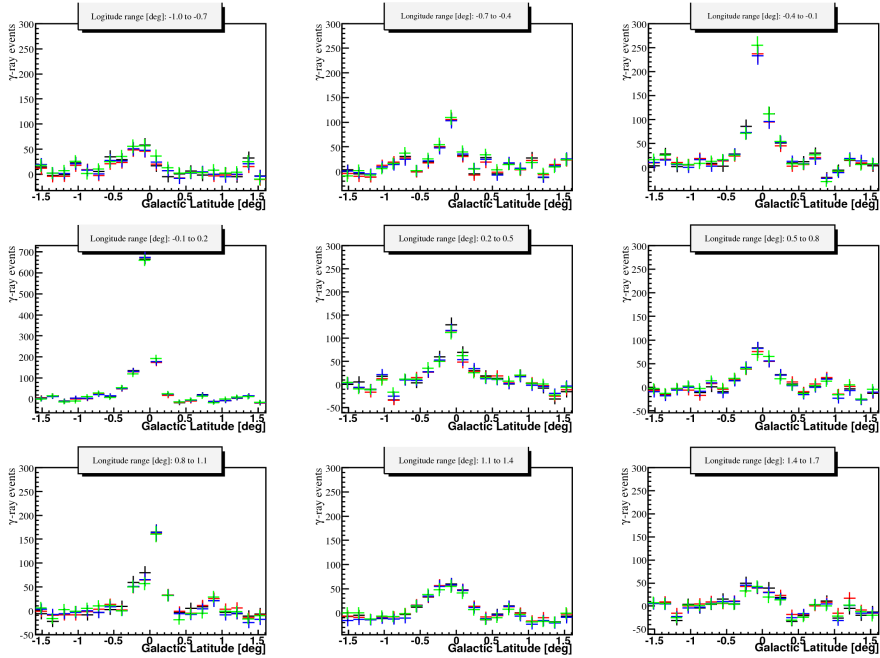


Figure A.7: Latitude profiles of the exposure corrected excess events for the high energy band before source subtraction, obtained for the indicated longitude ranges.

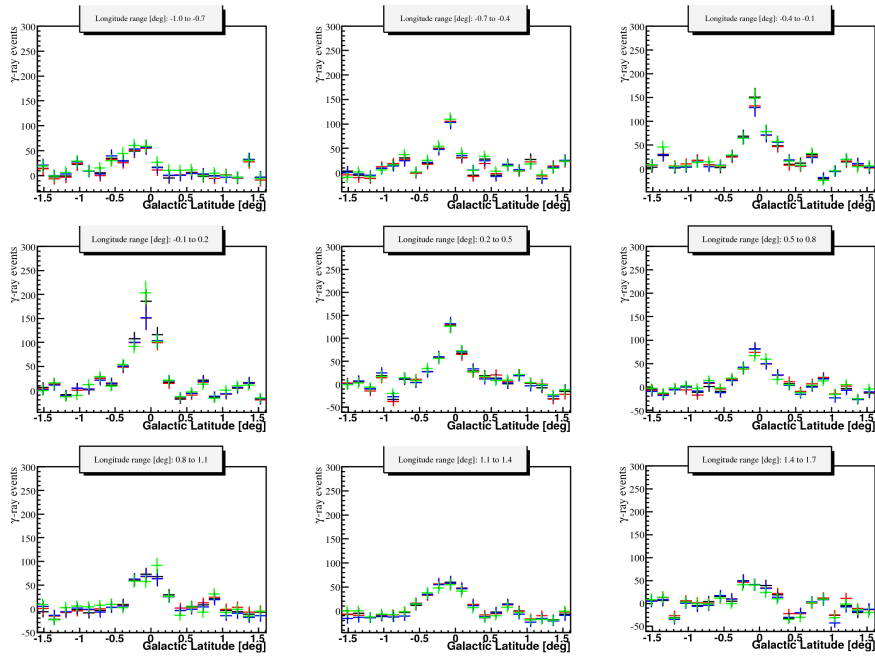


Figure A.8: Latitude profiles of the exposure corrected excess events for the high energy band after source subtraction, obtained for the indicated longitude ranges.

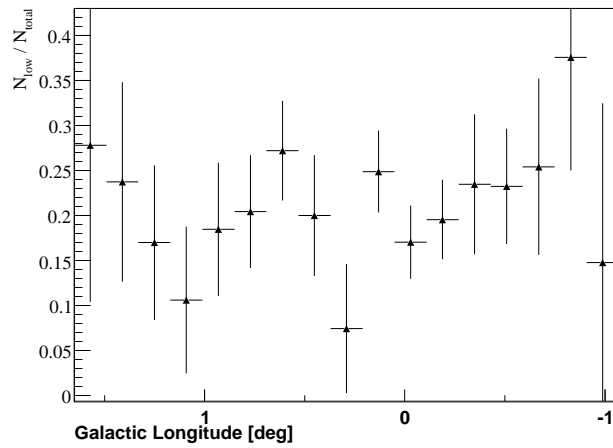


Figure A.9: Ratio between longitude excess profiles for the low energy band (see Fig. 3.10) and the total profile (see Fig. 3.27).

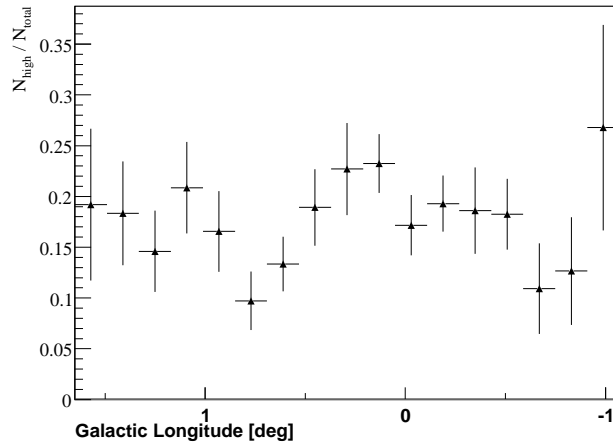


Figure A.10: Ratio between longitude excess profiles for the high energy band (see Fig. 3.10) and the total profile (see Fig. 3.27).

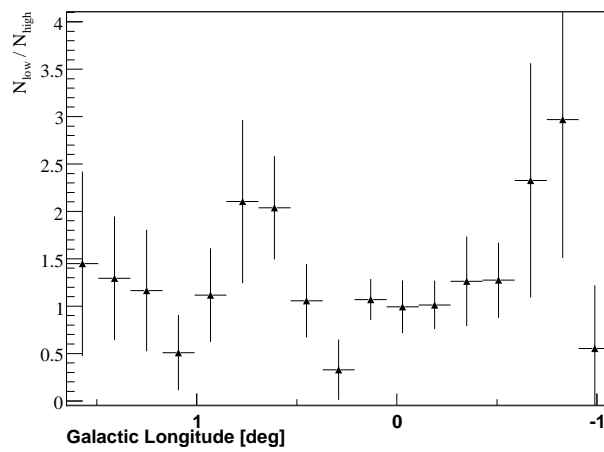


Figure A.11: Ratio between longitude excess profiles for the low and high energy bands (see Fig. 3.27).

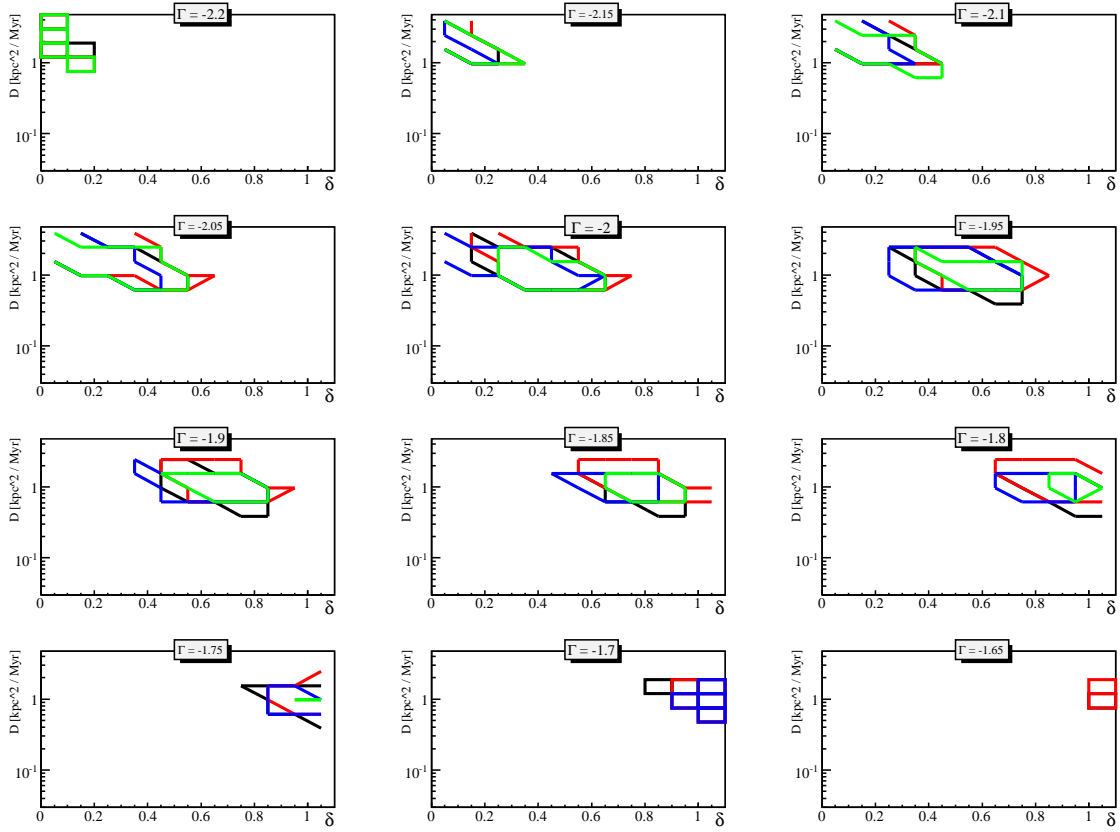


Figure A.12: Allowed regions obtained with all scan methods of the diffusion parameter space for the 2-D model for every configuration of background subtractions. Color code: Ring 1.0° : red, Ring 1.2° : black, Ring 1.4° : blue, Template: green. For illustration reasons, in some plots contours of the overall regions are replaced by contours of individual bins, that lie inside the allowed parameter space. All configurations yield similar allowed regions, no obvious systematic trends are visible (see also Fig. 3.10 and Fig. 3.27).

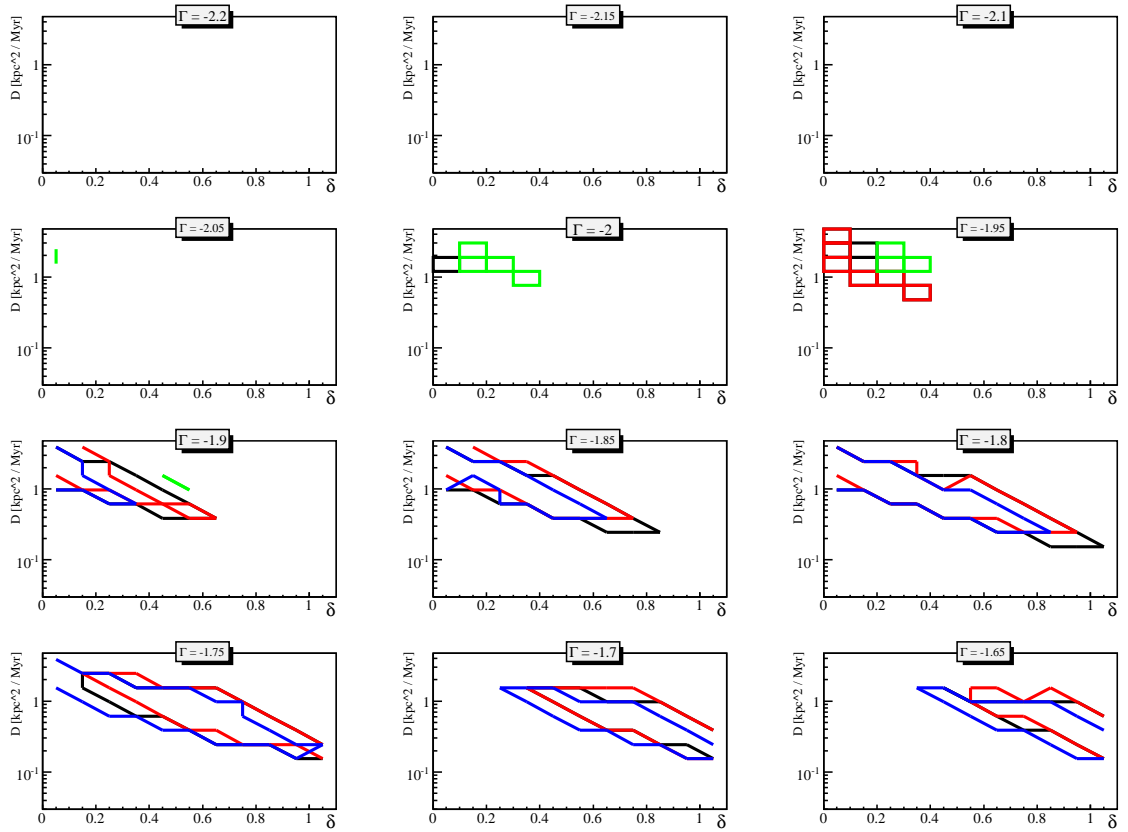


Figure A.13: Allowed regions obtained with all scan methods of the diffusion parameter space for the 3-D model for every configuration of background subtractions. Color code: Ring 1.0° : red, Ring 1.2° : black, Ring 1.4° : blue, Template: green. For illustration reasons, in some plots contours of the overall regions are replaced by contours of individual bins, that lie inside the allowed parameter space. All configurations yield similar allowed regions, no obvious systematic trends are visible (see also Fig. 3.10 and Fig. 3.27).

Γ_p	δ										
	0	0.1	0.2	0.3	0.4	0.5	0.6	0.7	0.8	0.9	1
$\Gamma_p = -2.2$	1.19 .. 1.89	1.19 .. 1.89	—	—	—	—	—	—	—	—	—
$\Gamma_p = -2.15$	—	0.754 .. 3	0.754 .. 1.89	—	—	—	—	—	—	—	—
$\Gamma_p = -2.1$	—	—	0.754 .. 3	0.754 .. 1.89	0.754 .. 1.19	—	—	—	—	—	—
$\Gamma_p = -2.05$	—	—	0.754 .. 3	0.475 .. 3	0.475 .. 1.89	0.475 .. 1.19	—	—	—	—	—
$\Gamma_p = -2$	—	—	0.754 .. 3	0.475 .. 3	0.475 .. 3	0.475 .. 1.89	0.475 .. 1.19	—	—	—	—
$\Gamma_p = -1.95$	—	—	1.89 .. 3	0.754 .. 3	0.475 .. 3	0.475 .. 3	0.3 .. 1.89	0.3 .. 1.19	—	—	—
$\Gamma_p = -1.9$	—	—	—	—	0.754 .. 3	0.475 .. 3	0.475 .. 1.89	0.3 .. 1.89	0.3 .. 1.19	—	—
$\Gamma_p = -1.85$	—	—	—	—	—	1.19 .. 1.89	0.475 .. 1.89	0.475 .. 1.89	0.3 .. 1.89	0.3 .. 1.19	—
$\Gamma_p = -1.8$	—	—	—	—	—	—	1.19 .. 1.89	0.754 .. 1.89	0.475 .. 1.89	0.3 .. 1.89	0.3 .. 1.19
$\Gamma_p = -1.75$	—	—	—	—	—	—	—	1.19 .. 1.89	0.475 .. 1.89	0.475 .. 1.89	0.3 .. 1.89
$\Gamma_p = -1.7$	—	—	—	—	—	—	—	—	1.19 .. 1.89	0.754 .. 1.89	0.475 .. 1.89
$\Gamma_p = -1.65$	—	—	—	—	—	—	—	—	—	—	0.754 .. 1.19

Table A.3: Allowed diffusion coefficients (at 95% confidence level) D_0 in $\frac{\text{kpc}^2}{\text{Myr}}$ as a function of initial spectral index Γ_p and the energy-dependence δ .

Γ_p	δ										
	0	0.1	0.2	0.3	0.4	0.5	0.6	0.7	0.8	0.9	1
$\Gamma_p = -2.2$	—	—	—	—	—	—	—	—	—	—	—
$\Gamma_p = -2.15$	—	—	—	—	—	—	—	—	—	—	—
$\Gamma_p = -2.1$	—	—	—	—	—	—	—	—	—	—	—
$\Gamma_p = -2.05$	—	—	—	—	—	—	—	—	—	—	—
$\Gamma_p = -2$	1.19 .. 1.89	—	—	—	—	—	—	—	—	—	—
$\Gamma_p = -1.95$	—	0.75 .. 3	0.75 .. 1.19	0.47 .. 0.75	—	—	—	—	—	—	—
$\Gamma_p = -1.9$	—	0.75 .. 3	0.47 .. 3	0.47 .. 1.89	0.3 .. 1.19	0.3 .. 0.75	0.3 .. 0.475	—	—	—	—
$\Gamma_p = -1.85$	—	0.75 .. 3	0.47 .. 3	0.47 .. 1.89	0.3 .. 1.89	0.3 .. 1.19	0.19 .. 0.754	0.19 .. 0.47	0.19 .. 0.3	—	—
$\Gamma_p = -1.8$	—	0.75 .. 3	0.47 .. 3	0.47 .. 1.89	0.3 .. 1.89	0.3 .. 1.89	0.19 .. 1.19	0.19 .. 0.75	0.12 .. 0.47	0.12 .. 0.3	0.12 .. 0.19
$\Gamma_p = -1.75$	—	1.19 .. 3	0.75 .. 3	0.47 .. 1.89	0.47 .. 1.89	0.3 .. 1.89	0.19 .. 1.89	0.19 .. 1.19	0.19 .. 0.75	0.12 .. 0.47	0.12 .. 0.3
$\Gamma_p = -1.7$	—	—	—	1.19 .. 1.89	0.75 .. 1.89	0.47 .. 1.89	0.3 .. 1.19	0.3 .. 1.19	0.19 .. 1.19	0.19 .. 0.75	0.12 .. 0.47
$\Gamma_p = -1.65$	—	—	—	—	1.19 .. 1.89	0.75 .. 1.19	0.47 .. 1.19	0.3 .. 1.19	0.3 .. 1.19	0.19 .. 1.19	0.12 .. 0.75

Table A.4: Allowed diffusion coefficients (at 95% confidence level) D_0 in $\frac{\text{kpc}^2}{\text{Myr}}$ as a function of initial spectral index Γ_p and the energy-dependence δ .

A.2 Standard spectral analysis

In Sec. 2.3.6 it was described how spectra of γ -ray sources are derived by the H.E.S.S. experiment. From the number of excess events within the source region it is possible to calculate corresponding (differential) flux values by using those effective areas, which are valid for the particular analysis, and fit the spectral points with a function, e.g. a power law. In this way one obtains the spectrum of the whole source region. If one is interested in studying a possible energy-dependent morphology of a source, this source is divided into smaller regions most suitable for the effect that is expected to show up, and spectra are derived for each of these regions (see Berge (2006), The H. E. S. S Collaboration: S. Funk et al. (2007)). In the case of diffuse emission, the expected effect due to a possible energy-dependence of the diffusion is a spectral hardening with increasing distance from the GC source (see Fig. 3.2), if $\delta > 0$. In this case, it seems appropriate to divide the area of the diffuse emission into, as far as possible, equally sized rectangles aligned along the galactic plane (see Fig. A.14). However, this is not possible for regions containing HESS J1745–290 and G0.9 + 0.1, here two smaller squares are positioned around both point sources.

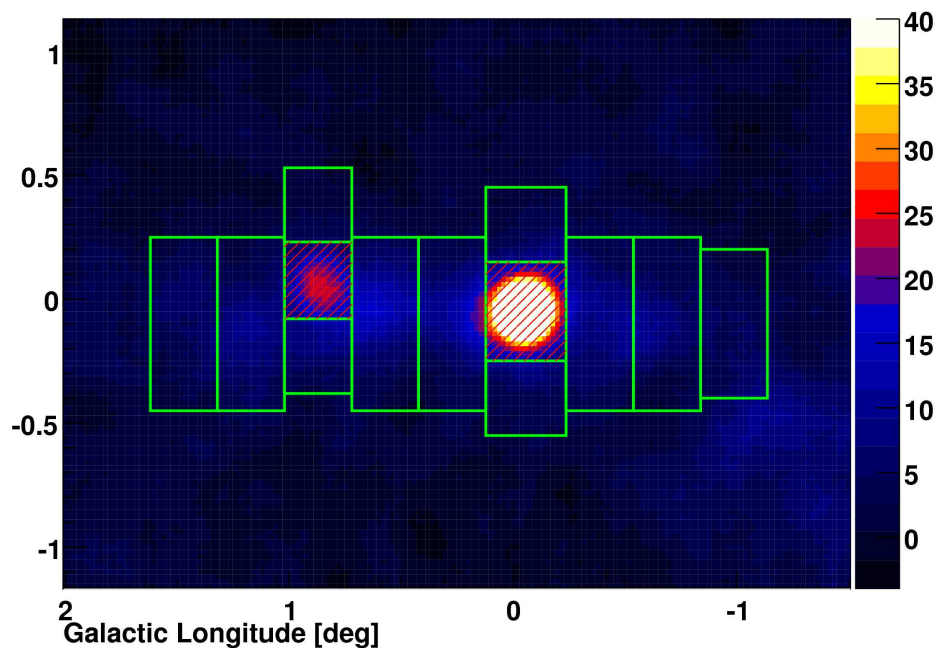


Figure A.14: Significance map of the GC area divided into smaller regions selected for determination of spectral parameters. Both point sources HESS J1745–290 and G0.9 + 0.1 are not included in the spectral analysis, as indicated by the red-dashed areas.

For the standard spectral analysis the background subtraction is done by using the reflected-method (see Sec. 2.3.4), which has the advantage that off-regions are selected such that they have the same detector acceptance as the on-region, thus rendering the use of the same

set of effective areas possible. It is worth mentioning, that for every particular on-region, off-regions have to be determined for every run separately, and given the large exclusions regions in the field of view, not for every run adequate off-regions could be found, resulting in different number of processed runs for various regions, see Tab. A.5.

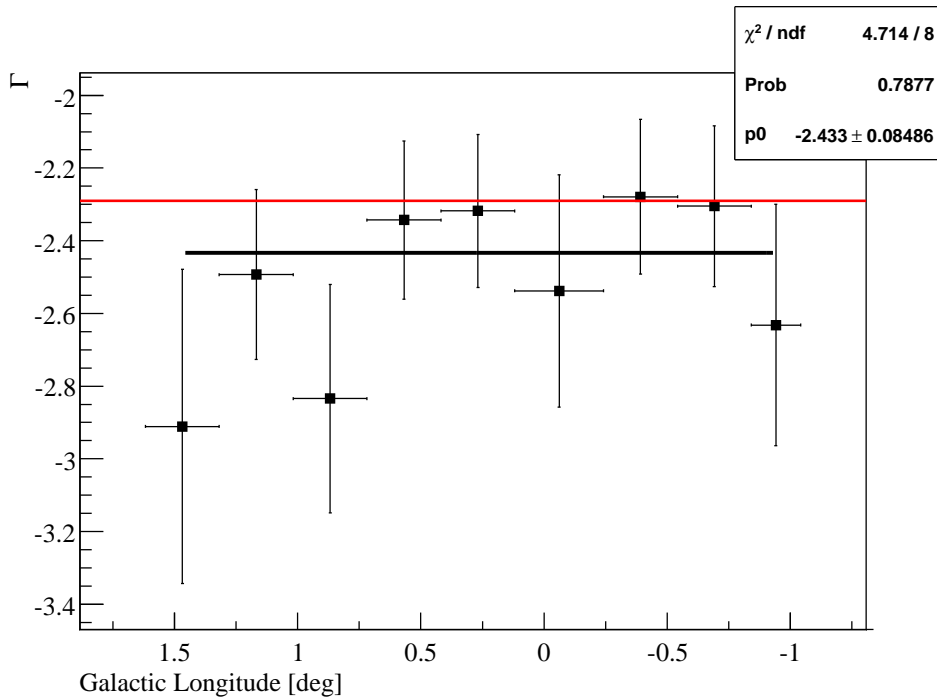


Figure A.15: Distribution of spectral indices obtained by power-law fits of the spectra of the regions defined in Fig. A.14. The errors on position indicate the width of the corresponding regions. The errors on the spectral index Γ stem from the statistical error obtained from the fit and a systematic error of $\Delta\Gamma = 0.2$. The red line corresponds to the index of $\Gamma = -2.29$, which was obtained in (nat), while the black line corresponds to a constant fit to new results and yield $\Gamma = -2.43 \pm 0.08$.

In the same table spectral properties of the selected regions are summarized. These are obtained by fitting a power law function to the γ -spectrum of the particular region. Despite the large dataset the significance of some regions is very low, once again emphasizing the fact that this analysis deals with a very faint emission. The low statistics consequently affects the determination of the spectral parameters Φ_0 and Γ , resulting in large uncertainties. In Fig. A.15, spectral indices from Tab. A.5 are plotted as a function of the longitude coordinate of the corresponding regions. The systematic error of $\Delta\Gamma = 0.2$ is included. One observes that overall, the spectra tend to be steeper than the one published in (Aharonian et al. 2006d). Fitting the indices distribution with a constant yields $\Gamma = -2.43 \pm 0.08$, thus being consistent with the previous result within 2σ .

The distribution of spectral indices can as well be used for a scan of the parameter space of diffusion. This is done by determination of predicted Γ -distributions (using the same regions as for the data analysis) from the 2-D diffusion model and their comparison to the

data by means of a χ^2 -test, see Fig. A.17. The spectral indices are determined by calculating the slope between the logarithmic spectral points at $E = 0.5$ TeV and $E = 5$ TeV: $\Gamma = \log_{10}(\Phi(5 \text{ TeV})) - \log_{10}(\Phi(0.5 \text{ TeV}))$. The normalisation of the model is not affecting the spectral index and therefore does not play a role, so the number of free parameters is 3. The 95% confidence region is defined by $\chi^2 \leq \chi_{min}^2 + 7.82$. One can see that unlike the scan described in Sec. 3.2.2, it is possible to restrict the allowed values of δ for a given initial spectral index Γ (mainly for $-2.5 \leq \Gamma \leq -2.25$), hence it is indeed possible to constrain these parameters by using spectral information. Besides, an interesting systematic effect reveals for this index range, showing up as a non-smooth shape of allowed parameter region in the transition between $\delta = 0.1$ and $\delta = 0$. The fact that $\delta = 0$ is preferred can already be seen by eye in Fig. A.15, since for $\delta > 0$ a spectral hardening is expected towards the outer regions of the emission, whereas one rather observes a slight softening, which is however statistically not significant.

Despite the apparent constraining power from the current scan, addressing the aspect of a possible energy-dependent morphology based on the results presented in Fig. A.15 appears problematic mainly because of two reasons. First of all, for some regions about 25% of available data is not used because for these runs no suited off-regions were found. Additionally, a possible correlation between fitted index and normalisation (see Fig. A.16) could be due to a systematic effect of the fit procedure, given the fact that the flux measured around point sources is not intrinsically low but is affected by the exclusion of the point source regions. Finally, the most important point is that the point source regions are not taken into account, while primarily the region of HESS J1745–290 contributes a significant fraction to the overall flux of the diffuse emission (see Fig. 3.10). This fact is believed to be at least partly responsible for the observed shape of allowed parameter region for $\delta = 0$ and $-2.5 \leq \Gamma \leq -2.2$. An inclusion of these regions in the analysis would require their spectra to be fitted simultaneously by contributions of point sources and the diffuse component, which is obviously non-trivial if all spectral parameters are left free.

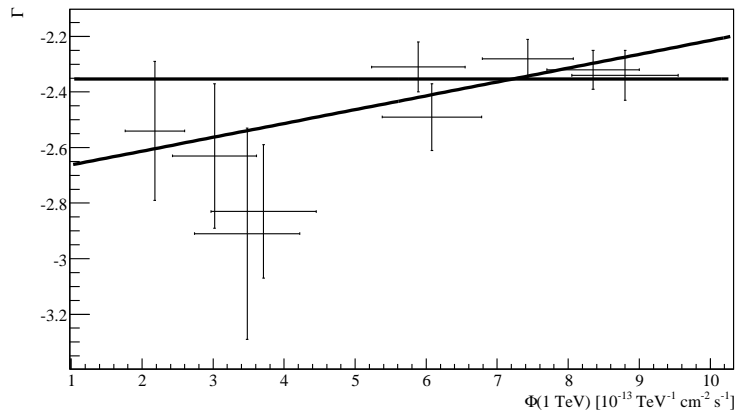


Figure A.16: Distribution of spectral index values Γ vs. flux normalisation Φ_0 obtained for the regions of spectral analysis. There is a hint that regions with lower fluxes tend to have steeper spectra, which is based on the results from the constant and linear fits, yielding $\chi^2/\text{NDF} = 10.7/8$ and $\chi^2/\text{NDF} = 6.0/7$, respectively. This might be due to some physical effect or a systematic problem of spectrum reconstruction. Further discussion in the text.

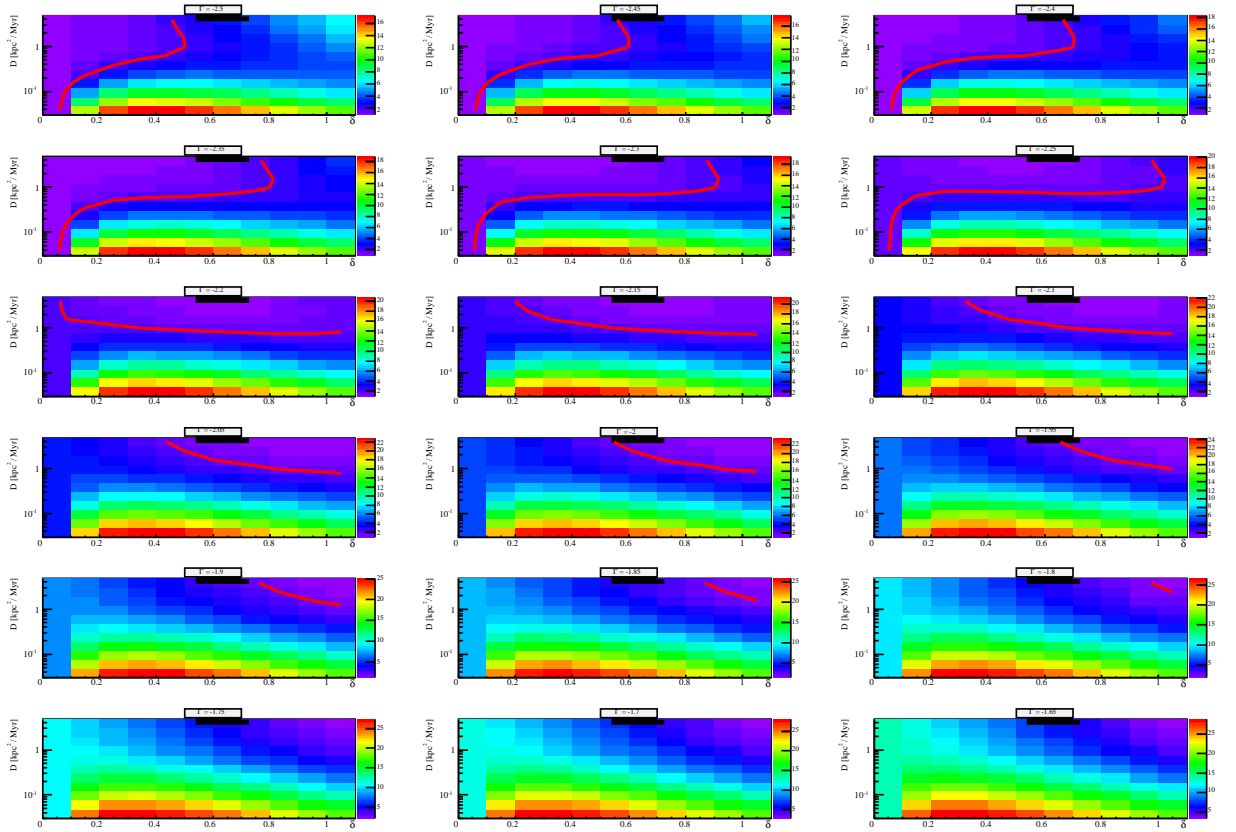


Figure A.17: Scan of the parameter space of diffusion done by comparison of predicted index distribution from the diffusion model with the results from the data (Fig. A.15). Simulated spectral slopes were determined within the same regions as adopted for the data analysis (Fig. A.14) by using spectral points at $E = 0.5$ TeV and $E = 5$ TeV. The reduced χ^2 is plotted as a function of (D, δ, Γ) . The black line denotes the 95% confidence regions (see text). The minimum χ^2 -value $\chi^2_{min} = 0.36$ is obtained for $D = 0.03 \frac{\text{kpc}^2}{\text{Myr}}$ (for $t = 10^4$ yr), $\Gamma = -2.45$ and $\delta = 0$.

	Regions								
	1	2	3	4	5	6	7	8	9
Number of processed runs	326	316	231	244	248	306	252	251	252
Number of OnEvents	4618	5468	3191	5135	5663	3284	5521	4858	2420
Number of OffEvents	31474	30900	20308	16751	13523	12513	18608	22234	20360
α	0.13	0.15	0.14	0.25	0.35	0.24	0.25	0.19	0.10
Number of excess events	443.10	789.0	299.2	927.2	996.7	272.3	898.9	688.9	290.7
Significance [σ]	6.32	10.43	5.11	12.26	12.06	4.38	11.41	9.49	5.85
Significance per $\sqrt{\text{hour}}$	0.54	0.90	0.52	1.21	1.18	0.38	1.11	0.92	0.57
Γ	-2.91 ± 0.38	-2.49 ± 0.12	-2.83 ± 0.24	-2.34 ± 0.09	-2.32 ± 0.07	-2.54 ± 0.25	-2.28 ± 0.07	-2.31 ± 0.09	-2.63 ± 0.26
Φ_0 [$10^{-13}\text{TeV}^{-1}\text{cm}^{-2}\text{s}^{-1}$]	3.48 ± 0.74	6.08 ± 0.70	3.71 ± 0.74	8.80 ± 0.75	8.35 ± 0.65	2.18 ± 0.42	7.43 ± 0.64	5.89 ± 0.66	3.02 ± 0.59

Table A.5: Statistical and spectral results from the analyses of a set of regions covering the diffuse emission in the GC area (see Fig. A.14). One notices that for most of the chosen regions approximately 25% of runs could not be used due to a lack of suitable OffRegions. Regions 3 and 6, being located above and below the point sources HESS J1745–290 and G0.9 + 0.1 suffer from low statistics.

B Supplementary information for the dark matter analysis

B.1 Supplementary figures

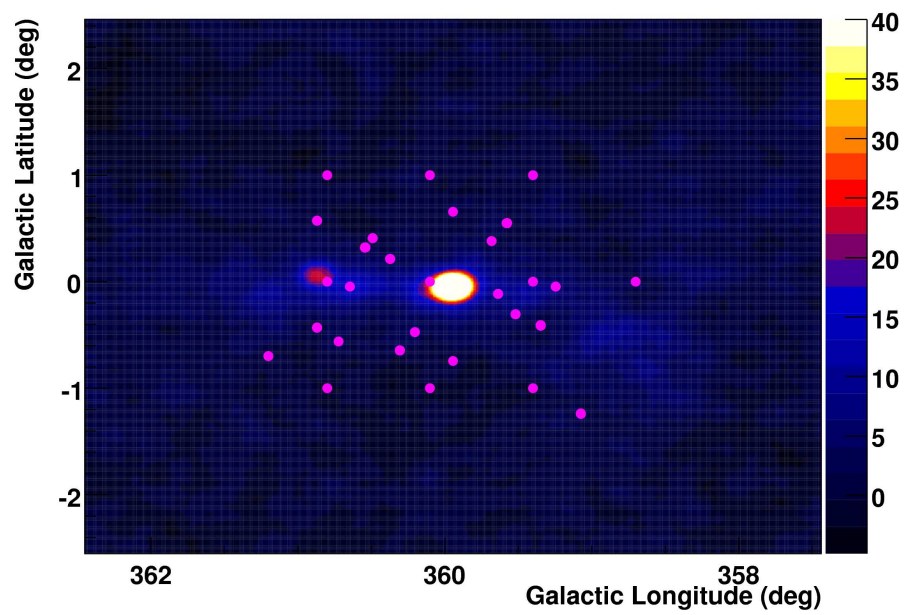
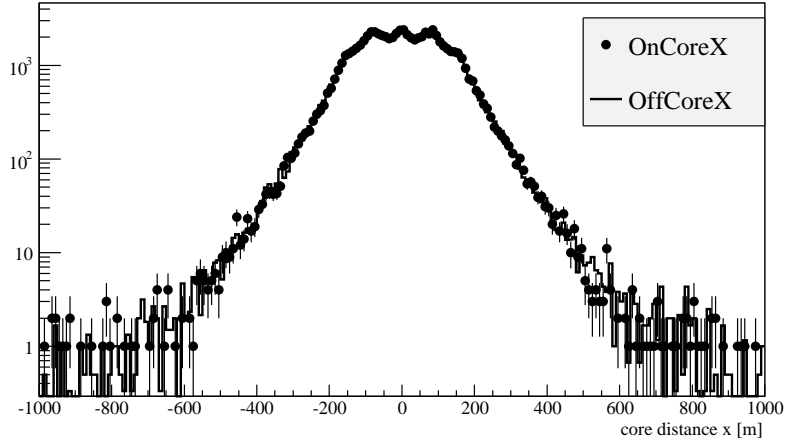
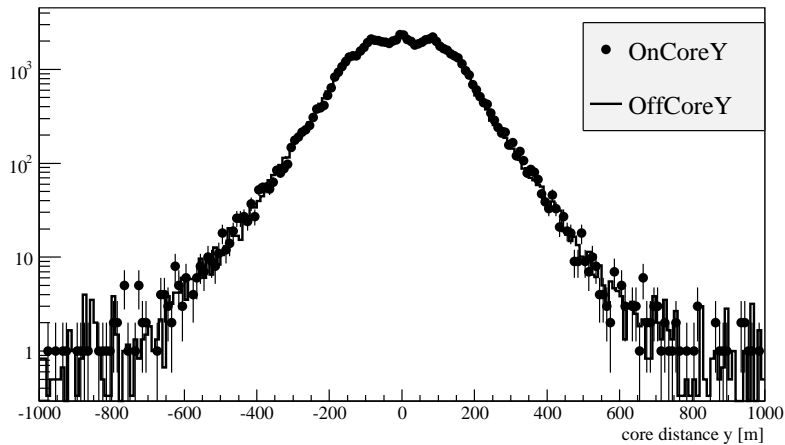


Figure B.1: Map of the GC region with pointing positions of the dataset, used for the diffuse emission and the GC halo analysis, shown as magenta circles.

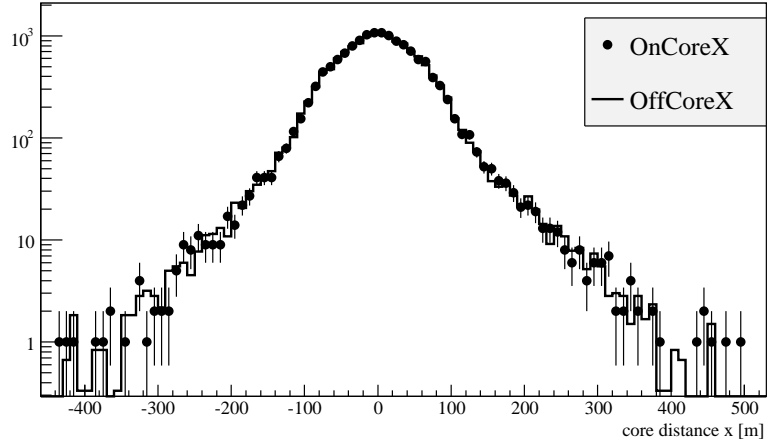


(a) Distribution of the x-projection of the core distance coordinate.

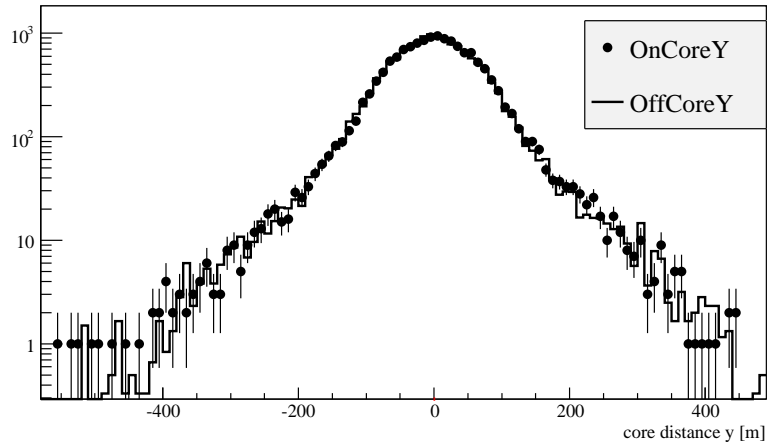


(b) Distribution of the y-projection of the core distance coordinate.

Figure B.2: Distributions of the core distance coordinates for on and off-regions for the all-tel configuration. The core distance, or impact point, is defined as the position of the intersection of the shower axis with the ground. The coordinate system has its origin in the center of the H.E.S.S. array, the x-axis is pointing towards north, while the y-axis points towards west. The core distance is one of the parameters necessary for the energy reconstruction (see Sec. 2.3.3). There is a good agreement between distributions from the on- and off-region. The peaks in the distribution, located close to 0, correspond to the positions of the telescopes, for which there is an increase of triggering events, because in this case the shower directly hits the telescope.

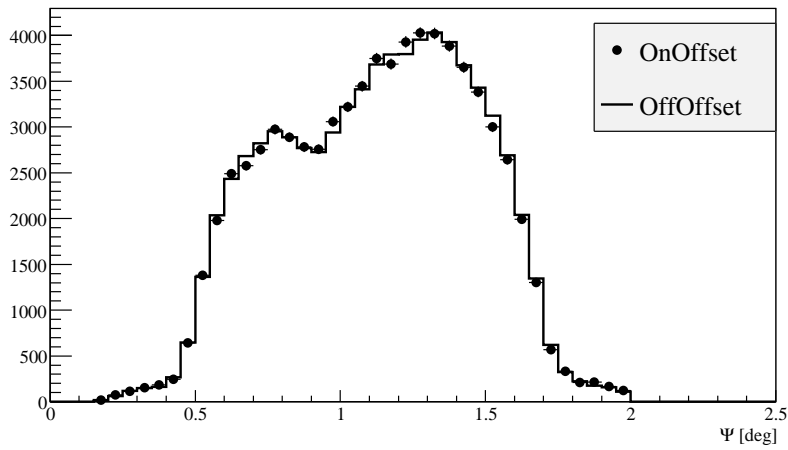


(a) Distribution of the x-projection of the impact point coordinate

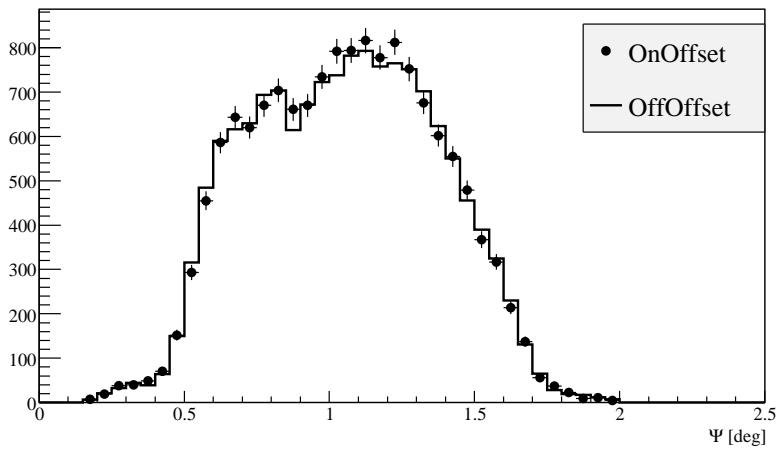


(b) Distribution of the y-projection of the impact point coordinate

Figure B.3: Distributions of the core distance coordinates for on and off-regions for the 4-tel configuration. The core distance, or impact point, is defined as the position of the intersection of the shower axis with the ground. The coordinate system has its origin in the center of the H.E.S.S. array, the x-axis is pointing towards north, while the y-axis points towards west. The core distance is one of the parameters necessary for the energy reconstruction (see Sec. 2.3.3). There is a good agreement between distributions from the on- and off-region. Compared to Fig. B.2, pronounced peaks are not observed at the telescope positions. That means that the peaks for the all-tel configuration are mainly due to 2- and 3-telescope events.



(a) Distribution of offset angles for the all-tel configuration.



(b) Distribution of offset angles for the 4-tel configuration.

Figure B.4: Distributions of the offset angles for on and off-regions for the all-tel (a) and 4-tel (b) configurations. The offset angle is one of the parameters necessary for the energy reconstruction (see Sec. 2.3.3). There is a good agreement between distributions from the on- and off-region for both multiplicity configurations.

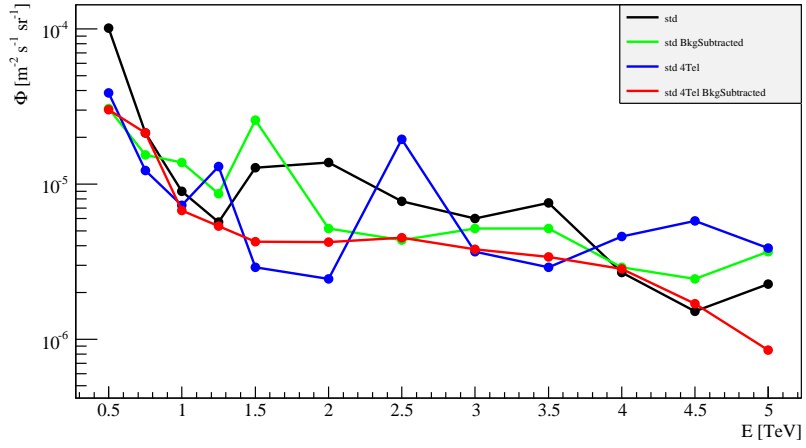


Figure B.5: Upper limits on the flux from a Gaussian signature, assuming 10% energy resolution, for all configurations at 95% conf. level. See Sec. 4.3 for further details.

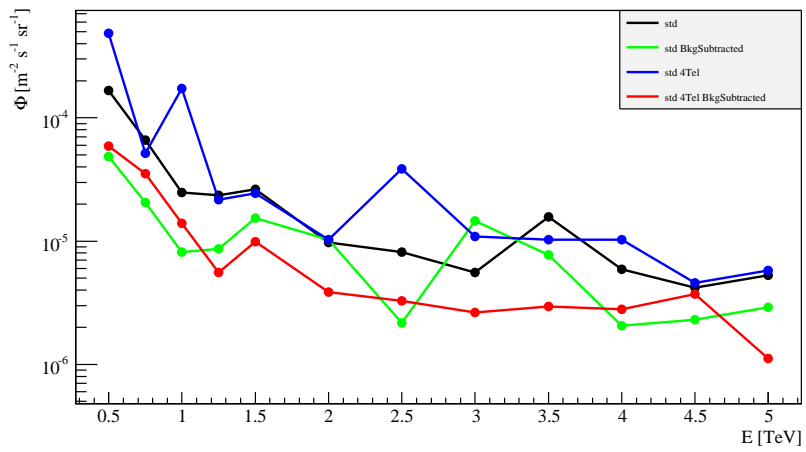


Figure B.6: Upper limits on the flux from a Gaussian signature, assuming 20% energy resolution, for all configurations at 95% conf. level. See Sec. 4.3 for further details.

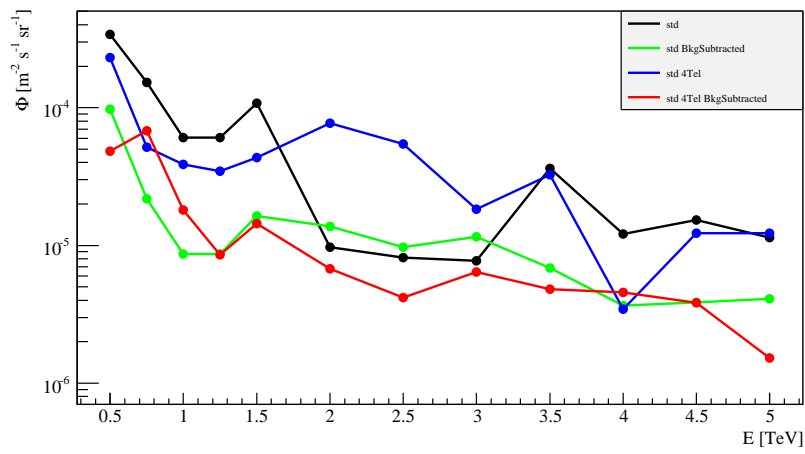


Figure B.7: Upper limits on the flux from a Gaussian signature, assuming 30% energy resolution, for all configurations at 95% conf. level. See Sec. 4.3 for further details.

B.2 Analysis of off-data

In Sec. 4.3 the development of an algorithm, searching for spectral features, and its application to the H.E.S.S. data from the GC halo was described. The GC halo region was used due to the high local DM density and the absence of sources of astrophysical background. Spectral features may arise due to an enhanced annihilation process, in which two DM particles annihilate into two γ -rays or a γ/Z pair (Hisano et al. 2004), or a large contribution of hard internal bremsstrahlung (Bringmann et al. 2008), see Fig. 4.2.

The peak search algorithm can as well be applied to other data. In this section, its application to the off-data is described (see Sec. 4.2.4 for definition). The off-data comprises contributions from mis-identified hadrons as well as a small electron fraction. The contribution of the smooth extragalactic γ -ray component is negligible (Egberts 2009). Since the hadronic background is once again expected to be smooth, spectral features might originate either from intrinsic spectral features of the electron¹ spectrum, like the infamous ATIC peak (Chang et al. 2008), or features of extragalactic γ -rays (Bergström et al. 2001). Since in both cases DM interactions would be at least one of the natural explanations for the occurrence of such spectral feature, its detection or determination of upper limits (like it is done in Sec. 4.3) is interesting from the point of view of searches for DM signals.

	$N_{\text{tel}} \geq 2$	$N_{\text{tel}} = 4$
Number of runs	2903	
Livetime [hr]	1227.2	
Number of events after shape cuts	18691660	1921530
Number of selected events	7798090	595429
Energy threshold [GeV]	282	309
Number of events with $E < 1$ TeV	7107187	507678

Table B.1: Summarized statistics concerning the analysis of the off-data. The much lower number of events with $N_{\text{tel}} = 4$ is due to a low size cut (60 p.e.) for the standard cut configuration, for which many events with lower multiplicity pass the cuts.

The dataset of off-observations comprises 3000 runs, taken from summer 2004 until December of 2007, with a total observation time of 1000 hrs (see Fig. B.8 for the distribution of events in RA-Dec.). Once again, two multiplicity configurations were used: $N_{\text{tel}} \geq 2$ (all-tel) and $N_{\text{tel}} = 4$ (4-tel). No background subtraction is applied, since for the off-analysis, contrary to the GC region, the signal flux is expected to be isotropic. Beside shape cuts, it is again required that the camera offset Ψ is $\Psi < 2$. Regions containing γ -ray sources were excluded (see Tab. B.1). The corresponding spectral distributions for both configurations are shown in Fig. B.9. These distributions were used for the peak search procedure as described in Sec. 4.3. No significant peaks were found, thus upper limits on the flux from Gaussian peaks for various energies were determined at 95% confidence level for both multiplicity configurations. These can be found in Fig. B.10 - B.13. These results are at the same time upper limits on extra-galactic γ -ray signatures, as well

¹ The term electron denotes here both electrons and positrons.

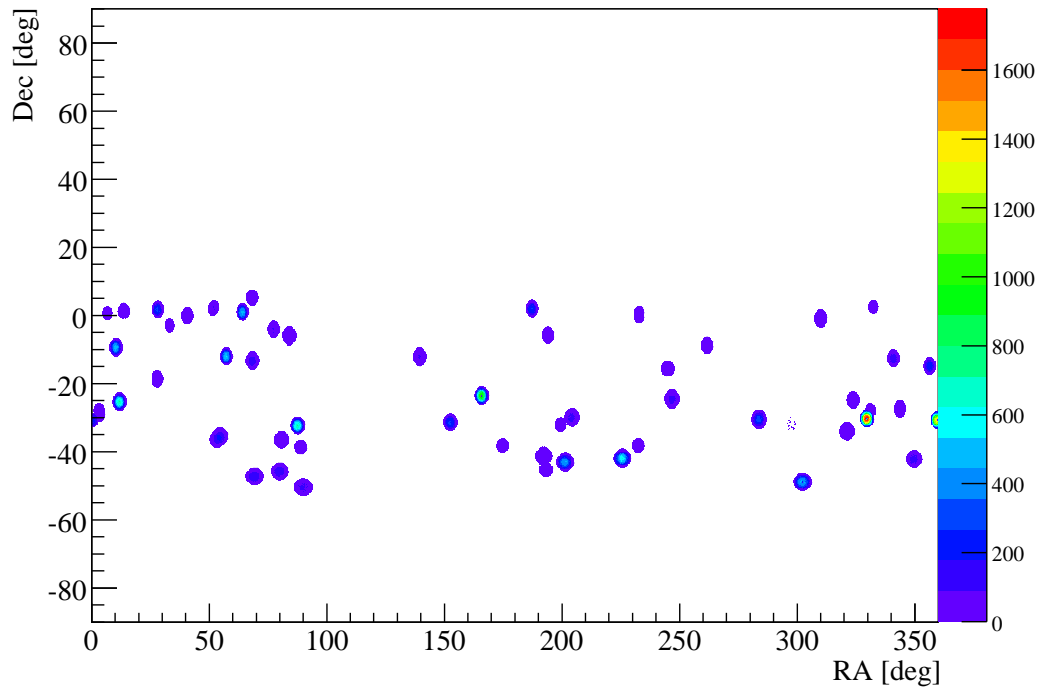


Figure B.8: Distribution of events in RA-Dec, which are used for the off-analysis, indicating the distribution of pointing positions.

as on signatures of the electron spectrum. To take into account systematic uncertainties, for each peak the limits obtained with both configurations are compared and the larger number is used, similar to the estimation of the systematic uncertainties performed in Sec. 4.3.5. Calculated upper limits are also summarized in Tab. B.2. Despite better statistics, the upper limits from the off-analysis are for most energies less sensitive than the results from the GC halo analysis (see Tab. 4.2). This is, on the one hand, due to the lack of possibility of a background subtraction (see Sec. 4.3.4), and on the other hand also possibly due to a worse sensitivity of the `TSpectrum`-algorithm for the off-spectrum due to its steeper shape for $E < 1.5$ TeV. An improvement of the sensitivity might be object of a future work. Nevertheless, a combination of these results with the peak search results obtained by the FERMI experiment (The Fermi LAT Collaboration et al. 2010) is shown in Fig B.14 and represents the most sensitive upper limit on extragalactic peak signatures to date.

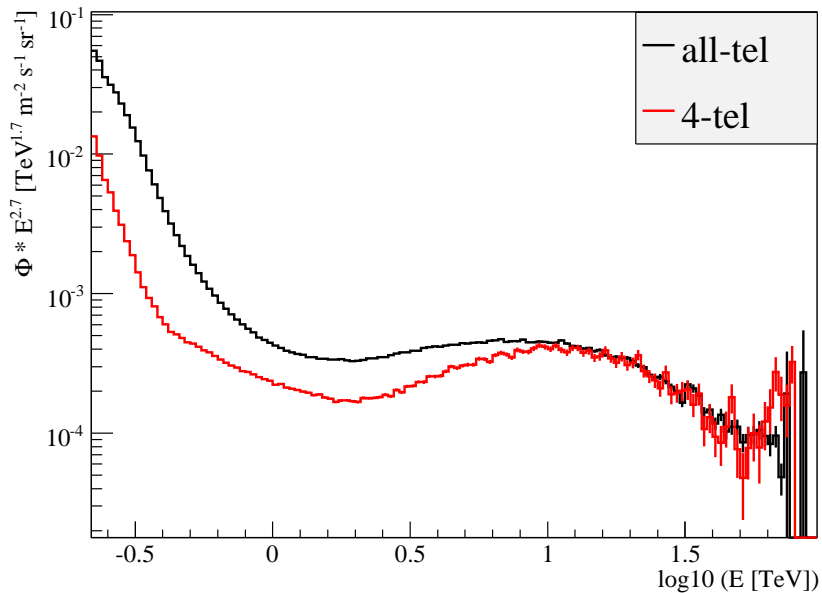


Figure B.9: Spectral distribution of the off-events, shown for both multiplicity configurations. The shape of the distributions is similar to the one obtained for the GC halo analysis. The curvature of both spectra appears more pronounced than for the spectrum of the GC halo (see Fig. 4.9).

Energy [TeV]	$\Phi * 10^{-5} [\text{m}^{-2} \text{s}^{-1} \text{sr}^{-1}]$				
	std all-tel	std 4-tel	$\langle \Phi \rangle$	$\Delta \Phi$	Final: $\langle \Phi \rangle + \Delta \Phi$
0.75	54.6	29	41.8	12.8	54.6
1	19.4	4.6	12	7.39	19.4
1.25	8.18	1.37	4.77	3.4	8.18
1.5	4.1	0.917	2.51	1.59	4.1
2	2.3	0.46	1.38	0.922	2.3
2.5	1.22	0.729	0.976	0.247	1.22
3	0.818	0.325	0.571	0.246	0.818
3.5	0.688	0.259	0.473	0.215	0.688
4	0.345	0.516	0.43	0.0855	0.516
4.5	0.29	0.0729	0.181	0.109	0.29
5	0.23	0.0516	0.141	0.0894	0.23

Table B.2: Upper limits on the flux from Gaussian peaks for the analysis of off-data. The final upper limits are calculated from the mean values and the spreads of the individual measured limits as $\langle \Phi \rangle + \Delta \Phi$.

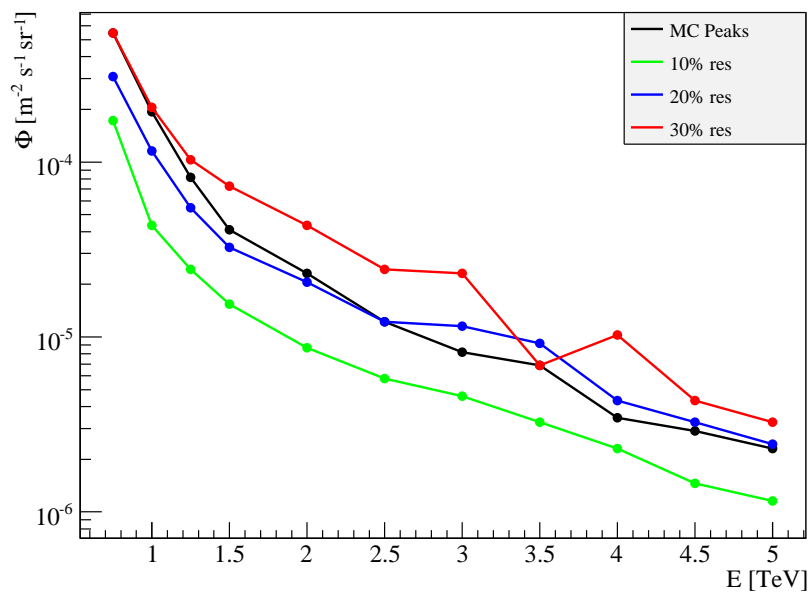


Figure B.10: Upper limits on the flux from a Gaussian signature, obtained from the off-data for the all-tel configuration for MC peaks and different assumed energy resolutions. It is obvious that the sensitivity of the method improves with energy resolution for the most peaks under study. Due to the steep shape of the spectral distribution for energies below 1 TeV, no upper limits could be obtained for $E = 0.5$ TeV for all peak widths except 10%. See Sec. 4.3 for details.

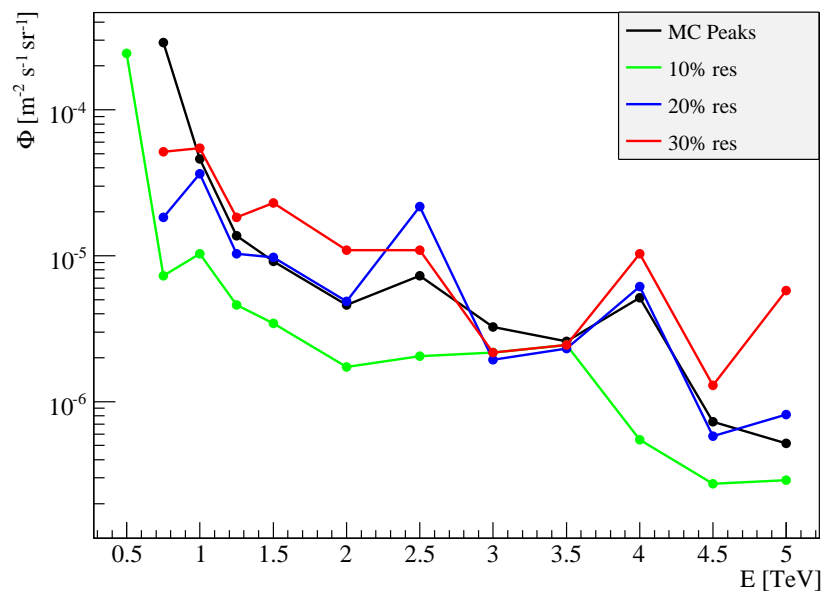


Figure B.11: Upper limits on the flux from a Gaussian signature, obtained from the off-data for the 4-tel configuration for MC peaks and different assumed energy resolutions. It is obvious that the sensitivity of the method improves with energy resolution for the most peaks under study. Due to the steep shape of the spectral distribution for energies below 1 TeV, no upper limits could be obtained for $E = 0.5$ TeV for all peak widths except 10%. See Sec. 4.3 for details.

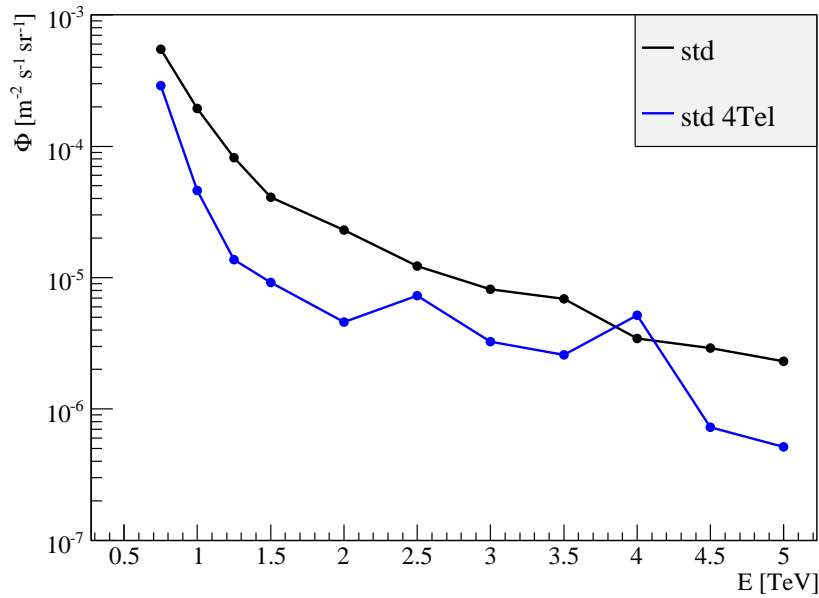


Figure B.12: Upper limits on the flux from a Gaussian signature for MC peaks for both multiplicity configurations at 95% conf. level. No background subtraction can be applied for the off-analysis, thus only two analysis configurations are used. See Sec. 4.3 for details.

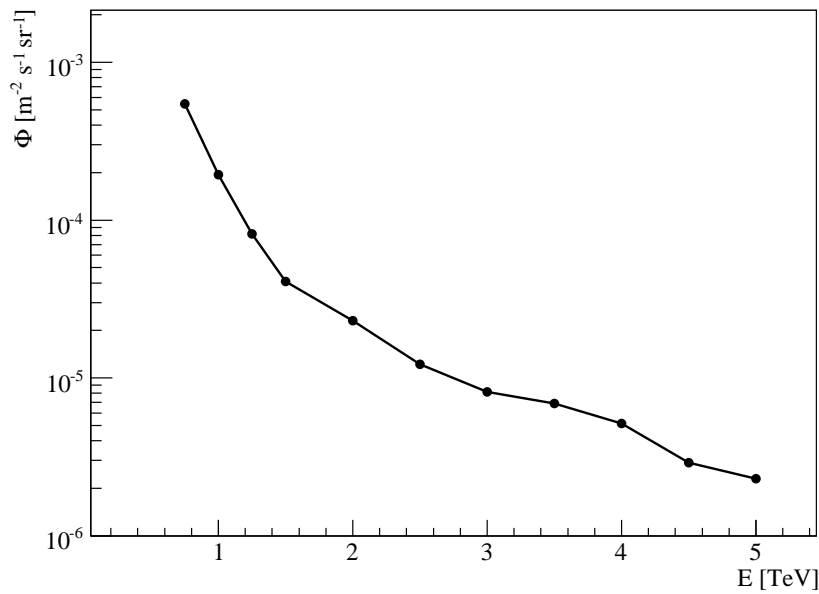


Figure B.13: Upper limits on the flux from a Gaussian signature for MC peaks at 95% conf. level, obtained by combining measurements for both multiplicity configurations. See Tab. B.2 for details.

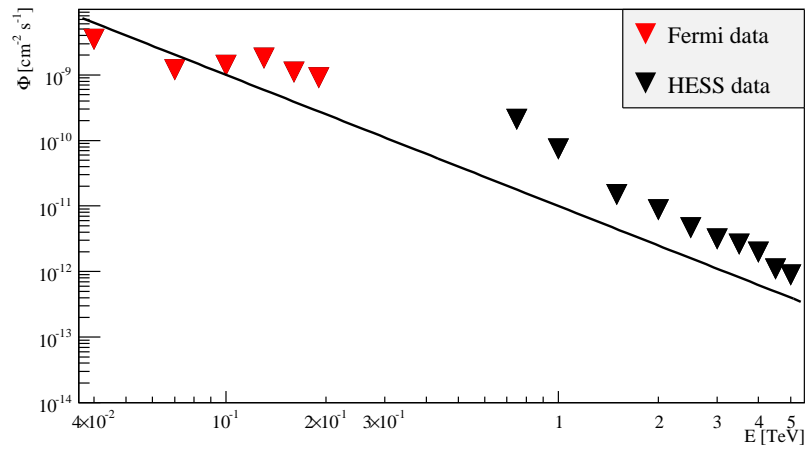


Figure B.14: Combined upper limits from the measurement presented in this work and from FERMI experiment (The Fermi LAT Collaboration et al. 2010). For the FERMI analysis, extragalactic regions ($b > 10^\circ$) and a $20^\circ \times 20^\circ$ square around the GC were used. A power-law function with an index of -2 (spectral index of diffuse extragalactic γ -rays (Egberts 2009)) is plotted to guide the eye.

Bibliography

- Abdo, A. A., Ackermann, M., Ajello, M., et al. 2009, *ApJS*, 183, 46
- Aharonian, F., Akhperjanian, A. G., Anton, G., et al. 2009a, *A&A*, 508, 561
- Aharonian, F., Akhperjanian, A. G., Anton, G., et al. 2009b, *A&A*, 503, 817
- Aharonian, F., Akhperjanian, A. G., Aye, K., et al. 2004a, *A&A*, 425, L13
- Aharonian, F., Akhperjanian, A. G., Aye, K., et al. 2004b, *Astroparticle Physics*, 22, 109
- Aharonian, F., Akhperjanian, A. G., Aye, K., et al. 2004c, *Astroparticle Physics*, 22, 109
- Aharonian, F., Akhperjanian, A. G., Barres de Almeida, U., et al. 2008a, *A&A*, 483, 509
- Aharonian, F., Akhperjanian, A. G., Bazer-Bachi, A. R., et al. 2007, *ApJ*, 664, L71
- Aharonian, F., Akhperjanian, A. G., Bazer-Bachi, A. R., et al. 2006a, *A&A*, 457, 899
- Aharonian, F., Akhperjanian, A. G., Bazer-Bachi, A. R., et al. 2006b, *Physical Review Letters*, 97, 221102
- Aharonian, F., Akhperjanian, A. G., Bazer-Bachi, A. R., et al. 2006c, *ApJ*, 636, 777
- Aharonian, F., Akhperjanian, A. G., Bazer-Bachi, A. R., et al. 2006d, *Nature*, 439, 695
- Aharonian, F., Akhperjanian, A. G., Bazer-Bachi, A. R., et al. 2008b, *Astroparticle Physics*, 29, 55
- Aharonian, F., Akhperjanian, A. G., Bazer-Bachi, A. R., et al. 2006e, *A&A*, 449, 223
- Aharonian, F., Akhperjanian, A. G., de Almeida, U. B., et al. 2008c, *Phys. Rev. D*, 78, 072008
- Aharonian, F., Akhperjanian, A. G., de Almeida, U. B., et al. 2009c, *ApJ*, 691, 175
- Aharonian, F. & Neronov, A. 2005, *Ap&SS*, 300, 255
- Aharonian, F. A. 2004, *Very high energy cosmic gamma radiation : a crucial window on the extreme Universe* (World Scientific Publishing Company; 1st edition (April 30, 2003))
- Albert, J., Aliu, E., Anderhub, H., et al. 2006, *ApJ*, 638, L101
- Atwood, W. B., Abdo, A. A., Ackermann, M., et al. 2009, *ApJ*, 697, 1071
- Baganoff, F. 2005, *APS Meeting Abstracts*, 3001

- Balick, B. & Brown, R. L. 1974, *ApJ*, 194, 265
- Bamba, A., Yamazaki, R., Kohri, K., et al. 2009, *ApJ*, 691, 1854
- Bania, T. M. 1977, *ApJ*, 216, 381
- Beilicke, M., Benbow, W., Cornils, R., et al. 2005, *ArXiv Astrophysics e-prints*
- Bélangier, G., Goldwurm, A., Renaud, M., et al. 2006, *ApJ*, 636, 275
- Berezhko, E. G. & Völk, H. J. 1997, *Astroparticle Physics*, 7, 183
- Berezinsky, V., Dokuchaev, V., & Eroshenko, Y. 2003, *Phys. Rev. D*, 68, 103003
- Berge, D. 2006, PhD thesis, Ruperto-Carola University of Heidelberg
- Bergström, L. 2000, *Reports on Progress in Physics*, 63, 793
- Bergström, L. 2009, *New Journal of Physics*, 11, 105006
- Bergström, L., Bringmann, T., Gustafsson, M., & Eriksson, M. 2006, in *American Institute of Physics Conference Series*, Vol. 861, Albert Einstein Century International Conference, 814–820
- Bergström, L., Edsjö, J., & Ullio, P. 2001, *Physical Review Letters*, 87, 251301
- Bergström, L., Ullio, P., & Buckley, J. H. 1998, *Astroparticle Physics*, 9, 137
- Bertone, G., Hooper, D., & Silk, J. 2005, *Phys. Rep.*, 405, 279
- Bertschinger, E. 1998, *ARA&A*, 36, 599
- Biermann, P. L., Becker, J. K., Caceres, G., et al. 2010, *ApJ*, 710, L53
- Bohm, G. & Zech, G. 2004, *Einführung in Statistik und Messwertanalyse für Physiker*, 2006 (Deutsches Elektronen-Synchrotron in der Helmholtz-Gemeinschaft, Zentralbibliothek)
- Bolz, O. 2004, PhD thesis, Ruperto-Carola University of Heidelberg
- Briel, U. G., Henry, J. P., & Boehringer, H. 1992, *A&A*, 259, L31
- Bringmann, T., Bergström, L., & Edsjö, J. 2008, *Journal of High Energy Physics*, 1, 49
- Brun, R., Rademakers, F., & Canal, P. 2006, <http://root.cern.ch>
- Büsching, I. & de Jager, O. C. 2008, *Advances in Space Research*, 42, 491
- Büsching, I., de Jager, O. C., & Snyman, J. 2007, *ApJ*, 656, 841
- Casse, F., Lemoine, M., & Pelletier, G. 2002, *Phys. Rev. D*, 65, 023002
- Catena, R. & Ullio, P. 2009, *ArXiv e-prints*
- Cesarsky, C. J. 1980, *ARA&A*, 18, 289
- Chang, J., Adams, J. H., Ahn, H. S., et al. 2008, *Nature*, 456, 362

- Clapson, A., Dyrda, M., Nekrassov, D., & Renaud, M. 2008, in American Institute of Physics Conference Series, Vol. 1085, American Institute of Physics Conference Series, ed. F. A. Aharonian, W. Hofmann, & F. Rieger, 681–684
- Crocker, R. M., Jones, D. I., Melia, F., Ott, J., & Protheroe, R. J. 2010, *Nature*, 463, 65
- Dame, T. M., Hartmann, D., & Thaddeus, P. 2001, *ApJ*, 547, 792
- Daum, A., Hermann, G., Hess, M., et al. 1997, *Astroparticle Physics*, 8, 1
- Davies, J. & Cotton, E. 1957, *Journal of Solar Energy Science and Engineering*
- de Naurois, M. & Rolland, L. 2009, *Astroparticle Physics*, 32, 231
- Diemand, J., Kuhlen, M., Madau, P., et al. 2008, *Nature*, 454, 735
- Dimitrakoudis, S., Mastichiadis, A., & Geranios, A. 2009, *Astroparticle Physics*, 31, 13
- Dobler, G., Finkbeiner, D. P., Cholis, I., Slatyer, T. R., & Weiner, N. 2009, ArXiv e-prints
- Duschl, W. J. & Lesch, H. 1994, *A&A*, 286, 431
- Egberts, K. 2009, PhD thesis, Ruperto-Carola University of Heidelberg
- Eisenhauer, F., Genzel, R., Alexander, T., et al. 2005, *ApJ*, 628, 246
- Feng, J. L., Matchev, K. T., & Wilczek, F. 2001, *Phys. Rev. D*, 63, 045024
- Ferrière, K. 2009, *A&A*, 505, 1183
- Ferrière, K., Gillard, W., & Jean, P. 2007, *A&A*, 467, 611
- Finkbeiner, D. P. 2004, in *Bulletin of the American Astronomical Society*, Vol. 36, *Bulletin of the American Astronomical Society*, 1478–+
- Finkbeiner, D. P. & Weiner, N. 2007, *Phys. Rev. D*, 76, 083519
- Freese, K. 2009, in *EAS Publications Series*, Vol. 36, *EAS Publications Series*, ed. E. Pécontal, T. Buchert, P. di Stefano, & Y. Copin, 113–126
- Funk, S., Hermann, G., Hinton, J., et al. 2004, *Astroparticle Physics*, 22, 285
- Gabici, S., Aharonian, F. A., & Casanova, S. 2009, *MNRAS*, 396, 1629
- Gaensler, B. M., Pivovarov, M. J., & Garmire, G. P. 2001, *ApJ*, 556, L107
- Gaisser, T. K. 1991, *S&T*, 82, 46
- Gast, R. 2009, Systematic studies of the energy reconstruction of H.E.S.S..
- Ghez, A. M., Salim, S., Weinberg, N. N., et al. 2008, *The Astrophysical Journal*, 689, 1044
- Ghez, A. M., Wright, S. A., Matthews, K., et al. 2004, *The Astrophysical Journal Letters*, 601, L159

- Goldwurm, A. 2008, in American Institute of Physics Conference Series, Vol. 1085, American Institute of Physics Conference Series, ed. F. A. Aharonian, W. Hofmann, & F. Rieger, 135–145
- Goldwurm, A., Brion, E., Goldoni, P., et al. 2003, *Astronomische Nachrichten Supplement*, 324, 377
- Haber, H. E. & Kane, G. L. 1985, *Physics Reports*, 117, 75
- Hartman, R. C., Bertsch, D. L., Bloom, S. D., et al. 1999, *VizieR Online Data Catalog*, 212, 30079
- Hillas, A. M. 1985, in *International Cosmic Ray Conference*, ed. F. C. Jones, Vol. 3, 445–448
- Hinshaw, G., Weiland, J. L., Hill, R. S., et al. 2009, *ApJS*, 180, 225
- Hinton, J. A. 2004, *New Astronomy Review*, 48, 331
- Hinton, J. A. & Aharonian, F. A. 2007, *ApJ*, 657, 302
- Hisano, J., Matsumoto, S., & Nojiri, M. M. 2004, *Physical Review Letters*, 92, 031303
- Hooper, D. 2001, *Nuclear Physics B - Proceedings Supplements*, 101, 347
- Hooper, D. & Dingus, B. 2002, *ArXiv Astrophysics e-prints*
- Hoppe, S. 2008, PhD thesis, Ruperto-Carola University of Heidelberg
- Ibata, R. A., Gilmore, G., & Irwin, M. J. 1995, *MNRAS*, 277, 781
- Kachelriess, M. 2008, *ArXiv e-prints*
- Kelner, S. R., Aharonian, F. A., & Bugayov, V. V. 2006, *Phys. Rev. D*, 74, 034018
- Kennel, C. F. & Coroniti, F. V. 1984, *ApJ*, 283, 710
- Kosack, K., Badran, H. M., Bond, I. H., et al. 2004, *ApJ*, 608, L97
- Kosack, K. P. 2005, PhD thesis, Washington University, United States – Missouri
- Kubo, H., Asahara, A., Bicknell, G. V., et al. 2004, *New Astronomy Review*, 48, 323
- LaRosa, T. N., Kassim, N. E., Lazio, T. J. W., & Hyman, S. D. 2000, *AJ*, 119, 207
- Latronico, L. & for the Fermi LAT Collaboration. 2009, *ArXiv e-prints*
- Le Guet, F. 1977, in *International Cosmic Ray Conference*, Vol. 2, *International Cosmic Ray Conference*, 208–+
- Li, T. & Ma, Y. 1983, *ApJ*, 272, 317
- Linden, T. & Profumo, S. 2010, *ArXiv e-prints*
- Lombardi, S., Aleksic, J., Barrio, J. A., et al. 2009, *ArXiv e-prints*
- Lorenz, E. 2004, *New Astronomy Review*, 48, 339

- Maeda, Y., Baganoff, F. K., Feigelson, E. D., et al. 2002, *ApJ*, 570, 671
- Mariscotti, M. A. 1966, *Nuclear Instruments and Methods*, 309
- Mayer-Hasselwander, H. A., Bertsch, D. L., Dingus, B. L., et al. 1998, *A&A*, 335, 161
- Melia, F., Liu, S., & Coker, R. 2000, *ApJ*, 545, L117
- Mizukami, T. 2008, in *American Institute of Physics Conference Series*, Vol. 1085, American Institute of Physics Conference Series, ed. F. A. Aharonian, W. Hofmann, & F. Rieger, 364–367
- Muno, M. P., Arabadjis, J. S., Baganoff, F. K., et al. 2004, *ApJ*, 613, 1179
- Muno, M. P., Bauer, F. E., Baganoff, F. K., et al. 2009, *ApJS*, 181, 110
- Murakami, H., Koyama, K., Sakano, M., Tsujimoto, M., & Maeda, Y. 2000, *ApJ*, 534, 283
- Narayan, R., Mahadevan, R., Grindlay, J. E., Popham, R. G., & Gammie, C. 1998, *ApJ*, 492, 554
- Naumann-Godó, M., Lemoine-Goumard, M., & Degrange, B. 2009, *Astroparticle Physics*, 31, 421
- Navarro, J. F., Frenk, C. S., & White, S. D. M. 1996, *ApJ*, 462, 563
- Ohm, S., Horns, D., Reimer, O., et al. 2009, *ArXiv e-prints*
- Pieri, L., Lavalle, J., Bertone, G., & Branchini, E. 2009, *ArXiv e-prints*
- Ramírez, S. V., Arendt, R. G., Sellgren, K., et al. 2008, *ApJS*, 175, 147
- Rees, M. J. & Gunn, J. E. 1974, *MNRAS*, 167, 1
- Reid, M. J. & Brunthaler, A. 2004, *ApJ*, 616, 872
- Rowell, G. P. 2003, *A&A*, 410, 389
- Ryu, S. G., Koyama, K., Nobukawa, M., Fukuoka, R., & Tsuru, T. G. 2009, *PASJ*, 61, 751
- Sawada, T., Hasegawa, T., Handa, T., & Cohen, R. J. 2004, *MNRAS*, 349, 1167
- Servant, G. & Tait, T. M. P. 2003, *Nuclear Physics B*, 650, 391
- Skilling, J. & Strong, A. W. 1976, *A&A*, 53, 253
- Springel, V., White, S. D. M., Frenk, C. S., et al. 2008, *Nature*, 456, 73
- Strong, A. W., Moskalenko, I. V., Porter, T. A., et al. 2009, *ArXiv e-prints*
- Strong, A. W., Moskalenko, I. V., & Ptuskin, V. S. 2007, *Annual Review of Nuclear and Particle Science*, 57, 285
- Tasitsiomi, A. & Olinto, A. V. 2002, *Phys. Rev. D*, 66, 083006
- The Fermi LAT Collaboration, Abdo, A. A., Ackermann, M., et al. 2010, *ArXiv e-prints*

- The H. E. S. S Collaboration: S. Funk, Hinton, J. A., & deJager, O. C. 2007, ArXiv e-prints
- The HESS Collaboration & Acero, F. 2009, ArXiv e-prints
- Tibolla, O., Chaves, R. C. G., Domainko, W., et al. 2009, ArXiv e-prints
- Tsuboi, M., Handa, T., & Ukita, N. 1999, ApJS, 120, 1
- Tsuchiya, K., Enomoto, R., Ksenofontov, L. T., et al. 2004, ApJ, 606, L115
- Tyson, J. A., Kochanski, G. P., & dell'Antonio, I. P. 1998, ApJ, 498, L107+
- van Eldik, C. 2008, in American Institute of Physics Conference Series, Vol. 1085, American Institute of Physics Conference Series, ed. F. A. Aharonian, W. Hofmann, & F. Rieger, 146–156
- Wagner, R. G. & for the VERITAS Collaboration. 2009, ArXiv e-prints
- Wagner, R. M., Lindfors, E. J., Sillanpää, A., et al. 2009, ArXiv e-prints
- Wang, Q. D., Lu, F. J., & Gotthelf, E. V. 2006, MNRAS, 367, 937
- Weekes, T. C., Badran, H., Biller, S. D., et al. 2002, Astroparticle Physics, 17, 221
- Weekes, T. C., Cawley, M. F., Fegan, D. J., et al. 1989, ApJ, 342, 379
- Winkler, C., Courvoisier, T., Di Cocco, G., et al. 2003, A&A, 411, L1
- Wommer, E., Melia, F., & Fatuzzo, M. 2008, MNRAS, 387, 987
- Zwicky, F. 1933, Helvetica Physica Acta, 6, 110

Danksagung

Diese Arbeit wäre so nicht möglich gewesen, hätte ich nicht Menschen um mich rum, die Einiges zum Gelingen beigetragen haben. Ich werde hier bestimmt nicht jedem gerecht werden, aber ich versuch's mal trotzdem. Mein Dank gilt:

- ◇ Herrn Professor Werner Hofmann für die Möglichkeit, in der Heidelberger H.E.S.S.-Gruppe an meiner Promotion zu arbeiten und das damit entgegengebrachte Vertrauen, für die fruchtbaren Diskussionen und die Unterstützung speziell bei den konzeptionellen Fragen meiner Arbeit.
- ◇ Herrn Professor Heinz Völk für die Übernahme des Zweitgutachtens und für die ermutigenden Worte.
- ◇ Christopher van Eldik für die geduldige Art und Beantwortung aller Fragen, die sehr zahlreich waren: "Ich hab da mal so eine ganz kurze Frage!" :-). Desweiteren für die Motivation, die Unterstützung bei sämtlichen Gelegenheiten, für... Ok, das würde hier den Rahmen sprengen, du weißt aber, ohne dich wäre diese Arbeit nicht das, was sie jetzt ist! Danke!!!
- ◇ Andreas und Doug (thanks for reading my manuscript!) für das Korrekturlesen von Teilen der Arbeit. Willi für die Beantwortung aller Theorie-Fragen.
- ◇ Petter, for being such a nice roommate in and outside the office (super-black!) and for reading parts of my thesis.
- ◇ Isabel Braun für die viele Unterstützung am Anfang meiner Doktorarbeit, auch bei unserer Arbeit in Namibia.
- ◇ Stefan H., Kathrin, Rolf, Joachim, Anne, Robert für den Spaß, den wir zusammen hatten, für den tollen Zusammenhalt und die gegenseitige Unterstützung, vor allem wenn's mal nicht so lief!
- ◇ Der gesamten H.E.S.S.-Gruppe für die tolle Atmosphäre!
- ◇ Den Kollegen von den Werkstätten, danke für eure Unterstützung, auch wenn ich euch dadurch manchmal etwas mehr Stress verursacht habe, als es nötig wäre! :-)
- ◇ Der gesamten Kaffeetisch-Runde für die unermüdlichen Kommentare über mein Essen! Das hat Spaß gemacht und geschmeckt hat es umso besser! :-)
- ◇ Allen meinen Freunden, egal wo ihr seid, ob in Heidelberg, Hannover, Stuttgart oder sonst wo, ohne euch gehts einfach nicht!!! Danke für eine tolle Zeit, die hoffentlich noch lange so weitergeht!!!
- ◇ Ganz speziell meinem Freund UND Kollegen Stefan Ohm, der mich zu H.E.S.S. geholt hat. Unsere Freundschaft hat ganz besonders dafür gesorgt, daß die letzten drei Jahre so eine tolle Zeit hier waren, auch wenn ich das ein oder andere nicht mehr soooo genau weiß!!!

- ◇ Natürlich auch meiner Familie, die mich immer bedingungslos, in allen Lebenslagen unterstützt hat. Carmen für die hingebungsvolle Unterstützung speziell in der Endphase meiner Promotion, beim Korrekturlesen und überhaupt fürs da sein! :-)
- ◇ Last, but not necessarily least gilt mein Dank der Welt des Heavy Metals, für die vielen tollen Momente und die unerschöpfliche Quelle an Motivation! We keep the flame burning!